# Simulating the Effect of Global Cardiac Ischaemia on the Dynamics of Ventricular Arrhythmias in the Human Heart

Mitra Abbasi

Department of Computer Science

September 2016

A thesis submitted in partial fulfilment of the requirements for the degree of

Doctor of Philosophy

# Dedication

To my mother for her endless love, support and encouragement!

To my late father, Teymour Abbasi (1947-2014), who unfortunately didn't stay with us long enough to see me become a Doctor. Dad, this is for you!

# Acknowledgements

Finally, this journey has reached an end, considering all the sweet and bitter moments. It has made this period of my life very memorable. First and foremost, I thank God for supporting me all the way and seeing me through this whole process.

My happiness and feeling of satisfaction would not be complete without mentioning everybody who gave their support and help during this time. I am deeply grateful to my supervisor Prof. Richard Clayton, for his supervision and support during this study, and especially for his confidence in me. Through his extensive experience in this area of research, he has offered helpful and productive guidance, and direction to bring this PhD study to fulfilment. I would also like to thank Dr. Eugene Chang, who proofread the thesis. I also acknowledge all my friends, thank you for your understanding and encouragement in my many moments of crisis. I cannot list all the names here, but you are always on my mind.

I am thankful to the Department of Computer Science for all computing resources. Specifically, I am grateful to ICEBERG, the Linux based High Performance Computing Cluster at Sheffield University.

It is a great sadness for me that my father passed away during the last year of my PhD study. My father was a true friend and I could always turn to him in times of stress. My dad was the greatest teacher in my whole life. There are lots of things that I have achieved since his death and I wish I could share them with him. But, I feel that he is with me along the way.

My loving memories of him give me the strength to rise to the challenge of doing this PhD and to finish it on time. The world changes from year to year, our lives from day to day, but the love and memory of him, shall never pass away.

Also, I would like to thank my mother in a special way. I express my heartfelt gratitude for her patience, kindness and extensive emotional support through good times and bad. I acknowledge my whole family for their support during all these years. They always had me in their thoughts and their prayers gave me the energy to go on to reach for the stars and chase my dreams. I would like to thank my brother, Majid Abbasi for his inspiration, support and friendship, he always helped me to release my stress and his encouragement meant I never gave up.

# Abstract

Cardiac arrhythmias are significant causes of death in the world, and ventricular fibrillation is a very dangerous type of cardiac arrhythmia. Global myocardial ischemia is a consequence of ventricular fibrillation (VF) and has been shown to change the dynamic behaviour of activation waves on the heart.

The aim of this thesis is to use computational models to study the behaviour of re-entry in the human ventricles when the heart becomes globally ischaemic. The effects of two ischaemic components (hyperkalaemia and hypoxia) on spiral wave re-entry behaviour in two dimensional (2D) ventricular tissue using two ventricular action potential (AP) models were simulated (Ten Tusscher *et al.* 2006 (TP06) and O'Hara *et al*. 2011 (ORd)). A three dimensional (3D) model of the human ventricles is used to examine the influence of each ischaemic component on the stability of ventricular fibrillation. Firstly, the main ventricular AP models relevant to this thesis are reviewed. Then, the current-voltage properties of four different $I_{K(ATP)}$ formulations are examined to assess which formulation was more appropriate to simulate hypoxia/ischaemia. Secondly, how the formulation of $I_{K(ATP)}$ influences cell excitability and AP duration (APD) in models of human ventricular myocytes is studied. Finally, mechanisms underlying ventricular arrhythmia generation under the conditions of ischaemia are investigated.

# Table of Contents

# Definitions and Abbreviations

**Model names, current and formulation terminologies**

**BCF model**   Bueno-Orovio, Cherry and Fenton (Bueno-Orovio et al. 2008) human ventricular cell model

**GB model**   Grandi-Bers (Grandi et al. 2010) human ventricular cell model

**IMW model**   Iyer, Mazhari and Winslow (Iyer et al. 2004) human ventricular cell model

**ORd model**   O'Hara-Rudy (O'Hara et al. 2011) dynamic human ventricular cell model

**PB model**   Priebe and Beuckelmann (Priebe & Beuckelmann 1998) human ventricular cell model

**TNNP model**   ten Tusscher, Noble, Noble and Panfilov (Ten Tusscher et al. 2004) human ventricular cell model

**TP06 model**   ten-Tusscher-Panfilov (Tusscher & Panfilov 2006) human ventricular cell model

**AP**   Action Potential

**APD**   Action Potential Duration (ms)

**APD90**   Action Potential Duration at 90% of repolarization

**APDR**   Action Potential Duration Restitution

**APA**   Action Potential Amplitude (APA= $V_{max}$- $V_{dia}$)

**CL**   Pacing Cycle Length (ms)

**CV**   Conduction Velocity (m/s)

**CVR**   Conduction Velocity Restitution

**DI**   Diastolic Interval, relative to APD90 (ms)

**DF**   Dominant Frequency

**EADs**   Early After Depolarisations

| | |
|---|---|
| **DADs** | Delayed after Depolarisations |
| **ECC** | Excitation-Contraction Coupling |
| **ECG** | Electrocardiogram |
| **FDM** | Finite Difference Method |
| **FEM** | Finite Element Method |
| **FVM** | Finite Volume Method |
| **LV** | Left Ventricle |
| **RV** | Right Ventricle |
| **ODE** | Ordinary Differential Equation |
| **PDE** | Partial Differential Equations |
| **RMP** | Resting Membrane Potential |
| **VF** | Ventricular Fibrillation |
| **VT** | Ventricular Tachycardia |
| **1-D** | One Dimensional |
| **2-D** | Two Dimensional |
| **3-D** | Three Dimensional |
| **PS** | Phase Singularities |
| **ERP** | Effective Refractory Period |
| **PRR** | Post-Repolarization Refractoriness |
| **RP** | Refractory Period |
| **I-V Curve** | Current Voltage relationship |
| $C_M$ | total membrane capacitance, 1 μF |
| $E_{Na}$ | reversal potential for ion $Na^+$ (mV) |
| $E_K$ | reversal potential for ion $K^+$ (mV) |

| | |
|---|---|
| $I_{stim}$ | stimulus current (µA/µF) |
| $I_s$ | current through ion channel S (µA/µF) |
| $I_i$ | ionic current density for each specific ion channel |
| $I_m$ | transmembrane current (A $m^{-3}$) |
| $G_K$ | maximum conductance of ion channel K (mS/µF) |
| $\emptyset_e$ | extracellular potential |
| $\emptyset_i$ | intracellular potential |
| $\beta_m$ | membrane surface-to volume ratio ($m^{-1}$) |
| $D$ | diffusion tensor ($m^2 s^{-1}$) |

**Currents (µA/µF)**

| | |
|---|---|
| $I_{Na}$ | $Na^+$ current |
| $I_{to}$ | transient outward $K^+$ current |
| $I_K$ | potassium ions |
| $I_{Kr}$ | rapid delayed rectifier $K^+$ current |
| $I_{Ks}$ | slow delayed rectifier $K^+$ current |
| $I_{K1}$ | inward rectifier potassium |
| $I_{Na,K}$ | $Na^+/K^+$ ATPase current |
| $I_{Na,Ca}$ | total $Na^+/Ca^{2+}$ exchange current |
| $I_{CaL}$ | L-type calcium current |
| $I_{K,ATP}$ | ATP-sensitive potassium current |
| $[K^+]_o$ | Extracellular potassium current |
| $[ATP]_i$ | intracellular ATP concentration |
| $[ADP]_i$ | intracellular ADP concentration |
| $f_{ATP}$ | fraction of open ATP-sensitive $K^+$ channel |

## Definitions and Abbreviations-continued

| | |
|---|---|
| $K_{ATP}$ | ATP-sensitive $K^+$ channel |
| $I_{K,ATP}$ | ATP-sensitive $K^+$ current |
| $\Delta J_{efflux}$ | net increment in $K^+$ unidirectional efflux rate |
| $V_{dia}$ | minimum membrane voltage during the diastolic interval |
| $V_{max}$ | maximum membrane voltage reached during the AP upstroke |
| $V_{notch}$ | minimum membrane voltage reached during the AP notch |
| $V_{plateau}$ | maximum membrane voltage reached during the AP plateau or dome phase |

# 1 Introduction

## 1.1 Motivation

Cardiac death is the foremost cause of mortality in the world. Ventricular arrhythmias, especially ventricular fibrillation (VF) are known as the main cause of sudden cardiac death (Bernus et al. 2005). It is very challenging to understand the mechanisms of generation, maintenance and termination of these arrhythmias. Another major scientific challenge concerns their prediction and prevention. To meet these challenges subcellular, cellular, tissue, organ and system information on a huge scale must be integrated.

Properties of cardiac myocytes (biophysical and biochemical) and the anatomical structure of the heart can be modelled with computer simulations to study the mechanisms underlying cardiac arrhythmias. Theoretical and computational modelling studies have provided significant knowledge of the mechanisms underlying arrhythmias to surmount these challenges. Computational cardiac electrophysiology is the main progressive area in computational physiology and is concerned with the investigation of the electrical activity of the heart.

The heart is an electrical conductor and a mechanical pump, a complex system; basic science and clinical studies are insufficient to fully understand cardiac function. The study of ionic mechanisms of normal and abnormal heart rhythm, electrotherapy, and the electrocardiogram can be improved using multiscale cardiac modelling and simulation (Carusi et al. 2012). Computer simulations in a 3D model of the heart suggest that rotating 2D spiral waves, which form scroll waves in 3D, are a plausible underlying mechanism of VF (Mandapati et al. 1998). In addition, ischaemia produces changes in the dynamics of the spiral waves resulting in variations in the activation patterns during the development of VF. Although VF could be described in terms of electrical waves propagating throughout the 3D myocardium, incomplete information exists about the mechanisms responsible for the modifications in excitation patterns as global ischaemia progresses during the development of VF. Therefore, it is essential to develop multiscale modelling methods to clarify the mechanisms of cardiac arrhythmias as a result of the progression of global ischaemia.

## 1.2 Summary and Key Challenges

Previous work has attempted to investigate the mechanisms of cardiac arrhythmias in the ischaemic heart by exploring the mechanisms of onset, sustenance, and ending of these arrhythmias. However, the complication of ischaemia coupled with the limitations in current experimental methods have prevented detailed assessment of the role of ischaemia in the dynamic electrical behaviour of the heart and underlying mechanisms. Computer simulations are a useful tool to provide insight into different levels from the ionic channel to the whole organ to consider the behaviour of ischaemic abnormalities in cardiac electrophysiology (Rodríguez et al. 2006). Experimental models have constraints that prevent the assessment of arrhythmogenic mechanisms, and this poses difficulty in developing treatments for ischaemic cardiac disease. For example, electrophysiological variations resulting from coronary blockage are very fast, especially throughout the first stage of ischaemia, therefore making it challenging to completely evaluate the cause-and-effect connections between metabolic and electrophysiological parameters (Rodríguez et al. 2006). Therefore, computational research in electrophysiology with the contribution of mathematical models can explain various effects and highlight the main connections between electrophysiological parameters. This is important in determining the function of ischaemic abnormalities in the electrophysiological behaviour of the heart.

In this thesis, a systematic study using the most detailed human ventricular models is made to investigate the role of ionic current properties (under normal and ischaemic conditions) in modulating arrhythmias. More specifically, this study provides an efficient examination into how mutations in certain ionic current properties (affected by cardiac ischaemia) can modulate Action Potential (AP) shape, AP Duration (APD), Conduction Velocity (CV) and restitution (the rate adaption of cardiac cells and tissue) properties. Simulation results are compared with experimental data that exhibit the importance of the examinations accomplished in this study as a potent technique for the efficient and in-depth accuracy of AP models. The simulations show that the electrophysiological properties, in most cases, are compatible with experimental data achieved using human ventricular myocytes. Furthermore, in this study, the effects of the main ischaemic components causing AP modulation on the primary cellular biomarkers of arrhythmic risk are analysed. One significant part of the study focuses on analysing the role of the ATP-sensitive potassium current ($I_{K,ATP}$) models involved in hypoxia/ischaemia in modifying electrophysiological properties related to cardiac

arrhythmia. Hypoxia is mimicked by decreasing the intracellular ATP concentration that influences the ATP-dependent potassium, by testing four different $I_{K,ATP}$ models at the cellular and tissue levels and Shaw and Rudy's $I_{K,ATP}$ formulation is employed to model the hypoxia for the 3-D tissue simulations.

The effects of ischaemic components (hypoxia and hyperkalaemia) on the stability of spiral wave re-entry in modelled 2-D and 3-D cardiac tissue using the Ten Tusscher-Panfilov 2006 (TP06) (Ten Tusscher & Panfilov 2006) and the O'Hara-Rudy dynamic (ORd) (O'Hara et al. 2011) ventricular AP models are simulated. These models are used to test the assumption that global myocardial ischaemia reduces activation rate during ventricular arrhythmias in human hearts, as enhancing wavebreak, and the dynamic instability of spiral waves by targeting electrical restitution properties. For example, the activation of the $I_{K,ATP}$ channels is accountable for the major APD reduction noticed in hypoxic cardiomyocytes, as an enhancement in $[K^+]_o$ affects resting depolarization, therefore, resulting in low excitability and lengthened postrepolarization refractoriness in ischaemic cardiomyocytes (Rodríguez et al. 2006). Results indicate that the steady state APD and APD restitution (APDR) curve characteristics are well reproduced by the selected models under control (non-ischaemic) situations and how varying ischaemic components modulate them.

Spiral wave re-entry as a cause of cardiac arrhythmia has been simulated in selected cardiac tissue models. The dynamic stability of spiral waves has been investigated when the electrophysiological properties of the cardiac cell model have specified characteristics, such as the variability of the APDR curve under ischaemic conditions. The dynamic instability of cardiac electrical wave propagation associated with a variety of ischaemic components altering the electrophysiological characteristics is also examined in a 3-D computational model.

The structure of this thesis is summarised in Figure 1.1, where a brief physiological overview for each individual level of structure (cell and tissue) is provided containing the essential features of the study. The schematic of the entire thesis shows that the computational models were used to incorporate procedures from the ion channels (mainly focused on the $K_{ATP}$ channels studied in Chapter Five and potassium channels) to the whole cells and multi-cellular tissue (Chapters 6-9). The main focus of this study is to examine the mechanism of ischaemia (changes at the ion channels) and the interaction of these changes (e.g. increasing

extracellular potassium currents and decreasing $I_{KATP}$) in different cell types (epicardium, midmyocardium and endocardium) and their influence on tissue behaviour. As presented in Figure 1.1, the ventricular cell models are studied in Chapter Four to select two human ventricular cell models. Then in Chapter Five the current-voltage properties of $I_{K,ATP}$ through the activation of $K_{ATP}$ channels is studied to show the voltage dependency of $I_{K,ATP}$ models and their effects on action potential at the cell and tissue level. The cellular AP and ionic currents (ion concentration changes as consequences of ischaemia) were the main properties linking the models at the different scales. For instance, the restitution (the rate adoption of cardiac cells and tissue) properties (APDR and CVR), which are studied in Chapters 6-7, have been shown to be the important aspect in controlling the dynamic instability of spiral wave re-entry in 2D and 3D tissue models (Chapter Nine).

The main concerns associated with the modelling of ischaemia at each level and the dynamic behaviour of ischaemia are discussed; this is mainly focused at the tissue level. More details of the structure of this thesis are presented in Section 1.4.

Cell level (Chapter 4)

Action potential

Model comparison (Chapter 4)

$$I_{stim} = C\frac{dV_m}{dt} + I_m$$

Cardiac Muscle Cells

Tissue level
(Chapter 6-9)

Models selection (Chapter 4)

1D

Characteristics of KATP
Channels (Chapter 5)

Ion channel
(Chapter 5)

2D

Restitution studies (Chapter 6-7)

Re-entry Spiral wave (Chapter 9)

Propagation model

$$\frac{\partial V_m}{\partial t} = \nabla \cdot \mathbf{D}\nabla V_m - \frac{i_{ion}}{C_m}$$

3D

Scroll wave re-entry (3D Model) – Arrhythmias
(Chapter 9)

**Figure 1.1 A schematic plot of multiscale modelling of cardiac electrophysiological function (based on integrated data from ionic to whole organ level). Numerical models are used to integrate and build models at different levels. The cellular AP and ionic currents (ion concentration changes resulting from ischaemia) were the main properties linking the models at the different scales. The ionic components of cardiac ischaemia at the cell level will be examined for investigation of the cellular and sub-cellular process in the different populations of cardiac cells. Then, a tissue model will be simulated to investigate how combinations of ischaemic parameters influence the dynamic properties of the model (i.e. APD, CV restitution and tissue wavelength). Electrophysiological properties computed in cardiac tissue were the main focus of this thesis.**

## 1.3 Aims and Objectives

In this thesis, the emphasis is on the mechanism of modification of sustainability of human ventricular arrhythmias by global cardiac ischaemia. One of the important arrhythmia mechanisms is spiral wave re-entry, which acts to sustain VF. A basic mechanism in the maintenance of VF is wavebreak and wavelet formation. Most studies in animal models (Mandapati et al. 1998) have shown a decrease in wavebreak during ischaemic VF, whereas the opposite effect has been found in the intact and in-situ human heart (Nash et al. 2006). In contrast to animal models, an increase in wavebreak with a higher number of Phase Singularities (PS) (PS is a point in the 2-D spiral wave where the wavefront and wave tail meet) and an increased proportion of shorter wavefronts are expected (Bradley et al. 2011). Increasing wavebreak during ischaemia could be explained by prolonged refractoriness dependent on APD. The restitution properties of APD and CV, and the period of re-entry will be investigated to explain increased organisation during global ischaemia. Experimental data from human hearts indicate that during VF, ischaemia acts to enlarge the re-entry period, and enhance the complexity (number of re- entrant waves). However, based on flattening of the restitution curve, it would be expected that ischaemia decreases the complexity. Thus, the question here is how do the restitution properties apply to ischaemic VF?

The research goal is to examine the effects of global cardiac ischaemia on the dynamics of ventricular arrhythmias in a model of the human heart. Detailed objectives are summarised here. A comprehensive review of the current realization of the mechanism of ventricular arrhythmias, focusing on the effect of global cardiac ischaemia in the human heart, is provided based on mathematical modelling and scientific examination. The main targets to prepare a fundamental level outline of cardiac excitation and conduction corresponding to ventricular arrhythmia dynamics under ischaemic conditions are summarised here:

- To evaluate the quantitative influence of four different $I_{K,ATP}$ models and to examine the assumption that the ATP activated $K^+$ current $I_{K,ATP}$ plays a significant role in repolarization differences during global ischaemia.
- To test the contribution of different $I_{K,ATP}$ models to the dynamic behaviour of the electrical activity of cardiac tissue.
- To examine the dynamic behaviour of re-entry spiral wave to investigate quantitatively the impact of various $I_{K,ATP}$ formulations on tissue electrical activity.

- To investigate different types of heterogeneity that lead to wavebreak during ventricular arrhythmia with global myocardial ischaemia in the human heart.

- To study the dynamic behaviour and impact of simulated global cardiac ischaemia on a human ventricular 2-D tissue model.

- To study ventricular arrhythmia using a 3-D model of the human ventricles to determine the influence of each ischaemic component on the stability of ventricular fibrillation.

- To analyse the effects of ischaemic components on the difficulty of VF demonstrated by the number of scroll wave filaments.

The main ionic components of cardiac ischaemia at the cell level will be examined for a better understanding of the cellular and sub-cellular process in the different populations of cardiac cells. For this purpose, model parameters will be provided to represent the combined effects of hyperkalaemia (increased extracellular potassium) and hypoxia (reduction of oxygen). Moreover, a tissue model will be simulated to investigate how combinations of ischaemic parameters influence the dynamic properties of the model (i.e. APD, CV restitution and tissue wavelength).

## 1.4   Thesis Outline

This thesis examines ventricular arrhythmia focusing on the effect of global ischaemia in the human heart. **Chapter Two** introduces the necessary biological background and the basic structure of the heart. Cardiac electrophysiology, the role of ion channels, and cellular and tissue electrophysiology in the normal electrical functioning of the heart are discussed. Dynamic properties of excitation and propagation in cardiac muscle, electrophysiological heterogeneities and different types of arrhythmia mechanisms are described in this chapter. The ischaemia mechanism, the main electrophysiological changes and different types of arrhythmia mechanisms, which occur during ischaemia are also described. Finally, an outline of cardiac electrophysiology modelling of ischaemia and arrhythmias to investigate arrhythmia mechanisms relevant to this thesis is presented. **Chapter Three** describes the main mathematical and computational framework and implementation techniques on which the rest of the work is based. Models of transmembrane ionic currents starting with a description of the Hodgkin-Huxley equations on which most cell models are based are presented. The main ventricular AP models relevant to this thesis are reviewed. Then, the main ionic current formulations used in cell models are described followed by a description

of Ordinary Differential Equation (ODE) solvers for these models. Mathematical models of cardiac tissue electrophysiology using the bidomain and monodomain equations of electrical conduction are described. Furthermore, an outline of the mathematical methods applied for simulation of tissue electrophysiology is provided in this chapter. Strategies for recognizing and tracking phase singularities in computational re-entrant models in 2-D and 3-D are outlined. Finally, the chapter concludes with a description of the state-of-art in computational modelling and a brief review of the software packages used in computational modelling of cardiac electrophysiology. Validation strategies are discussed as is the necessity of using validation in computational cardiac electrophysiology.

In **part I**, consisting of **Chapters 4-5**, the cellular electrophysiology mechanisms of human ventricular myocytes in two cell models (TP06 and ORd) are investigated (**Chapter Four**). Current-voltage properties of each $I_{K(ATP)}$ formulation, which is an important component of cardiac ischaemia, are also considered (**Chapter Five**). In **part II**, consisting of **Chapters 6-9**, a 2-D tissue model of human ventricles is used to examine the dynamic behaviour of normal tissue (**Chapter Six**) and how the formulation of $I_{K(ATP)}$ influences cell excitability and action potential duration in the TP06 and ORd models of human ventricular myocytes is investigated (**Chapter Seven**). In **Chapter Eight**, the changes in effective refractory period (ERP) and post-repolarisation refractoriness (PRR) during global cardiac ischaemia are explored in two 2-D tissue models. The electrical activity in the human ventricles under conditions of ischaemia is studied (**Chapter Nine**). 2-D and 3-D tissue models are used to investigate mechanisms underlying ventricular arrhythmia generation under the conditions of ischaemia (**Chapter Nine**). The contents of each chapter are summarised in more detail below.

**Part I**

**Chapter Four**

In this chapter, the current most detailed human ventricular models are studied. The TP06 (Ten Tusscher & Panfilov 2006) and ORd (O'Hara et al. 2011) models were used to analytically examine the ionic foundation of electrophysiological characteristics associated with arrhythmic risk in human ventricular cardiomyocytes. A short description is provided of the different human ventricular cells models and the chapter concludes with selection of two human ventricular cell models for further study (TP06 and ORd).

**Chapter Five**

In this chapter, different formulations of the ATP sensitive $K^+$ current which is important for myocardial hypoxia/ischaemia as the most common conditions leading to development of serious arrhythmias and to a decrease in cardiac contractility are studied. Current Voltage (I-V) dependence of each model and the influence of $I_{K,ATP}$ on the enhancement in the rate of cellular $K^+$ efflux during ischemia (hypoxia) are computed.

**Part II**

**Chapter Six**

In this chapter the concept of the mechanistic rate-dependent phenomena, which is important for characterising the heart's behaviour to arrhythmias will be investigated. The activation of three cell types of cardiac tissue will be simulated during normal condition with electrophysiological computational models (TP06 and ORd models), which use the concepts of reaction-diffusion systems. The aim of this chapter is to perform precise simulation of rate-dependent properties of action potential models and systematically improve that leads to more accurate multicellular simulations of arrhythmia.

**Chapter Seven**

The aim of this chapter is to consider the dynamic behaviour of the electrical activity of cardiac tissue using different $I_{K,ATP}$ models. This chapter highlights the main differences in the observed electrophysiological properties related to $I_{K,ATP}$ models to changes in the dynamic behaviour of the electrical activity of two 2-D monodomain tissue models. Restitution properties of APD and CV, and the dynamic behaviour of re-entry spiral wave are examined.

**Chapter Eight**

In addition to considering APD as a measure of refractory period in ischaemia, PRR has been suggested to be a proarrhythmic phenomenon that may protect the heart from re-entrant arrhythmias during ischaemia. The aim of this chapter is to evaluate the refractory period and post-repolarisation refractoriness for the ischaemic condition in two 2-D monodomain tissue models.

**Chapter Nine**

In this chapter, simulations incorporating ischaemic components into tissue models are performed to assess the effect of the different cellular mechanisms influenced by ischaemic variations on the APD. Each mechanism will be described using a computational model that is integrated into a whole cell model allowing the evaluation of changes in APD and CV. Analysis of electrophysiological phenomena is performed to analyse different effects and to examine important associations between electrophysiological parameters in determining the role of ischaemic abnormalities in cardiac electrophysiological behaviour. In this chapter, the electrophysiological consequences of global cardiac ischaemia and the mechanisms of arrhythmia creation under ischaemia conditions are elucidated. The focus of this chapter is to represent events (arrhythmia mechanisms) during global cardiac ischaemia by examining the dynamics of scroll-wave filaments in the human ventricles and measuring the number of filaments (demonstrated in the number of phase singularities).

**Chapter Ten**

The thesis ends with a discussion in which the most challenging problems in the study of ventricular arrhythmias under ischaemic conditions are discussed. The discussion sections of each chapter, limitations and future work are briefly reviewed. It is concluded that the simulation results provide an insight to better understand the behaviour of ventricular arrhythmias and the mechanisms that sustain arrhythmias during global cardiac ischaemia.

## 2 Background

*The main focus of this thesis is to gain insight into the underlying mechanisms of ventricular arrhythmias with a focus on global cardiac ischaemia, using electrophysiological models of the human heart. This chapter as a general introduction in this thesis introduces the basic electrophysiology and anatomy of the human heart from the whole organ to the ionic level with a detailed description of the ionic currents involved in cardiac cell excitation. Furthermore, the underlying electrophysiological processes are presented from subcellular to organ level. Next, basic information on cardiac arrhythmias that will be most relevant to this thesis is provided. The main focus, as a main core of this thesis, will be on global cardiac ischaemia alternation with an emphasis on electrophysiological changes and underlying arrhythmias. The focus then shifts to the modelling of cardiac arrhythmias with different patterns of arrhythmias. Finally, a short outline of multiscale modelling of the heart for the study of ventricular arrhythmias is provided.*

## 2.1 Cardiac Anatomy and Physiology
### The Heart

**Size, Location, Orientation and Layer of the heart wall**

The human heart is a muscular organ between 250 and 350 grams and is almost the size of a human fist. The heart is located between the lungs and superior to the diaphragm in the chest cavity. The heart wall can be divided into three layers, all richly supplied with blood vessels: the outer epicardium; the myocardium (muscle heart); and the inner endocardium layer. The heart is separated into two halves and the halves are also separated into four chambers, named the right atrium, right ventricle, left atrium and left ventricle (Figure 2.1). Valves allow blood to flow in one direction from atria to ventricles. Oxygenated blood is collected by the left atrium from the pulmonary circulation; the right atrium gets deoxygenated blood from the circulatory system. Then, the oxygenated blood is received by the left ventricle from the left atrium, and pumped to the whole body, excluding the lungs. To oxygenate the blood, the right ventricle collects deoxygenated blood from the right atrium and pumps it into the lungs. This muscle produces electrical impulses that instigate cardiac contraction, pumping 4300 gallons of blood throughout the body a day (Marieb & Hoehn 2010).
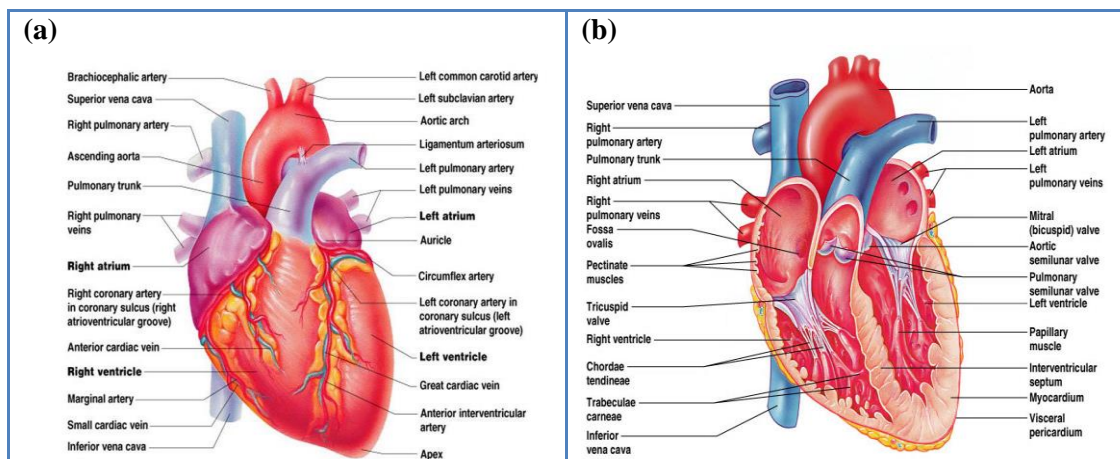


**Figure 2.1. Anatomy of the heart (Marieb & Hoehn 2010). (a) Anterior view, vessels transporting oxygen-rich blood are red; those transporting oxygen-poor blood are blue (Marieb & Hoehn 2010, p. 679). (b) Frontal section showing interior chambers and valves (Marieb & Hoehn 2010, p. 681).**

## Structure of the Heart

### Properties of Cardiac Muscle Fibres, Microscopic Anatomy

The cardiac muscle has a striated shape and contracts with the sliding filament system, tube formed fibres that generate mechanical tension in the cells. Cardiac cells are short, fat, branched, and interconnected like the ribs of two sheets of striped cardboard at dark-staining junctions called intercalated discs (Figure 2.2). These discs contain connecting gap junctions, which allow ions to move from cell to cell, diffusing a depolarizing current through the entire heart. Fibroblasts, the largest population of the cells in the heart, are organised in sheets, which can perform a dynamic function in tissue electrophysiology. The shape and arrangements of myocytes are important and effective in AP shape, APD and CV (Gilbert et al. 2007). Electrical excitation across the surface membrane leads to an action potential to propagate along the surface and along the transverse tubules (T-tubule) (Bers 2002).
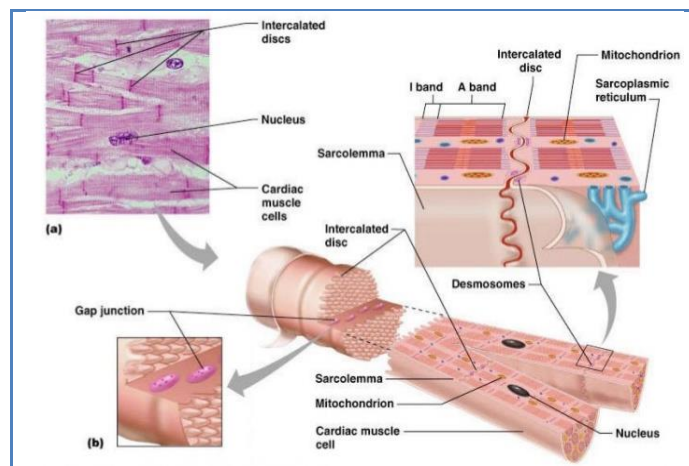


**Figure 2.2. Microscopic anatomy of cardiac muscle (Marieb & Hoehn 2010,p. 688). (a) Photomicrograph of cardiac muscle. (b) Cardiac cell relationships at the intercalated discs.**

## Conduction System

### Mechanism and Events of Contraction

The heart contracts by the diffusion of the depolarization wave within the heart from cell to cell through ion channels via gap junctions, which link all cardiac muscle cells together into a single contractile component. The cardiac muscle contracts by action potentials that sweep across cell membranes. About one percent of cardiac cells are auto-rhythmic with the capability to depolarize automatically and consequently pace the heart; however, most heart muscle consists of contractile muscle fibres accountable for the heart's pumping activity

(Marieb & Hoehn 2010). The sequence of electrical events in these contractile cells is as follows (Figure 2.3) (Marieb & Hoehn 2010):

1. Entry of $Na^+$ from extracellular fluid into cardiac cells initiates a positive feedback cycle. This causes the rising phase of action potentials by opening voltage-regulated fast $Na^+$ channels. The period of increased $Na^+$ permeability is very short, because the sodium gates are rapidly inactivated and the $Na^+$ channels close.

2. Spread of the depolarization wave to the T tubules triggers the Sarcoplasmic Reticulum (SR) to distribute $Ca^{2+}$ through the sarcoplasm (Marieb & Hoehn 2010).

3. A signal is generated from the excitation-contraction coupling of $Ca^{2+}$ that passes activation and the depolarization wave via myofilaments slides (Marieb & Hoehn 2010).
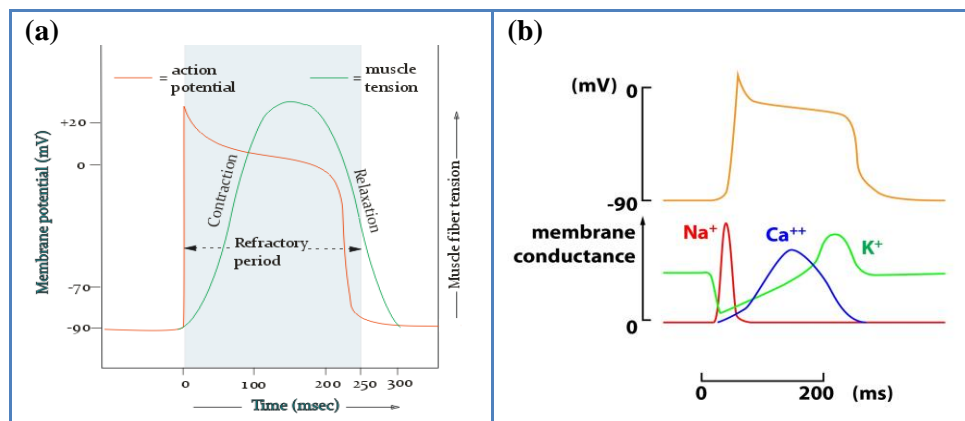


**Figure 2.3. Changes in membrane potential and permeability during action potential of contractile cardiac muscle cells based on (Marieb & Hoehn 2010,p. 689). (a) Association between AP and period of contraction in a single ventricular cell. (b) Membrane permeability changes during action potential. (Figure used from: http://physiologyplus.com and http://fblt.cz/ with permission).**

## Heart Physiology, Electrical Events

One important property of heart muscle is its capacity to depolarize and contract dependent on the nervous system. The activity of the heart is a function of the presence of gap junctions, and the action of the cardiac conduction system. The intrinsic cardiac conduction system initiates and distributes impulses within the heart, thus it depolarizes and contracts in a systematic, consecutive way. This system works by initiation of action potential via autorhythmic cells, which are continuously depolarizing to reach a threshold. They have

unstable resting membrane potential and initiate the action potentials by changing membrane potentials. Rhythmic contractions are triggered when action potentials spread throughout the heart by pace maker potentials (Figure 2.4). The mechanism of the pacemaker potential results from gradually reduced membrane permeability to $K^+$. The $Na^+$ continues to transmit slowly into the cell because of the $Na^+$ penetration. Then the intracellular membrane potential becomes more positive because the $Na^+$ concentration inside the cell stays high and the $K^+$ ion concentration low. Eventually, fast $Ca^{2+}$ channels open at threshold (about -40 mv), accepting an influx of $Ca^{2+}$ from the extracellular space. Hence, the climbing phase of the action potential produced by the influx of $Ca^{2+}$. The declining phase of the action potential and repolarization indicate increased $K^+$ permeability and efflux from the cell. After completion of repolarization, $K^+$ channels are inactivated, $K^+$ permeability reduces, and the slow depolarization to threshold begins again. The autorhythmic heart cells are found in sinus (SA) node via atrial, atrioventricular (AV) node, atrioventricular (AV) bundle, right and left bundle branches, and Purkinje fibres in ventricular septum. Impulses pass across the heart in the same order (sequence of excitation is shown in Figure 2.4) (Marieb & Hoehn 2010).
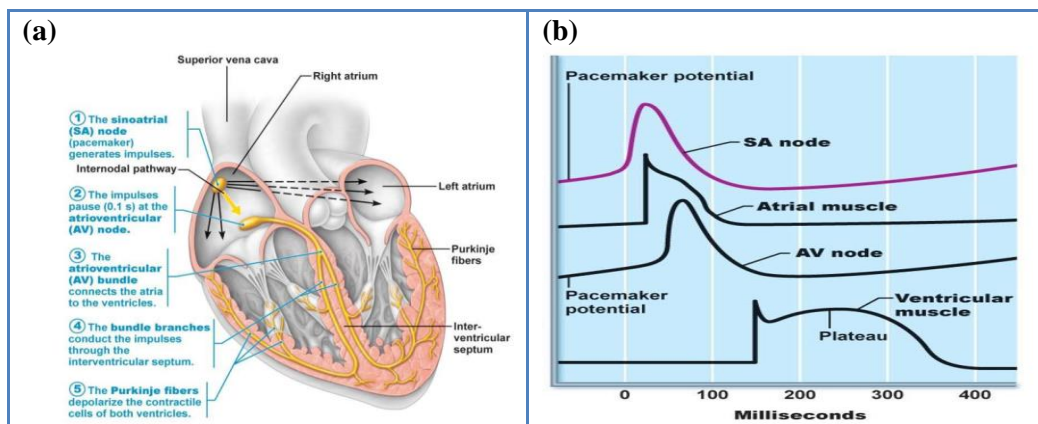


**Figure 2.4. The cardiac intrinsic conduction system and action potential succession during one heartbeat (Marieb & Hoehn 2010,p. 691). (a) Anatomy of the basic conduction system presenting the order of electrical activation. (b) Comparison of action potential shape at various locations in the heart.**

## 2.2 Cardiac Electrophysiology (Normal Condition)

The cellular basis of cardiac electrical activity, cardiac tissue electrical function and mechanisms of arrhythmia are addressed in this section.

### 2.2.1 Structure of Ion Channel Function

**Sodium Channels**

The $Na^+$ channels and their properties are important in physiological and cardiological studies. Voltage-gated $Na^+$ channels are accountable for the initial rising phase of the AP in excitable heart tissue. They regulate conduction of excitation by mediating rapid transmission of depolarizing electrical pulses throughout the myocardium (Li et al. 2000).

**Cardiac Calcium channels**

The $Ca^{2+}$ channels are essential contributors to cardiac electrophysiological properties that initiate cardiac excitation-contraction (E-C) coupling. There are two main types of $Ca^{2+}$ channels expressed in cardiac myocytes: L-type ($I_{Ca,L}$) which is presented in all cardiac myocytes; and T-type ($I_{Ca,T}$) that is more prominent in atrial and cardiac Purkinje cells. $I_{Ca,L}$ is the main route of $Ca^{2+}$ entry into the cell and $I_{Ca}$ plays a central role in cardiac electrophysiology, influencing AP shape and arrhythmogenesis (via EADs) (Bers 2000).

**Potassium channels**

The cardiac AP is governed by the complex interaction between depolarisation of inward currents and repolarisation of outward currents. The repolarising currents originate from the outward movement of $K^+$ ions through $K^+$ channels. Functional changes in $K^+$ channels lead to the modulation of the electrical and contractile properties of the heart and are associated with a number of cardiovascular disorders, including the long QT syndromes (Sah et al. 2003).

**Membrane pumps and exchangers**

Membrane pumps and exchangers are responsible for the maintenance of ion gradients and the intracellular ionic environment to enable electrical signalling. Four prominent membrane pumps and exchangers which are well researched are: membrane ion pumps including the sarcolemmal sodium ($Na^+$)-potassium ($K^+$)-adenosine triphosphatase (ATPase), and calcium

$(Ca^{2+})$-ATPase, and membrane ion changers including the sarcolemmal $Na^+$-$Ca^{2+}$ exchanger and $Na^+$-hydrogen $(H^+)$ exchangers. The maintenance of $Na^+$ and $K^+$ concentration gradients in cells depends on the constitution of the $Na^+$ pump of cardiac sarcolemma by the magnesium $(Mg^{2+})$-activated $Na^+$- $K^+$-ATPase. This function is important to normal cellular operation due to the existence of these ion gradients that underlie electrical excitability, cell volume and pH regulation, and the provision of energy for the active transport process (Marieb & Hoehn 2010). The sarcolemmal $Ca^{2+}$-ATPase does not appear to contribute substantially to diastolic $Ca^{2+}$ removals in cardiac tissue; however, it plays a role in myocardial relaxation. The $Na^+$-$H^+$ exchanger maintains pH in cardiac sarcolemmal membranes. The regulation of intracellular pH is important to tissue for energy utilization and metabolic acids generated during repetitious contractile activity (Marieb & Hoehn 2010). The $Na^+$-$Ca^{2+}$ exchanger is the primary system for trans-sarcolemmal $Ca^{2+}$ removal. This mechanism removes the same amount of $Ca^{2+}$ that inserts through L-type $Ca^{2+}$ channels on a beat-to-beat basis (Lee & Hryshko 2004).

### 2.2.2  Ion Channels, Cellular and Tissue Electrophysiology

#### *2.2.2.1  Expression of Ion Channels in the Myocardium*

The normal contraction of the heart (mechanical pump) depends on action potential generation. Action potential propagation is accompanied by a sequence of relaxation and a refractory period until the next impulse is triggered. Action potentials indicate the consecutive stimulation of inward ($Na^+$ and $Ca^{2+}$) and efflux ($K^+$) current moving ion channels (Figure 2.5.b). The outward $K^+$ currents and properties underlie causes of myocardial action potential repolarization which are associated with the initiation of normal cardiac rhythms. Myocardial action potential depolarization is related to the activation of the voltage-gated inward $Ca^{2+}$ channel currents and the $Na^+$ channel currents.

Figure 2.5.a shows the electrical function of the heart in different cardiac cells. These activations start from pacemaker areas in the heart and propagate through the ventricles. The normal cardiac rhythms are generated by contribution of the direct propagation of excitation through the myocardium (Figure 2.5.a) in which the action potential waveforms are separated in different regions (Nerbonne & Kass 2005). The pacemaker cells initiate action potential and then distribute it within the atria to the atrioventricular (AV) node (Figure 2.5.a). Excitation propagates in the conducting Purkinje fibres to the ventricles after a short delay in

the AV node. Excitation-contraction in cardiac muscle is the process caused by propagation of action potential in each myocardial cell. Action potential triggers a myocyte to contract. The propagation of action potential is continued after a refractory period (during the refractory period it is impossible to generate another action potential). This process continues until induction of the next impulse (Nerbonne & Kass 2005). The differences in ion channels can produce heterogeneities in action potential waveforms. The depolarisation of the action potential (phase 0) is fast in ventricular and atrial myocytes and in Purkinje fibres (Figure 2.5.a) due to triggering of $Na^+$ channels. However, the upstroke of AP is markedly slower in pacemaker cells (SA and AV nodes) in comparison with atria/ventricles (Figure 2.5.a) that show voltage-gated $Na^+$ channels do not perform a significant role in these regions.

This section illustrates that the differences in the functional of ion channels and their properties can have significant influences on AP waveforms, propagation, and rhythmicity which are important in a variety of myocardial diseases (Nerbonne & Kass 2005).
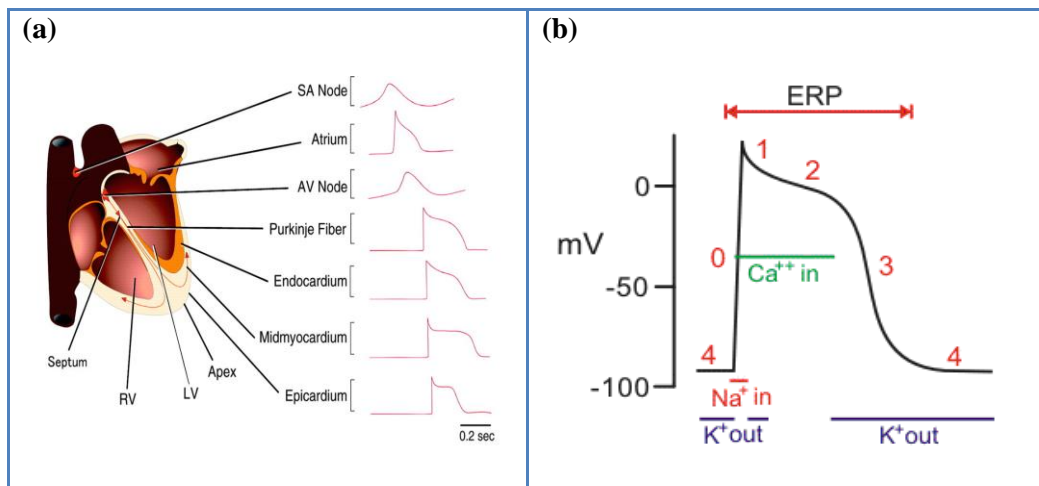


**Figure 2.5. Schematic of electrical activity in the human myocardium with (a) presentation of action potential waves in different regions, (figure from Nerbonne & Kass 2005 with permission) and (b) the action potential waveform underlying ionic currents in human ventricular myocytes.**

### 2.2.2.2 Cardiac Tissue Architecture

The characteristics of conduction and propagation in tissue structure under normal and abnormal conditions have been determined in numerous studies (Marieb & Hoehn 2010). It has been shown that the tissue structure of the heart is an important modifier of impulse conduction under both physiological and pathophysiological conditions.

The cellular tissue architecture of myocardium presents a multiple branching structure (Chabiniok et al. 2016) (Figure 2.6). Ventricular myocardium is a hierarchy of discrete muscle layers, which are connected to each other by bridges. At the microscopic level, heart tissue contains different cell types, myocytes and fibroblasts (Camelliti et al., 2005) (Clayton et al, 2011). The main component of cardiac tissue is cardiac myocytes that produce mechanical tension. Gap junctions have a cylindric shape, placed between the two-coupled cells in the membrane. Gap junction channels link myocytes, which allow AP to propagate through the intracellular myocytes. Ventricular myocytes are structured into sheets that have laminar structure. They are detached by layers of tissue (cleavage planes) (HORT 1960). In this network, the shape and arrangements of myocytes play a significant role in the propagation and velocity of conduction (Wellens 2004). For instance, conduction velocities are faster along than across the cardiomyocytes.
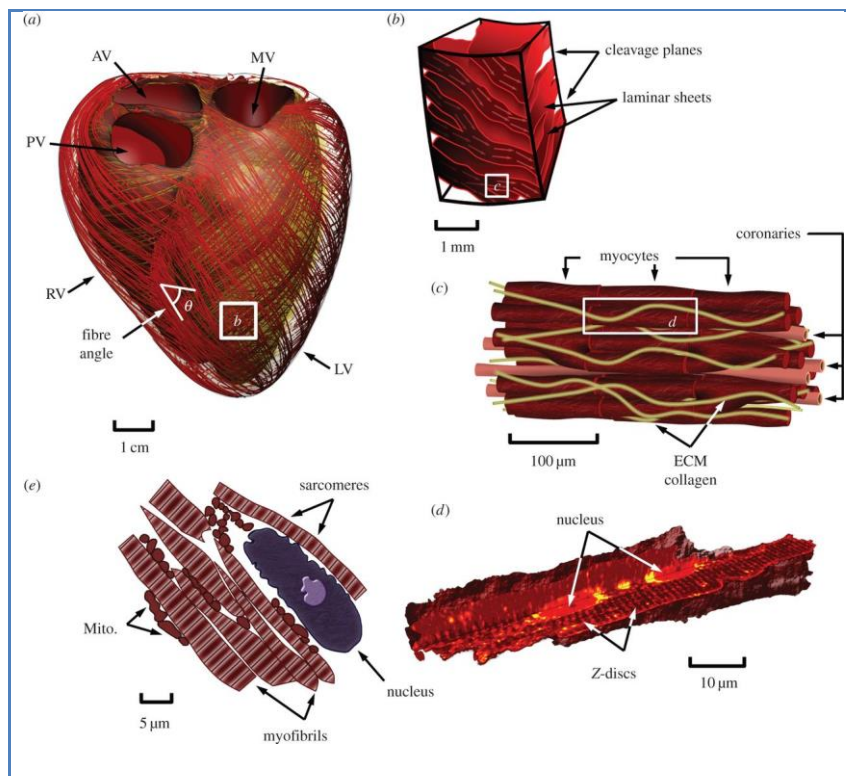


**Figure 2.6. Example of cardiac tissue architectures, (figure from Chabiniok et al. 2016 with permission), showing a layered organisation of the cardiomyocytes that might influence conductions.**

### 2.2.2.3 Ionic Mechanisms of Cardiac Electrical Activity

This section describes the generation of the normal cardiac action potential by heart cells and its transmission in the multicellular tissue. A complex interaction and communication of cardiac cell electrical activity generate AP conduction in the cardiac tissue (Kléber & Rudy 2004).

**Action potential in the cardiac cell**

The normal sequence contraction of the ventricles requires the rapid activation of groups of cardiac cells to facilitate rapid changes in heart rate. Figure 2.7 (Grant 2009) shows the five phases of the normal action potential. The full description of these phases has been discussed in detail in Section 2.2.2.1. The main fundamental properties of ion channels are ion permeation and gating. Ion permeation is the mechanism of the movement through the open channels (e.g., $Na^+$, $K^+$, and $Ca^{2+}$ channels) (Grant 2009).
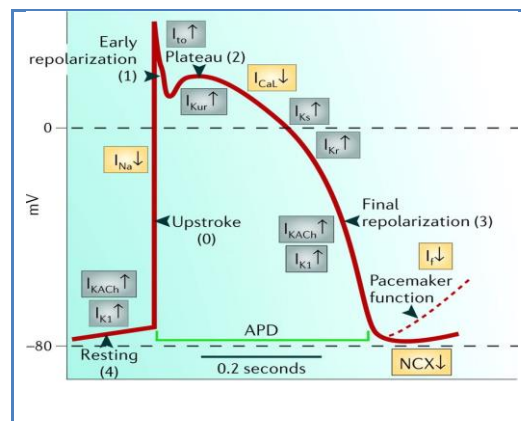


**Figure 2.7.** **The generation of the action potential results from the selective permeability of ion channels distributed on the cell membrane (Grant 2009).**

Gating is the mechanism of opening (activation) and closing (by deactivation or inactivation) of ion channels in response to membrane potential. The variations in membrane potential change the conductance of voltage-gated ion channels. The ion channels generally open in response to depolarization (Grant 2009). However, if the membrane potential is back to its resting value while the channel is open, it closes by deactivation. The mathematical description of the cardiac excitation involving generation of the action potential and its conduction with the diffusion of this process by flow of electric charge will be explained in Section 2.4.1.

**Action potential propagation in multicellular tissue**
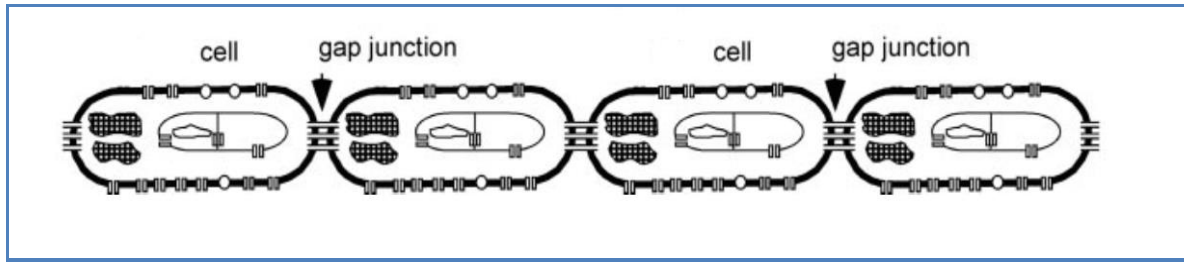


**Figure 2.8. The multicellular fibre is composed of cells, interconnected through gap junctions** (Kléber & Rudy 2004b)**.**

Heart tissue contains different cell types at the microscopic level. Myocytes' function is to produce mechanical tension in the heart muscle. Cardiac muscle cells are separated by gap junction channels (Figure 2.8) that allow the cell-to-cell movement of ions (cell-to-cell conduction). They propagate AP by intercellular signalling. Electrophysiological studies have used mathematical models of AP diffusion. These models can link cell electrophysiology models, cardiac mechanics, and blood circulation. The AP diffusion characteristics in one dimensional (1D), 2D, and 3D tissue (Kléber & Rudy 2004a; Bernus et al. 2004; Caldwell et al. 2009) are described briefly below. In the next two sections the electrical diffusion in 2D, and 3D cardiac muscle will be described in detail.

1-D propagation

This propagation is described by Conduction Velocity (CV) and defined by various factors. The most important of these are membrane excitability and the conductivities of cardiac tissue. In addition, a main attribute of myocardium is the gradient of the CV restitution (CVR) curve affects the start of dynamic heterogeneity in the heart (Kléber & Rudy 2004).

2-D propagation

Tissue anisotropy and wave front curvature influence cardiac AP propagation in 2-D and the conduction velocity. Two important factors, which may contribute to anisotropy, are gap junction localisation at the end of myocytes and the degree and direction of gap junction coupling. In addition, the dependency of velocity on curvature can be introduced as a key element for specifying normal and irregular (re-entry) wave circulation in heart tissue (Bernus et al. 2004).

3-D propagation

This propagation is affected by tissue anisotropy and wave front curvature; however, it is affected by the shape of cardiac tissue such as fibre-sheet forms (Caldwell et al. 2009).

### *2.2.2.4 Two-dimensional Propagation in Cardiac Muscle*

Cardiac tissue functions because intracellular channels couple each cell to its neighbours. The anisotropic structure of tissue and wavefront curvature contribute to cardiac action potential propagation in 2-D models.

CV is measured in anisotoropic tissue with respect to linear CV parallel to fibres and diagonal CV vertical to fibres. Another significant feature of 2-D propagation is curvature (Figure 2.9). Curvature is important when a wave front propagates from a thin layer of tissue into a big area. Wave fronts are shaped into three categories (plane, convex and concave) (Cabo et al. 1994) shown in Figure 2.9. A plane wave front keeps its length as a simplest form in which each cell must be depolarised from the cell in front of it; hence in this case, the conduction velocity is equal to the steady-state velocity. However, the current initiating depolarisation spreads to a bigger membrane region as the wave front bends outward (convex) due to the increment in length of a convex wave front. Consequently, the conduction velocity for a convex wave front is lower than a plane front (Fast & Kléber 1997). Conversely, as the wave front twists inwards (concave), its length decreases, thus generating an extra fast membrane depolarization. Although the dependency of conduction velocity on curvature can be explained as normal and irregular re-entry wave propagation in heart tissue, the link between CV and curvature in actual heart tissue remains challenging due to regional variation in CV and restitution (Nash et al. 2006; Yue et al. 2005).



| Plane | Convex | Concave |
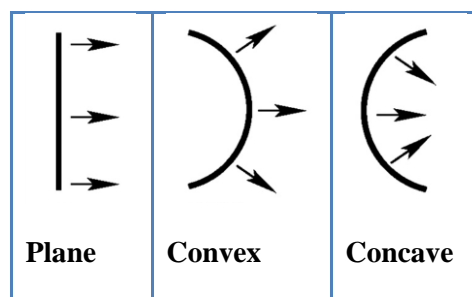
**Figure 2.9.  Three types of wave fronts: plane, convex and concave. 2-D reaction-diffusion models describe wave-front propagation in cardiac tissue.**

### 2.2.2.5 *Three-dimensional Propagation in Cardiac Muscle*

The three-dimensional computational model of the heart allows a wider scope of examinations to explain the principal relationships among biophysical factors, the potential distributions and current flow. The 3-D tissue model gives information about the spread of excitation that is not possible to obtain through direct experimental measurements (Muzikant & Henriquez 1998). The tissue anisotropy and curvature affect the wave front conduction in 2-D and 3-D propagation. To create a full 3-D computational model, detailed descriptions of the ventricular/atrial geometry and the local fibre orientation are needed. In addition, to govern the activation and recovery processes, essential intracellular and extracellular spatial characteristics and spatial ion channel allocation (Henriquez et al. 2004) are required. It is important to combine both realistic representations of anatomy and tissue properties with realistic models of ion fluxes to achieve an integrative model (Henriquez et al. 2004).

## 2.3 Cardiac ion concentrations and electrophysiology changes during ischaemia (Experimental and clinical studies)

Different experimental methods have been used to analyse the changes in ionic currents involved in the ischaemic process. For example, voltage-clamp measurements have been applied at single cells or multiple cells subjected to hypoxia, hyperkalaemia and acidosis that occur during ischaemia.

A description of ionic channels and their mechanisms in generation of excitation and propagation of electrical conductance has been reviewed in the previous section. Here, the ion concentration changes during ischaemia with their effects on channels will be described to show the variation in electrical properties at the cellular and multi-cellular level and to examine their role in generation of cardiac arrhythmias.

### 2.3.1 Changes in ion concentrations during Ischaemia

Cardiac ischaemia is characterised by a lack of energetic input when oxygen falls below the critical level resulting in a failure in contraction and electrical behaviour and finally death of the cell. The main ischaemic modulatory processes are examined in five groups of ion concentrations ($[K^+]_o$ , $[H^+]$, $[Na^+]_i$, $[Ca^{2+}]_i$, and $[Mg^{2+}]_i$ ) (Carmeliet 1999) to describe their effects on channels and the metabolism changes. In each group, a description of the ion changes and their effect on channels, the involved mechanisms and the final effects on electrical activity and arrhythmia level will be analysed.

*Accumulation of $[K^+]_o$*
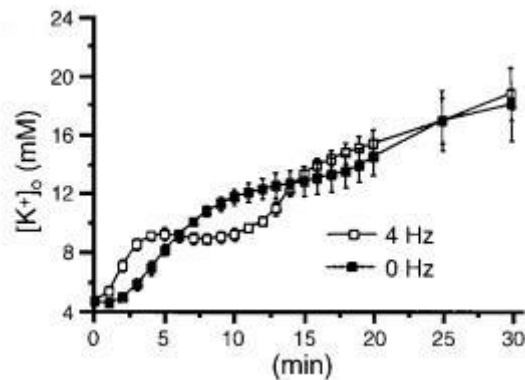


**Figure 2.10.** $[K^+]_o$ **accumulation during ischaemia in stimulated (4 Hz) rat hearts . Figure from Carmeliet (1999) with permission.**

## Description of changes

$[K^+]_i$ is increased under aerobic condition and consequently $[K^+]_o$ decreased. The $Na^+$-$K^+$ pump makes a balance between the active $K^+$ influx and passive $K^+$ efflux. However, under ischaemic conditions, this dynamic equilibrium is changed and $[K^+]_o$ elevates. During ischaemia, potassium changes occur in three stages (Figure 2.10): the occlusion of a coronary artery within 20s; a fast accumulation of $[K^+]_o$ reaches a plateau after 3–10 min; slower increase between 15 and 30 min (Wilde et al. 1990). The highest level of $[K^+]_o$ at 20 mM is reached after 30 min; this leads to inexcitability and elevation of the resting membrane (Weiss & Shine 1982; Cascio et al. 1990). The 3 minutes of ischaemia are simulated using the maximum value of 8 mM for $[K^+]_o$ in this thesis.

## The mechanisms involved

The mechanisms responsible for the $[K^+]_o$ alternation are summarised as: reduction of extracellular space; reduction of active $K^+$ influx; and increase of passive $K^+$ efflux (Carmeliet 1999). The extracellular space is restricted by 15% after 10 minutes of ischaemia which acts as an amplification mechanism that could be involved in $[K^+]_o$ elevation (Carmeliet 1999). The activation of $K^+$ influx decreases when the $Na^+$-$K^+$ pump activity is reduced due to partial inhibition of the pump which leads to increased $K^+$ loss. Under ischaemic conditions, the pump activity is reduced; subsequently, the energy delivered from ATP hydrolysis or the phosphate potential is significantly depleted. In this condition, the

Nernst potential ($E_{rev}$) of the pump, which is -180 mV, reaches -60 mV corresponding to the transmembrane potential ($E_m$) of the cell during elevation of $[K^+]_o$ (Glitsch & Tappe 1995). Thus, the pump stops functioning at the membrane potential during ischaemia. It has been shown that the conductance of $K^+$ and the electrochemical gradient are the key products for quantitatively electrogenic $K^+$ movement according to the equation: $I_K = g_K(E_m - E_K)$. According to this equation, when the $K^+$ conductance ($g_K$) is elevated the outward movement ($K^+$ efflux) will occur if the $E_m$ is positive to the $K^+$ equilibrium potential ($E_K$) (Kanda et al. 1997). During ischaemia, the enhancement of the conductance of the ATP-sensitive $K^+$ channel is expected to emphasise the elevation of $[K^+]_o$ (Kanda et al. 1997). In summary, the voltage-gated $K^+$ channels with high conductance can be triggered during metabolic inhibition, while inward currents are insufficient to make an electrical gradient for $K^+$ efflux (Carmeliet 1999).

**The electrophysiological changes and arrhythmia level**

The elevated $[K^+]_o$ is the cause of cell depolarisation and the reduction of action potential ampilitude. The depolarisation associated with inactivation of the $Na^+$ conductance is responsible for the action potential amplitude decline and the reduction in excitability. When $[K^+]_o$ accumulates, post-repolarization refractoriness is prolonged (Janse & Wit 1989). The speed of depolarization conduction (CV) is decreased particularly during the RRP (Kléber et al. 1987). These electrophysiological changes in excitability, refractoriness and conduction with the AP shortening consequences of cardiac ischaemia support the incidence of re-entry arrhythmias (Carmeliet 1999).

*Intracellular and extracellular acidosis*
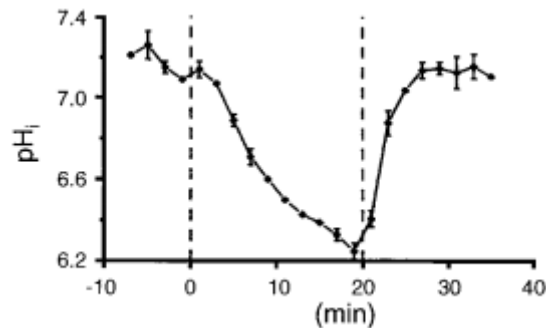


**Figure 2.11. Reduction of intracellular $pH$ during ischaemia and fast recovery consequent to reperfusion in perfused ferret hearts. Figure from Carmeliet (1999) with permission.**

## Description of changes

During ischaemia, internal and external pH has been described as changing quickly (Clarke et al. 1993). For example, $pH_i$ fell from a control value of 7.15-7.2 to 6.5 after 4 minutes of ischaemia and to 6.2-6.0 after 10-20 minutes of ischaemia (Marban et al. 1990; Wagner et al. 1990; Camacho et al. 1993; Clarke et al. 1993; Clemo et al. 1998) (Figure 2.11). The internal and external pH become the same during total global ischemia (Clarke et al. 1993).

## The mechanisms involved

The fall in internal and external pH during ischaemia is caused by an increased production of protons and insufficient removal (Dennis et al. 1991). The intracellular protons are actively transported outward when $pH_i$ is around 7.2. The $Na^+/H^+$ exchanger is activated when the proton concentration is enhanced to achieve equilibrium to protect the cell against acidosis (Wu & Vaughan-Jones 1994). However, the exchanger is inhibited by extracellular acidosis (Wu & Vaughan-Jones 1994; Carmeliet 1999).

## The electrophysiological changes and arrhythmia level

The electrophysiological changes at the multicellular level caused by acidosis at the channel level have been described as a reduction in membrane resting potential, a fall in upstroke velocity, action potential prolongation, oscillations at the AP plateau level and consequently, the appearance of early after-depolarizations (EAD) (Coulombe et al. 1980). Due to slow recovery of Na current, the refactoriness is prolonged (Carmeliet 1999). The AP conductance

is reduced as a result of reduction in excitation of current (Shaw & Rudy 1997). During ischaemia, the AP is shortened as a result of elevated $[K^+]_o$ and activation of outward currents mainly carried by $K_{ATP}$ channels (Carmeliet 1999), thus the acidosis-induced changes are pro-arrhythmic which can explain the reduction of threshold during ventricular fibrillation in acidosis (Surawicz 1985).

*Increase of $[Na^+]_i$*
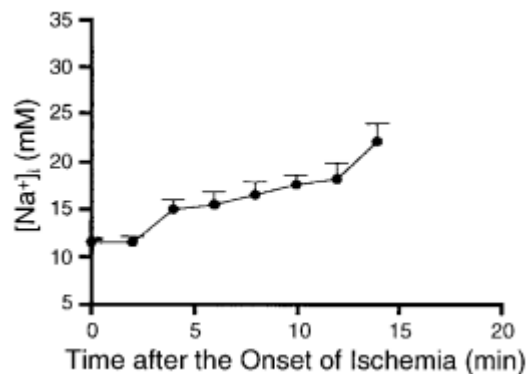


**Figure 2.12. Increment of $[Na^+]_i$ during ischaemia in isolated, blood-perfused rabbit papillary muscle. Figure from Carmeliet (1999) with permission.**

**Description of changes**

There is an increase in $[Na^+]_i$ during ischaemia or metabolic inhibition (Malloy et al. 1990; van Echteld et al. 1991; Pike et al. 1993). A two fold increase of $[Na^+]_i$ (values of 20–25 mM) after 15 minutes of ischaemia has been reported (Yan et al. 1995) in the rabbit heart (Figure 2.12). However, it has also been reported that $[Na^+]_i$ reduced and normalised during 20-30 minutes of ischaemia (Malloy et al. 1990).

**The mechanisms involved**

The reason for increasing $[Na^+]_i$ during ischaemia is a reduction of active outward movement. This is probably due to the partial block of the pump during early ischaemia (Donoso et al. 1992). A reduction of pump activity and inhibition of the pump result from the decrease in free energy of ATP hydrolysis caused by changes in [ATP], [ADP] (Tanaka et al. 1992). The amount of energy normally available from ATP hydrolysis is 61.5 kJ/mol, however, this can drop to 49 kJ/mol or less in the course of ischaemia. Accompanying this

drop, the $E_{rev}$ of the pump moves in the depolarized direction towards the resting potential (Carmeliet 1999).

**The electrophysiological changes and arrhythmia level**

The increase in $[Na^+]_i$ from 10 to 20 mM after 15 minutes of ischaemia decreases the active outward pumping and tends to hyperpolarize the membrane and shortening of APs combined with low $[K^+]_o$; these effects are only visible during reperfusion (Carmeliet 1999). These electrophysical changes are favourable to arrhythmias (Carmeliet 1999).

*Changes in the $[Ca^{2+}]_i$*
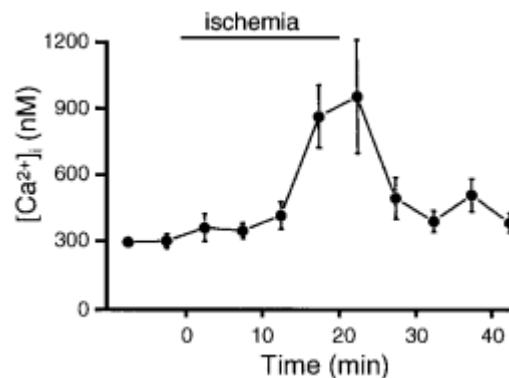


**Figure 2.13. Changes in $[Ca^{2+}]_i$ during 20 min of ischaemia in perfused ferret hearts. Figure from Carmeliet (1999) with permission.**

**Description of changes**

During ischaemia, $[Ca^{2+}]_i$ enhances with some delay, which is variable and depends on the time course of ischaemia (Carmeliet 1999). A delay of 10-20 minutes has shown slight enhancement of $[Ca^{2+}]_i$ (Marban et al. 1990; Wagner et al. 1990) (Figure 2.13). Different variations in time course have been reported in different experiments (Kihara et al. 1989; Mohabir et al. 1991; Russ et al. 1996) subject to hypoxia or metabolic inhibition. The reason for these divergent results is unknown but might be associated with the level of metabolic blockade.

**The mechanisms involved**

Under normal conditions, $Ca^{2+}$ influx and efflux through the plasma membrane are in equilibrium (Trafford et al. 1997; Wang et al. 1997), but the balance is changed during ischaemia by increasing $[Ca^{2+}]_i$ more than $Ca^{2+}$ efflux. The reason for increase in $[Ca^{2+}]_i$ in the cells subjected to ischaemia is less removal from the cell via $Na^+/Ca^{2+}$ exchanger and increased influx through the plasma membrane (Lamont & Eisner 1996; Trafford et al. 1997). Under ischaemic conditions, this exchanger is less efficient due to an increase in $[Na^+]_i$ and $[H^+]_i$ that stimulates the reversed mode of the $Na^+/Ca^{2+}$ exchanger (Smith & Allen 1988; Tani & Neely 1989; Haigney et al. 1994). It has been noted that acidosis effectively reduces the efficiency of the exchanger (Bountra and Jones 1989; Donoso et al. 1992).

**The electrophysiological changes and arrhythmia level**

Increased $[Ca^{2+}]_i$ will lead to the AP shortening, generation of EAD, DAD, and occurrence of arrhythmias (Kihara et al. 1989; Thandroyen et al. 1991).

*Modulation of* $[Mg^{2+}]_i$
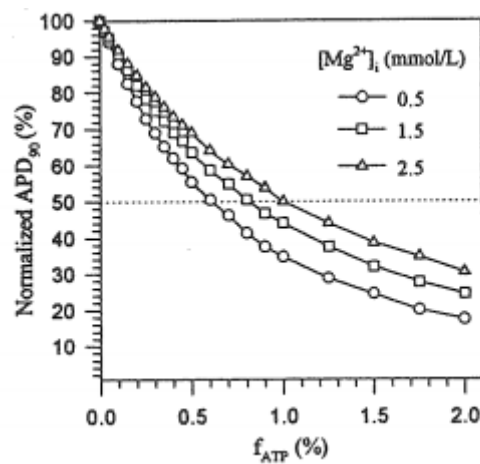


**Figure 2.14. Effect of $[Mg^{2+}]_i$ modulations on AP behaviour. Figure from Ferrero et al. (1996) with permission. This description is based on published experimental data (guinea-pig ventricular cells) (Horie et al., 1987).**

**Description of changes and the mechanisms involved**

It has been found that free $[Mg^{2+}]_i$ increased from its normal value of 0.5–0.8 mM to 2–6 mM after 10-15 minutes of ischaemia (Murphy et al. 1989; Kirkels et al. 1989; Schreur et al. 1993). The main mechanisms for increasing $[Mg^{2+}]_i$ during ischaemia are a $Mg^{2+}$-ATPase and a $Na^+/Mg^{2+}$ exchange process (Silverman et al. 1994). The KATP channels are influenced by increasing $[Mg^{2+}]_i$ levels during hypoxia. Outward currents through IKATP are reduced by $[Mg^{2+}]_i$ .

**The electrophysiological changes and arrhythmia level**

The enhancement of $[Mg^{2+}]_i$ during hypoxia/ischaemia has a significant effect on APD (AP shortening) caused by reduced KATP mediation (Ferrero et al. 1996) (Figure 2.14).

### 2.3.2    Electrophysiology Changes during Ischaemia

This section describes the electrophysiological changes at the cellular and multicellular level during ischaemia. These changes are summarised in two subsections: a description of electrophysiological changes including the changes in resting and AP, in refractoriness, excitability and conduction. Then, the mechanisms underlying these changes are discussed.

**Description of electrophysiological changes**



C Electrophysiologic and metabolic characteristics of different layers below the endocardium after 10 to 12 min of global ischemia with maintained superfusion (average values ± SD)

| Depth below endocardium | Resting membrane potential (mV) | Action potential amplitude | Action potential duration | Extracellular [K⁺] (mM) | pH | Phospho-creatine (μmol/g dry weight) |
|---|---|---|---|---|---|---|
| To 650 $\mu$m | 73±3 | 81±13 | 116±42 | 7.68±2.08 | 6.81±0.27 | 18.01±8.34 |
| Deeper than 650 $\mu$m | 53±4 | 44±11 | 102±42 | 11.09±1.81 | 6.36±0.32 | 3.72±2.56 |
| p value (two-tailed Student's t test) | p<.01 | p<.01 | NS | p<.05 | p<.05 | p<.01 |

**Figure 2.15 ECG and AP recording (from Carmeliet (1999) with permission) in an ischaemic pig heart. A: at start of ischaemia, B: after 12 minutes of ischaemia, C: electrophysiological characteristics of 10-12 minutes of global ischaemia (Table 1 from Wilensky et al. (1986) with permission).**

The blood flow stops quickly within 2-3 minutes of ischaemia and the normal resting potential depolarises from -85 mV to -60 mV. The amplitude and maximum rate of

depolarization during AP upstroke is decreased and excitability is reduced when $[K^+]_o$ is elevated. The conduction slowly decreases after 2 minutes of ischaemia (Coronel et al. 1989), the cells are more depolarized after 30 minutes of ischaemia, and conduction is completely blocked (Coronel et al. 1989). Thus, the activation time of ventricles increases to 200-300 ms during ischaemia; under normal conditions activation completes in 80-100 ms. Conduction delay is more prominent in the epicardium than in the endocardium layer (Wilensky et al. 1986). Wilensky et al. (1986) have discussed how the subendocardial cells affect typical alternations associated with ischemia, such as hypoxia, hyperkalaemia, and acidosis due to a greater resistance which may be related to diffusion of intact heart oxygen from the cavitary blood. Typical electrophysiology changes for ischaemia are shortening of APD (Kleber et al. 1986; Verkerk et al. 1996; Watanabe et al. 1997) (Figure 2.15) and lengthening of refractory period (ERP) (Coronel et al. 1992; Carmeliet 1999). A summary of electrophysiological characteristics of 10-12 minutes of global ischaemia in the rabbit heart is shown in Figure 6.C (Wilensky et al. 1986). They have shown that the resting membrane potential is changed from the normal value of 86 ± 3 mV to -60 mV (average 53 ± 4 mV) during ischaemia. A reduction in action potential amplitudes of normal value of 109 ± 7 mV to 44 ± 11 mV and in APD from normal value of 194 ± 27 ms to 102 ± 42 ms. The mechanisms underlying these changes are described in the following section.

**Mechanisms underlying the electrophysiological changes during ischaemia**

Based on the electrophysiological descriptions from the previous section, the following underlying mechanisms are summarised here.

**The large depolarization**

The elevated $[K^+]_o$ and increase of inward current (described above) are the main reasons for the large depolarisation during ischaemia. As noted above, increased $K^+$ efflux and reduction of $K^+$ influx, and to a certain level, decrease of the extracellular space are the mechanisms responsible for increased $[K^+]_o$. Inward current is accountable for holding the transmembrane potential positive to the $K^+$ equilibrium potential. This contributes to outward $K^+$ movement. The possible mechanisms associated with inward escape involve multiple $Na^+$, $Ca^{2+}$, and $Cl^-$ channels and exchangers (Carmeliet 1999).

**The fall in upstroke velocity and amplitude of the AP**

Reduction in $Na^+$ influx and increased outward currents are the main reasons for the reduction of upstroke velocity and amplitude of the AP. The reduction of $Na^+$ conductance is caused by inactivation of sodium channels and the decrease in resting membrane potential and by oxidative stress, acidosis (Watson & Gold 1995) and the action on the $Na^+$ channel protein (Zhang & Siegelbaum 1991). The fast $Na^+$ current ($I_{Na}$) is effective on generating the AP upstroke which is reduced by the outward current effects, such as $I_{KATP}$ (Carmeliet 1999).

**Changes in APD**

The APD shortening is caused by enhancement in outward current at plateau phase and minor effects of decreasing inward current (Carmeliet 1999). The enhanced outward current is carried by $K^+$ currents (such as $I_{KATP}$) which become triggered under ischaemic conditions (Terzic et al. 1995). The $Cl^-$channel activation, which is responsible for enhancement of inward leaks at resting potential and increase of $[Ca^{2+}]_i$ is the second current source for APD shortening. Because the activated $Cl^-$channels will carry outward currents at potential positive to -30 mV and are associated with repolarisation promotion from the AP peak to the plateau phase (Carmeliet 1999). The role of $I_{Ca}$ changes in the AP shortening is negligible (Carmeliet 1999).

**The changes in excitability and conduction**

Carmeliet (1999) states that conduction velocity is decided by active cell properties such as amplitude and upstroke velocity of the action potential, and passive muscle bundle cable properties. He specifies the resistance of the cell membrane, the longitudinal resistance of the cell, the resistance of the extracellular compartment, and the tissue architecture (on a larger scale) as decisive. The CV is affected during ischaemia by the fall in amplitude and in rate of increase of the AP, and increasing cell membrane conductance at rest (Kléber et al. 1987). The excitability is decreased during ischaemia because of inactivation of the $Na^+$ channel by the membrane depolarization. Increasing membrane resting potential is the reason for delay in the AP propagation. It has been shown that conduction is slowed during ischaemia in experimental and theoretical studies (Rohr et al. 1997; Shaw & Rudy 1997). This is due to increase in $[K^+]_o$ concomitant with a reduction in $[ATP]_i$ (Carmeliet 1999). Despite APD

reduction, ERP is prolonged (Sutton et al. 2000; Coronel et al. 2012) during ischaemia mainly caused by slow recovery from inactivation of $Na^+$ channels to the depolarisation and $Na^+$ channel blockade by acidosis (Watson & Gold 1995).

### 2.3.3 Summary of Arrhythmias during Ischaemia

Arrhythmias occur depending on the ischaemic period. The arrhythmia of phase I of ischaemia, which is the first 30 minutes of ischaemia, is briefly described here and the arrhythmia of phase II (ischaemia between 5 and 72 hours) and phase III ( the chronic stage after an infarct) are omitted from this study. In addition, study of the incidence of arrhythmia during reperfusion is also not in the scope of this thesis. In this section, a general description of the type of arrhythmia occurring during ischemia with underlying mechanism is given.

**Description**

In human hearts, arrhythmias result in VF and sudden death. Observation of 2-10 minutes of ischaemia has shown the occurrence of irregular VT in most animals; however, development into VF is infrequent (Knopf et al. 1988; Knopf et al. 1988; Smith et al. 1995). Animal observations have shown less arrhythmia during 10-20 minutes of ischaemia compared to the beginning of ischaemia (the first 10 minutes of ischaemia) but the development of VF is more frequent which results in the animal's death (Carmeliet 1999).

**Mechanism**

It has been shown that most tachycardia type arrhythmias infrequently progress into VF and occur during 2-10 minutes of ischaemia. Mapping studies have shown these arrhythmias (Pogwizd & Corr 1987) to result from the following changes in re-entry: the irregular electrical impulses due to the long spiral circle within the ischaemic zone; or movement of two spiral wave fronts around a conduction block point.

Therefore, activation and conduction is slowed especially in the epicardial region (Carmeliet 1999). Tachycardia is an abnormally rapid heart rate caused by dispersion of activation and repolarisation (Kaplinsky et al. 1979; Smith et al. 1995) of the electrical impulses.

Non-reantrant mechanisms in the generation of arrhythmias can be involved such as triggered activity (EAD (Coulombe et al. 1980)  and DAD (Pogwizd et al. 1986)) as a result of increase in $[Ca^{2+}]_i$ and by extreme stretch of border zone cells. Arrhythmias occurring after 20

minutes of ischaemia are associated with increasing $[K^+]_o$ (Kléber 1983), $Ca^{2+}$ overload and increase in longitudinal resistance (Smith et al. 1995) which favour re-entry. Conditions for re-entry are summarised as heterogeneous ERP (Coronel et al. 1992; Sutton et al. 2000; Coronel et al. 2012) and slow conduction due to slow recovery from inactivation of $Na^+$ channels and enhancement of longitudinal resistance (Carmeliet 1999).

## 2.4 Excitation and Propagation in Heart Muscle

The real heart has many heterogeneities, both structural and electrophysiological. Different mathematical models and measurements have been proposed to investigate the dynamics of excitation and propagation in cardiac muscle. A short overview of the theory of re-entrant wavelets, spiral wave in 2-D and scroll waves in 3-D, which are important for investigation of mechanisms of cardiac arrhythmias, is given in this section. A full numerical explanation of heart tissue electrophysiology and 2-D models of re-entry is provided in Chapter Three.

### 2.4.1 Theory of Re-entry

The theoretical study of re-entry, as an important mechanism underlying the start of heart arrhythmias and cardiac fibrillation, is a vast area of investigation in excitable media (Panfilov & Keener 1995). Re-entry is defined as an experimental phenomenon, which is shaped after an irreversible conduction block as the wave travels around the blocked area and completes one full alteration (Tran et al. 2007). The concept of re-entry is shown in Figure 2.10, in which the electrical signals move down each arm with the same velocity in normal tissue. In case of an irreversible block (shown in red) (2) in one of the branches, the electrical signal will move down only one arm (1). In this situation, if the signal enters the common branch at a time where it is backward signalling (3), re-excitation may happen subsequent to self-sustained propagation (4) (Figure 2.16) (Schmitt et al. 2014).
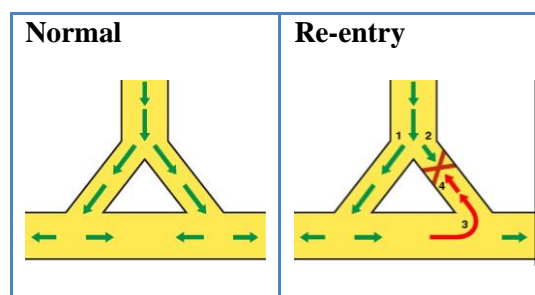


**Figure 2.16. Re-entry arrhythmias. Left: Circulation of normal action potential, right: a re-entrant excitation (Schmitt et al. 2014)**

Many experimental studies (Biktashev & Holden 1998; Cassia-Moura et al. 2004; Garfinkel et al. 2000; Xie et al. 2002; Weiss et al. 2005) support the idea that cardiac arrhythmias of ventricular tachycardia (VT) and fibrillation (VF) are maintained by re-entry(Tran et al. 2007). Action potential propagates into recovered tissue continuously during re-entry and turns around a point in 2-D (named phase singularity) and a filament in 3-D. VF can be maintained by a single re-entry wave in which conduction is fibrillated, or by breakup of an original re-entrant wave to multiple wavelet re-entries. Breakup of re-entrant waves can occur due to these mechanisms: fundamental 3-D instabilities; the APD restitution curve steepness; and the effects of rotational anisotropy in the ventricular wall (Clayton & Holden 2004b).

### 2.4.2  Spiral Waves in Two Dimensions

A spiral wave is more precisely a 2-D demonstration of a consecutive, fast travel of electrical signals that turns around a middle core (PS). The spiral wave drives with a curved wave front, the curved wave tail, and the point of intersection of wave front and wave tail as displayed in Figure 2.17.A (Pandit & Jalife 2013). Electrical activity (depolarizing) initiates from a middle core and diffuses away from the centre. The curved depolarization wave front is described as a region of depolarized cells when the cardiac impulse moves onward (shown by the solid black line and the black arrows display the propagation path). The wave tail includes the collection of cells that have sustained full excitation (associated with action potential upstroke) and are coming back to rest (associated with action potential repolarization) (Pandit & Jalife 2013). As a consequence of the curvature of the wave, the phase singularity of the spiral wave is a point or region in which depolarizing and repolarizing fronts cross (represented in Figure 2.17.A by an asterisk); that allows the exploration of the spiral wave and its tip's dynamic movements, in space, over time.

**A**

**B**
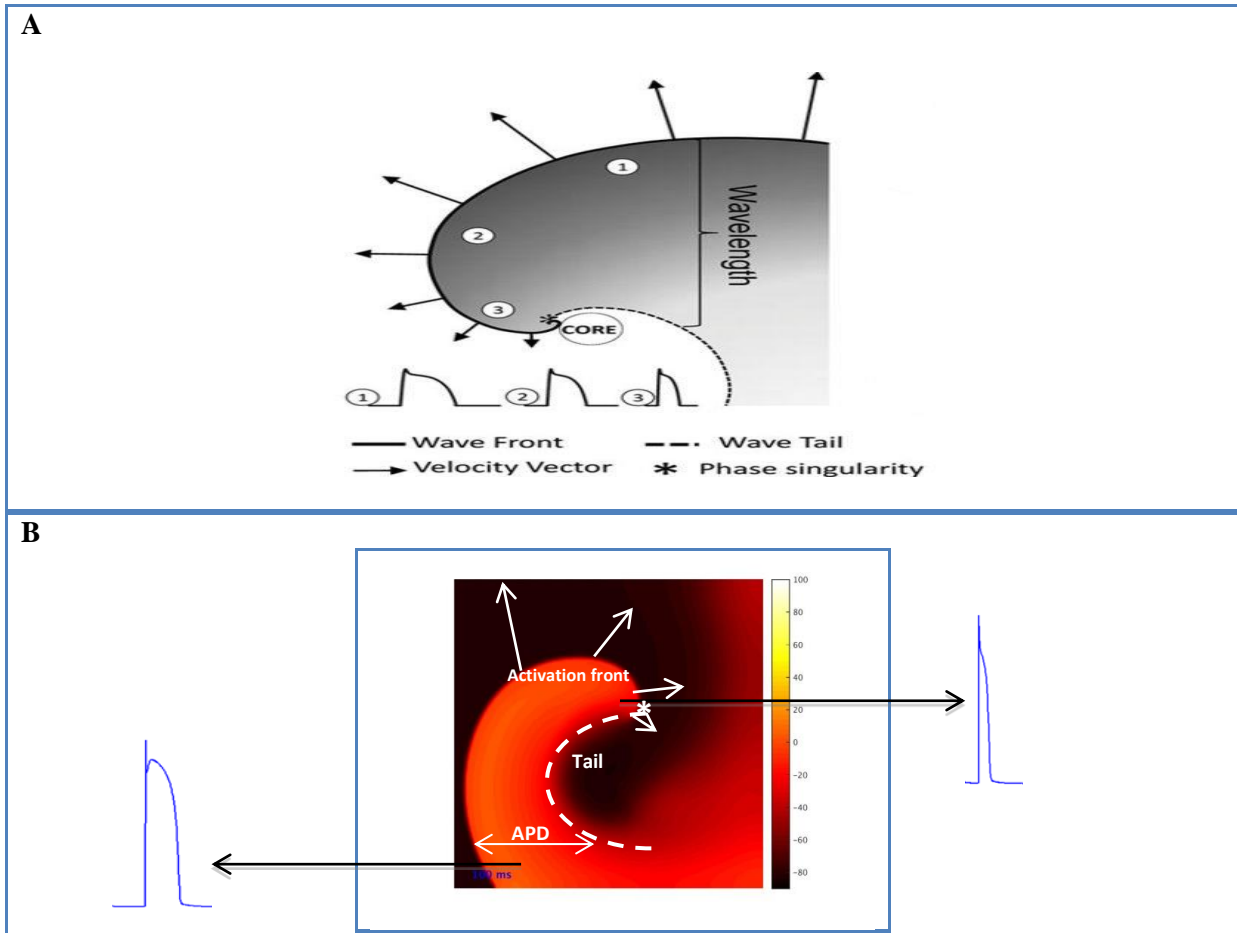
**Figure 2.17. Basic concepts of Spiral waves: A: Schematic of a spiral wave (Pandit & Jalife 2013): arrows from the core show the reduction of conduction velocity (CV) and action potential duration (displayed from locations 1, 2, and 3). The wavelength is the distance from the wave front to the wave tail (dashed line). CV is reduced when the wave front curvature more closely approaches the phase singularity (PS). PS is the point where the wave front and the wave tail cross (*). B: Snapshot of the re-entry in 2-D tissue generated from the human ventricle ionic math models (Figure generated in our 2D tissue model based on Clayton et al. (2006)).**

One main concept of the spiral wave principle is the comprehensiveness of meandering. Spiral meandering is the rotating and twisting travel of the wave front within the cardiac tissue, where the accurate route of a certain spiral wave will relate to the wave tip dynamics (Schmitt et al. 2014). The idea of decreasing meandering is considered pro-arrhythmic explained by the decreased possibility for travelling into refractory tissue and thus the reduced probability of wave-breaks that can stop the re-entry (Schmitt et al. 2014). For example, the degree of meandering and the number of wave- breaks in fibrillatory conduction, are important factors for investigation of drug effects on re-entry (Pandit & Jalife 2013). Figure 2.17.B displays a distribution of membrane voltage in a 2-D sheet that incorporates numerical ionic models of human ventricle cells (Ten Tusscher & Panfilov

48

2006). This figure demonstrates the potential distribution (mV), in which the depolarized group of cells is shown in red and the resting membrane potential of tissue is in black.

### 2.4.3    Scroll Waves in Three Dimensions

The VF simulation studies (Panfilov & Keener 1995; Gray et al. 1994) suggest that scroll waves (scroll wave breakup) are a main source of re-entrant cardiac arrhythmias; VF in particular is the prominent cause of sudden cardiac death. Scroll wave breakup represents the continual creation and destruction of wavelets. It is extremely important to understand the determinants of scroll wave stability. The scroll wave is represented as a spiral wave in 3-D, which turns around a vortex filament (a line of phase singularity) (Figure 2.18). It is important to understand how filament behaviour is affected by tissue properties due to the role of vortex filaments as the establishing centres of the complex activation patterns during VF (Clayton 2008). The filament can be formed as a linear cylinder (I-shape) or as fluctuating nonlinear forms (L-shape, U-shape, O-shape, etc.) (Pandit & Jalife 2013); their configuration and shape has a serious effect on performance and communication with other filaments (Clayton et al. 2006). Filament interactions are the changes in filament number resulting from  birth, death, amalgamation and bifurcation of filaments (Clayton et al. 2006) that have been used to measure filament behaviour in tissue (slabs and whole ventricle geometries) simulations quantitatively (Clayton & Holden 2004a).
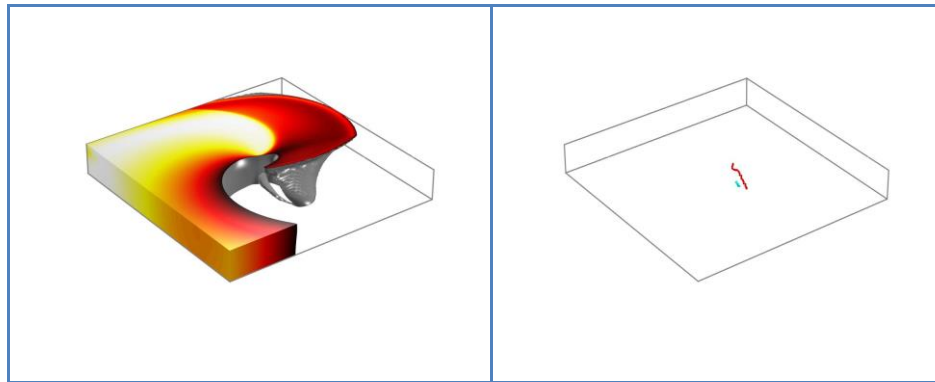


**Figure 2.18.  Three-dimensional scroll wave (left), Snapshots of filaments (right). Figure produced based on  Clayton et al. (2006).**

## 2.5  Arrhythmia Mechanisms

Arrhythmia is a disturbance to the normal heart rhythm that results in the heart beating too slowly, too quickly, or irregularly. There are different electrophysiological mechanisms that cause arrhythmias. The general causes of arrhythmias are categorised into two groups (Hoffman & Dangman 1987; Marchlinski & Betensky 2012):

- Abnormal initiation of wave of cardiac excitation
- Abnormal propagation of a wave of cardiac excitation

Abnormal initiation occurs when an electrical impulse can result from a single cell or set of closely connected cells through depolarization of the cell membrane. In this case, the problem is an abnormal location of impulse formation since transformations in ionic currents flow through the single cell membranes within the rest of the heart. Two examples of impulse starts that may result in arrhythmias are: automaticity can result from spontaneous depolarization. Triggered activity is caused by after-depolarization: after-depolarizations (early or delayed after-depolarizations EADs / DADs) are spontaneous membrane potential oscillations during or immediately following a previous action potential.

Abnormal propagation occurs when the propagating impulse fails to conduct. Re-entry excitation is the most common abnormal conduction and the most common arrhythmia mechanism seen in clinical arrhythmias (Marchlinski & Betensky 2012), referring to a repetitive propagation of the wave of activation. One example of this arrhythmia could be alternations of APD that happen during re-entry, resulting in block and termination (Clayton & Holden 2004b).

### 2.5.1  Ventricular Arrhythmias and Dynamics of Electrical Activities

The electrical activity initiates regionally in the ventricles during ventricular arrhythmias where the ratio of excitation is usually much quicker than the sinus rhythm, thus altering the QRS complex and electrocardiogram (ECG) morphology (Qu et al. 2014). Different kinds of ventricular arrhythmias display different ECG patterns. Ventricular fibrillation (VF) is a potentially lethal cardiac arrhythmia with a faster heart rate and irregular ECG pattern (Figure 2.19); VF is possibly chaotic, and leads to cardiac arrest and death unless normal rhythm is restored.

Experimental study of VF has shown that it is sustained by multiple circulating waves of electrical activity. Theoretical and computational studies enable the probing of mechanisms

that lead from one wave to many. On the ECG, VF is characterized by changes in frequency and amplitude, and with disordered beat-to-beat variations in the ventricular electrical network, for instance, a chaotic electrical disturbance of the ventricles occurring with irregular impulses at a rate of 300-500 per minute (Julian et al., 2005).
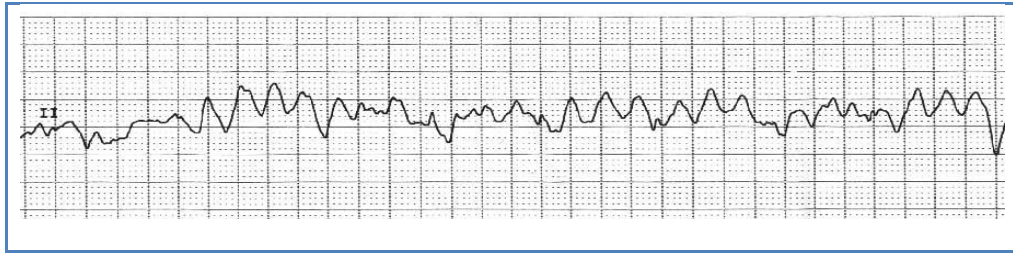


**Figure 2.19.  Ventricular Fibrillation, irregular complexes**

Multiple electrical waves occur during VF. Large numbers of meandering wavelets are a cause of fibrillation in the human heart. A combination of human VF recordings and computational studies of VF shows a small number of rotors and a reduced frequency and prolonged excitation wavelength in human models in comparison with animal models (Ten Tusscher et al. 2007). During VF, electrical turbulence initiates and is maintained by the process of wave break, because of the replacement of new waves with those that are extinguished and then contraction of them with each other (Xie et al. 2004). Wave breaks result from multiple wave front-wave tail correlations that underlie ventricular excitation. VF is also described by re-entry as an important mechanism for self-sustaining activity (Jalife 2000). Re-entry occurs when an excitation wave continually travels along a locked path. Cardiac re-entries are known as dangerous pathologies (Wellens 2004) and during VF, the heart becomes ischaemic where cardiomyocytes die because of shortage of blood supply.

### 2.5.2   Cardiac Ischaemia-Main Effects (Mechanisms of Myocardial Ischaemia)

Ischaemia means reduced blood supply of the heart muscle, which results in a shortage of energetic input and lack of waste elimination. This results in the abortion of contraction, decline of electrical performance, and subsequent death of the cell (Carmeliet 1999). Membrane ionic transporters refer to mechanisms sensitive to intracellular and extracellular ions and metabolites (Rodríguez et al. 2006). Ion concentration changes in ischaemia can be summarised as follows (Rodríguez et al. 2006):

- Increment of intracellular $Na^+$ and $Ca^{2+}$, augmented extracellular $K^+$, reduced extracellular $Na^+$, and reduced intracellular ATP. (ATP: transport of chemical energy within cells) (Rodríguez et al. 2006).

- Accumulations of external $K^+$; however, high $[K^+]_i$ and slow $[K^+]_o$ result under aerobic conditions.

- Three main reasons associated with increment of $[K^+]_o$ during ischaemia (Rodríguez et al. 2006):

  1. Reduction of the extra cellular space

  2. Reduction of active $K^+$ influx

  3. Increment of passive $K^+$ efflux

- Reducing the high conductance of the L-type $Ca^{2+}$ current $GCa_L$ (acidosis) (Kodama et al. 1984).

The relative effect of reduced $I_{Ca,L}$ associated with acidosis is small in global cardiac ischaemia (Clayton et al. 2011), which is consistent with empirical studies (Kodama et al. 1984).

The increase of $[K^+]_o$ is a cause of increment of conductance of $K^+$ channels through depolarization, which results in inexcitability and block of conduction (Carmeliet 1999). In ischaemia, a rise in $[K^+]_o$ results in large depolarization and increment of threshold.

Long effective refractory period (ERP) and short action potential (AP) may cause electrical disturbance during ischaemia because of a reduction in influx and enhancement in outward current during ischaemic condition. ERP is the period of time that the cardiac cell is unable to initiate another action potential for some duration of time.

**Electrical activity in the heart under conditions of ischaemia**

Changes in the AP caused by ischaemia: (Fozzard & Makielski 1985)

- Reduction of upstroke velocity of the depolarization phase of AP ($V_{max}$) and slowing conduction

- $I_{Na}$ (The current carrier responsible for excitation) is changed. By reduction of $I_{Na}$, consequently $V_{max}$ and CV are reduced.

- AP is shortened by increase in outward current, because of high $[K^+]_o$ and reduction of inward current.

**Mechanisms underlying arrhythmia generation under the conditions of ischaemia**

The increase in $[K^+]_o$ depolarization causes deactivation of $Na^+$ channels and reduction in the current produced during the action potential upstroke increasing the likelihood of re-entry in ischaemic cells (Carmeliet 1999). By increasing the number of wavelets and re-entrant sources, wave break occurs (wave break is an essential mechanism in the maintenance of VF) (Bradley et al. 2011). Re-entry in cardiology is a single impulse, which returns into a region of cardiac tissue that it has recently activated. Two essential conditions to originate re-entry in ischaemic cells are:

1. Conduction block at a particular site because the cells are still refractory.
2. Mixture of slow conduction and small refractory period.

**Investigating the effects of simulated ischaemia at the cell level on the re-entry behaviour at the tissue level**

Some studies have examined the influences of the various ischaemic components on the tissue model. For example, Clayton et al. (2011) investigated the effect of combinations of accumulated $[K^+]_o$ and decreased $[ATP]_i$ on the dynamic properties of the model (i.e. APD, CV restitution, ERP, and the tissue wavelength). For this study, tissue simulations were run with an initial condition. They have shown that accumulated $[K^+]_o$ results in CV reduction and ERP increment that acts to raise the period of re-entry and thus reduce activation rate. Whereas, the period of re-entry is decreased when lowered $[ATP]_i$ acts to reduce ERP and unchanging CV. In this case, activation rate is increased. In general, experimental studies predict that the re-entry remains stable in ischaemic tissue when the APD restitution is flattened, and ERP is prolonged from reduced $[ATP]_i$ and accumulated $[K^+]_o$ (Weiss et al. 2000).

The electrical activation of cardiac myocytes and the changes of activation rate are slow between the endocardial and epicardial layers during the period of ischaemia (Massé et al. 2009). In addition, there are variations between the pericardium and endocardium with respect to wave break. More wave breaks occur on the epicardium during ischaemia (Massé et al. 2009). VF progression may not be the same in all species, hence results in dogs or pigs should be separated from humans, because of differences in ion channels (Huang 2003). Thus, action potential duration differs among different species (Huang 2003). VF

characteristics are modified by electrophysiological remodelling associated with heart failure, for example a decrease in the number of wave breaks. Experimental studies in dogs show that VF in heart failure is related to a lower number of wave fronts and re-entrant waves than in normal hearts. It has been shown that the numbers of fibrillation waves are decreased in HF animals (Moreno et al. 2005). Reduced excitability results in an expansion in the region of the core of rotating spiral waves. Re-entrant spiral waves are a fundamental mechanism of VF (optical mapping is used to demonstrate rotating spiral waves). During ischaemia, conduction velocity reduces due to an increase in the re-entrant period of spiral waves (Mandapati et al. 1998). The dynamic variability of AP shape has been shown to define factors of VF dynamics at advanced stages of VF/ischaemia. In addition, dynamic instabilities affect defibrillation outcome during ischaemic VF. More studies are needed to assess whether ischaemia-specific AP instability is an operator of defibrillation success or failure (Huizar et al. 2007). (Defibrillation terminates the arrhythmia, returning the heart to sinus rhythm).

**Limitations of heart studies related to ischaemia**

Global histological evaluation is absent in heart studies to assess the correlation of fibrosis with experimental findings relate to ischaemia. For example, a study by Massé et al. (2009) included global fibrillation dynamics during ischaemia and reperfusion in the whole heart. However, defibrillation efficacy was not evaluated in their research (Massé et al. 2009). In addition, optical recordings were restricted to the epicardial surface; access to those other parts of the ventricle that had a various time course of VF development could not be denied (Huizar et al. 2007). Epicardial areas were mapped and performed in most studies, so whole activation pathways could not be assessed and thus all re-entrant waves were not obtained (Huang 2003; Moreno et al. 2005; Venable et al. 2010). Additionally, most studies were based on the normal heart. However, cardiac disease in addition to drugs can alter epicardial findings and clinical results (Huizar et al. 2007). The development of VF in unhealthy hearts might differ from normal hearts (Huang 2003; Venable et al. 2010).

### 2.5.3 Repolarisation and Refractoriness during Ischaemia

**Refractory Period (RP)**

The term refractory period is defined as the interval from depolarization to the recovery of excitability in the cardiac cell which is unable to respond to any stimulus (initiation of another action potential) to protect the heart. This period of time corresponds with the systole (contraction) of the cardiac muscle (Burton & Cobbe 2001).

**Effective refractory period (ERP)**

The effective refractory period is defined as the period of time in which a second stimulus can again activate sodium channels to generate a propagated AP (Kanki et al. 1998).

**Post-repolarization refractoriness (PRR)**

Post-repolarization refractoriness means excitability recovery time closely succeeds repolarization time (S1S2 interval (ms) (Downar et al. 1977).

#### 2.5.3.1 Relationship between Repolarization and Refractoriness in the Human Heart

Myocardial cell excitability is mainly mediated by the changes in the cardiac sodium channels. The depolarization phase and the upstroke of the cardiac AP are produced after activation of sodium channels. The CV is determined by the maximum upstroke velocity (dV/dtmax) of the AP. The channel enters the resting state (inactivation of channels) after full repolarization of the AP so that a new activation may occur. Under normal conditions, the end of the RP corresponds with the end of repolarization (Hoffman & Cranefield 1960) when the channel recovers from inexcitability after the resting membrane potential has been reached (Coronel et al. 2012). The APD is usually used as a measure of the RP and can be seen as a surrogate for ERP (Bode et al. 2001) under normal conditions.

Myocardial cells reach excitability as repolarization progresses (in a time and voltage dependent manner). Thus, there is a close relationship between the duration of repolarization (APD) and the duration of ERP (Davidenko & Antzelevitch 1986; Bode et al. 2001). Myocardial disease or anti-arrhythmic drugs may change this relationship by causing PRR (Nattel & Zeng 1984; Franz et al. 1988; Janse & Wit 1989; Lee et al. 1992).

Experimental studies (Han & Moe 1964; Kuo et al. 1983) indicated the enhancement of dispersion of refractoriness with arrhythmogenesis. A short RP placed between regions of longer RP helps the formation of re-entrant circuits (Janse & Wit 1989).

Experimental studies have shown that during the first few minutes of ischaemia, the RP changes from being voltage-dependent to time-dependent, independent of APD. This alternation is clinically relevant as the main serious ventricular arrhythmias during ischaemia are caused by re-entry (Janse & Wit 1989). Although the dispersion of RP is an essential mechanism in most re-entrant arrhythmias, it is not sufficient condition for initiation of re-entry (Burton & Cobbe 2001). Thus, it is necessary to use a premature beat as a trigger to gain the critical degree of conduction delay for re-entry (Burton & Cobbe 2001).

### 2.5.3.2    *Repolarisation and Refractoriness During Ischaemia in Humans*

Ventricular arrhythmias (VT and VF) caused by re-entrant electrical activity in the heart ventricles (Jalife 2000) usually occur during myocardial ischaemia (Janse & Wit 1989). Electrophysiological and metabolic properties of the cell are affected by the lack of blood supply and flow during the acute phase of myocardial ischemia. These changes produce variations in the AP morphology and propagation. The mechanisms (i.e., hyperkalemia, hypoxia, and acidosis) responsible for these changes, such as reduction of CV and excitability and shortening of APD have been reviewed in detail in Chapter Two (section 2.3). These heterogeneities in electrophysiological properties (i.e., CV, membrane excitability and refractoriness) in the ventricular tissue have been shown to set the stage for re-entrant arrhythmias in many experimental (Coronel 1994; Kuo et al. 1983) and theoretical studies (Faber & Rudy 2000; Burton & Cobbe 2001; Ferrero et al. 2003; Franz 2003). The dispersion of refractoriness as a factor that determines generation and maintenance of arrhythmic episodes during regional acute ischemia has been well investigated (Romero et al. 2009).

One study by Coronel et al. (2012) showed that during ischaemia, the heart reacted to a premature stimulus 100 ms shorter than under control conditions; however, with a delay of 100ms between stimulus and local response the refractory period in the ischemic zone had decreased to a value shorter than that in control conditions. They showed that the anoxic cells with $[K^+]_o$ concentration between 6 to 9 mM have short refractory periods, and anoxic cells with $[K^+]_o$ concentrations 9 mM exhibit PRR. This dispersion of refractoriness forms the basis for re-entrant arrhythmias (Coronel et al. 2012). Although the shortening of APD occurs

in the ischaemic area, the refractory periods may shorten, lengthen or remain unchanged (Burton & Cobbe 2001). During ischaemia, the recovery of excitability may be delayed behind the completion of repolarisation (termed post-repolarisation refractoriness) due to delayed reactivation of sodium channels (Burton & Cobbe 2001). The RP and its dispersion are difficult to measure because the stimulation threshold and refractoriness are not at steady state in acute ischaemia (Burton & Cobbe 2001). This prevents the measurement of dispersion by the standard extra-stimulus technique. Therefore, the ERP is conventionally measured with regular pacing stimuli trains succeeded by premature stimuli at progressively shorter coupling intervals (Burton & Cobbe 2001). They concluded that although the increment of dispersion of refractoriness in the ischaemic zone is not by itself arrhythmogenic, it increased the possibility of conduction block leading to initiation of re-entry when CV is reduced.

### 2.5.4 Ischaemia and Ventricular Fibrillation

The mechanisms underlying ventricular arrhythmias correlated with ischaemic cardiac disease are demanding for clinical studies to explain. Animal models have been developed to examine the electrophysiological variations related to myocardial ischaemia and how they result in the formation of VF. This helps to address the limitations of clinical studies and provide new hypotheses and theories that have been examined in clinical studies, therefore increasing the level of information about arryththmogenesis in cardiac ischaemia (Bradley et al. 2011).

Ischaemia results from a reduction of blood supply to the heart cells and tissue, and also it is a certain consequence of VF. Study of ischaemia is important for two reasons: firstly, regional ischaemia resulting from coronary artery disease can initiate re-entry and VF; and secondly, global ischaemia results from VF. In global ischaemia, the number of activation waves increases during ischaemia VF. One study associated with ischaemic VF by Bradley et al. (2011) reported the following findings:

- Increasing activation frequency increases the number of re-entrant sources.
- Although activation rate was decreased, the number of wavelets and re-entrant sources increased.
- In case of fluctuation of activation frequency, the number of wavelets and re-entrant sources remained constant.

They proposed several mechanisms that may operate during VF which depend on the type of VF as ischaemia progresses. These mechanisms include: the restitution properties of APD and conduction velocity; expansion of the spiral wave core; and stability of the scroll wave filament. Restitution (rate dependent behaviour) is an important factor in re-entry behaviour in the human heart ventricles.

## 2.6   Computational Modelling of Cardiac Electrophysiology

Computational models of cardiac cell electrophysiology are known as important resources in consideration of the mechanisms of cardiac arrhythmias. Significant advantages of models are reproducibility, the capacity to systematically change parameters, and accessibility to all experimental components at high spatial and temporal resolution (Elshrif & Cherry 2014). They are helpful integrations with biological experiments and could be utilized to improve and to implement initial examinations of hypotheses. Modelling of cardiac electrophysiology as an important investigative tool has been expanded to demonstrate different parts of the heart, involving atria, ventricles, sinoatrial node, atrioventricular node, and Purkinje network (Elshrif & Cherry 2014). Models have been designed to reproduce the behaviour of cells of individual species, occasionally under different disease circumstances.

Cardiac electrical activation depends on biophysical events at cell and tissue scale. The mechanical function of the heart depends on its muscular architecture that contributes to the electrical properties of cardiac tissue. Therefore, experimental studies are needed to link structural and electrical function. For this purpose, computer models provide a means of considering the possible effects of cell and tissue structure on electrical activation. The models provide studies of the limitations of experimental recordings (Austin et al. 2006). The importance of cardiac models as research tools can be summarized as:

- Heart models are useful tools in cardiac disease studies which combine clinical and experimental approaches.
- To study the abnormality of electrical activities in the heart.
- To provide a quantitative understanding of the effect of the complex structure of cardiac muscle.
- To allow relation of arrhythmic (irregular heart beat) behaviour with its clinical counterparts, for instance electrograms on the cardiac surface (Trenor et al. 1952).

### 2.6.1 Modelling of Cardiac Ischaemia (Regional Ischaemia and Global Ischaemia)

Myocardial ischaemic injury results from a lack in both energetic input and waste removal that progressively reduces electrical activity in the region of injury, leading to failure of contraction, and finally, cell death (Rodríguez et al. 2006). There are limitations in clinical studies and experimental models in assessing the consequences of arrhythmia mechanisms in ischaemic cardiac disease. For example, during the early acute stage of ischaemia (first 10-min post occlusion), electrophysiological variations subsequent to coronary blocking are very rapid; thus, it is difficult to completely examine the cause-and-effect relations between metabolic and electrophysiological parameters (Rodríguez et al. 2006). Therefore, electrophysiological computing research using mathematical models can separate different effects and obtain the main relations among electrophysiological parameters associated with myocardial ischaemia. This is essential in determining the function of ischaemic abnormalities in cardiac electrophysiological behaviour. In this section, the electrophysiological variations associated with global cardiac ischaemia and regional ischaemia are briefly reviewed to study the role of ischaemic abnormalities in cardiac electrophysiological behaviour.

**Global cardiac ischaemia**

Global cardiac ischemia is characterised by the influence of three main components (hyperkalemia, hypoxia and acidosis) on cardiomyocyte electrophysiological activities, presenting homogeneously in the tissue. These components lead to depolarization of resting potential from -85mV to -66mV, APD shortening from 138 to 67ms, and a 32% decrease of action potential amplitude (Rodriguez et al. 2003). Changes in membrane dynamics occur following 5–7 minutes (phase 1 of ischaemia) and 10–12 minutes (phase 2) after the onset of ischaemia (Rodríguez et al. 2004). To illustrate these two levels of ischaemia (Rodriguez et al. 2003; Rodríguez et al. 2004):

- The extracellular potassium concentration ($[K^+]_o$) was raised from its normal value (5.4mmol/L) to 12mmol/L.
- The maximum conductances of the $Na^+$ and L-type $Ca^{2+}$ current ($I_{Na}$ and $I_{CaL}$) were reduced to 75% of their normal values in ischaemia to simulate their blockage because of intracellular and extracellular acidosis.

- A formulation of the ATP-dependent $K^+$ current was embedded into the model, in which the values of 6.8mM and 15μM, and 4.6mM and 99μM were defined for the intracellular ATP and ADP concentrations for normal and ischaemic conditions respectively (Rodriguez et al. 2003).

**Regional Ischaemia**

Figure 2.20 describes the structure of a 2-D tissue model, in which the various zones shaped by cardiac regional ischaemia correspond to 10 min after the onset of ischaemia. The sizes of these zones and the values of the relevant model parameters have been derived from experimental data presented in the literature (Ferrero et al. 2003). The ischaemic zones were considered as (Ferrero et al. 2003):

- A central ischaemic zone (CZ) - cells are directly influenced by the inadequacy of blood flow in this area.
- A ring-shaped border zone (BZ) - relevant components influenced by ischaemic variation in this area as displayed in the upper part of Figure 2.20.
- The normal zone (NZ) - corresponding to normal tissue surrounds the BZ circle.

The main ischaemic components were simulated in the ischaemic regions as follows (Ferrero et al. 2003):

- Hyperkalemia was modelled by elevating $[K^+]_o$ from the normal value of 5.4 mmol/L in the NZ to 12.5 mmol/L in the CZ.
- Simulation of acidosis by reducing the conductance of the $Na^+$ and L-type $Ca^{2+}$ current ($I_{Na}$ and $I_{CaL}$) channels by 25%, in which currents were scaled by factors $pNa$ and $pCa$, respectively, with values of 1.0 in the NZ and 0.75 in the CZ.
- Hypoxia was modelled by decreasing intracellular ATP levels and increasing intracellular free ADP concentration; the values are shown in the upper part of Figure 2.20. The ATP and ADP levels generate values for $fATP$ of ≈ 0% and ≈ 0.7% in the NZ and CZ, respectively.
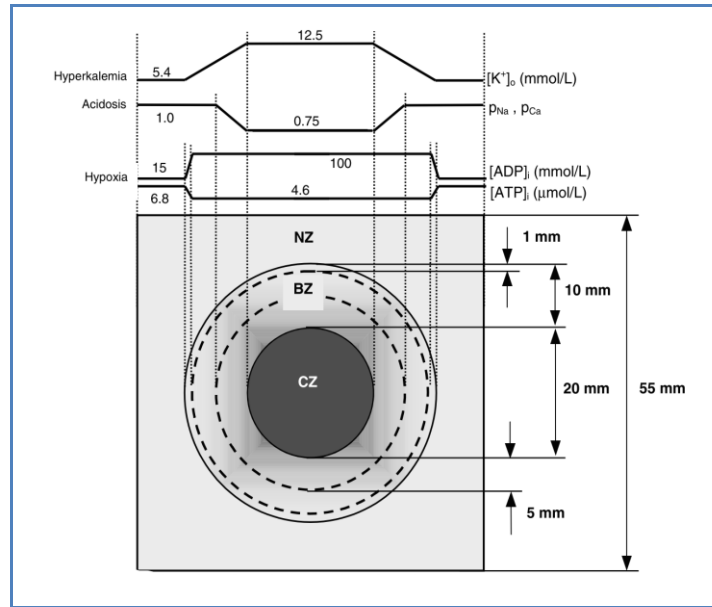
**Figure 2.20. Schematic of regional ischaemia in the 2-D tissue model with the relevant components (Ferrero et al. 2003). Ischaemic zones were considered as a circular central ischemic zone (CZ), border zone (BZ) and normal zone (NZ). The spatial variations of ischaemic components across the different transition zones were presented in the upper traces.**

During regional ischaemia, cardiac vulnerability (vulnerability occurs when the stimulus successfully initiates propagation in some directions but fails in other directions) depended on the place and size of the blockade, the heterogeneity structure because of a border zone, and the difficulty of the electrophysiological variations at the cell level in the ischaemic zone (Rodriguez et al. 2003). Another study by Romero et al. (2008) proved that vulnerability to re-entry depends on the size and location of the ischaemic zone.

Here, the effects of global rather than regional ischaemia are examined; therefore, the spatial heterogeneities are not considered.

**The electrophysiological alterations in cardiac ischaemia**

Computer simulations provide a high degree of electrophysiological detail for study of ischaemia at the ionic level. The main electrophysiological changes in these models can be summarised as follows (Rodríguez et al. 2006):

- Activation of the $I_{K,ATP}$ channels is accountable for the major APD reduction observed in hypoxic cardiomyocytes.
- Elevated $[K^+]_o$ plays a lesser role in APD reduction.
- The $[K^+]_o$ increment affects resting membrane depolarization, which causes reduced

accessibility of $Na^+$ channels and slow recovery of the $Na^+$ channel inactivation gates, thus decreasing AP upstroke and reducing propagation velocity. Consequently, this leads to reduced excitability and prolonged post-repolarization refractoriness in ischaemic cardiomyocytes (Rodríguez et al. 2006).

- Acidosis reduces the excitability of ischaemic myocytes by acting to reduce the maximum conductance of the $Na^+$ and $Ca^{2+}$ channels (Rodríguez et al. 2006).

- The AP upstroke and propagation velocity are significantly influenced by the ischaemia-induced alterations in $Na^+$ and $Ca^{2+}$ currents.

- $Ca^{2+}$ current is another important factor in the incidence of propagation block and the development of oscillations in the ischaemic region that are originators of re-entrant activity in ischaemia (Rodríguez et al. 2006).

### 2.6.2  Modelling of Cardiac Arrhythmias

In this section, a brief overview of computational models is provided with some examples that have been used to simulate arrhythmias.

### 1.      The dynamics of cardiac fibrillation

Ventricular fibrillation is a primary reason for sudden cardiac death. This arrhythmia results from various clinical conditions. Ischaemia can be the cause of these arrhythmias. Fibrillation occurs due to an electrical wave break and re-entry (Weiss et al. 2005). Re-entry happens once the electrical wave propagates over the ventricles and breaks to a rotor form. Fibrillation results when the waves propagate outside of a rotor and expand additional wave breaks (Weiss et al. 2005). In diseased hearts (ischaemic heart), tissue heterogeneity is increased, affected by structural and electrical remodelling related to disease processes. This has been discussed as the main cause of developing wave break and fibrillation (Weiss et al. 2005).

### 2.      Electrical waves and wave break

An electrical spiral wave is described with a wave front and a wave back. The wave front corresponds to the AP depolarization and the wave back is related to fast repolarization (Weiss et al. 2005). The wavelength which is the product of APD and CV is measured as distance between wave front and wave back (Weiss et al. 2005). Wave front and wave back never touch each other when a wave propagates across normal tissue. Otherwise, a wave break is defined at their point of intersection (called phase singularity). In this case, re-entry

occurs at a localised wave break and thus fibrillation results if the process of wave break continues (Weiss et al. 2005).

## 3. Tissue Heterogeneity and Wave Break

Several mechanisms are associated with wave break caused by tissue heterogeneity (Weiss et al. 2005):

- Wave break will happen when a wave moves into a region with a prolonged APD while the excitability has not yet recovered in the tissue from the earlier wave (Weiss et al. 2005).

- Wave break will appear when there is a contradiction between wave front and excitable tissue. In this case, the diffusion of depolarizing current is too low to reach the excitable tissue threshold (Weiss et al. 2005). This may result from regional excitability depression because of ischaemia or drugs.

- A wave break could localize in an area with an excessive electrophysiological dispersion. This would be due to disease processes that raise tissue heterogeneity and enhance the possibility that physiological premature ventricular extrasystoles are not enough to stimulate rotors (Weiss et al. 2005). Therefore, a large electrical stimulus or a rapid pacing is required to replace the VF threshold.

- Tissue heterogeneities in the heart (Weiss et al. 2005) are categorised as:
  - Anatomic because of infarction, fibrosis
  - Structural remodelling
  - Electrophysiological because of electrical remodelling, drugs, and genetic faults
  - Heterogeneous autonomic innervation (Weiss et al. 2005)

## 4. Dynamic Factors and Wave Break

Dynamic factors produce different electrophysiological properties in different regions arising from the dynamic properties of $V_m$ and $Ca^{2+}$ cycling on APD and wavelength (Weiss et al. 2005). These are determined in computer models in which all cardiomyocyte cells have the same properties and normal ventricular AP. Factors regulating APD and CV are divided into $V_m$ and $Ca^{2+}$ elements (Weiss et al. 2005).

***$V_m$-related dynamic factors present as follows:***

1. **APD Restitution**

   APD reduces physiologically when the heart rate rises to maintain an appropriate diastolic interval (DI) for filling ventricles. APD is too sensitive to small variations in DI if the APD restitution (Restitution: the rate adaption of cardiac cells and tissue) curve has a steep slope.

2. **CV Restitution**

   CV controls the wave front position; hence, this state occurs dynamically when CV strongly depends on the previous DI (CV restitution).

3. **Short-Term Cardiac Memory**

   This term states when everything in the pacing history is defined except the last DI that controls APD and CV in the short term. Due to the short-term cardiac memory, APD and CV restitution curves measured by protocols must be seen as calculations of electrical restitution arising during an arrhythmia (Weiss et al. 2005). In this situation pacing history is different.

***$Ca_i$-related dynamic factors:***

The importance of $Ca^{2+}$ cycling is because of its regulatory role in dynamic wave instability and also to initiation and destabilization of re-entry. In normal physiological conditions, $V_m$ controls the regulation of contraction that is influenced by $Ca^{2+}$ in the beating heart. In this state, systolic and diastolic $Ca^{2+}$ levels are influenced by pacing rate, which affects calcium-sensitive currents that modify APD and consequently, wavelength (Weiss et al. 2005).

**The importance of study of restitution in this research**

Restitution is defined as the rate adoption of cardiac cells and tissue. Electrical restitution of the action potential duration (APD) and conduction velocity (CV) in ventricular muscle (Panfilov & Zemlin 2002) has been indicated to be a main element in controlling the dynamic instability of spiral wave re-entry. APD restitution (APDR) is defined as the correlation between APD and the last diastolic interval (DI) in electrophysiological calculations. DI is the time which has passed between the end of the previous AP and the onset of the following

one (Panfilov & Zemlin 2002). The CV restitution (CVR) is the relation between the propagated speed of the S2 AP and the corresponding DI (Xie et al. 2002). In cardiac tissue, diffusive currents are generated by coupling myocytes into neighbouring cells, thus affecting APDR. In addition, CVR is a key factor in wave stability that it is not possible to calculate in a single cell (Xie et al. 2002a). Theoretical and computer studies have indicated that fibrillation is maintained by the characteristic of the APDR. For example, the steep slope restitution (>1) curve generates unstable wave propagation that arises in wave break; therefore, this state is essential for fibrillation. However, flattening restitution curves inhibits wave break and consequently stops fibrillation (Garfinkel et al. 2000). Several mechanisms may contribute to the slope of restitution curve. For instance, it has been shown that ischaemia flattens APD restitution in animal and human hearts (Nash et al. 2006). In this study, restitution methods are used to investigate the function of electrical restitution on wave stability. Human cell models are used to examine the role of electrical restitution in unstable spiral wave re-entry in simulated 2-D ventricular tissue.

### 2.6.2.1   *Spiral Wave Dynamics and Mechanisms of Spiral Wave Breakup*

Re-entry is the most common cardiac arrhythmia to have been performed with optical imaging on the surface of the heart (2-D) and in the shape of scroll waves (3-D) (Qu et al. 2014). Different spiral wave dynamics have been detected in the real heart involving stable spiral waves, meandering spiral waves, and spiral wave breakup (Qu et al. 2014). The mechanism of spiral waves in normal ventricles has been described as unstable with break up into electrical instability, established as cardiac fibrillation. Experimental studies (Riccio et al. 1999; Garfinkel et al. 2000; Wu et al. 2002; Lou et al. 2012) show that reduction in the steepness of the APD restitution curve converts multiple re-entrant wavelets (irregular and unstable fibrillation) dynamics into stable spiral waves (periodic tachycardia), supporting the concept developed via computer modelling studies (Qu et al. 2014). Although these studies have shown the significance of dynamic variability and the steepness of the APD restitution curve in cardiac arrhythmias, the role of tissue heterogeneity in arrhythmia creation and continuation has been found to be extremely important. For example, computer simulations (Qu et al. 2014) show that in case of tissue heterogeneity, wave breaks can happen in areas of steep APD slope, arising in multiple waves and rapid changes in frequency. In this case, disconnected frequency diffusion no longer survives in the spiral wave breakup regime, but associates locally with the heterogeneity. This behaviour is also in agreement with

experimental findings (Choi et al. 2001; Choi et al. 2002; Valderrábano et al. 2002), supporting the multiple wavelet hypothesis in which dynamic instabilities play the major role rather than tissue heterogeneities (Qu et al. 2014).

**Mechanism of Spiral Wave Breakup in 2-D**

Identification of the detailed dynamics of re-entrant arrhythmias is challenging due to the complex structure of cardiac tissue and the complicated cell ionic currents (Fenton et al. 2002). Important mechanisms of spiral wave breakup that can happen in cardiac tissue have been demonstrated here.

*Steep APD restitution*: the steepness of APD restitution curves with gradient larger than one can generate alternations in APD that can result in spiral wave breakup in 2-D (Fenton et al. 2002). In this case, the minimum diastolic interval (DI) for a fixed period is larger than zero, and a long APD created by the alternations can require a DI lower than the minimum and originate conduction block. Thus, small changes in DI are increased into bigger variations in APD, while alterations in APD because of changes in DI are suppressed at smaller gradients (Figure 2.21) (Fenton et al. 2002).
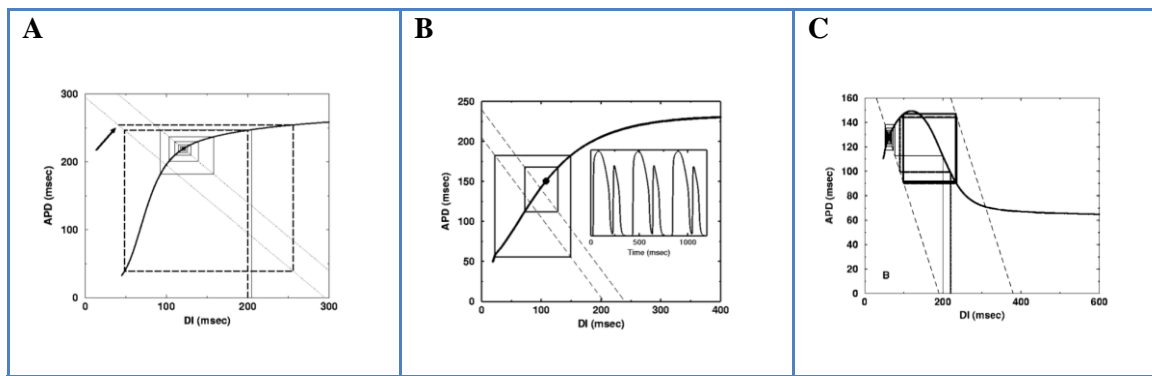


**Figure 2.21. Spiral wave breakup structure in 2-D: Effect of steep APD restitution and Biphasic APD restitution curves (Fenton et al. 2002). A: APD restitution curve acquired in a cable by alternations of APD and conduction block. B: APD restitution curve with gradient larger than one (slope >1) for a model with a bigger scope of DIs in the gradient larger than one area (because of decreased steepness and reduced minimum DI). C, oscillations due to a biphasic APD restitution curve, conduction block can be created and result in breakup.**

***Biphasic APD restitution curve****;* APD restitution curves are shown with a range of DIs for which the APD is prolonged as DI is reduced. These biphasic APD restitutions have been shown as a cause of complex dynamics in 1-D electrical maps (Fenton et al. 2002). The conduction block created in 2D due to the biphasic part of the APD restitution curve at fixed DIs can originate spiral wave breakup.

**Mechanism of spiral wave breakup in 3-D**

The significant causes of the scroll breakup in 3-D models are reviewed below (Qu et al. 2000):

***Steep APD restitution****;* the steep APD restitution curve slope mechanisms can produce strong meander, therefore encouraging big alternations in tip velocity that result in large excitable spaces in the scroll core region (Qu et al. 2000).

***Fibre rotation or filament twist****;* the ventricular muscle structure, which is composed of fibres (three times faster conductance along their axes than across) can cause the scroll wave to travel in various stages at different tissue complexities (Qu et al. 2000). This could be an initiation of a phase delay on the waves within the sheets arising from the thickness of the tissue (Fenton et al. 2002).

***Transmural propagation in the z direction****;* this allows the filament to curve. This property incorporates a functional form of filament. The filament can break both by crashing with an edge or by crashing intramurally with itself to generate a scroll circle if filament curving is great enough (Qu et al. 2000).

***The stable or weak meander regime****;* in this case, the excitable region of the centre is not large enough to adopt into two counter rotating spiral waves; therefore, scroll breakup does not occur (Qu et al. 2000).

***Curvature of the scroll wave front and wave back****;* in this case, fibre rotation lengthens APD in limited areas, assisting wave break along the scroll branch (Qu et al. 2000).

# 3 Computational Cardiac Electrophysiology Methods

*In this chapter, methods to simulate activation and propagation in simulated cardiac tissues are presented for studying the mechanisms of normal and abnormal activation. The importance of computational modelling is presented at the start of this chapter. The second section describes cardiac cell models to simulate the action potential based on the electrical activity of cardiomyocytes. A brief overview of several cardiac cell models built on the Hodgkin–Huxley model is provided. Then, the two main ventricular action potential models used in this thesis are described.*

*The third part of the chapter describes the quantitative description of conductivity at the tissue level to support numerical representation of AP propagation. The model assessment and analysis of the characteristics of AP propagation in tissue models are presented. Then, monodomain and bidomain equations are given followed by a short description of tissue geometries.*

*The mathematical execution of cardiac tissue models is described in part four. Methods for solving the monodomain and bidomain tissue models based on finite difference, finite volume and finite element methods are considered. In the fifth part of the chapter, approaches for identifying and tracking phase singularities and filaments based on the phase distribution technique are described. In section six, a description of the software implementation of heart simulation is discussed. A brief summary of software packages that are used in heart simulations is provided. The pathological models are discussed in the next section, and then, strategies and aspects for validation are discussed. Finally, mathematical modelling approaches used in this thesis are summarised.*

## 3.1 Rationale for Modelling

Computational modelling could transform biomedical research with in silico experiments that would be unthinkable in animals or patients (Clayton 2001). Models are used for interpretation of clinical and physiological measurements (Vigmond et al. 2009) to improve the understanding of dysfunction in disease such as arrhythmias, myocardial ischaemia and heart failure. The central focus of clinical heart research is cardiac structure and operation in health and disease. In addition, experimental studies investigate the behaviour of animals and humans in healthy and diseased cases from molecular to whole body levels. Thus, integration of different levels of structural scale from ion channel activation to cardiac propagation and regional strain formation is a major challenge in these studies. It is necessary to describe the potential properties at all scales in the hierarchy of biological complexity from the single building blocks to the whole heart. However, integrative approaches have their challenges because of the difficulty of the structure-function correlation in the heart. Mathematical modelling can address the knowledge of integration regarding heart behaviour. Models have a major impact on data combination, extraction of knowledge, understanding and systematic insight. These processes are not available by direct experimental operation or examination. In contrast, computational models that are validated experimentally can predict 3D behaviour in cases where the experiment aborts (the validation process is explained in Section 3.7). New quantitative tools are needed to integrate information on and prediction of human heart behaviour. Developed mathematical modelling can address this need (Vigmond et al. 2009).

## 3.2 Modelling Transmembrane Ionic Current

The heart can demonstrate various complicated excitation and conduction dynamics. Modifications of these dynamics are accountable for the changes from normal heart rhythm to arrhythmia and between various forms of arrhythmia (Qu et al. 2014). This section presents an overview of some of the basic biophysical activities of ionic current, excitable cells and mathematical modelling of cardiac dynamics at cell scale. Firstly, the electrical circuit model of excitable cells will be demonstrated by a description of the development of the first action potential model by Hodgkin and Huxley. The mathematical description of this model will be presented followed by a brief review of the *ODE solvers*. After which, a brief overview of the two ventricular action potential models which have been used in this thesis is presented.

## 3.2.1    Hodgkin-Huxley Model

The first mechanistic model of the AP of excitable cells was developed by Hodgkin and Huxley (Hodgkin & Huxley 1952). The Hodgkin–Huxley model was the first model that experimentally characterized the kinetics of ion channel transport and gating using a mathematical model (Noble 2007). This model investigates the quantitative behaviour of a model nerve under a variety of conditions which correspond to experiments. The Hodgkin–Huxley formulation showed the properties of excitable membrane current by moving ions through call membrane resistances in parallel with capacitance (Noble 1962).
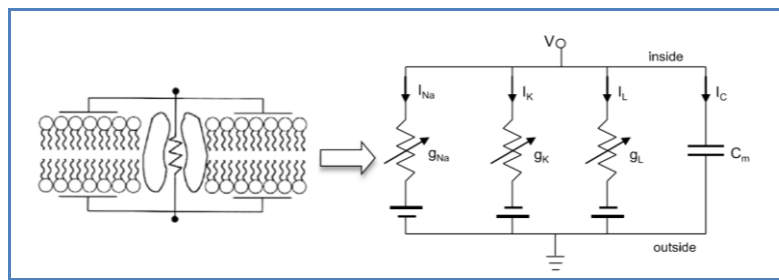


**Figure 3.1. The Hodgkin–Huxley model. Graphic plot demonstrating a battery (the cell membrane) and a conductor (the ion channel) with the electrochemical circuit of the Hodgkin–Huxley model of the squid giant axon (Qu et al. 2014).**

The fundamental method of the model described by a simple electrical circuit was used to examine the excitation and propagation of action potentials. The biophysical cell membrane was modelled as capacitors and the ion channels as electrical conductances (Figure 3.1), indicating the current flowing through the capacitor as $I_C$ and the current through the conductors as $I_i$. Figure 3.1(right) shows the electrochemical circuit displaying the giant axon. The simplest formulation is accurate and sufficient for theoretical measurement of the action potential and refractory period is presented here (Hodgkin & Huxley 1952):

$$I = C_m \frac{dV}{dt} + I_i \qquad (3.1)$$

$I$: Total membrane current density

$C_m$: The Capacity current per unit area

$I_i$: The ionic current density for each specific ion channel

$V$: The membrane potential

$t$ : Time

The total ionic current is:

$$I_i = I_{Na} + I_K + I_L \qquad (3.2)$$

$I_{Na}$: Sodium ions

$I_K$: Potassium ions

$I_L$: Other ions

The mathematical formulation of ionic currents based on Ohm's law is:

$I_{Na} = g_{Na}(V - E_{Na})$ (a)

$I_K = g_K(V - E_K)$     (b) $\qquad\qquad$ (3.3)

$I_L = g_L(V - E_L)$     (c)

where $g_{Na}$ and $g_K$ (shown in Figure 3.2) are variable conductances depending on V, and $g_L$ is a small constant. $E_{Na}$, $E_K$ and $E_L$ are the membrane potentials.
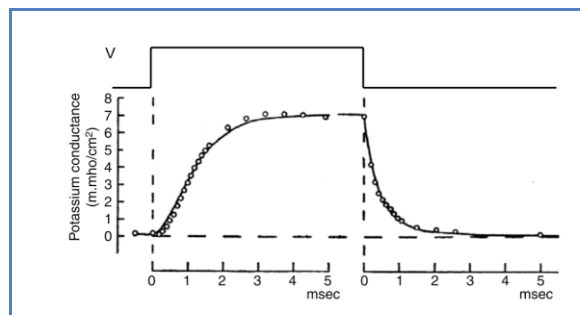


**Figure 3.2. $K^+$ channel conductance ($g_K$) in squid giant axon (Qu et al. 2014).**

Figure 3.2 displays the main voltage clamp experimental data of $g_K$. In this case, voltage is depolarized from resting potential by 25 mV and then repolarized to resting potential after a specific time period (Qu et al. 2014). The decay of the conductance $g_K$ after repolarization can be fitted by an exponential decay (Qu et al. 2014).

Hodgkin and Huxley showed that their equations could reproduce many electrical attributes of the squid nerve involving the shape and size of the action potential (Hodgkin & Huxley 1952).

### 3.2.2 Ordinary Differential Equation Solvers

In this section, solution approaches will be described for the cell model ODE system representing excitability in ventricle simulations. Biophysically detailed cardiac cell models are presented by Equation (3.1) above. The gating variables for cardiac cell models are presented by the voltage-dependent terms $x_\infty(V_m)$ and $\tau_x(V_m)$.

Different approaches have been used to solve ODE equations involving explicit Euler, fourth-order Runge-Kutta and implicit techniques, but the most extensively used method has been the discrete form defined by Rush and Larsen (1978):

$$x_{n+1} = x_\infty(V_n) + (x_n - x_\infty(V_n))e^{-\Delta t/\tau_x(V_n)} \qquad (3.4)$$

where $V_n$ is the membrane voltage at time step n , and $\Delta t$ is the time step. The membrane currents can be calculated at each time step, and the new value of membrane voltage can be computed from Equation (3.1). To improve computational efficiency the voltage-dependent terms $x_\infty(V_m)$ and $\tau_x(V_m)$ can be premeasured and saved in a lookup table (Clayton & Panfilov 2008).

### 3.2.3 Ventricular Action Potential Models

In recent decades the number of cardiac cellular modelling has expanded for the purpose of model development with the focus on describing specific tissue types, animal species and physiological functions (Fink et al. 2011). There are many examples of these models available in the cardiac cellular modelling literature which integrated data from multiple sources (Fink et al. 2011), and using biophysical models and multiscale models to represent specific biophysical mechanisms. Along with these models, electrophysiological cell models with combination of ion currents through ion channels, transporters and exchanges have more focused on generation of key physiological properties of the AP and calcium signalling (Niederer et al. 2009). Several cell electrophysiology models (Table 3.1) have been developed for different species and regions that ventricular cell models are more favourable (Fink et al. 2011). These models have been developed for different mammalian species (Table 3.1).

**Table 3.1. Mammalian electrophysiology models (Fink et al. 2011).**

| Species | Model names (references) |
|---|---|
| guinea pig | (Luo & Rudy 1991)<br>(Nordin 1993)<br>(C H Luo & Rudy 1994)<br>(Noble et al. 1998)<br>(Faber & Rudy 2000)<br>(Matsuoka et al. 2003) |
| canine | (Winslow et al. 1999)<br>(Fox et al. 2002)<br>(Greenstein & Winslow 2002)<br>(Cabo & Boyden 2003)<br>(Hund & Rudy 2004)<br>(Flaim et al. 2006) |
| rabbit | (Puglisi & Bers 2001)<br>(Shannon et al. 2004)<br>(Mahajan et al. 2008) |
| rat | (Pandit et al. 2001) |
| mouse | (Bondarenko et al. 2004)<br>(Wang & Sobie 2008)<br>(Niederer & Smith 2007) |
| human | (Priebe & Beuckelmann 1998)<br>(Iyer et al. 2004)<br>(Ten Tusscher et al. 2004)<br>(Ten Tusscher & Panfilov 2006)<br>(Grandi et al. 2010),<br>(O'Hara et al. 2011) |

Ventricular models have differences among species that produce different cellular properties and mechanisms which can lead to differences in model predictions (Fink et al. 2011). For instance, although the Fox et al. (2002) and Hund and Rudy (2004) canine models have the same currents, these models behave differently. For example, $Na^+/Ca^{2+}$ exchanger current acts in opposite mode through the AP plateau phase in the Hund and Rudy model in comparison with the Fox et al. model (Figure 3.3). The differences in the $I_{Ks}$ and $I_{Kr}$ currents (Figure 3.3) have an important role during early and late repolarisation of AP which is more significant in the Hund and Rudy model (Fink et al. 2011).
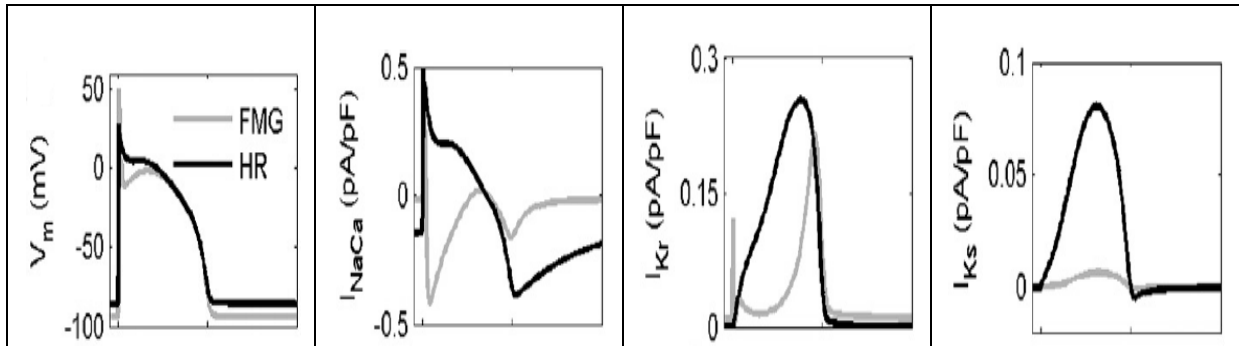
**Figure 3.3. Differences in action potentials, and selected $Na^+/Ca^{2+}$ exchanger, $I_{Ks}$ and $I_{Kr}$ ion currents in the Fox et al. (FMG) and Hund and Rudy (HR) canine ventricular models at pacing rates of 500 ms. Graphs are taken from (Fink et al. 2011) publication with permission.**

The human ventricular myocyte AP models were developed to describe normal and failing human myocytes. These computational models were designed to identify the connection between alterations caused by disease at the level of transmembrane ionic currents and features of the AP of human myocytes (Fink et al. 2011). The recent human ventricular cell models (Ten Tusscher & Panfilov 2006; O'Hara et al. 2011) provided more details on ion channel functions that describe the electrophysiological properties of different cell types. The characteristics of each model and differences between them can be explained by the differences in the experimental data and the use of different model structure and fitting parameters (Fink et al. 2011). Thus, it is important to recognise and apply appropriate models using relevant data in order to develope *in silico* models of cardiac electrophysiology to investigate arrhythmias in virtual human subjects.

Among these ventricular cell models, human ventricular cell models (Priebe & Beuckelmann 1998; Iyer et al. 2004; Ten Tusscher et al. 2004; Ten Tusscher & Panfilov 2006; Grandi et al. 2010; O'Hara et al. 2011) which favour this study will be discussed in more detail in Chapter 4, section 4.1.1. The detailed comparison of ion currents and AP shape are investigated to assess the similarities and differences of these models. A summary of the two main human ventricular cell models (Ten Tusscher & Panfilov 2006; O'Hara et al. 2011) is provided here. Because these two models are used as the main simulation models, a detailed description of them is provided in Chapter four.

**Ten Tusscher and Panfilov (TP model)**

The Ten Tusscher and Panfilov (TP) model is based on experimental measurement of human APDR and contains a wide description of intracellular calcium dynamics (Ten Tusscher & Panfilov 2006). The influence of $I_{Na}$ recovery dynamics combined with APDR on alternans

and spiral breakup can be investigated in this model. Alternans, a beat to beat oscillation in AP formation and APD, have been investigated with this model; however, other mechanisms which may lead to spiral breakup, have not been examined (Ten Tusscher & Panfilov 2006). With this model, electrical instability and spiral breakup are examined to investigate the theories of spiral breakup of human VF. However, this study did not examine the effect of electrotonic coupling and cardiac memory on alternans and spiral breakup. This model found that CV restitution did not change while DI of spiral wave rotation was constant. The spiral breakup differences can be explained by DI effect for the different $I_{Na}$ dynamics. The spiral breakup suppression occurred by reducing spiral wave rotation, due to slower fast $I_{Na}$ recovery that leads to longer $DI_S$.

**O'Hara-Rudy dynamic (ORd model)**

O'Hara et al. presented the O'Hara-Rudy model in 2011. The cellular electrophysiological mechanisms of human ventricular myocytes are investigated in this model. This model simulates the healthy human ventricular action potential. The mechanisms of APD restitution and the effects of ionic currents are studied. Phenomena regarding abnormal electrical activity of the human heart can be reproduced in this model. For instance, when abnormal depolarization (early after-depolarization) occurs during action potential before normal repolarisation is completed. In addition, oscillation in the strength of cardiac muscle contraction (alternans) is shown to be an important phenomenon in abnormal electrical activity of the human heart (O'Hara et al. 2011). This model might be more accurate than previous models because of a new set of non-diseased human data. Moreover, these new data expand validation to reproduce important physiological behaviour.

## 3.3  Numerical Representation of Cardiac Tissue Electrophysiology

The cardiac tissue electrophysiology models present a numerical picture of AP propagation by encoding data concerning excitability at the cell level. These models also describe conduction velocity at the tissue level. The cardiac tissue is divided into explicit individual cells to represent the importance of AP propagation effects at the cell scale (Clayton et al. 2011). However, most of the cardiac models consider tissue as a regular set of excitable elements coupled by intracellular and extracellular resistances or characterised as a syncytium function where membrane voltage is expected to diffuse easily (Clayton & Panfilov 2008). These approaches engage in parameter selection in addition to tissue

geometry description. The two types of cardiac tissue model will be reviewed in this section with a focus on functional electrical conduction in coupled cells; the differences between them will be discussed.

### 3.3.1  Bidomain Model

The Bidomain model is focused on current flow, diffusion of electrical excitation and accumulation of charge and current (Henriquez 1993). Tissue-level cardiac electrophysiology models are generally displayed by bidomain equations, which involve two partial differential equations (PDEs) joined at points in space with an array of ordinary differential equations (ODEs) (Pathmanathan et al. 2010). This model is more detailed for cardiac tissue. Furthermore, it is necessary to separate intracellular from extracellular spaces to embed the insertion of current within the extracellular space for outer simulation and fibrillation (Trayanova 2006).

The bidomain approach considers cardiac tissue as functional myocardium on a macroscopic scale by involving membrane ionic current, membrane potential ($V_m$), and extracellular potential ($\emptyset_e$) (Potse et al. 2006). This model demonstrates cardiac tissue contains intracellular and extracellular domains that are described by conductivity tensors. For description of this approach, a two-phase medium including intracellular and extracellular spaces is used in which the transmembrane potential of this model is described by the difference between the intracellular and extracellular potentials (Equation 3.5).

$$V_m = \emptyset_i - \emptyset_e \qquad (3.5)$$

The intracellular domain is described by conductivity tensors $G_i$ and $G_e$, respectively. A transmembrane current $I_m$ (A $m^{-3}$) flows between the two domains. The electrical potential in the intracellular $\emptyset_i$ and extracellular $\emptyset_e$ spaces is subject to the bidomain equations (Potse et al. 2006).

$$\nabla.(G_i \nabla \emptyset_i) = \beta_m I_m \qquad (3.6)$$

$$\nabla.(G_e \nabla \emptyset_e) = -\beta_m I_m \qquad (3.7)$$

Here $\beta_m$ ($m^{-1}$) is the membrane surface-to volume ratio.

The transmembrane current density $I_m$ is composed of a capacitive part and ionic part $i_{ion}$ $(V_m, t)$. This current density is generated from current flow per ion channels and the function of pumps and exchangers in the cell membrane.

$$I_m = \beta_m(C_m \frac{dV_m}{dt} + i_{ion})  \qquad (3.8)$$

where $C_m$ is defined as the membrane capacitance per unit area, and $V_m$ is the transmembrane voltage, given by Equation (3.5).

Combining equations:

$$\nabla . G_i(\nabla V_m + \nabla \emptyset_e) = \beta_m(C_m \frac{dV_m}{dt} + i_{ion}) \qquad (3.9)$$

$$\nabla . ((G_i + G_e \nabla \emptyset_e) = -\nabla . (G_i \nabla V_m) \qquad (3.10)$$

In terms of numerical integration, bidomain equations are more complex than monodomain equations due to the difficulty of solving the model. For example, in the bidomain model the complete elliptic problem has to be resolved for every parabolic equation time step (Clayton & Panfilov 2008). To resolve this problem, finite difference approaches have been proposed (Keener & Bogar 1998a) combining a multi-grid approach and the Crank Nicolson method (Clayton & Panfilov 2008).

The overall system of the bidomain model is presented by equations 3.9 and 3.10.

### 3.3.2 Monodomain Model

The monodomain model is fundamentally similar to the bidomain model with assumption of the same anisotropy of intracellular and extracellular space. Therefore, the monodomain conductivity tensors in the extracellular and intracellular spaces are equal. The mathematical solutions are simpler in this model because of use of a single PDE (Clayton 2001).

The monodomain equation can be extracted from the bidomain model of cardiac tissue (Equation (3.6) above) by assuming that the monodomain conductivity tensors:

$$G_e = \lambda G_i \qquad (3.11)$$

$\lambda$ represents the proportion of the conductivity of the extracellular and intracellular spaces.

Equation 3.12 is obtained by substituting equation 3.11 into equation 3.6 in which $\emptyset_e$ does not occur.

$$\nabla . \frac{\lambda}{1+\lambda} G_i \nabla V_m = \beta_m (C_m \frac{dV_m}{dt} + i_{ion}) \qquad (3.12)$$

Effective conductivity: $G = (\lambda)/(1 + \lambda)G_i$

The monodomain equation (3.13) is written as:

$$\nabla . G \nabla V_m = \beta_m (C_m \frac{dV_m}{dt} + i_{ion}) \qquad (3.13)$$

If there is no current flow within the boundary, the condition is as: $n.(G \nabla V_m) = 0$

Then, the monodomain model occurs as:

$$\frac{\partial V_m}{\partial t} = \nabla . D \nabla V_m - \frac{i_{ion}}{C_m} \qquad (3.14)$$

where a diffusion tensor is shown as $D$ $(m^2 s^{-1})$, which is a numeric quantity for models of isotropic tissue. To describe the fibrous and sheet structure of cardiac muscle, $D$ is used as a tensor for models of anisotropic tissue (Nielsen et al. 1991). $\nabla$ is the Laplacian operator.

Although the monodomain equation creates accurate activation patterns and $V_m$, it cannot be implemented in all states because extracellular currents are not permitted to influence ionic currents (Potse et al. 2006). This influence (the current flux within the extracellular and extracardiac areas) is important and may affect cardiac sources, which can only be described by a bidomain model (Clayton 2001). Mathematical solutions are simpler to gain with a monodomain model (a single PDE) (Potse et al. 2006). The description of action potential propagation is similar for both models in case of no insertion of current within the extracellular space ($\emptyset_e$ has no role). In terms of no external stimuli ($\emptyset_e$ has no role), the models gained by monodomain simulations were more uniform than those achieved by a bidomain model (Potse et al. 2006).

**The monodomain tissue model and finite difference solutions**

For models of isotropic tissue, the diffusion term of the monodomain equation 3.14 can be described (equation 3.15) for a Cartesian co-ordinate system (Clayton & Panfilov 2008) when the effective diffusion coefficient D is a scalar (Clayton & Panfilov 2008).

$$\nabla . D\nabla V_m = D\nabla^2 V_m = D[\frac{\partial^2 V_m}{\partial x^2} + \frac{\partial^2 V_m}{\partial y^2} + \frac{\partial^2 V_m}{\partial z^2}] \qquad (3.15)$$

The second-order derivative for a regular Cartesian grid can be described in finite difference form as:

$$\frac{\partial^2 V_m}{\partial x^2} = \frac{V(x+\Delta x,y,z) - 2V(x,y,z) + V(x-\Delta x,y,z)}{\Delta x^2} \qquad (3.16)$$

$D$ is a diffusion tensor for anisotropic tissue with axial symmetry. In this case a Cartesian coordinate system x1, x2, x3 the diffusion term (Clayton & Panfilov 2008) develops as:

$$\nabla . D\nabla V_m = \sum_{i=1}^{3}\sum_{j=1}^{3}\frac{\partial}{\partial x_i}\left(d_{ij}\frac{\partial V_m}{\partial x_j}\right) = \sum_{i=1}^{3}\sum_{j=1}^{3}(\frac{\partial d_{ij}}{\partial x_i}\frac{\partial V_m}{\partial x_j} + d_{ij}\frac{\partial^2 V_m}{\partial x_i \partial x_j}) \qquad (3.17)$$

where the elements $d_{ij}$ are assumed regarding the effective diffusion coefficients for a longitudinal coefficient $D_\parallel$ for transmission along fibres, and a transverse coefficient $D_\perp$ for propagation orthogonal to the fibres with the local fibre orientation cosines $a_1$, $a_2$ and $a_3$ (Clayton & Panfilov 2008). The derivatives of these elements are shown as:

$$\frac{\partial d_{ij}}{\partial x_i} = (D_\parallel - D_\perp)(a_i\frac{\partial a_j}{\partial x_i} + a_j\frac{\partial a_i}{\partial x_i}) \qquad (3.18)$$

To estimate all the derivatives in equation 3.17, it is necessary to calculate the second derivatives approximated by 3.16 and the first derivatives and the cross-derivatives. A numerical approximation with a space step $\Delta x$ can then be obtained as:

$$\frac{\partial V}{\partial x} \approx \frac{V(x+\Delta x,y,z) - V(x-\Delta x,y,z)}{2\Delta x}, \qquad (3.19)$$

$$\frac{\partial^2 V}{\partial x \partial y} = \frac{[V(x+\Delta x,y+\Delta y,z) - V(x+\Delta x,y-\Delta y,z)] - [V(x-\Delta x,y+\Delta y,z) - V(x-\Delta x,y-\Delta y,z)]}{2\Delta x 2\Delta y}, \qquad (3.20)$$

with similar terms for the derivatives in other directions (Clayton & Panfilov 2008).

### 3.3.3 Bidomain and Monodomain Model Comparison

There is good agreement between computational and experimental studies for both the monodomain and bidomain models that allow large-scale calculations for propagation of action potential (Clayton & Panfilov 2008). However, this supposes that cardiac tissue acts as a functional syncytium in which the size, shape and connectivity of individual cells are disregarded; these perform important roles in action potential propagation (Clayton 2001).

A small-scale 1-D model constructed using the ODE systems is assumed, showing: single cardiac cell plasma membrane patches are separated by resistances representing gap junctions, intracellular resistances, and leakage to extracellular space (Clayton 2001) (Figure 3.4). Figure 3.4 represents the architecture of electric circuits corresponding to 1-D continuous monodomain and bidomain (Clayton 2001) models of cardiac tissue; the bidomain method reflects the extracellular and intracellular spaces explicitly, and therefore, specifies a more complete model in comparison with the monodomain model (Clayton & Panfilov 2008).
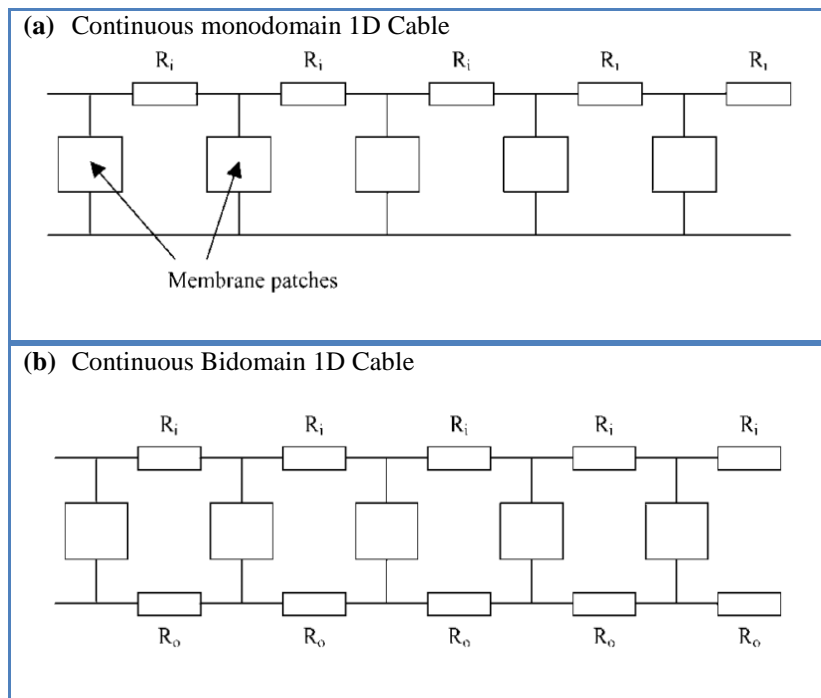


**Figure 3.4. Tissue models represented by electrical circuits (Clayton 2001). (a) The monodomain model including separate membrane patches that connected in intracellular space by resistances $R_i$. They connected in extracellular space by zero resistance connections. (b) The bidomain model includes extracellular space shown by resistances $R_o$.**

As is shown in Figure 3.4, representations of action potential propagation were similar in both monodomain and bidomain models, when current was removed from the extracellular space. A noticeable importance of monodomain models is their mathematical efficacy: Mathematical solutions are easy to achieve because the monodomain is a single PDE (as described in Section 3.2.2) and can be quicker for simulation of the same subject in comparison with bidomain models (Clayton & Panfilov 2008). Thus, monodomain models in an appropriate setting could be used for simulation of wave propagation in cardiac tissue and still reproduce several elements that are detected experimentally (Clayton & Panfilov 2008).

The bidomain equations provide a more detailed description of tissue to model phenomena where these details have a significant effect. For example, in this model intracellular space was separated from extracellular space to adjust the insertion of current into the extracellular space when external stimulation and defibrillation were applied to produce forms of polarisation and depolarisation that are obtained experimentally (Trayanova 2006).

### 3.3.4 Tissue Geometries

Cardiac cells are organised in fibre bundles, in which gap junctions connect individual cells. In this structure, an AP transmits faster along fibres than across fibres (Clayton 2001). Cardiac muscle fibres are bunched and connected to one another in parallel to the ventricular wall but rotate through 120◦ in a wave-like pattern between the endocardial and epicardial surfaces (Clayton 2001). Cardiac fibres are organised in discs that are layered over each other when the myocardium contracts (Legrice et al. 1997). Cardiac tissue models can be applied with anatomically detailed geometries constructed from anatomy or imaging data in the form of 2D sheets, 3D slabs or whole organs (Clayton et al. 2011) that support the importance of anatomical structures in evaluation of efficient models. However, propagation can be considered without anatomical detail in a simplified geometry (1D string, 2D slice or 3D slab). Propagation in a fibre can be simulated in 1D tissue models by simulating a thin layer of cells from ventricular endocardium to epicardium (Viswanathan & Rudy 2000), or from the centre to the boundary of the SAN (Zhang et al. 2000). Less computational power is required for the solution of 1D models compared to 2- or 3-D models (Clayton 2001). Cardiac arrhythmias have been investigated widely in both uniform (Biktashev & Holden 1999) and heterogeneous (Xu & Guevara 1998) sheets of tissue using 2D tissue models (Clayton 2001). 3D computational models can be used for simulation of AP propagation in accurate anatomical geometry, with anisotropy because of fibre and disc organisations. The

behaviour differences among 1D, 2D and 3D models can be distinguished from the method of modelling of current flow (Holden & Biktashev 2002). For example, in a 1D model, current can simply move in one direction in which insertion of a certain amount of charge may be adequate to extract an AP. However, if the same charge is injected into a 2D or 3D model, the resulting current circulation may not be adequate to lead the simulated membrane to threshold and originate an AP(Clayton 2001).

## 3.4   Mathematical Implementation of Cardiac Tissue Models

In this section, the numerical implementation of cardiac tissue electrophysiology modelling will be addressed to provide a brief introduction of techniques and numerical simulations of tissue electrophysiology used in this thesis.

### 3.4.1   Modelling Methods

To represent the cellular action potential and current flow between cells (the diffusion process), cardiac tissue electrophysiology is created on reaction diffusion systems. Most cardiac tissue modelling approaches are monodomain or bidomain (Potse et al. 2006; Clayton et al. 2011), thus the mathematical applications reviewed in this section are related to these approaches.

### 3.4.2   Numerical Methods

Ohm's law and Poisson's equation are used to represent the bidomain (equations 3.9 and 3.10) and monodomain (equations 3.13 and 3.14) approaches for static electrical currents. The mathematical methods for solving Poisson's equation will be presented in this section to describe the anisotropic electrical properties of cardiac tissue. For some cases, these sets of partial differential equations (PDEs) exist in analytical solutions. To solve these PDEs, numerical techniques implemented on computers are used to estimate the PDEs. The linear systems of equations (LSE), with a form of $Ax + b = 0$, are used to describe these techniques (Clayton et al. 2011).

The most frequent techniques performed for converting Poisson's equation into LSEs in cardiac electrophysiology are:

**The Finite Difference Method (FDM)**

The FDM, the oldest method based upon the application of a local Taylor expansion, was created by difference quotients for estimating the partial derivatives of PDEs. The topology of FDM uses a square network of lines to construct the discretization of the PDE, which is a potential method for handling complex geometries in multiple dimensions. For instance, in 3D, the mesh contains equal cubic voxels, structured by the underlying spatial mesh. This capacity motivated many groups (Pullan et al. 2003; Potse et al. 2006; Seemann et al. 2010) to apply FDM in examining tissue electrophysiology during many years. This method can be comprehensive for complex geometries with unequal spacing in grids (Trew et al. 2005) for multi-dimensional problems. Although the FDM is the easy and simple performance of the method, there are difficulties in describing smooth surfaces of the heart without steps. For this reason, applying boundary conditions becomes more difficult (Clayton et al. 2011).

**The Finite Volume Method (FVM)**

The FVM is another classical choice for the numerical solution of PDEs. The FVM general approach uses volume integral formulation including a divergence component to transform to multiple integrals over surfaces using Gauss's theorem (Stolze 1978) . This method allows a more general approach to non-equispaced meshes and can be implemented simply with unstructured meshes for complex geometry domains. FVM also has been used as a more flexible finite difference method in bidomain modelling (Henriquez & Papazoglou 1996; Jacquemet & Henriquez 2005; Courdiere & Pierre 2006). With this approach, curvature is more naturally dealt with in two and three dimensions due to the integral nature of the equations used.

**The Finite Element Method (FEM)**

The FEM is another powerful computational method for solving PDEs. This method is based on consistent approximations of the solution with a finite number of unknowns $x$ that can be determined by solving an algebraic equation $Ax=b$. This method provides a systematic approach for representing discrete space. The general approach is to divide construction of

heart tissue geometry into small subdomains (finite elements that have non-uniform size and shape) that can be demonstrated and controlled in a basic method. The numerical technique for approximating solutions is to interpolate function inside each element. This method has potential for mutant mesh description and incorporation of material properties. For example, complex curved geometries can be demonstrated precisely with this method (Vigmond et al. 2002) by subdividing a whole domain into simpler parts. This method has been applied mainly for simulations with anatomically detailed geometry in which a structure is cut into several parts and then the elements (nodes) are reconnected. However, this method is more labour-intensive in comparison with the FDM in terms of developing and performing the software (Clayton et al. 2011).

Methods for solving the FDM, FVM and FEM are described in Section 3.3.3.

### 3.4.3    Solution Schemes (Implicit, Explicit and Semi-implicit)

To obtain numerical solutions for the time dependence of AP propagation, numerical analysis including explicit (Barr & Plonsey 1984; Pollard & Barr 1991; Vigmond et al. 2002; Penland et al. 2002), implicit (Press et al. 1992), and semi-implicit (Ethier & Bourgault 2008) approaches can be used. The choice of numerical method can affect the computational cost, precision and stability of the model. For example, explicit methods are easy to implement and the computational cost is low for each time step, thus they have been used extensively (Barr & Plonsey 1984; Pollard & Barr 1991; Vigmond et al. 2002; Penland et al. 2002). However, to support stability for the diffusion operator, the time step may need to be small. In contrast, longer time steps can be used in implicit schemes that require much less computational time (Press et al. 1992). For this, equations must be solved at each time step to achieve the required accuracy (Cherry et al., 2003).

The semi-implicit scheme is an applicable agreement of explicit and implicit methods. In this method, the linear and nonlinear equations are solved implicitly and explicitly respectively (Ethier & Bourgault 2008). The stability limitations of semi-implicit methods are less difficult than completely explicit methods, but more demanding than completely implicit methods. The semi-implicit methods can be classified on the basis of the order of calculation. First-order methods are the most common (Keener & Bogar 1998; Colli Franzone & Pavarino 2004) One example of large stability analysis of semi-implicit methods for solving equations

can be found in (Ethier & Bourgault 2008) with a comparison of computational costs, in which a FitzHugh-Nagumo kinetic model is coupled with the bidomain equations.

### 3.4.4    Temporal and Spatial Resolution

Selecting a suitable spatial and temporal resolution is an important decision in a cardiac tissue model. This selection depends on numerical procedure, the model of cell electrophysiology, coefficients of diffusion and anisotropy ratio, and the geometrical characteristics of tissue anatomy (Clayton et al. 2011). The necessity of this choice is to support numerical stability and to guarantee that the solution achieves needs concerning precision. Suitable spatial and temporal settings are required to guarantee the fast processes related to propagation of the action potential, for example, that the fast process of the action potential upstroke is adequately assigned in time and a distributing wave front (sharp spatial gradients) is appropriately assigned in space. In consideration of these requirements, the resolution related to the aspects of the reaction diffusion properties should be selected. In the study by Clayton et al. (2011), different approaches are presented to show the practical use of finer spatial and temporal resolution in cardiac electrophysiological models. They discuss the issues regarding choice of inadequate spatial resolution, which affect the dynamics of conduction velocity, wave-front shape, spiral trajectory, and rotation period (Fenton et al. 2002; Panfilov & Keener 1995) For example, the conduction velocity is susceptible to spatial resolution that could be compared with a solution achieved by minor or bigger resolutions to assess the sufficiency of resolution after these solutions converge. The system dynamics in 2-D or higher dimension models can be determined by spatial resolution. Nevertheless, this method may not be suitable for 3-D simulations because of high computational cost when applying a spatial resolution twice (Clayton et al. 2011). Another example is that spatial resolution can influence characteristics of spiral waves in which the spiral period depends more strongly on resolution. Changes in spiral wave period can create substantial variations in the dynamics of complex spiral waves and, therefore, outcome in stability (Fenton et al. 2002; Panfilov & Keener 1995) or instability (Bueno-Orovio et al. 2008; Panfilov 2002).

## 3.5 Identifying and Tracking Phase Singularities in Spiral Wave Re-entry Computational Models

Re-entry, an excitation wave-front continually propagating around functional obstacle or core (Zhuchkova & Clayton 2005), is the principal mechanism in cardiac arrhythmias of tachycardia and fibrillation. Cardiac arrhythmias are most frequently continued by re-entry. Re-entrant waves rotate around a phase singularity (PS), the points where the wave front encounters the back, and the identification and tracking of PSs permits observation of the complicated movement in both experimental and mathematical models of arrhythmias. PSs are formed when the re-entrant spiral waves tips are enclosed by tissue during every activation-recovery cycle stage (Zhuchkova & Clayton 2005). Identifying the tips of spiral wave re-entry on the surface of the heart is one of the techniques to clarify the complex activity detected from the heart; this can be done by changing the calculated voltage distribution measured on the surface of the heart into phase (Zhuchkova & Clayton 2005). Optically recorded heart surface voltage signals are frequently noisy (Zhuchkova & Clayton 2005); however, change of voltage into phase eliminates the noise and allows accurate location of phase singularities (Zhuchkova & Clayton 2005).  Therefore, this approach (recognition of PSs) is a useful method for analysing the complex electrical activities of the heart. In addition PSs present a useful connection between experimental data and computational simulation. In this section, methods for identifying phase singularities and track phase singularities during the breaking of a spiral wave in a 2D computational model are presented.

### 3.5.1 Initiation of Re-entry

The phase distribution technique is a method for initiation of re-entry. In this method, initial conditions are set by imposing spiral waves on the tissue to create an untwisted scroll wave filament connecting the top and bottom faces. The filament is angled at 71◦ to the transmural direction, which encourages filament breakup and multiple wavelet fibrillation (Clayton 2009). The large surfaces of the slab are connected by filament, and therefore, a transmural alignment in the ventricle can be characterised by a filament (Clayton 2009).

### 3.5.2 Detecting Phase Singularities and Filaments

One method for detecting filaments is the intersection of isosurfaces of membrane voltage $V_{iso}$ and $\frac{dV_m}{dt} = 0$ (Fenton & Karma 1998; Clayton & Holden 2002b). Due to the sensitivity of

choosing $V_{iso}$, an approach based on phase space analysis (Clayton & Panfilov 2008; Zhuchkova & Clayton 2005) was used in this thesis (Figure 3.6). The idea was to transform membrane voltage into phase by means of time delay embedding employing a 4 ms delay (Clayton 2009). Phase space trajectory was adjusted to the mean values of $V_m$ and time delayed $V_m$ (Clayton 2009) originally. However, these average values reduced under a threshold of −75 mV, where the source co-ordinate was set to −60 mV. For phase mapping in cardiac electrophysiology, the spatial distribution of membrane voltage achieved from an experimental arrangement or mathematical model can be transformed into a spatial distribution of phase. Then, the membrane voltage current value is obtained at each point $V_m(t)$ with a prior value of the membrane voltage $V_m(t - tau)$. Assuming the time delay tau is selected to be a few milliseconds, next, a plot of $V_m(t - tau)$ against $V_m(t)$ for a spiral wave demonstrates that the points track a trajectory (trajectory in state-space is anticlockwise) around a central reference point (Figure 3.5).

The phase at every point, which is the rise over the $V_m$ axis, can be calculated by the following equation, whenever the coordinates $(V_{ref,x}, V_{ref,y})$ of the central reference point are achieved (Zhuchkova & Clayton 2005).

$$phi(t) = \arctan[\frac{V_m(t-tau)-V_{ref,y}}{V_m(t)-V_{ref,x}}] \qquad (3.21)$$

Here, arctan returns a value between [-π, π]. The average value of $V_m$ is used to present both $V_{ref,x}$, and $V_{ref,y}$.
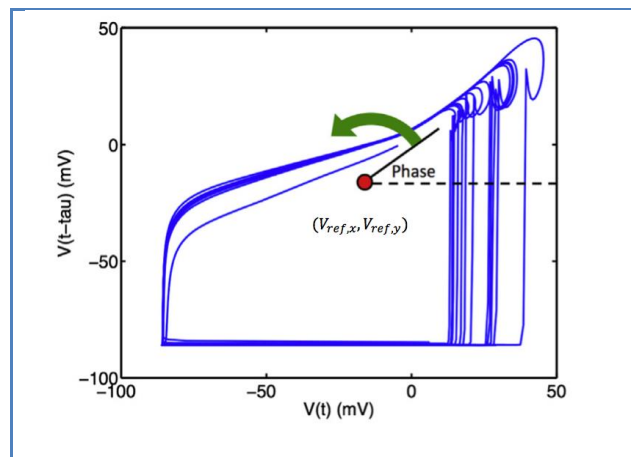


**Figure 3.5. State-space demonstration of time series of action potentials derived from a simulation of unstable re-entry with time delay setting and a time delay of 20 ms (Clayton & Nash 2015). The red circle and the green arrow indicate an origin at the mean value of voltage, and the direction of trajectory in state-space is anticlockwise respectively.**

The method based on convolution kernels is used to identify voxels containing filaments. Then a smoothing algorithm based on a 3×3×3 boxcar filter was employed to guarantee continuous filaments (Clayton 2009). After that, a grassfire algorithm is used for identification and tagging these continuous filaments. In this process, an unlabelled filament voxel is detected; then, it is labelled with a unique tag to all connected filament voxels with the same label. This algorithm is repeated until all of the filament voxels are labelled (Clayton 2008).
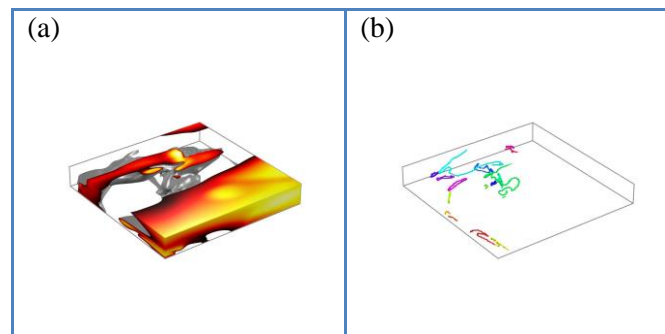


**Figure 3.6. Recognition of filaments; (a) 3-D activation in a slab of tissue, 900 ms following onset of re-entry, (b) Linked filaments after spatial filtering of the data. Figure produced based on Clayton et al. (2006).**

### 3.5.3    Tracking Phase Singularities and Filaments

The method for tracking phase singularities and filaments presented by (Clayton 2009) shows schematics of the marked filaments were kept at 2ms intervals. Single filaments were tracked by detecting the intersection of filament voxels from one snapshot to the next. This method is used to detect filament births, deaths, divisions, and amalgamations.

The method showed that an individual filament could interrelate with many others via division and amalgamation events, and hence the lifetime of a specific filament is unclear. In this method, the time interval concerning communication actions is defined, and this factor applied to represent filament lifetime (Ten Tusscher et al. 2007). A two-stage approach is used in order to tag and track surface PS from the upper ($z = 0$) sheet of the simulated tissue operating the same 2 ms snapshots. The first is to search a radius of 1mm to connect the PS from one snapshot to the next. Then, PSs which did not remain within the search radius are tagged in case of dying or having been born. Next (analysis step), birth and death cases are refined, to consider fast moving PSs. In this case (tracking), PS were considered to be rapidly surface moving if a PS birth and PS death were linked to the same filament tag, and were found within 3 mm of each other (Clayton 2009). This evidence helps in approximation of PS

lifetime and the number of PSs related to each filament. When a filament touched the surface, a solo surface PS appeared and a PS could persevere as its related filament combined or divided; thus, the PS lifetime could be longer than the filament lifetime. However, an individual filament would be linked with some PS events as the filament moved in the tissue to contact the upper surface, the side, and then the upper surface again (Clayton 2009).

## 3.6   Tools

Software implementation for heart simulation has been developed to provide deeper insight into the detailed modelling and to characterise the complexity. Computational models predict outcomes that can be difficult or impossible to test directly in the laboratory or clinic.
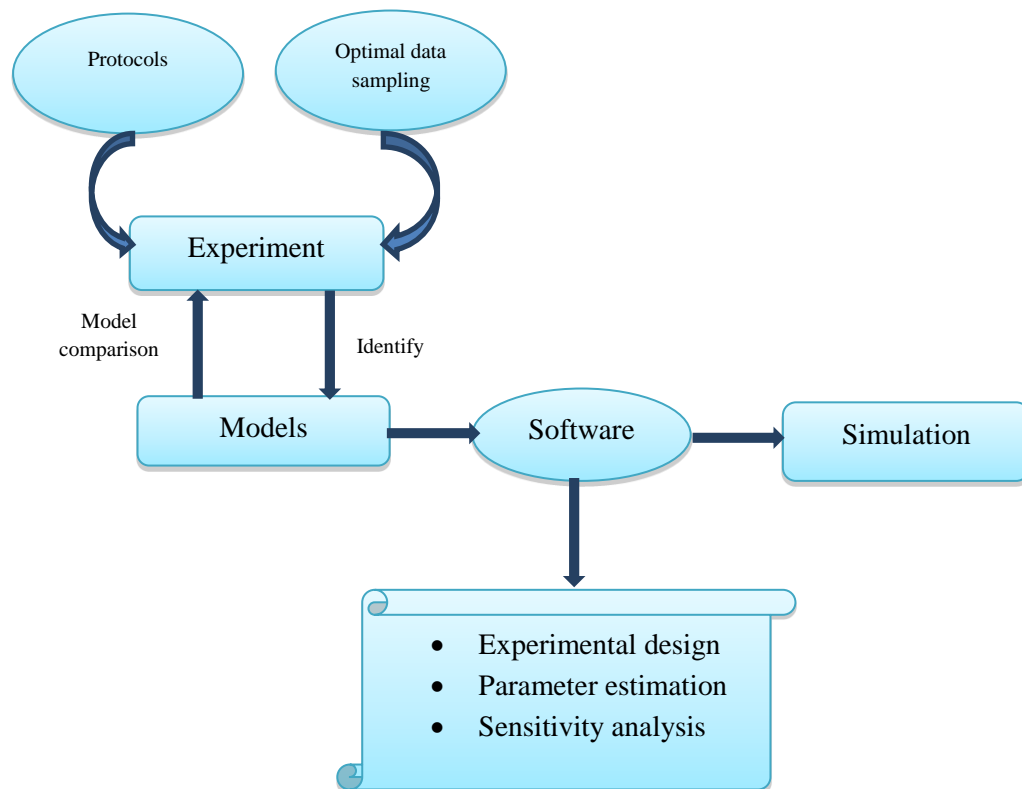


**Figure 3.7. Development of heart simulation by software implementation**

Figure 3.7 presents the relationship between the experimental data and model development and the role of software implementation in adapting model complexity to data availability. To identify a complex model and validate model structure, an assessment of a set of

experimental data is required. It is necessary to define appropriate experimental protocols and optimal data sampling (Fink et al. 2011) to reduce errors. For this purpose, initial models are required to simulate potential experiments. This process also requires repetition between simulation and experiment. In addition, synchronisation in operating models is needed to adjust the finest possible experiments and apply them to recognise the best potential models. In this case, software developments facilitate the process of adapting optimal design approaches (Fink et al. 2011). Various software packages for model simulation integrate tools for parameter stimulation and sensitivity analysis. These packages are used to specify parts of the whole model, usually relating to electrophysiology or tissue mechanical properties (Physiomeproject.org). A summary of the packages is presented in the following table (Table 3.2).

**Table 3.2. Overview of software packages used for computational modelling studies**

| Software package | Affiliation | Type and References | Features | Scales | Pros and Cons |
|---|---|---|---|---|---|
| SCAM | University of Sheffield | in-house (University of Sheffield) | monodomain simulation package | Tissue | • simulation of cardiac activity<br>• studying re-entry and fibrillation<br>• using large anatomically based ventricular meshes<br>• available only to direct collaborators |
| Opencell (CellML simulator) | the Auckland Bioengineering Institute | open source Cellml.org | an environment for working with CellML models | cell | • ability of building complex models by importing models into another model<br>• integrate CellML models made up of ODEs<br>• ability to plot and edit graphs for simulations and metadata<br>• construction of capabilities is limited to run simulations in OpenCell compared with COR |

**Table 3.2. Overview of software packages used for computational modelling studies- continued**

| Software package | Affiliation | Type and References | Features | Scales | Pros and Cons |
|---|---|---|---|---|---|
| OpenCOR | the Auckland Bioengineering Institute | open source Cellml.org | Cellular modelling for Microsoft Windows environment | cell | • large database of single cell models<br>• cross-platform modelling environment<br>• can be used to organise, edit, simulate and analyse CellML files on Windows, Linux and OS X.<br>• utility to organize, edit, simulate and analyse models of ODEs or DAEs encoded in the CellML format<br>• source code is available via the github opencor repository |
| Jsim | the National Simulation Resource at the University of Washington | open source Physiom.org | • Java-based simulation system<br>• making quantitative numeric models and analysis | Multi-scale | • appropriate to a wide range of scientific fields due to general computational engine<br>• JSim's compiler is compatible with physical units<br>• focus is in physiology and biomedicine<br>• free for non-commercial use |
| CARP | the University of Calgary and Graz University | in-house carp.medunigraz.at | • cardiac arrhythmia research package<br>• finite-element solver of the cardiac bidomain equations | Tissue | • the most developed code in terms of linear solvers and parallel efficiency on distributed-memory clusters<br>• not freely available to the scientific community<br>• available only to direct collaborators |

**Table 3.2. Overview of software packages used for computational modelling studies-continued**

| Software package | Affiliation | Type and References | Features | Scales | Pros and Cons |
|---|---|---|---|---|---|
| Continuity | the University of California San Diego | Open-source Continuity.ucsd.edu | Multi-physics simulation package | multi-scale | • multi-scale modelling in bio-engineering and physiology<br>• modelling platform for cardiac, biomechanics, transport and electrophysiology<br>• capable of performing an extensive range of computer architectures and operating systems<br>• portable, object-oriented<br>• has separate GUI client and computational server components<br>• compatible for Windows, MacOS or Linux, including Linux clusters |

**Table 3.2. Overview of software packages used for computational modelling studies- continued**

| Software package | Affiliation | Type and References | Features | Scales | Pros and Cons |
|---|---|---|---|---|---|
| Chaste | University of Oxford | open source cs.ox.ac.uk/chaste/ | software package for cardiac electrophysiology and cancer modelling | multi-scale | • code modularity and reuse as possible<br>• ability to share code among all developers<br>• agile approaches for pair programming<br>• models derived easily from CellML using PyCml<br>• fastest available bidomain solver<br>• suitable for academic research<br>• not easily adapted for industrial purposes<br>• needs programming skills to use<br>• computationally expensive to use in terms of memory usage<br>• needs high performance computing tools for simulations in tissue scale (2D-3D) and whole heart models<br>• not ideally suited for industrial purposes |
| OpenCMISS | the Bioengineering Institute at the University of Auckland | open source physiomeproject.org/ software/opencmiss | finite element analysis techniques | multi-scale | • suitable for complex bio-engineering simulations- multi-scale<br>• appropriate for studying coupling of cardiac electrophysiology, muscle contraction, tissue mechanics and fluid mechanics |

**Table 3.2. Overview of software packages used for computational modelling studies-continued**

| Software package | Affiliation | Type and References | Features | Scales | Pros and Cons |
|---|---|---|---|---|---|
| GIMIAS | CISTIB-Department of Electronic and Electrical Engineering, University of Sheffield | open source gimias.org | software framework for medical image analysis and simulation | multimodal image analysis | • stand alone application for visualization and processing of medical data<br>• framework for clinical workflow navigation<br>• multimodal 2D and 3D image interactive visualization<br>• multiplatform compatibility (Windows, Linux)<br>• capacity for manual segmentation and quantification<br>• extensible through custom plug-ins |

**General limitations of these software packages**

Although these packages are helpful for understanding cardiac behaviour, they have some limitations:

- Not general: developed only for specific applications for the certain scientific aims.
- They have not been fully examined and validated, or outcomes are not publicly accessible.
- Lack of adeptness on high-performance computing platforms
- Available only to direct collaborators, not freely to the scientific community
- They do not involve modern mathematical and computational techniques (Pitt-Francis et al. 2008).

## 3.7 Validation of Computational Cardiac Electrophysiology

### 3.7.1 Model Testing (Test-driven Development)

Components of cardiac codes can be categorised in one of the following three classes:

- Structures: (mesh class) are easy to test because they are defined systematically and have relatively simple functionality.
- Numerical algorithms: with an analytical solution for solving generic problems with capacity of testing.
- Models (cardiac models): are very challenging to test.

The qualitative assessment against experimental outcomes is the only available type of test that could be done by comparison with other software. For example, each essential module of a cardiac bidomain model (ODE solvers, a mesh class, a finite-element assembler, and a liner system solver) needs to be tested individually, and then brought together. There is no problem for testing classes (mesh) and solvers (ODEs, liner system), and solutions are easy to set up. Furthermore, finite-element solvers can be verified by solving basic problems (such as the diffusion equation) and comparing them against identified solutions. Nevertheless, it is difficult to test cell models because of their complexity; systematic solutions are not accessible and if a parameter is incorrect, it may not affect the outcomes achieved using that

cell model. Moreover, it is challenging to test the complete bidomain code, because of unknown correct solutions and the complexity of the system (Pitt-Francis et al. 2008). Despite the difficulty in testing the complex final model, all the basis parts of a scientific computing system must be verified to provide a consistent final model.

### 3.7.2 Validation of Computational Cardiac Electrophysiology

Computational cardiac electrophysiology is the most progressive area of computational physiology and attempts to investigate the electrical activity of the heart. Multi-scale cardiac modelling and simulation have been improved for better interpretation of the ionic mechanisms of heart rhythm, electrotherapy, and the electrocardiogram. During the last decades, many studies have been made on mathematical models and simulation tools and research techniques in cardiac electrophysiology. Nonetheless, few studies have attempted to develop strategies for validation, especially validation of whole organ models in cardiac electrophysiology; however, various levels of models are validated individually (Clayton 2001; Clayton & Panfilov 2008). Thus, it is important to understand the nature of multi-scale modelling.

Integrations of functional and structural models at various levels from ionic to the whole organ must be validated. One strategy for validation is bridging models, simulation and experiments in cardiac electrophysiology. The model-simulation-experiment (MSE) system (Carusi et al. 2012) is constructed with the following steps:

1. **Mathematical formulation** (involving equations and parameter values): Mathematical models are defined by background assumptions, current information, and hypotheses based on biophysical implementation of ion channels and assumptions about best fit between experimental data and model outcomes.

2. **The mesh mediates between models and simulations**: this stage is used to solve the equations on tissue domain in the computational model. In addition, the mesh provides the visual representation of the model and visual interpretation of the simulation outcomes in spatial and temporal terms.

3. **The simulation methods**: these techniques have approached the target domain (specific aspects of cardiac electrophysiology), and models in the form of equations.

4. **The scientific hypothesis**: this is derived from the information obtained from experimental data. In addition, the related aspects of cardiac electrophysiology are reproduced in this stage.

This technique (computational integrative model) is aimed to make and test predictions. Representation is achieved through the process of MSE.

**Physiological validation of computational models:**

Assessment of comparison with different experimental data sets is a common method in validation of computational models. A comparison method between simulations and experiments is suggested (Carusi et al. 2012) to provide a systematic evaluation at the single cell level and at the whole ventricular level. The evaluation can be accomplished by:

1. Checking the value for a particular electrophysiological property in simulations (quantitative method). For example, checking the value of APD in simulation within the scope described in experiments.
2. Detecting the result of a specific intervention (qualitative method), for instance, abnormality in repolarisation or re-entry occurs because of blocking by a particular drug (e.g. blocking the rapid component of the delayed rectifying current ($I_{Kr}$)).

**Validation aspects** (Carusi et al. 2012)**:**

1. **Variability**: understanding the source of variability (from single or multi-scale data source) to advise effective techniques for comparing experiments and simulations (Carusi et al. 2012).
2. **Robustness of techniques and tools**: the robustness of numerical techniques and software must be considered in model construction and simulation. The chaste and CMISS software provided an environment to develop testing strategies.
3. **Standards**: standards at model, experiment, and simulation levels will provide the dynamic relationship between components in the MSE system. For example, CellMl reuses components from one model in another.

**Physiological validation**: the dynamic process of iteration and adjustments is driven from the target domain to other components of the MSE system. This aspect would be useful for better understanding critical human health phenomena, for example, the dynamics of ventricular

fibrillation and the success or failure of electrical defibrillation. In this case, whole ventricular electrophysiology simulations are integrated with clinical and experimental approaches to find new possibilities for the prevention of ventricular fibrillation (Carusi et al. 2012).

## 3.8 Summary of Computational Modelling Process and Numerical Algorithms

### 3.8.1 Mathematical description of cardiac tissue electrophysiology

As described in Chapter Two, at a microscopic scale cardiac tissue is structured as a collection of cardiac cells connected by gap junctions. The simplest electrical coupling model is the propagation of AP in a thin layer of cells when current flows from a depolarised cell to less depolarised neighbours via gap junctions (intercellular resistive pathways) (Kléber & Rudy 2004). The numerical representation of cardiac tissue electrophysiology is described in detail in section 3.3 of this thesis. The cardiac tissue was modelled with mathematical equations describing reaction-diffusion systems, like cable equations in which the reaction terms explain the total current flow through ion channels, pumps, and exchangers in the cardiac cell membrane. The diffusion system describes current flow due to the gradients in transmembrane potential. In this thesis, the detailed structure of real tissue was ignored and the continuous propagation of the cardiac tissue was modelled using the monodomain approximation (the details of the monodomain model are described in section 3.3.2 of this thesis).

#### 3.8.1.1 Numerical implementation of cardiac tissue models

Numerical simulations were performed in the 2D and 3D tissue. A brief description of the reaction-diffusion systems in 2D and 3D monodomain equations applied in this thesis is presented here.

**Reaction System used in this thesis**

The reaction system (based on cell models) used was the total currents in the ventricular cell membrane achieved based on the TP06 (Ten Tusscher & Panfilov 2006) and ORd (O'Hara et al. 2011) models, which is given by:

$$I_m = I_{Kr} + I_{Ks} + I_{K1} + I_{to} + \dots.$$

## Reaction-diffusion systems in 2D isotropic monodomain model

The general equation describing reaction-diffusion systems (Clayton & Taggart 2005) in the multicellular tissue described in this thesis is:

**Diffusion system** ⟶     ⟵ **Reaction system**

$$\frac{\partial V_m}{\partial t} = \boxed{D\left(\frac{\partial^2 V_m}{\partial x^2} + \frac{\partial^2 V_m}{\partial y^2}\right)} - \boxed{\frac{I_m}{C_m}}$$

$\frac{\partial V_m}{\partial t}$: Rate of change of transmembrane potential (mV)

$D$: The diffusion tensor ($m^2 s^{-1}$)

$I_m$: The total ionic current flow through the cell membrane ($\mu A/cm^3$ )

$C_m$: The membrane capacitance (1 $\mu F/cm^2$ )

## Reaction-diffusion systems in 3D isotropic monodomain model

Action potential propagation in 3D slabs of tissue can be described using axially symmetric anisotropy (Keener & Sneyd 2008), where diffusion in all directions orthogonal to the fibre direction is assumed to be the same (Spach et al. 2000). The following equation describes the ventricular conductivity tensor in the diffusion system (Panfilov & Keener 1995).

**Diffusion system** ⟶     ⟵ **Reaction system**

$$\frac{\partial V_m}{\partial t} = \boxed{\nabla.\left(D_{3\times3}\nabla V_m\right)} - \boxed{\frac{I_m}{C_m}}$$

$V_m$: The trans-membrane potential (mV)

$\nabla$: The gradient operators including spatial derivatives

$D_{3\times3}$: The diffusion tensor ($m^2 s^{-1}$) as $3 \times 3$ diffusion matrix written by Panfilov & Keener (1995)

$$d_{ij} = D_2 I_{ij} + (D_1 - D_{2)}) f f^T$$

$$d_{ij} = \begin{cases} D_2 + (D_1 - D_2) \times f_i f_j & i = j \\ (D_1 - D_2) \times f_i f_j & i \neq j \end{cases}$$

$D_1$ : Diffusion coefficients longitudinal along fibres

$D_2$: Diffusion coefficients longitudinal across fibres

$i$ and j : The matrix rows and columns number

$I_{ij}$: The identity matrix

$f$: A vector for the fibre direction

$f^T$: The transposition of $f$

$I_m$: The total ionic current flow through the cell membrane ($\mu A/cm^3$ )

$C_m$: The membrane capacitance (1 $\mu F/cm^2$ )

### 3.8.1.2 Parameters, Tissue geometry and Stimulus protocol

The conduction properties of the tissue model can be determined by key parameters (i.e., the tissue conductivities, surface-to-volume ratio and specific capacitance) that are elements of the effective diffusion coefficient (Winfree 1998). To achieve CVs within the experimental range, a commonly-employed method to determine appropriate parameter values is to vary the conductivities (or diffusion coefficients) (Clayton et al. 2011). To ensure the CV for the ORd tissue model would be in the observed range (Jongsma & Wilders 2000; Taggart et al. 2000; Nanthakumar et al. 2007) between 0.6 - 0.7 m/s, the value of the diffusion coefficient (**D**) was changed and the ORd formulation of $I_{Na}$ was substituted by the TP06 $I_{Na}$ formulation.

| | TP06 | ORd |
|---|---|---|
| **Diffusion coefficient ($cm^2\ s^{-1}$ )** | 0.0012 | 0.0003 |
| Membrane capacitance ($\mu F/cm^2$ ) | 1.0 | 1.0 |

The geometries specified for this thesis are a simple geometrical model in the absence of anatomical detail. The tissue simulations were performed in three groups of tissue size (Table 3.3).

**Table 3.3. Three groups of tissue geometries used: grid points in the tissue represent a section of the left ventricle wall (Keener & Sneyd 2008); blue arrows represent the region where the tissue is triggered; the red dashed line is where membrane voltages were extracted from the centre region.**

| Geometry | Tissue size (mm) | Dimensions (grid points) | Tissue scheme |
|---|---|---|---|
| 2D (thin strip of tissue) | $0.75 \times 25$ | $3 \times 100$ |  |
| 2D (tissue slab) | $50 \times 50$ | $200 \times 200$ |  |
| 3D (tissue slab) | $100 \times 100 \times 15$ | $400 \times 400 \times 60$ |  |

## Simulation protocol

A standard S1S2 stimulus protocol was used with S1 CL of 1000 ms and S2 CL that changed between 1000 ms and 300 ms. A stimulus current of -52.0 (TP06 model) and -80 $pA\ pF^{-1}$ (ORd model) was used to deliver each stimulus to a small slab of tissue for 1ms. The 10 S1-1S2 stimulus was delivered with a CL of 1000 ms. The tissue was returned to its initial state after each S2 before the next S1S2 cycle.

### 3.8.2 Integration of cell and tissue models of cardiac electrophysiology

The tissue electrophysiology models that integrate individual cells together are described here as electrically connected multiple neighbours. The connection between cells is characterized as a diffusive process. The electrotonic (diffusive) current between neighbouring cells can modify cellular electrophysiology in tissue (Spach et al. 2000). Speed of depolarization conduction (called conduction velocity) is a key element associated with simulating cardiac tissue electrophysiology. The strength of cell-to-cell coupling is represented by CV determined by the characteristics of the AP upstroke. The conduction velocity between two cells (A and B) was measured with:

$$\text{CV} = \frac{Distance\ between\ cell\ A\ and\ B\ (mm)}{activation\ time\ at\ B\ (ms) - activation\ time\ at\ A\ (ms)}$$

In this thesis, the CV was measured for premature S2 beats from long to short S1S2 intervals (ms) in 2D tissue with a thin strip of tissue where the membrane potential (Vm) is extracted from the middle of the tissue from row 3 and columns 5 to 60.

### 3.8.3 Modelling Cardiac Ischemia

Global cardiac ischaemia was modelled applying the effect of two main components of ischaemia. The effects of $[ATP]_i$ reduction and $[K^+]_o$ accumulation (Table 3.9) were investigated independently. Four different formulations of the ATP activated $K^+$ current $I_{K,ATP}$ (Table 3.10) to simulate hypoxia are explored in Chapter Five. The details of these formulations are described in section 5.2 of Chapter Five.

**Table 3.9. Input parameters used in this thesis to simulate ischaemia**

| Simulated model | Parameters | | |
|---|---|---|---|
| | $[ATP]_i$ (mM) | $f_{ATP}$ (%) | $[K^+]_o$ (mM) |
| Non-ischaemic | 6.8 | | 5.4 |
| Ischaemic | 6.0 | 0-0.5 | 6.0 |
| | 5.0 | | 7.0 |
| | 4.0 | | 8.0 |

**Table 3.10. List of $I_{K,ATP}$ Formulations used in this thesis to model hypoxia**

| $I_{K,ATP}$ study | Adenosine three phosphate (ATP) dependent potassium current $I_{K,ATP}$ Formulation |
|---|---|
| **Ferrero et al., 1996 (modified version)** | $I_{K,ATP} = g_0 \left(\dfrac{[K^+]_0}{5.4}\right)^{0.24} f_{ATP}(V_m - E_k)$ |
| **Shaw & Rudy 1997** | $I_{K,ATP} = G_{K,ATP} \dfrac{1}{1 + \left(\dfrac{[ATP]_i}{K_{0.5}}\right)^H} \left(\dfrac{[K^+]_0}{5.4}\right)^n (V_m - E_k)$ |
| **Matsuoka et al., 2003** | $I_{K,ATP} = G_{K,ATP} \dfrac{0.8}{1 + \left(\dfrac{[ATP]_i}{0.1}\right)^2} \left(\dfrac{[K^+]_0}{6.019 \times 10^6}\right)^{0.24} (V_m - E_k)$ |
| **Kazbanov et al., 2014** | $I_{K,ATP} = A f_{ATP} \left(\dfrac{[K^+]_0}{5.4}\right)^{0.3} \dfrac{1}{40 + 3.5 e^{0.025V}} (V_m - E_k)$ |

## 3.9 Model repositories and Software frameworks

**Contribution to SCAM** (Clayton & Holden 2004b) **: Computational simulations in this thesis**

The simulations in this thesis have been run with SCAM (Clayton & Holden 2004b), a monodomain simulation package developed at the University of Sheffield. All computational simulations have been written in C to generate configurations of transmembrane voltage in whole tissue. This package provided computational simulations for the investigation of re-entry and fibrillation on ventricles to provide substantial insight into cardiac electrophysiological behaviours. Two human cardiac ventricular cell models (TP06 and ORd) were implemented in this package and all the ischaemic modifications applied in these models. The computational implementations were run in a Linux and Sun Microsystems Grid Engine. Execution scripts were written in Linux and were run in Iceberg (Iceberg: The University of Sheffield HPC cluster). The transmembrane potential data were extracted in MATLAB to calculate and visualise desired data. MATLAB software was used for post processing and to produce spiral wave figures and movies for 2D and 3D tissue simulations. A brief description of programs used in this thesis is provided in the Appendix.

# Part I

# Cardiac Cell Modelling: Comparison of Electrophysiological Models for Human Ventricular Cells and Tissue

# 4 Electrophysiology Models of Human Ventricular Myocytes: TP06 and ORd

*Recently, several models have been developed for regions of the heart to illustrate the foundation and form of the human ventricular myocyte action potential, a significant step in improvement of human heart multiscale models and the possibility for patient-specific modelling. However, confusion over cellular properties and mechanisms can result from using multiple same species models (Fink et al. 2011).Therefore, in these models, it is important to recognize the differences between models and the effective role of every individual current (Fink et al. 2011). Differences may arise from the source of variability and lack of human data, which are poorly characterized (preventing proper re-use and continued development). Different cell models of human ventricular myocytes will be compared in this chapter. Two human ventricular cell models for the tissue arrhythmias studies are selected.*

## 4.1 Introduction

The cardiac cell is a complicated biological system and understanding how ion-channel properties control function is a major challenge. The reason for this is that different procedures cooperate to produce electrical excitation and contraction. The first attempt to measure separate ion channel currents was formulated by Hodgkin and Huxley (1952). The idea is that the cell membrane acts as an electrical capacitor, and that there is a potential difference between inside and outside the cell. They constructed the first mathematical model to test how ion channel currents contribute to AP morphology; their model forms the basis for many cardiac AP models (Rudy et al. 2007). The mechanism of cardiac excitation and recovery is important for accurate diagnosis and efficient treatment of cardiac arrhythmia. Thus, the incorporation of procedures at different levels, from the ion channel, to the whole cell, to the multicellular tissue, to the heart is required. For this purpose, computational models are becoming powerful tools to identify and explain the mechanisms of interaction among different components of the cell and their influence on whole-cell behaviour (Rudy et al. 2007). Quantitative and detailed models of the cardiac cell provide a framework for understanding cardiac physiology (Fink et al. 2011). Various computational models of cardiac cellular electrical activity were presented over the following decades. Computational models of the cellular AP and its fundamental ionic currents could assist in explaining potential arrhythmogenic processes at a cellular level. For example, ion concentration changes (increased extracellular potassium and decreased intracellular ATP) during ischaemia could be the possible cause of the failure of contraction and changes in the electrical activities in the heart. In this chapter, a comparison of the various models is made for human ventricular cells; the chapter concludes with selection of two human ventricular cell models for study of tissue arrhythmias. For this purpose, the differences in the action potential morphology of the different models are compared.

### 4.1.1 Overview of Electrophysiological Models

Recently, numerous models of human ventricular cells have been developed. The first model for human ventricular myocytes was published by Priebe and Beuckelmann (PB model) in 1998. The PB model was mainly based on the Luo–Rudy phase 2 model (Luo & Rudy 1994) for guinea pig ventricular cells. However, their formulations for the main ionic currents were adapted to the limited data accessible for human ventricular cells. In 2004, Ten Tusscher, Noble, Noble and Panfilov (TNNP model) formulated a new model for human ventricular

myocytes (Ten Tusscher et al. 2004) by adjusting all main ionic currents based on experimental data, mostly from human ventricular cell experiments, with the aim of accomplishing large-scale spatial simulations. Later on in 2004, Iyer, Mazhari and Winslow (IMW model) published another model for human ventricular myocytes (Iyer et al. 2004), which, in contrast to the TNNP model, is mainly based on expression data on human cardiac ion channels rather than data on human ventricular cells. In 2006, a new version of the TNNP model was developed by Ten Tusscher and Panfilov (Tusscher & Panfilov 2006). In this new model (TP06 model) based on more recent experimental measurements of human ventricular APD restitution, they included additional description of intracellular calcium dynamics. In 2008, Bueno-Orovio, Cherry and Fenton (BCF model) (Bueno-Orovio et al. 2008) presented a minimal ventricular human model to reproduce important tissue-level characteristics of different cell types. The focus of this model was on reproducing electrophysiological properties such as AP shape and restitution behaviour. Two years later in 2010, another mathematical model of the human ventricular myocyte with more detail on $Ca^{2+}$ handling and ionic currents was developed by Grandi, Pasqualini and Bers (GPB model) (Grandi et al. 2010). Finally, the most recent human ventricular cell model (O'Hara et al. 2011) was developed by O'Hara, Vira, Varro and Rudy (ORd model) in 2011. This model provides an extensive range of parameter values, involving maximal conductance of most transmembrane currents for three different epicardial, mid-myocardial, and endocardial cells (Elshrif & Cherry 2014). Each of these models has advantages and limitations and can be more suitable for specific studies. The goal of this section is to provide a short description of each cell model in order to present their suitability for selection to study the mechanisms of arrhythmias at tissue level in Chapters 6-9.

**Priebe and Beuckelmann, 1998 (PB model)**

The PB model (Priebe & Beuckelmann 1998) was created to analyse the cellular electrophysiological results of heart failure and abnormal automaticity. The model, which consists of 22 state variables and 10 trans-membrane currents, was derived from the Luo-Rudy phase-2 (Luo & Rudy 1994) of guinea pig ventricular myocyte model based on experiments on human myocytes. This model relies primarily on Hodgkin-Huxley representations of trans-membrane currents. In addition, the PB model includes only epicardial formulations to represent trans-mural heterogeneity. The recognition of associations between disease-related modifications at the level of trans-membrane proteins

and descriptions of the AP of human myocytes was the main achievement of this modelling study (Fink et al. 2011).

**Iyer, Mazhari and Winslow, 2004 (IMW model)**

The IMW model, which contains 67 state variables and 13 trans-membrane currents, was based on data achieved from both recombinant human channels and isolated human (Elshrif & Cherry 2014) ventricular epicardial myocytes (Iyer et al. 2004). This model provides more detail on ion channel function and compartmentalisation of ion handing inside the cell. The Markov chains (Irvine et al. 1999) model is used in the IMW model, due to the much larger number of state variables, to model the dynamics of ion channel gates; this is in contrast to the PB, TP06, GPB and ORd models, which use Hodgkin–Huxley-type equations. The IMW model, similar to the PB model, includes only epicardial formulations.

**Ten Tusscher and Panfilov, 2006 (TP06 model)**

Ten Tusscher and Panfilov (Ten Tusscher & Panfilov 2006) developed a new version of their human ventricular cell model (Ten Tusscher et al. 2004). The model involves a wider description of intracellular calcium dynamics and was established based on experimental measurements of human APD restitution. The TP06 model has 21 state variables and 12 trans-membrane currents. This model was applied to examine the states for electrical variability in single cells, for re-entrant waves in a string of cells, and for re-entry wave in two-dimensional slabs of ventricular tissue. The model also relies on Hodgkin-Huxley demonstrations of trans-membrane currents, and includes formulations for epicardial, endocardial, and mid-myocardial cells.

**Bueno-Orovio, Cherry and Fenton, 2008 (BCF model)**

The BCF model (Bueno-Orovio et al. 2008), representing a minimal ventricular human model, was designed to mimic three experimentally measured cell type (epicardial, endocardial, and midmyocardial) properties in addition to reproducing dynamic electrophysiological properties, for example, AP shape and restitution properties. This model, which contains four state variables and tracks the sum of fast inward, slow inward, and slow outward trans-membrane currents (Elshrif & Cherry 2014), uses different formulations to mimic the dynamics of the two earlier developed ionic models (PB and TNNP models) for human ventricular cells.

**Grandi, Pasqualini and Bers, 2010 (GPB model)**

The GPB model (Grandi et al. 2010), which includes 14 trans-membrane currents and 38 state variables, was formulated for endocardial and epicardial myocytes. This model describes the mathematical human ventricular myocyte model with more detail for $Ca^{2+}$ handling and ionic currents based on features from previous models mixed with newer data. The model uses Hodgkin-Huxley type formulations of ionic currents. The GPB model was developed to simulate fundamental excitation-contraction coupling phenomena, using accurate re-polarizing $K^+$ current densities and attain steady-state (for example, steady-state APs in epicardial and endocardial cells are 364 and 385 ms at 0.25 Hz respectively).

**O'Hara, Vira, Varro and Rudy, 2011 (ORd model)**

The ORd model (O'Hara et al. 2011) was developed for different trans-mural cell types using new un-diseased human ventricular data. These data could expand validation to reproduce important physiological behaviour. The ORd model, which includes 12 trans-membrane currents and 41 state variables, uses the Hodgin-Huxley formulation. The model was published to reproduce three different cell types (epicardial, midmyocardial, and endocardial) by adjusting a vast number of parameter values, involving maximal conductance of the majority of trans-membrane currents and certain parameters determining calcium flows (Elshrif & Cherry 2014). It is possible to reproduce abnormal electrical activity in this model, for instance, the occurrence of abnormal depolarization (early after-depolarization) during action potential before normal repolarisation is completed. In addition, an oscillation in the strength of cardiac muscle contraction (alternans) was shown to be an important phenomenon in abnormal electrical activity of the human heart (O'Hara et al. 2011).

## 4.2 Methods

All models considered in this chapter have been employed using CellML tool (Cellml.org), an XML language for standard software-independent description of mathematical models (Nickerson & Buist 2008). The features of CellML can be found here: (Cellml.org). All simulations were performed using the CellMLSimulator (Cellml.org). The electrical activity of a cardiac myocyte resulting from current flux through ion channels and transporters inserted in the cell membrane at the cell level was simulated. In this chapter, the epicardial cell type of the models, in particular, is used.

The total current flux through a membrane patch can be declared as:

$$C_m \frac{dV_m}{dt} = \sum I_n \qquad\qquad (4.1)$$

Where $\sum I_n$ is the total trans-membrane current, $C_m$ the capacitance of the cell membrane per unit area, $V_m$ the trans-membrane voltage and $I_n$ are the currents per unit area flowing through $n$ individual ion channels, exchangers and pumps (Clayton & Panfilov 2008). All post-processing of results (graphing) was completed in Matlab (Mathworks).

## 4.3  Modelling Electrical Activity

In this section, the action potential characteristics of each cell model are shown, before the action potential morphology of all models is compared. At the end of this section, two cellular human ventricular models are short-listed for analysis of ventricular arrhythmias at tissue level. Figure 4.1 shows APs computed from the PB, IMW, TP06, BCF, GPB and ORd models for an epicardial cell. For comparison, the action potentials of all models are illustrated in the same graph (Figure 4.2). As can be appreciated from Figures 4.1 and 4.2, the spike-and-dome action potential morphologies for epicardial cells are similar for all models in single cells. However, phase 1 of the AP (the peak of the action potential notch) and the plateau potential and the resting membrane potential (RMP) differ between the models. Figure 4.2 shows that the largest AP amplitude and upstroke peak belongs to the PB model, while the IMW model has the lowest peak and AP amplitude; the IMW model has the lowest RMP (-90.7 mV), while the GPB model has the highest RMP (-81.4 mV) in comparison with the other models. It is also clear from the figure that the PB model has an apparent two-phase re-polarization, compared to the other models where the transition is flatter. The maximum voltage at the plateau is even larger than at the upstroke peak in the IMW model. The plateau phase for the TP06 model is flatter than the other models, whereas the PB has a significantly longer duration and an announced biphasic re-polarization. The ORd AP has a higher plateau in comparison to the other models. Model properties (Elshrif & Cherry 2014) and electrophysiological characteristics of human cardiac ventricular cells models (Priebe & Beuckelmann 1998; Iyer et al. 2004; Ten Tusscher & Panfilov 2006; Bueno-Orovio et al. 2008; Grandi et al. 2010; O'Hara et al. 2011) are summarised in Table 4.1.

**Table 4.1. Model properties and electrophysiological characteristics of human cardiac ventricular cells**

| Parameter /Model name | PB (Priebe & Beuckelmann 1998) | IMW (Iyer et al. 2004) | TP06 (Ten Tusscher & Panfilov 2006) | BCF (Bueno-Orovio et al. 2008) | GPB-epi (Grandi et al. 2010) | ORd-epi (O'Hara et al. 2011) |
|---|---|---|---|---|---|---|
| Number of model variables | 22 | 67 | 21 | 4 | 38 | 41 |
| Resting membrane V (mV) | -90.6 | -90.7 | -85.4 | -83.9 | -81.4 | -87.8 |
| Phase 0 amplitude (mV) | 140.1 | 125.6 | 124.2 | 126 | 121.8 | 123.1 |
| $V_{notch}$ | 14.1 | 19.5 | 16.0 | 6.3 | 20.8 | 27.3 |
| $V_{plateau}$ | 29.1 | 31.9 | 25.2 | 21.9 | 23.9 | 31.6 |
| APD (ms) | 393.2 | 324.5 | 304.3 | 264.3 | 276.1 | 228.9 |

## Cellular Human Ventricular Models

### ORd (2011)



### GPB (2010)



### BCF (2008)



### TP06 (2006)



### IMW (2004)



### PB (1998)
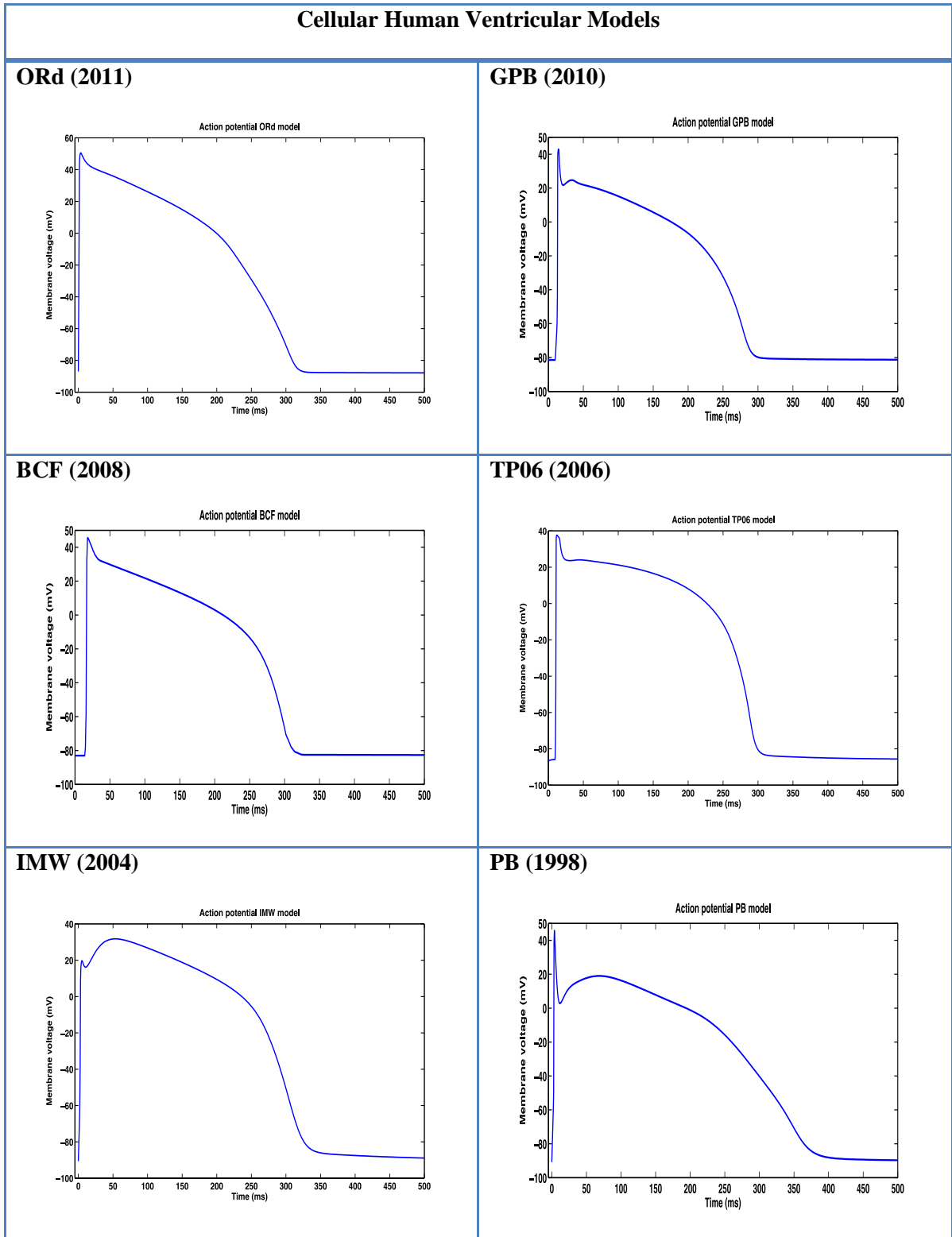


**Figure 4.1 APs computed with the PB, IMW, TP06, BCF, GPB and ORd cellular human ventricular models. AP features achieved from the epicardial cell type of all six models.**
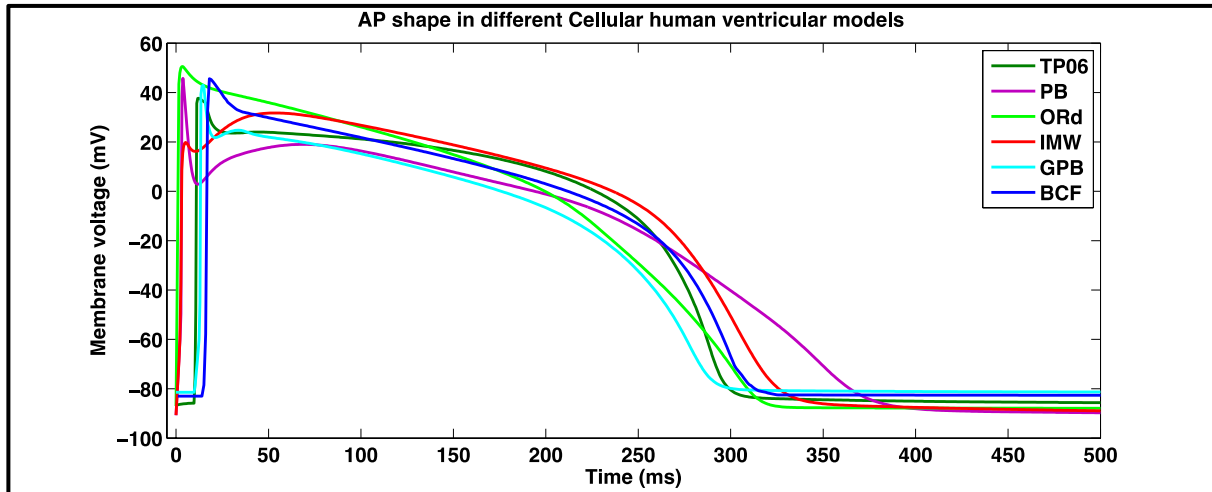
**Figure 4.2 Comparison of AP features taken from the epicardial cell type of all six cellular human ventricular models: the largest AP amplitude and upstroke peak belongs to the PB model, whereas the IMW model has the smallest peak and AP amplitude. The IMW model has the lowest RMP (-90.7 mV), while the GPB model has the highest RMP (-81.4 mV). The highest plateau belongs to the ORd AP shape.**

## 4.4 Limitations and Model Selection

With the accessibility of an extensive number of cardiac cell computational models, it is necessary to consider the advantages and weaknesses of each model in selecting an applicable model for the research question. Model selection is challenging for simulations in tissue, where cells are linked to each other as a string of neighbours and the potential properties in higher spatial dimensions can vary from the specifications of isolated cells. This section aims to identify model potential and present some of the issues associated with each human cell model.

The PB model is built largely using guinea pig data; therefore, it limits human particular data to main currents (O'Hara et al. 2011). The IMW model, based almost completely on data from human channels represented in non myocytes, presents a full description of calcium homeostasis and produces various characteristics of the excitation-contraction coupling (ECC) (Carro et al. 2011; O'Hara et al. 2011). The important limitations reported (Niederer et al. 2009; Carro et al. 2011) for this model are the sensitivity to differences in the sodium-potassium pump ($I_{Na,K}$) and inward rectifier potassium ($I_{K1}$) current densities; it exhibits very prolonged APs and relatively flat restitution curve in tissue (Bueno-Orovio et al. 2008). To add to these limitations, the IMW uses Markov chains to describe ionic currents (more than 60 state variables). This increases complexity, introduces serious limitations on the time step ranges essential for stability, and raises the total computational time for tissue simulations

114

(Bueno-Orovio et al. 2008; Carro et al. 2011). The TP06 model, which contains many reformulated currents, computes physiological restitution and alternans, and is the most extensively used model. This model was improved from the previous version of the TNNP model relative to the 2004 paper by reformulating the calcium dynamics, the slow delayed rectifier potassium current ($I_{Ks}$) and the L-type calcium current ($I_{CaL}$) (Carro et al. 2011). Most of the main ionic currents adjusted in this model are based on experimental human data. The major advantage of this model is the accurate restitution properties of the AP duration. The model's major weaknesses are unresponsiveness to modifications in specific ionic current densities, and the inefficient expression of the rate dependency of intracellular calcium levels (Carro et al. 2011).

The BCF model was constructed simply to reproduce total slow outward, slow inward and fast inward currents. The main advantage of this model is the small number of parameters. This helps to understand the function of each specific parameter in defining the dynamics, and its simplified system makes the process of adjusting the model to data achieved from experiments or from other models more straightforward (Bueno-Orovio et al. 2008). This model also allows us to connect mechanisms to the general overall features of cardiac tissue, such as APD restitution and CV restitution. The model was developed with the aim of avoiding the complexity of more detailed models that give rise to very serious limitations such as uncertainty in developing equations and fitting their parameters (Bueno-Orovio et al. 2008). However, the BCF model is inadequate in terms of providing insight into the behaviour and effect of particular ion channels and other intracellular functions on transmission and propagation because they are excluded. Therefore, this kind of model should be applied to determine general effects in the heart (Clayton & Panfilov 2008).

The GPB model, from the rabbit ECC model of Shannon *et al*. (Thomas R Shannon et al. 2004), contains the sub-sarcolemmal and junctional compartments in the formulation of the currents and represents a full description of calcium handling. This model also involves new terms of ionic current densities and kinetics regarding the latest human myocyte experimental data. The model specifies two kinds of cells (epicardial and endocardial) that vary only in the maximum conductivity of the fast and slow components of the transient outward potassium current ($I_{to}$) (Carro et al. 2011). The GPB model represents a more accurate action potential response to frequency variations and an improved performance against blockages of potassium currents ($I_{k1}, I_{Ks}$ and $I_{kr}$) compared to the TP06 model. A limitation is that S1S2

restitution properties and $APD_{90}$ restitution are not adequately reproduced in this model (Carro et al. 2011). Although the GPB model, which involves $K^+$ current reformulations, uses healthy human data for validation, it does not reproduce AP or $Ca^{2+}$ transient alternans. Both TP06 and GPB models suffer from a lack of sufficient $I_{CaL}$ data for validation and thus cannot generate EADs. In simulation studies of human arrhythmias, EADs and alternans are identified as significant mechanisms of arrhythmogenesis (O'Hara et al. 2011).

The ORd model, which was created based on un-diseased human data, reformulates the exceptions of $Ca^{2+}$ buffers, $CaMK$ kinetics, and background currents. The current and flux equations were not adopted from other human or animal models without fundamental changes (O'Hara et al. 2011). Currents and fluxes were founded on human-specific rate dependence of intracellular $Na^+$ and $Ca^{2+}$ concentration measurements (O'Hara et al. 2011). Not reproduced in other models, abnormal human heart electrical activity is reproduced in the ORd model. For instance, abnormal depolarization (early after-depolarization) occurs during action potential before normal repolarisation is completed in this model. In addition, an oscillation in the strength of cardiac muscle contraction (alternans) is shown to be an important phenomenon in abnormal electrical activity of the human heart. However, the CV of the ORd model is un-physiologically slow. This short velocity is associated with the formulation of the $Na^+$ channel. An easy solution is to replace this with the $I_{Na}$ formulation of the TP06 model that almost doubles the maximum CV. The $I_{Na}$ replacement produces an accurate CV for the ORd model, especially in tissue, whereas the other model properties are unchanged.

**Reason for model selection**

Despite the variety of the human ventricular AP models for mimicking specific electrophysiological properties, they are unsuccessful in demonstrating other related features. In addition, due to the enormous variability in the experimental data, model comparison becomes difficult. Differences between models may arise for many possible reasons that emphasize differences among them. For instance, the biological variability may affect spatial heterogeneity, such as regional differences.

This chapter attempts to highlight the electrical behaviour of each model. Thus, the cell models that simulate cellular APs by reproducing the ionic current level activity are described. Similar electrical behaviour was observed in all models. However, these simulations are not a comprehensive statement of all situations; because several conditions are not included here, no definitive model can be proposed for use in the simulations. Therefore, to study the electrical activity of ventricular cells at tissue level, two human ventricular cell models were selected: Ten Tusscher and Panfilov (TP06) model (Ten Tusscher & Panfilov 2006) and the O'Hara, Vira, Varro and Rudy (ORd) model (O'Hara et al. 2011). The most extensively used model (TP06) was selected because it is convenient to use, involves essential reformulated currents, and mimics physiological restitution and alternans. The ORd model is the most recent model and provides a detailed description of human ventricular cells; this model integrates further detailed physiological data regarding intracellular calcium dynamics and trans-membrane currents. The AP behaviour of a single cell is explored in this chapter, and the effects on tissue are investigated in Chapters 6-9.

It is also important to highlight the need for model validation and understand the model parameter sensitivity that influences tissue-level behaviour.

**Selection of Human Ventricular Cell Models for this study**

The PB, IMW, BCF, and GPB models were not considered in tissue level simulations because of the limitations pointed out above. The two human ventricular AP models selected for tissue-level investigation of ventricular arrhythmias will be further examined by simulation of ischaemic conditions in tissue in Chapters 6-9.

The action potential properties of the different cell types of the two cellular human ventricular models are represented in this section. The values of dV/dtmax for the endocardial, epicardial and midmyocardial formulations are 300, 325 and 380 for the TP06 model and 290, 260 and 425ms for the ORd models (Figure 4.3). The APDs for both endocardial and epicardial cells in the ORd model are smaller than those of the related cell types in the TP06 model as shown in Figure 4.3. The same figure shows that the endocardial APs are longer than epicardial APs and do not have a prominent notch in the ORd model due to reduction of $I_{to}$ density. The ORd AP displays a noticeable dome with the top of the plateau higher than the peak of the upstroke for the mid-myocardial cell type. The mid-myocardial APD for both models is longer than that of the endocardial and epicardial cells.

| Selected Cellular Human Ventricular Models for this study | |
|---|---|
| **(A) ORd** | **(B) TP06** |
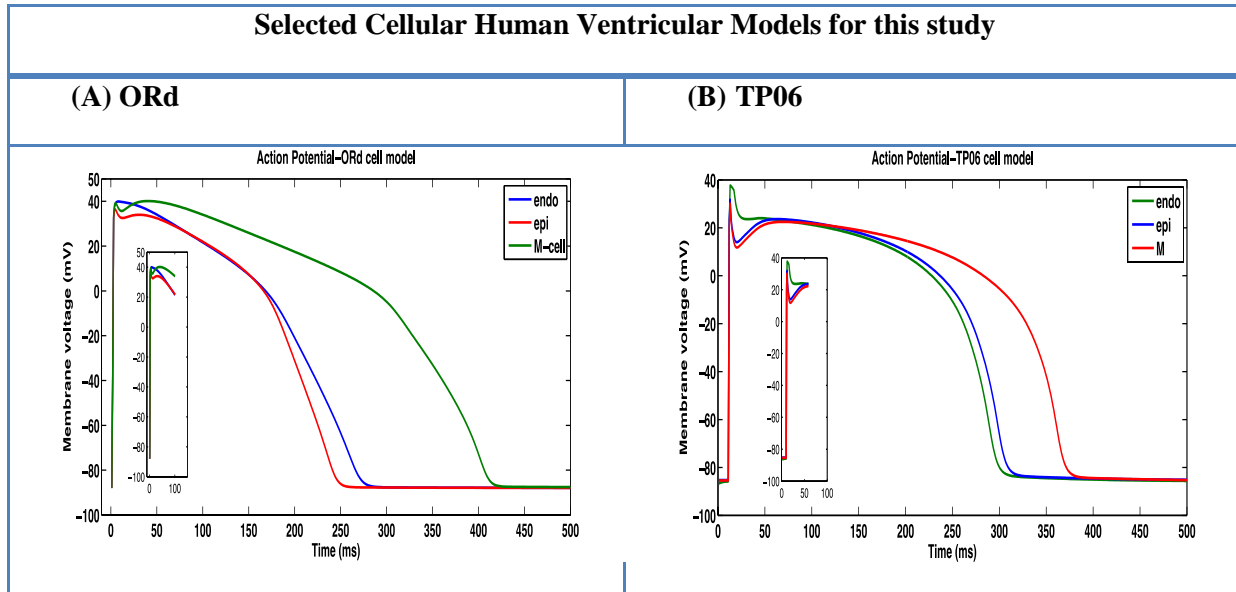


**Figure 4.3 Transmural cell types. (A) Endocardial, epicardial, and midmyocardial APs for the ORd model. (B) Endocardial, epicardial, and midmyocardial APs for the TP06 model. The ORd model APDs for both endocardial and epicardial cells are shorter than those of the related cell types in the TP06 model.**

## Human cardiac ventricular cell models basic parameters

In silico assessment of mechanisms underlying ventricular arrhythmias in ventricular cardiomyocytes have been based on the TP06 (Ten Tusscher & Panfilov 2006) and ORd (O'Hara et al. 2011) models. Despite availability of several human ventricular models discussed in previous sections, these two human ventricular models are suitable for study of arrhythmias. The main differences between the TP06 and ORD models is that the ORd model is a biologically detailed description of the individual ventricular cells including 41 State variables, 16 Currents (Table 4.4) and the $Ca^{+2}$ subsystem and $Ca^{+2}$ extrusion dynamics which are important for APD alternans in the model (O'Hara et al. 2011). This model has frequently been used in human studies of pro-arrhythmia due to its capacity to represent repolarisation antennas as an important arrhythmogenesis risk factor which is favourable for drug regulatory authorities (see CiPA initiative). The TP06 model with 21 state variables and 14 Currents (Table 4.3) has also been extensively used and as a robust model is suitable for studying ventricular fibrillation at tissue level. Table 4.5 presents the sources of experimental data used to formulate three main ionic currents ($I_{Na}$ , $I_{CaL}$ and $I_{Kr}$) in the TP06 and ORd human ventricular AP models. The initial parameters of these two models are presented in Table 4.2.

**Table 4.2. Human cardiac ventricular cell model basic parameters**

| Model | Stimulus | | Threshold (mV) | Number of state variables |
|---|---|---|---|---|
| | Amplitude (μA/μF) | Duration (ms) | | |
| TP06 | -52 | 1.0 | -65 | 21 |
| ORd | -80 | 1.0 | -75 | 41 |

**Table 4.3. The TP06 human cardiac ventricular cell model (TenTusscher & Panfilov 2006) Current equations and gate variables**

| TP06 model (TenTusscher & Panfilov 2006): 21 State variables, 14 Currents | |
|---|---|
| **Gate variables** | **Currents (μA/μF)** |
| **m**: activation for fast $I_{Na}$ <br><br> **h** : fast development of inactivation for fast $I_{Na}$ <br><br> **j**: recovery from inactivation for fast $I_{Na}$ | **Fast $Na^+$ current** <br> $$I_{Na} = G_{Na}m^3hj(V - E_{Na})$$ |
| | **Transient outward $K^+$ current** <br> $$I_{to} = G_{to}rs(V - E_K)$$ |
| **r**: a voltage-dependent activation gate for $I_{to}$ <br><br> **s**: a voltage-dependent inactivation gate for $I_{to}$ | **$Ca^{+2}$ current through the L-type $Ca^{+2}$ channel** <br> $$I_{CaL} = G_{CaL}dff_2f_{cass}.4\frac{(v-15)F^2}{RT}\frac{0.25Ca_{ss}e^{2(v-15)F/RT} - Ca_0}{e^{2(v-15)F/RT} - 1}$$ |
| **$X_{r1}$**: an activation gate for $I_{Kr}$ <br><br> **$X_{r2}$**: an inactivation gate for $I_{Kr}$ | **$Na^+/Ca^{+2}$ exchange current** <br> $$I_{NaCa} = K_{NaCa}\frac{e^{\gamma VF/RT}Na_i^3 Ca_0 - e^{(\gamma-1)VF/RT}Na_0^3 Ca_i\alpha}{(K_{mNai}^3 + Na_0^3)(K_{mCa} + Ca_0)(1 + K_{ss1}e^{(\gamma-1)VF/RT})}$$ |
| **$X_s$**: an activation gate for $I_{Ks}$ | **Rapid delayed rectifier $K^+$ current** <br> $$I_{Kr} = G_{Kr}\sqrt{\frac{K_0}{5.4}}X_{r1}X_{r2}(V - E_K)$$ |
| **d**: a voltage-dependent activation gate for $I_{CaL}$ | **Slow delayed rectifier $K^+$ current** <br> $$I_{Ks} = G_{Ks}X_s^2(V - E_K)$$ |
| **f** : a slow voltage inactivation gate for $I_{CaL}$ <br><br> **$f_2$**: a fast voltage inactivation gate for $I_{CaL}$ | **Inward rectifier $K^+$ current** <br> $$I_{K1} = G_{K1}\sqrt{\frac{K_0}{5.4}}X_{K1\infty}(V - E_K)$$ |
| **$f_{cass}$**: a fast subspace calcium inactivation gate for $I_{CaL}$ | **$Na^+$ background current** <br> $$I_{bNa} = G_{bNa}(V - E_{Na})$$ |
| **Cass** : free dyadic subspace calcium concentration | **$Ca^{+2}$ background current** <br> $$I_{bCa} = G_{bCa}(V - E_{Ca})$$ |
| **Ki**: intracellular potassium concentrations <br><br> **Cai**: free cytoplasmic calcium concentration <br><br> **Nai**: intracellular sodium concentrations <br><br> **CaSR**: free sarcoplasmic reticulum calcium concentration | **Sarcolemmal $Ca^{+2}$ pump current** <br> $$I_{pCa} = G_{pCa}\frac{Ca_i}{K_{pCa} + Ca_i}$$ |

**Table 4.3. The TP06 human cardiac ventricular cell model (TenTusscher & Panfilov 2006) Current equations and gate variables- continued**

| TP06 model (TenTusscher & Panfilov 2006): 21 State variables, 14 Currents | |
|---|---|
| **Gate variables** | **Currents (µA/µF)** |
| | **Sarcolemmal $K^+$ pump current** $$I_{pK} = G_{pK} \frac{(V - E_K)}{1 + e^{(25-V)/5.98}}$$ |
| | **$Na^+/K^+$ Pump current** $$I_{NaK} = P_{NaK} \frac{K_0 Na_i}{(K_0 + K_{mK})(Na_i + K_{mNa})(1 + 0.1245 e^{-\frac{0.1VF}{RT}} + 0.0353 e^{-\frac{VF}{RT}})}$$ |
| $C_m = 1.0 \ \mu F$ $$\frac{dV_m}{dt} = -\frac{1}{C_m}.(I_{Na} + I_{to} + I_{CaL} + I_{Kr} + I_{Ks} + I_{K1} + I_{NaCa} + I_{NaK} + I_{bNa} + I_{bCa} + I_{pK} + I_{pCa} + I_{stim})$$ | **Voltage** |

**Table 4.4. The ORd human cardiac ventricular cell model (O'Hara et al. 2011) Current equations and gate variables**

| ORd model: 41 State variables, 16 Currents | |
|---|---|
| **Time Dependent Gates** | **Currents (µA/µF)** |
| **m**: activation for fast $I_{Na}$ $h_{fast}$: fast development of inactivation for fast $I_{Na}$ $h_{slow}$: slow development of inactivation for fast $I_{Na}$ **j**: recovery from inactivation for fast $I_{Na}$ $h_{CaMK,fast}$: fast development of inactivation for CaMK phosphorylated fast $I_{Na}$ $h_{CaMK,slow}$ slow development of inactivation for CaMK phosphorylated fast $I_{Na}$ $j_{CaMK}$ recovery from inactivation for CaMK phosphorylated fast $I_{Na}$ $m_L$ activation for late $I_{Na}$ $h_L$ inactivation for late $I_{Na}$ $h_{L,CaMK}$: inactivation for CaMK | **$Na^+$ current** $$\overline{G_{Na,fast}} = 75 \ mS/\mu F$$ $$I_{Na,fast} = \overline{G_{Na,fast}}.(V - E_{Na}).m^3.((1 - \emptyset_{INa,CaMK}).h.j + \emptyset_{INa,CaMK}.h_{CaMK}.J_{CaMK})$$ $$\overline{G_{Na,late}} = 0.0075 \ mS/\mu F$$ $$I_{Na,late} = \overline{G_{Na,late}}.(V - E_{Na}).m_L.((1 - \emptyset_{INaL,CaMK}).h_L + \emptyset_{INaL,CaMK}.h_{L,CaMK})$$ $$I_{Na} = I_{Na,fast} + I_{Na,late}$$ **Transient outward $K^+$ current** $$\overline{G_{to}} = 0.02 \ mS/\mu F$$ $$I_{to} = \overline{G_{to}}.(V - E_{Na}).((1 - \emptyset_{Ito,CaMK}).a.i + \emptyset_{Ito,CaMK}.a_{CaMK}.i_{CaMK})$$ **$Ca^{+2}$ current through the L-type $Ca^{+2}$ channel** $$I_{CaL} = \overline{I_{CaL}}.d.(1 - \emptyset_{ICaL,CaMK}).(f.(1 - n) + f_{Ca}.n.j_{Ca}) + \overline{I_{CaL,CaMK}}.d.\emptyset_{ICaL,CaMK}.(f_{CaMK}.(1 - n) + f_{Ca,CaMK}.n.j_{Ca})$$ **$Na^+$ current through the L-type $Ca^{+2}$ channel** $$I_{CaNa} = \overline{I_{CaNa}}.d.(1 - \emptyset_{ICaL,CaMK}).(f.(1 - n) + f_{Ca}.n.j_{Ca}) + \overline{I_{CaNa,CaMK}}.d.\emptyset_{ICaL,CaMK}.(f_{CaMK}.(1 - n) + f_{Ca,CaMK}.n.j_{Ca})$$ **$K^+$ current through the L-type $Ca^{+2}$ channel** |

| | |
|---|---|
| phosphorylated late $I_{Na}$ | $I_{CaK} = \overline{I_{CaK}}.d.\left(1 - \emptyset_{ICaL,CaMK}\right).\left(f.(1-n) + f_{Ca}.n.j_{Ca}\right)$ $+ \overline{I_{CaK,CaMK}}.d.\emptyset_{ICaL,CaMK}.(f_{CaMK}.(1-n)$ $+ f_{Ca,CaMK}.n.j_{Ca})$ |
| $\boldsymbol{a}$: activation for $I_{to}$ | |
| $\boldsymbol{i_{fast}}$: fast inactivation for $I_{to}$ | **Rapid delayed rectifier $K^+$ current** $\overline{G_{Kr}} = 0.046 \; mS/\mu F$ $I_{Kr} = \overline{G_{Kr}}.\sqrt{\dfrac{[K^+]_o}{5.4}}.X_r.R_{Kr}.(V - E_K)$ |
| $\boldsymbol{i_{slow}}$: slow inactivation for $I_{to}$ | |
| $\boldsymbol{a_{CaMK}}$: activation for CaMK phosphorylated $I_{to}$ | |
| $\boldsymbol{i_{CaMK,fast}}$ fast inactivation for CaMK phosphorylated $I_{to}$ | **Slow delayed rectifier $K^+$ current** $\overline{G_{Ks}} = 0.0034 \; mS/\mu F$ |
| $\boldsymbol{i_{CaMK,slow}}$: slow inactivation for CaMK phosphorylated $I_{to}$ | $I_{Ks} = \overline{G_{Ks}}.\left(1 + \dfrac{0.6}{1 + \left(\dfrac{3.8.10^{-5}}{[Ca^{2+}]_i}\right)^{1.4}}\right).X_{s1}.X_{s2}.(V - E_K)$ |
| $\boldsymbol{d}$: activation for $I_{CaL}$ | |
| $\boldsymbol{f_{fast}}$: fast voltage dependent inactivation for $I_{CaL}$ | **Inward rectifier $K^+$ current** $\overline{G_{K1}} = 0.1908 \; mS/\mu F$ |
| $\boldsymbol{f_{slow}}$: slow voltage dependent inactivation for $I_{CaL}$ | $I_{K1} = \overline{G_{K1}}.\sqrt{[K^+]_o}.X_{K1}.R_{K1}.(V - E_K)$ |
| $\boldsymbol{f_{Ca,fast}}$: fast development of $Ca^{+2}$ dependent inactivation for $I_{CaL}$ | **Myoplasmic component of $Na^+/Ca^{+2}$ exchange current** $\overline{G_{NaCa}} = 0.0008 \; \mu A/\mu F$ $I_{NaCa,i} = \overline{G_{NaCa}}.0.8. allo_i.(Z_{Na}.J_{NaCa,Na,i} + Z_{Ca}.J_{NaCa,Na,i})$ |
| $\boldsymbol{f_{Ca,slow}}$: slow development of $Ca^{+2}$ dependent inactivation for $I_{CaL}$ | **Subspace component of $Na^+/Ca^{+2}$ exchange current** $I_{NaCa,ss} = \overline{G_{NaCa}}.0.2. allo_{ss}.(Z_{Na}.J_{NaCa,Na,ss} + Z_{Ca}.J_{NaCa,Na,ss})$ |
| $\boldsymbol{j_{Ca}}$: recovery from $Ca^{+2}$ dependent inactivation for $I_{CaL}$ | **total $Na^+/Ca^{+2}$ exchange current** $I_{NaCa} = I_{NaCa,i} + I_{NaCa,ss}$ |
| $\boldsymbol{n}$: fraction in $Ca^{+2}$ dependent inactivation mode for $I_{CaL}$ | **$Na^+/K^+$ ATPase current** $Z_{Na} = 1, Z_K = 1$ $I_{NaK} = 30.(Z_{Na}.J_{NaK,Na} + Z_K.J_{NaK,K})$ |
| $\boldsymbol{f_{CaMK,fast}}$: fast development of $Ca^{+2}$ dependent inactivation for CaMK phosphorylated $I_{CaL}$ | **$Na^+$ background current** $P_{Nab} = 3.75.10^{-10} \; cm/s, Z_{Na} = 1$ |
| $\boldsymbol{f_{Ca,CaMK,fast}}$: slow development of $Ca^{+2}$ dependent inactivation for CaMK phosphorylated $I_{CaL}$ | $I_{Nab} = P_{Nab}.Z_{Na}{}^2.\dfrac{VF^2}{RT}.\dfrac{[Na^+]_i.\exp\left(\frac{Z_{Na}VF}{RT}\right) - [Na^+]_o}{\exp\left(\frac{Z_{Na}VF}{RT}\right) - 1.0}$ |
| $\boldsymbol{X_{r,fast}}$: fast activation/deactivation for $I_{Kr}$ | **$Ca^{+2}$ background current** $P_{Cab} = 2.5.10^{-8} \; cm/s, \gamma_{Cai} = 1.0, \gamma_{Cao} = 0.341, Z_{Ca} = 2$ |
| $\boldsymbol{X_{r,slow}}$: slow activation/deactivation for $I_{Kr}$ | $I_{Cab} = P_{Cab}.Z_{Ca}{}^2.\dfrac{VF^2}{RT}.\dfrac{\gamma_{Cai}.[Ca^{2+}]_i.\exp\left(\frac{Z_{Ca}VF}{RT}\right) - [Ca^{2+}]_o}{\exp\left(\frac{Z_{Ca}VF}{RT}\right) - 1.0}$ |
| $\boldsymbol{x_{s1}}$: activation for $I_{Ks}$ | |
| $\boldsymbol{x_{s2}}$: deactivation for $I_{Ks}$ | **$K^+$ background current** $\overline{G_{Kb}} = 0.003 \; mS/\mu F$ |
| $\boldsymbol{x_{K1}}$: inactivation for $I_{K1}$ | |

| | | |
|---|---|---|
| | $$I_{Kb} = \overline{G_{Kb}}.X_{Kb}.(V - E_K)$$ | |
| | **Sarcolemmal $Ca^{+2}$ pump current**<br>$$\overline{G_{pCa}} = 0.0005 \ mS/\mu F$$ <br><br> $$I_{pCa} = \overline{G_{pCa}}.\frac{[Ca^{2+}]_i}{0.0005 + [Ca^{2+}]_i}$$ | |

**Voltage**

$C_m = 1.0 \ \mu F$

$$\frac{dV_m}{dt} = -\frac{1}{C_m}.(I_{Na} + I_{to} + I_{CaL} + I_{CaNa} + I_{CaK} + I_{Kr} + I_{Ks} + I_{K1} + I_{NaCa} + I_{NaK} + I_{Nab} + I_{NaL} + I_{Cab} + I_{Kb} + I_{pCa} + I_{stim})$$

**Table 4.5. Sources of experimental data used to formulate three main ionic currents ($I_{Na}$ , $I_{CaL}$ and $I_{Kr}$) in the TP06 and ORd human ventricular AP models (TenTusscher & Panfilov 2006) (O'Hara et al. 2011).**

| Model | $I_{Na}$ | | $I_{CaL}$ | | $I_{Kr}$ | |
|---|---|---|---|---|---|---|
| | Cell Type | Experimental Setup | Cell Type | Experimental Setup | Cell Type | Experimental Setup |
| TP06 | HEK-293, Xenopus oocytes, Human RA, Human Atria, tsA-201 cells, Human LV | Isolated cells, Tissue in vitro | Human LV and RV, Dog LV, Human ventricles/atrials | Isolated cells | HEK-293, CHO-K1, Xenopus oocytes, Human LV/RV/RA | Isolated cells |
| | References | | | | | |
| | (Sakakibara et al. 1992)<br>(Schneider et al. 1994)<br>(Drouin et al. 1998)<br>(Nagatomo et al. 1998)<br>(Makita et al. 2000)<br>(Wang et al. 2000)<br>(Wan et al. 2001)<br>(Viswanathan et al. 2001) | | (Bénitah et al. 1992)<br>(Mewes & Ravens 1994)<br>(Li & Nattel 1997)<br>(Pelzmann et al. 1998)<br>(Magyar et al. 2002) | | (Li et al. 1996)<br>(Zhou et al. 1998)<br>(Iost et al. 1998)<br>(Johnson et al. 1999)<br>(Smith & Yellen 2002) | |
| ORd | nonfailing human ventricular, Dog Purkinje, Rabbit/Mouse ventricles, Canine ventricels, Human LV | Isolated cells, Tissue in vitro, in vivo | Dog LV, Xenopus oocytes, Murine ventricles, Human ventricles, | Isolated cells | Human ventricles/ LV, Dog LV | Isolated cells |
| | References | | | | | |
| | (Hanck & Sheets 1992)<br>(SAKAKIBARA et al. 1993)<br>(DROUIN et al. 1995)<br>(Maltsev et al. 1998)<br>(Spach et al. 2000)<br>(Taggart et al. 2000)<br>(Wagner et al. 2006)<br>(Maltsev & Undrovinas 2006) | | (Aggarwal & Boyden 1995)<br>(Dzhura et al. 2000)<br>(Fülöp et al. 2004)<br>(Kim et al. 2004) | | (Jost et al. 2009)<br>(O'Hara et al. 2011) | |

# 5 ATP Sensitive K$^+$ Current Formulation in Models of Human Ventricular Myocytes

*In this chapter, the $I_{K,ATP}$ models used to simulate hypoxia/ischaemia are presented. A general overview of each model is provided to assess which formulation is more appropriate. Four different formulations of $I_{K,ATP}$ are compared that will be incorporated into a 2-D monodomain tissue model in Chapter 6. How hyperkalemia influences the characteristics of $I_{K(ATP)}$ is also investigated*

## 5.1 Introduction

**Background**

$K^+_{ATP}$ channels in cardiac myocytes were first described by Noma in 1983 (Noma 1983). The contribution of the $K^+_{ATP}$ channel to the reduction of the action potential during hypoxia/ ischaemia and to other electrophysiological modifications remains poorly understood. In addition, due to the complexity of empirically computing the fraction of open $K^+_{ATP}$ channels, the quantitative significance of $I_{K,ATP}$ channel opening in hypoxia/ischaemia episodes is still not fully appreciated (Ferrero et al. 1996). The $K^+_{ATP}$ channels open to repolarise the cell when ATP is depleted. Therefore, $K^+_{ATP}$ channels provide a means of linking cellular metabolism to electrical activity in the membrane. There are a variety of intracellular and extracellular factors (including MgADP and MgATP (the nucleotide substrates), pH, G-proteins, adenosine, and extracellular ATP) that contribute to regulate these channels (Ashcroft & Ashcroft 1990; Nichols et al. 1991). Several attempts have been made to integrate a simple formulation for the ATP regulation of the $K^+_{ATP}$ channel current into existing electrophysiological cell models (e.g. (Nichols et al. 1991; Shaw & Rudy 1997; Ferrero et al. 1996; Matsuoka et al. 2003)). However, there are some limitations with these ionic models. For example, intracellular free ATP, MgADP, and MgADP, which are known to regulate the ligand-gated channel activity, are not included in these ionic models (Michailova et al. 2005).

**Aim and general outline**

This chapter introduces basic information on the electrophysiological variations during ischaemia at the ion channel level. It also presents an overall description of the $K^+_{ATP}$ channels and an analysis of the electrical variations at the cell level, accompanied by simulation of arrhythmias during ischaemia.

**Objective**

This study will examine the importance of the role of the ATP activated $K^+$ current $I_{K,ATP}$ in repolarization changes during global ischaemia. Computer models are used to evaluate the quantitative influence of four different $I_{K,ATP}$ models. For this purpose, the I-V dependence of each model is computed, and the influence of $I_{K,ATP}$ on the augmentation of the amount of cellular $K^+$ efflux during hypoxia/ischaemia is investigated.

## 5.2 Methods

**Cell model and formulation of $I_{K,ATP}$**

From a theoretical point of view, computational models are used for better understanding $K_{ATP}$ channel function in in hypoxia-ischaemia; however, they cannot provide real data. From the literature, the number of studies that integrated a model of $I_{K,ATP}$ in an action potential model and investigated the influence of $I_{K,ATP}$ activation in cardiac myocytes is limited, especially for human ventricular cell models. Most $I_{K,ATP}$ formulations have used data from animal hearts (Ferrero et al. 1996; Shaw & Rudy 1997; Matsuoka et al. 2003; Michailova et al. 2005). To determine the impact of anoxia on cardiac cell electrophysiology, four different formulations of $I_{K,ATP}$ were compared. The aim was to evaluate the quantitative influence of three $I_{K,ATP}$ models based on animal data, and one $I_{K,ATP}$ model, based on in vitro experiments in human ventricular myocytes.

The Ferrero description of $I_{K,ATP}$ (Ferrero et al. 1996) is more comprehensive than the previous reported models (e.g. Nichols & Lederer 1990; Shaw & Rudy 1994; Cook et al. 1988). This model studies intracellular ionic concentration and intracellular ADP as well as $[K^+]_o$ and $[ATP]_i$ dependencies (Ferrero et al. 1996). In addition, the parameters of this model are well matched to experimental measurements. Our results are based on the simplified version of this model, which uses $f_{ATP}$. This simplified model does not include the dependence of the concentrations ($[Mg^{2+}]_i$ and $[Na^+]_i$) and intracellular nucleotide levels ($[ATP]_i$ and $[ADP]_i$). Another formulation described in this chapter is given by Shaw and Rudy (1994) and has been shown to be more effective for small $[ATP]_i$ changes in comparison to other formulations (Nickerson & Buist 2008; Clayton et al. 2011). The Matsuoka model was also considered (Matsuoka et al. 2003); this is also based on animal data, but is more recent. The model was established to reconstruct the AP of guinea-pig ventricular cells based on experimental data, and to clarify the role of ion channels in cardiac membrane excitation and contraction (Matsuoka et al. 2003). Finally, a model of the human $K_{ATP}$ channel by Kazbanov & Clayton (2014) was used based on experimental data from human cardiac cells (Babenko et al. 1998). This model uses a basic algorithm to fit the dynamics of hyperkalaemia and $K_{ATP}$ current activation using single patient recordings. In this section, a brief description of each chosen model is presented.

**Ferrero *et al*.**

A simplified Ferrero *et al*. formulation (Ferrero et al. 1996) is described by Equation 5.1 (Abbasi & Clayton 2014), with modifications from the original description described below:

$$I_{K,ATP} = g_0 \left(\frac{[K^+]_0}{5.4}\right)^{0.24} f_{ATP}(V_m - E_k) \qquad (5.1)$$

Ferrero et al. (1996) formulated $I_{K,ATP}$ model included in the LR-II (Luo & Rudy 1994) model of guinea pig-type ventricular cardiac AP. This mathematical model (Luo & Rudy 1994) was based on patch-clamp data and reproduced membrane dynamics with a great quantity of electrophysiological detail, including numerical descriptions of 12 different ionic currents, in addition to intracellular $Ca^{2+}$ buffering and the $Ca^{2+}$ induced $Ca^{2+}$ release process. The Ferrero $I_{K,ATP}$ model was based on published experimental data concerning the key features of the current (Weiss et al. 1992; Wilde et al. 1990; Kakei et al. 1985; Horie et al. 2014). They integrated data regarding $I_{K,ATP}$ ion concentrations ($[K^+]_0$, $[Mg^{2+}]_i$ and $[Na^+]_i$) and intracellular nucleotide levels ($[ATP]_i$ and $[ADP]_i$) dependencies in one set of equations (Ferrero et al. 1996) to reproduce the main electrical features of $K^+_{ATP}$ channels.

In this thesis, a simplified version of this formulation is used (shown as Equation 5.1), which does not include the dependence of the concentrations ($[Mg^{2+}]_i$ and $[Na^+]_i$), or intracellular nucleotide levels ($[ATP]_i$ and $[ADP]_i$) to be consistent with experimental observations of APD (Shaw & Rudy 1997; Matsuoka et al. 2003).

**Shaw and Rudy**

The mathematical model of $I_{K,ATP}$ that Shaw and Rudy formulated was based on data for guinea-pig ventricular cells (Noma 1983; Nichols et al. 1991) which were not the same as data used for the Ferrero model. They assigned a set of individual parameter values to combine ischaemic conditions. These conditions have been attempted as three various objects: 1) $[K^+]_O$ accumulation (hyperkalaemia); 2) intracellular and extracellular acidosis; and 3) anoxia and metabolic blockade. The method and theoretical implementation of each state can be found in their original paper (Shaw & Rudy 1997). In this section, the relative influence of anoxia/ischaemia condition on APD reduction is examined. $I_{K,ATP}$ can be the reason for similar AP morphology to the AP variations detected in anoxic guinea-pig cells

(Shaw & Rudy 1997). However, the effects of elevated extracellular potassium in a tissue model are investigated in Chapter Eight.

The general equation describing current density described in Shaw and Rudy (Shaw & Rudy 1997) is:

$$I_{K,ATP} = G_{K,ATP} \frac{1}{1+\left(\frac{[ATP]_i}{K_{0.5}}\right)^H} \left(\frac{[K^+]_0}{5.4}\right)^n (V_m - E_k) \tag{5.2}$$

In these formulations $I_{K,ATP}$ activated at $[ATP]_i$ level and the $K_{0.5}$ parameter was also assigned to highlight the potential role of pH dependence of the $K_{ATP}$ channel.

**Matsuoka *et al*.**

An alternative formulation of the time-independent current, $I_{K,ATP}$, by Matsuoka et al. (2003), also based on guinea pig ventricular cell data (Sasaki et al. 1999), is given by:

$$I_{K,ATP} = G_{K,ATP} \frac{0.8}{1+\left(\frac{[ATP]_i}{0.1}\right)^2} \left(\frac{[K^+]_0}{6.019 \times 10^6}\right)^{0.24} (V_m - E_k) \tag{5.3}$$

They examined the contribution of $I_{K,ATP}$ by depleting the $[ATP]_i$ by decreasing the rate of conversion of ADP to ATP to 1% of the control.

**Kazbahnov *et al*.**

The formulation described by Kazbahnov *et al*. was implemented as:

$$I_{K,ATP} = Af_{ATP} \left(\frac{[K^+]_0}{5.4}\right)^{0.3} \frac{1}{40+3.5e^{0.025V}} (V_m - E_k) \tag{5.4}$$

This model of $I_{K,ATP}$ was based on the results of in vitro experiments in human ventricular myocytes (Babenko et al. 1998). $[K^+]_0$ power dependency concentration functions and exponential functions of voltage were incorporated (Kazbanov & Clayton 2014) in a model of the $I_{K,ATP}$ current similar to functions that used in (Shaw & Rudy 1997; Rodriguez et al. 2008).

In each of these formulations, $V_m$ is the membrane voltage and $E_k$ indicates reversal potential for potassium ions. The maximum conductance of $I_{K,ATP}$ ($G_{K,ATP}$) was fixed at 3.9 $mS\ mm^{-2}$ and 0.17674 $mS\ mm^{-2}$ for the Shaw and Rudy et al. and Matsuoka et al. formulations

respectively (Clayton et al. 2011; Nickerson & Buist 2008). $g_0$ is the maximum channel conductance in the absence of $Na^+$, $Mg^{2+}$ and ATP, set to 2.01 $mS\ mm^{-2}$ for epi cell type (Heidenreich et al. 2012). In this thesis, a simplified version of the Ferrero et al. formulation which did not include the dependence of the concentrations ($[Mg^{2+}]_i$ and $[Na^+]_i$) and intracellular nucleotide levels ($[ATP]_i$ and $[ADP]_i$) was used (Heidenreich et al. 2012; Abbasi & Clayton 2014). Therefore, their formulation was replaced with a scaling factor $f_{ATP}$, the fraction of opened channels. The value of this parameter was set between 0% for a non-ischaemic condition and 0.4% for ischaemia (Kazbanov & Clayton 2014). The scaling coefficient A was fitted to the formulation with a value of 155 (Rodriguez et al. 2008; Kazbanov & Clayton 2014), where the value of APD reductions doubled if $f_{ATP} = 0.55\%$ of channels were open. Hypoxia was simulated by reducing $[ATP]_i$ from its normal value of 6.8 mM to 6.0, 5.0, 4.5 and 4.0 mM. The ischaemic parameter values used in the Shaw and Rudy et al. formulation are presented in Table 5.1. The Hill coefficient H was set at 2.0, and n was set at 0.24 (Nichols et al. 1991). These formulations reproduce the current-voltage dependency in a range between −100 and 50 mV.

Table 5.1. Ischaemic parameters values

| parameters/condition | normal | ischaemic | | |
|---|---|---|---|---|
| $[ATP]_i$ (mM) | 6.8 | 6.0 | 5.0 | 4.5 |
| $K_{0.5}$ (mM) | 0.042 | 0.117 | 0.212 | 0.259 |
| $[K^+]_0$ (mM) | 5.4 | 6.0 | 7.0 | 8.0 |

The code for these simulations was written in Matlab to describe the current-voltage (I-V) dependency of the $K_{ATP}$ current. The related $I_{K,ATP}$ simulation code is illustrated in Appendix (Code A.2.1 and A.2.2).

**General approach**

To evaluate the quantitative influence of $I_{K,ATP}$ models three different models were chosen of the ATP activated $K^+$ current $I_{K,ATP}$ : the current through a single fully activated channel (Ferrero et al. 1996; Shaw & Rudy 1997; Matsuoka et al. 2003); based on animal data; and

one formulation (Kazbanov & Clayton 2014) based on in vitro experiments in human ventricular myocytes. I-V dependence of each model was computed without the conditions of elevated $[K^+]_0$. Then, the influence of $I_{K,ATP}$ on cellular $K^+$ efflux during hypoxia/ischaemia conditions was examined. The current-voltage properties of each $I_{K,ATP}$ formulation were also compared. The slope of voltage dependency of each $I_{K,ATP}$ model was further explored. Further experiments in Chapter Seven will examine electrophysiological effects of the four different formulations of $I_{K,ATP}$ on dynamic characteristics of cardiac tissue. It will be shown that a reduction in $[ATP]_i$ is responsible for action potential shortening through activation of $K_{ATP}$ channels.

## 5.3    Results

### 5.3.1  Current-Voltage Dependency for the KATP Current

**Modulation of ATP sensitivity of KATP channel**

Figure 5.1 shows single channel current-voltage (I-V) curves computed for various values of $I_{K,ATP}$ in different models. This figure shows the voltage changes with reduction of $I_{K,ATP}$ in each model. The changes in the Matsuoka model are very small in comparison to the other models. Figure 5.2 shows a comparison of the current-voltage properties of each $I_{K,ATP}$ formulation. Figure 5.2a displays the current-voltage properties of each $I_{K,ATP}$ formulation under control conditions ($[ATP]_i$= 6.8 mM, $f_{ATP}$=0%, and $[K^+]_0$=5.4 mM). As shown in this figure, the behaviour of each model is similar. Figure 5.2b shows the current-voltage relationships of the channel under ischaemic conditions. This figure corresponds to the theoretically formulated single channel (I-V) curves of $I_{K,ATP}$ at $[ATP]_i$ of 4.0 mM and $[K^+]_0$ of 5.4 mM. The changes in $[ATP]_i$ in the Matsuoka model were a little small, thus the value of $[ATP]_i$ was specified at 0.1 mM for the ischaemic condition in this model. Furthermore, the slope of voltage dependency of each $I_{K,ATP}$ model was explored. Figure 5.3 shows that the Matsuoka et al. formulation has the least slope in comparison to the other formulations even with decreasing $[ATP]_i$ values dividing by 40 ($[ATP]_i$: 4.0 /40=0.1 mM) less than the Shaw and Rudy model. The figure shows that the Shaw and Rudy $I_{K,ATP}$ formulation has the most profound effect on voltage with reduction of $[ATP]_i$ current with the slope of 3.1 in comparison to the other models. It can also be seen that the maximum slope of the $I_{K,ATP}$-voltage curve is similar for the Shaw-Rudy and Ferrero models for $[ATP]_i$ reduction level

until 5.0 mM. This figure indicates that this formulation would produce a larger outward current for a given level of activation.
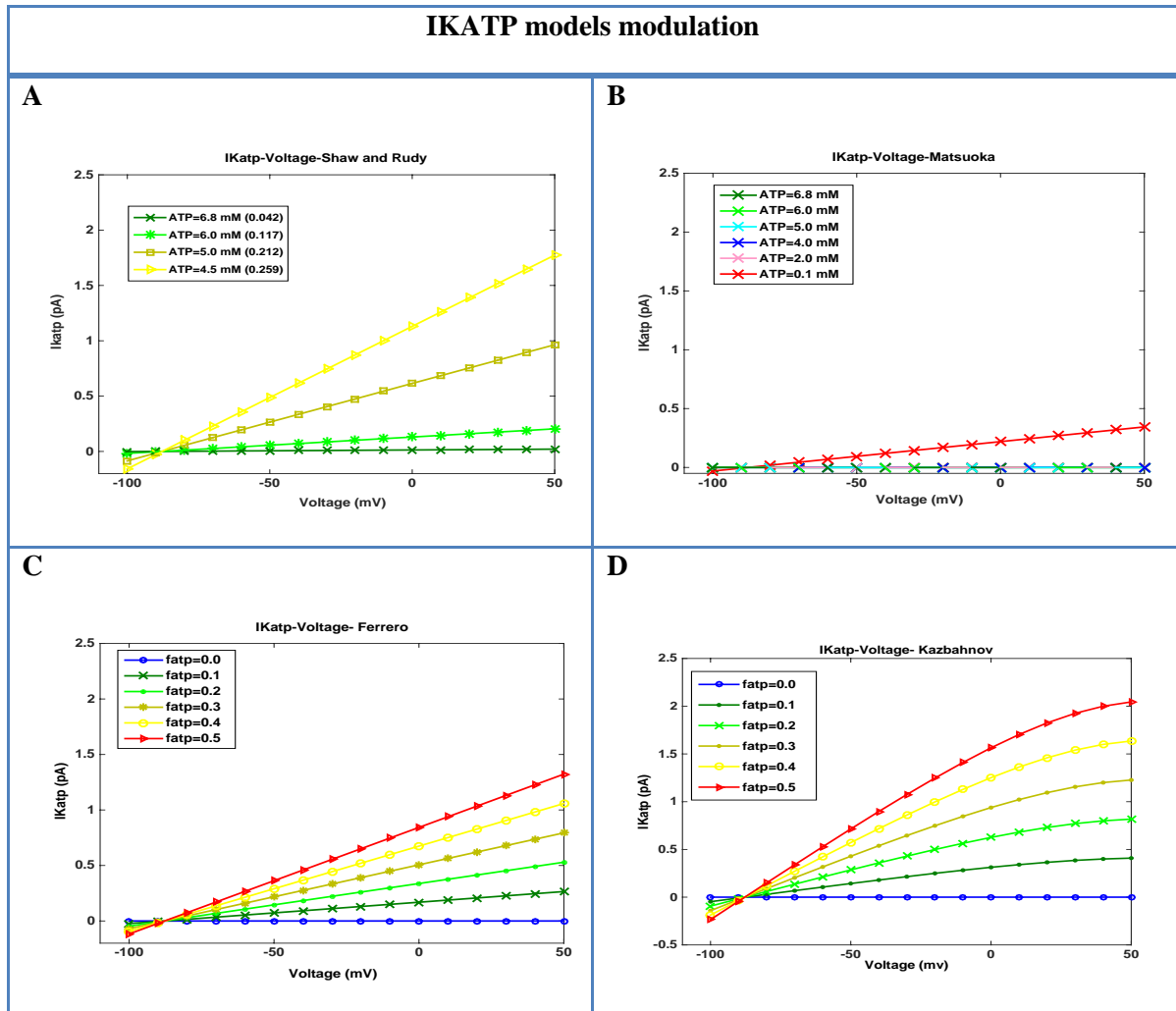


**Figure 5.1 Current-Voltage (I-V) characteristics of $K_{ATP}$ channels considered in each model. A, B, C and D single channel (I-V) associations for the $K_{ATP}$ channel in Shaw and Rudy, Matsuoka, Ferrero and Kazbahnov models respectively. The figure represents $I_{K,ATP}$ as the current through a single fully activated channel (Ferrero et al. 1996). Equations 5.1, 5.2, 5.3 and 5.4 were applied to produce these plots. Each plot in the Ferrero and Kazbahnov models correlates here to a particular value of $f_{ATP}$ (specified in percentages in the legend) and a certain value of $[ATP]_i$ for the Shaw-Rudy and Matsuoka model.**

## Comparison of Current-Voltage Dependency for the KATP Current

**A**



**B**
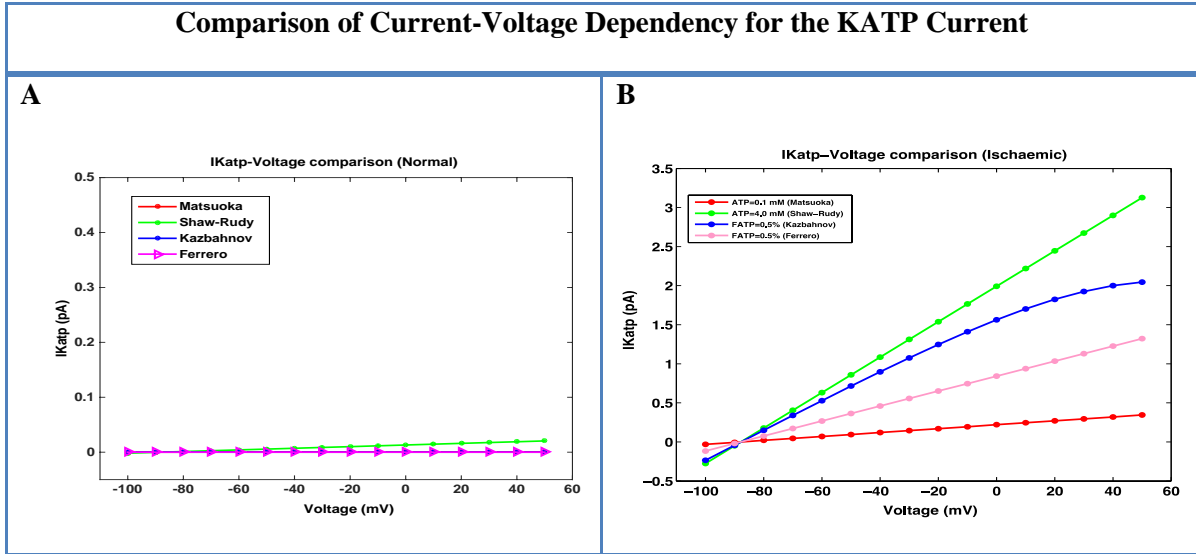


**Figure 5.2 Comparison of the current-voltage properties of four different $I_{K,ATP}$ models. (A) displays the current-voltage properties of each $I_{K,ATP}$ formulation under normal conditions ($[ATP]_i$= 6.8 mM, $f_{ATP}$=0%, and $[K^+]_0$=5.4 mM). (B) represents the current-voltage relationships of the channel under ischaemic conditions ($[ATP]_i$= 4.0 mM, $f_{ATP}$=0.5%, $[ATP]_i$= 0.1 mM for Matsuoka model) and $[K^+]_0$=5.4 mM.**
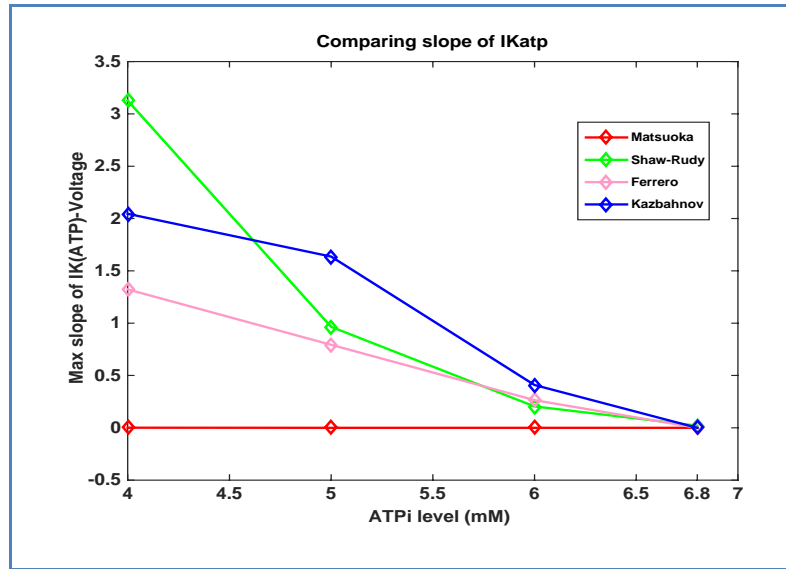
**Figure 5.3 shows the slope of voltage dependency of each $I_{K,ATP}$ model.**
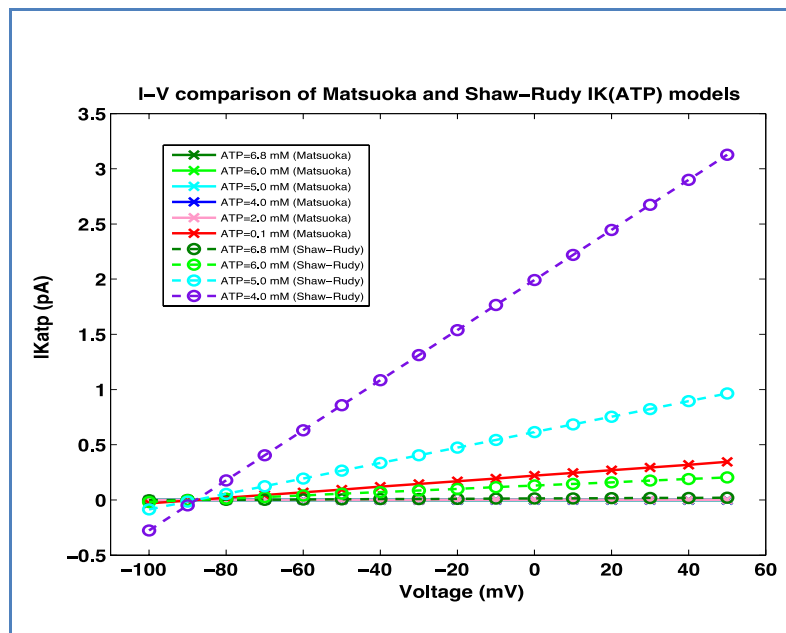


**Figure 5.4 Comparison of the current-voltage properties of the Shaw and Rudy and Matsuoka $I_{K,ATP}$ models corresponding to a certain value of $[ATP]_i$ (indicated in the legend). $[ATP]_i$ was reduced from its normal value of 6.8 mM to 6.0, 5.0, 4.0 (in the Shaw and Rudy $I_{K,ATP}$ model), 2.0 and 0.1 mM (in the Matsuoka $I_{K,ATP}$ model).**

## 5.3.2  Characteristics of KATP Channels with Development of Hyperkalemia

$[K^+]_0$ was modified from 5.4 mM to amounts between 6.0 and 8.0 mM to examine the contribution of $I_{K,ATP}$ I hyperkalaemia. Some experimental studies (Weiss et al. 1992; Gasser & Vaughan-Jones 1990; Kantor et al. 1990; Wilde et al. 1990) support the idea that $I_{K,ATP}$ channel activation concerns $K^+$ reduction from the cell in the first stage of a hypoxia.

Nevertheless, evidence in contradiction of a major role for $I_{K,ATP}$ in this aspect are shown in other experimental studies (Vanheel & Hemptinne 1992; Yan et al. 1993; Wilde & Aksnes 1994), which highlight the inefficacy of $K^+$ channel openers to increase the amount of $K^+$ efflux, the differentiation between $K^+$ loss, AP reduction, and intracellular ATP levels in hypoxia (Ferrero et al. 1996). Figure 5.5 shows a very small change in cellular $K^+$ loss through the $K_{ATP}$ channels in ischaemic conditions in which $[K^+]_0$ increment takes place. Results in this thesis confirm that the degree of cellular $K^+$ efflux affected by $I_{K,ATP}$ achieved with the model is considerably less than the values of total $K^+$ loss observed experimentally (Ferrero et al. 1996). Therefore, it can be noted from Figure 5.5 that according to the models, the activation of $I_{K,ATP}$ does not numerically account for the observed variations in extracellular potassium current. Further aspects are involved during the ischaemic episode. For example, the cell's capacity to regain its metabolite concentrations and ATP-buffering capacities (Terkildsen et al. 2007) resulting from the ischaemia may be fundamental to the $K^+$ efflux increment through the modification of ADP concentration (Terkildsen et al. 2007). Linking between hyperkalaemia and cellular metabolic status supports the involvement of metabolite concentrations during ischaemia. Terkildsen et al. (2007) presented a simulated study showing the modifications in metabolite concentrations (a 10% rise or fall in individual metabolite concentrations) were qualitatively in agreement with other studies (Allen & Orchard 1987; Fukuda et al. 2001; Hartmann et al. 1998; Ingwall 2002; Pike et al. 1993; Takayama et al. 2004; Emous et al. 1997). They argued that the effect of quantitatively small changes in metabolite concentrations on both the qualitative and quantitative nature of the $Na^+$-$K^+$ pump inhibition is negligible (Terkildsen et al. 2007). Other factors may affect both the metabolic status of the cell and cellular electrophysiology in the ischaemic myocyte. For example, the activation of the persistent $Na^+$ current and the inhibition of sarcoplasmic reticulum $Ca^+ - ATP$ase motivate only a very small change in the degree of increment of $K^+$ efflux; another element is acidosis-induced $Na^+$ currents that would increase $[Na^+]_i$, with a potential effect on $Na^+$-$K^+$ pump activity (Terkildsen et al. 2007) and hence $K^+$ efflux increment. This section does not aim to provide a comprehensive model of ischaemia, but a study of the $K^+$ dynamics under hypoxic/ischaemic situations that is able to show $I_{K,ATP}$ is not the only element contributing to $K^+$ elevation during ischaemia compatible with experimental data and observed trends.
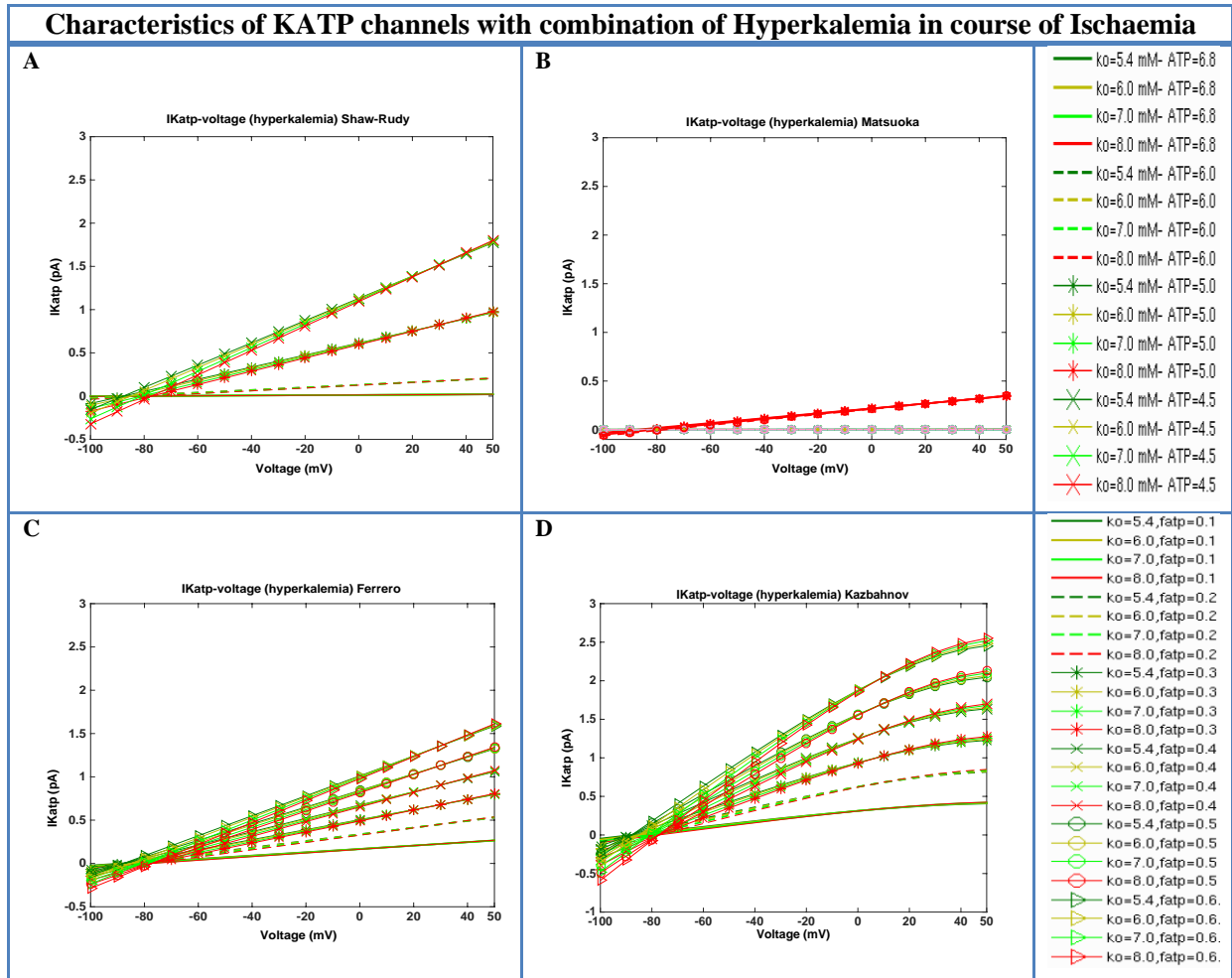
**Figure 5.5 The involvement of $I_{K,ATP}$ in cellular K$^+$ efflux during hypoxia/ischaemia conditions. A, B, C and D single-channel I-V associations for the $K_{ATP}$ channel in the Shaw and Rudy, Matsuoka, Ferrero and Kazbahnov models respectively under ischaemic conditions in which $[K^+]_0$ accumulation occurs. Hypoxia was simulated by reducing $[ATP]_i$ from its default value of 6.8 mM to 6.0, 5.0 and 4.5 mM. $[K^+]_0$ was elevated from 5.4 mM (normal) to 6.0 and 8.0 mM. Green lines show normal and red lines illustrate ischaemic conditions. This figure shows that the activation of $I_{K,ATP}$ does not appear to be involved quantitatively in the experimentally detected hypoxia/ischaemia cellular $K^+$ efflux.**

## 5.4   Discussion

Ischaemia was simulated by decreasing $[ATP]_i$ and activating $I_{K,ATP}$. The models of $I_{K,ATP}$ formulated in different studies (Ferrero et al. 1996; Shaw & Rudy 1997; Matsuoka et al. 2003; Kazbanov & Clayton 2014) reproduce the main electrical features of $K_{ATP}$ channels (increased outward current when ATP is depleted). Two formulations (Shaw & Rudy 1997; Matsuoka et al. 2003) involved just the dependence on $[ATP]_i$. However, the other two formulations (the simplified version of Ferrero *et al*. and Kazbahnov *et al*.) do not include the

dependence on the concentration of ATP, and MgADP, and instead use a scaling factor $f_{ATP}$. However, other factors which may contribute to $I_{K,ATP}$ during hypoxia/ischaemia situations are not considered in most of these models. For example, dependence on $pH_i$ and on other nucleotides and influence of $[Mg^{2+}]$ on the fraction of open channels are neglected in $I_{K,ATP}$ formulations considered in this chapter.

To determine the impact of anoxia on cardiac cell electrophysiology, different formulations of $I_{K,ATP}$ were studied in this thesis. I-V dependences of each model were computed to evaluate the quantitative influences of $I_{K,ATP}$ formulations. The current-voltage properties of each $I_{K,ATP}$ formulation under control and ischaemic conditions are presented. The results obtained from the simulated electrical behaviour showed that the behaviour of each model was qualitatively similar. However, there was a big difference in both I-V curve and the slope of voltage dependency in the Matsuoka $I_{K,ATP}$ formulation compared to other formulations indicating that variations in $[ATP]_i$ in this model were negligible under all simulation conditions implemented in the current study. In addition, in Figure 5.4, the effect of reduction of $[ATP]_i$ on I-V curve is shown using the Shaw and Rudy and Matsuoka $I_{K,ATP}$ models. The results show that the Shaw and Rudy formulation has a greater influence on max slope of $I_{K,ATP}$ -voltage than other $I_{K,ATP}$ formulations for modest changes in $[ATP]_i$.

In addition, simulations here support the idea that the activation of $K_{ATP}$ channel does not completely account for the experimental cellular $K^+$ efflux during hypoxia/ischaemia. This is because of $K_{ATP}$ channel activation due to an increment in $\Delta J_{efflux}$. $\Delta J_{efflux}$ is a net increment in $K^+$ unidirectional efflux rate that initially increases with $f_{ATP}$. However, $\Delta J_{efflux}$ reduces as $I_{K,ATP}$ is further increased, until it reaches zero value (Ferrero et al. 1996). This may be a reason for the stabilization of extracellular potassium in these models as shown in Figure 4.3. Thus, according to the $I_{K,ATP}$ models presented in this study, ischaemic $K^+$ efflux through $K_{ATP}$ channels is not involved in the total experimentally detected cellular $K^+$ efflux. Consequently, the models used in this study have several limitations.

The influence of acidosis on the cardiac $K^+$ current is neglected in these formulations. A rise in $[Ca^{2+}]_i$ is equivalent to the secondary phase of $[K^+]_0$ rise and fast reduction of $[ATP]_i$, and this may also promote electrical abnormalities related to ischaemia which are not included in Shaw & Rudy (1997). For a more complete model, $[ATP]_i$ reduction, free $Mg^{2+}$ increase, and catecholamine release should be considered. In addition, for more accuracy, a

more sophisticated $Na^+$-$K^+$ pump model is needed to determine net $K^+$ efflux during metabolic inhibition (Ferrero et al. 1996). In general, parameters used in models of $I_{K,ATP}$ shown here are in agreement with experimental measurements (Weiss et al. 1992a; Findlay & Faivre 1991; Nichols et al. 1991). Experimental studies (Weiss et al. 1992; Befroy & Powell 1999) indicated that the decrease in $[ATP]_i$ was almost 0.2 mM per minute in small mammals; however, the fast VF may result from a rapid reduction in $[ATP]_i$ in the human heart (Jessen et al. 1996). The question that arises here is whether models based on data from guinea pig cells are relevant for simulation $I_{K,ATP}$ in human myocytes. Our simulation study (Abbasi & Clayton 2014) showed that despite different formulations of $I_{K,ATP}$ , dynamic behaviour and response to simulated ischaemia in these models was similar. However, the theoretical simulations are not a comprehensive demonstration of all ischaemic conditions. Thus, this precludes proposal of the most appropriate $I_{K,ATP}$ model for use in simulations of ischaemia, because several conditions (as discussed above) are not included; either their influences need additional experimental description or their existence is not related during ischaemia. Chapter Seven explores the contribution of different $I_{K,ATP}$ models in the 2D tissue models with different types of heterogeneity to study the influence of $I_{K,ATP}$ activation on action potential propagation and wave break during ventricular arrhythmias in the human heart with global myocardial ischaemia.

Part II

# Tissue Modelling: the Dynamic Behaviour of Simulated Human Cardiac Tissue

# 6    The Dynamic Behaviour of Normal Tissue: Restitution Study

*This chapter is a review of cardiac tissue electrophysiology models, concentrating on two models of cardiac tissue electrophysiology with the contributions of different types of heterogeneity in the human heart, behaviours of action potential propagation and numerical techniques. The purpose is to compare the dynamic behaviour in two cell models: the Ten Tusscher-Panfilov 2006 (TP06) model, and the O'Hara-Rudy dynamic (ORd) model. The influences of action potential duration (APD) and conduction velocity (CV) restitution on a human ventricular 2-D tissue are examined.*

## 6.1 Introduction

**Background**

Action potentials are produced across the cell membrane as a result of the depolarising local current flux gain of the AP upstroke (Clayton & Panfilov 2008). The transmission of individual ions produces the currents across the membrane through ion channels. An action potential is initiated when depolarization opens $Na^+$ channels. At the microscopic level, cardiac tissue contains different cell types, myocytes and fibroblasts. The main components of cardiac muscle, cardiac myocytes, are connected to one another by gap junctions and structured in fibres organised in sheets. Gap junction channels link myocytes, which allow intracellular signalling and propagation of the AP. The structure and sequences of myocytes are important and effective in action potential form, action potential duration and conduction velocity (Gilbert et al. 2007).

As described in Chapter Two section 2.6.2, restitution studies have been shown to be an important aspect of controlling the dynamic instability of spiral wave re-entry (Panfilov & Zemlin 2002). Theoretical and computer studies have proposed that fibrillation is maintained by properties of the APDR.

The aim of this computational study is to examine the function of electrical restitution in wave stability using a human ventricular cell and tissue model. In this thesis, the TP06 and ORd human models are used to compare the role of electrical restitution in unstable spiral wave re-entry in simulated 2-D ventricular tissue. Spatial variation in restitution will be obtained by regional changes in ion channel density. The thesis investigates how changes in restitution resulting from ischaemia affect the stability of re-entry. In this chapter, an overview of restitution and different ways to measure restitution is provided.

**Measuring restitution**

Firstly, to measure APD restitution (APDR), a measurement of APD is required. APD is measured by gaining the time difference between the AP upstroke and the repolarization time (time to 90% of repolarization is used in this study). Different protocols have been used to obtain restitution curves. Two different pacing protocols are usually applied: the dynamic (or steady-state); and the standard (S1-S2) restitution protocols (Koller et al. 1998).

*Dynamic restitution protocol*. The tissue is initially stimulated at a particular cycle length (CL) until steady-state is achieved and the APD and previous DI are recorded. This process is repeated with other CLs.

*Standard restitution protocol*. The tissue is stimulated at a constant CL (S1) until steady-state is achieved and next single test pulse (S2) is delivered after waiting a variable-length interval. In this case, the DI of the last S1 and APD of S2 are recorded as coordinates on the restitution curve.

An additional restitution protocol is the constant cycle length (constant-CL) curve to obtain restitution information. In this protocol, APDs and DIs are taken and plotted against the time between a CL alteration and the achievement of steady-state. The constant-CL restitution curves (Kalb et al. 2004) normally have negative slopes when measuring the movement to steady-state resulting in a change in CL; however, typically, the slopes are positive for the dynamic and S1-S2 restitution curves in normal cardiac tissue.

**Aim and general outline**

Due to the limitations of experimental data from normal human cells, developing models of human cell and tissue electrophysiology, and mimicking experimental dynamic properties of the human ventricles is a significant modelling challenge (Fink et al. 2011; Elshrif & Cherry 2014). In spite of these limitations, many computational models present a wide variety of methods to represent cellular properties, thus an important goal of this study was to compare two models of human ventricular myocytes (TP06 and ORd) to examine the dynamic behaviour of tissue with the contribution of different types of heterogeneity in the human heart. The influences of APD and CV restitution on human ventricular 2-D tissue were investigated. This chapter is an introduction to Chapters Seven and Eight which propose the main study of the dynamic behaviour and impact of simulated global cardiac ischaemia on human ventricular 2-D tissue. The different types of heterogeneity which influence wave break during ventricular arrhythmias with global myocardial ischaemia in the human heart are investigated (Chapters 7 to 9).

**Objective**

Mathematical models of activation and propagation in simulated cardiac tissue are important research tools for studying mechanisms of normal and abnormal activation, and for understanding of abnormality resulting in disease such as arrhythmias, myocardial ischaemia and heart failure. It is possible to control parameters affecting activation and propagation in a computational model. Computational models can provide data that would be impossible or difficult to achieve experimentally, or where producing detailed measurements is technically challenging (Clayton 2001; Clayton & Holden 2004b). In this chapter, the activation of three cell types of cardiac tissue under normal (non-ischaemic) conditions is modelled.

## 6.2 Methods

**Numerical methods**

Action potential propagation in a two-dimensional cardiac tissue sheet can be represented by a non-linear reaction diffusion equation (Clayton 2001):

$$C_m \frac{dV}{dt} = -(I_{ion} + I_{stim}) + \nabla D \nabla V \qquad (6.1)$$

here $C_m$ is the membrane capacitance, $V$ is the transmembrane potential, $I_{stim}$ is the externally applied transmembrane current, and $I_{ion}$ is the sum of all transmembrane ionic currents. For $I_{ion}$, we use two human ventricular cell models (Ten Tusscher & Panfilov 2006; O'Hara et al. 2011). $D$ is a tensor describing the conductivity of the tissue and $\nabla$ is the gradient operator. The left side of the equation describes the current fluxes because of the capacitance of the cell membrane. The right side presents current flux as both trans-membrane potential gradients (diffusive term) and the flow of current in the cell membrane (reactive term) through ion channels, pumps and transporters (Clayton & Holden 2004b).

Equation 6.1 and the TP06 and ORd equations were solved using the method described by Rush and Larsen (1978) to incorporate the Hodgkin-Huxley type equations for the gating variables of the various time-dependent currents. For two-dimensional computations, the explicit Euler method with a fixed space step of 0.2 mm and time step of 0.005 ms was used. The gradient of membrane voltage was set to zero at boundary condition to show no-flux boundary conditions were applied at each edge. A 2-D monodomain tissue model described with an isotropic diffusion coefficient of 1.171 $cm^2\ s^{-1}$ (TP06 model), 0.2975 $cm^2 s^{-1}$ (ORd

model), and a membrane capacitance of 1 μF $cm^{-2}$ was applied to characterize restitution properties. To obtain reliable CV and stable re-entry in the ORd model, the $Na^+$ current formulation was replaced with the $Na^+$ current formulation from the TP06 model.

Each of the simulated tissues in this study was described and discretised into a thin strip of tissue 3 × 100 grid points (0.75 × 25 mm). S1-S2 restitution protocol was used to achieve APD and CV restitution curves for the models in a 2-D cable with S1=1000ms. A stimulus current of -52.0 (TP06 model) and -80 $pA\,pF^{-1}$ (ORd model) was used to deliver each stimulus at a small slab of tissue for 1ms. The CL for S2 interval was varied between 1000 ms and 250 ms. The 10 S1-1S2 stimulus was applied with a CL of 1000 ms. The tissue was returned to its initial state after each S2 before the next S1S2 cycle. In this thesis, all measurements of APD computed at 90% repolarization correspond to $APD_{90}$. CV was measured in the middle of the strand. The tissue simulations settings are summarised in Table 6.1.

Table 6.1. The tissue simulations settings

| Geometry | Tissue size (mm) | Dimensions (grid points) | Simulation protocol | CL |
|---|---|---|---|---|
| 2D (thin strip of tissue) | 0.75 × 25 | 3 × 100 | A standard 10 S1S2 stimulus TP06= -52.0 $pA\,pF^{-1}$ ORd= -80 $pA\,pF^{-1}$ | 1000 ms |

**Simulations**

The activation of three different cell types of cardiac tissue was simulated under normal conditions. For this purpose, homogeneous tissue with a combination of three uniform layers, of epicardial, mid-myocardial (M cell), and endocardial tissue was assumed for the simulation. The parameters for all three cell types were used for the TP06 and ORd models. To examine how different arrangements of the cell layers could influence the spatial distribution of repolarisation and APD (Clayton & Holden 2004b), a 2-D monodomain tissue model with isotropic diffusion was created to characterize restitution properties.

## 6.3 Results

**Action potential characteristics**

Figure 6.1 presents action potential shape for different cell types (epi, M and endo) of the TP06 and ORd models. The AP morphologies produced by these two human ventricular models are shown in this figure. The differences in AP properties of the TP06 and ORd models can be seen here. These differences are presented in detail in Table 6.2. Experimental data recorded by Drouin et al. (Drouin et al. 1998b) and Pereon et al. (Péréon & Demolombe 2000) were also used for evaluation of human ventricular tissue electrophysiological models.

Table 6.2 compares important AP characteristics for three cell types (epi, M and endo) of the TP06 and ORd models. Properties studied here are described as:

$V_{dia}$ : minimum membrane voltage during the diastolic interval

$V_{max}$ : maximum membrane voltage reached during the AP upstroke

$V_{notch}$ **:** minimum membrane voltage reached during the AP notch

$V_{plateau}$ **:** maximum membrane voltage reached during the AP plateau or dome phase

APA: action potential amplitude (APA= $V_{max}$- $V_{dia}$)

APD: Action potential duration at 90% of repolarization

The results show some differences between these two models. $V_{dia}$ and APD is almost the same for both models. The value of $V_{dia}$ for ORd is -87.9 mV, while the TP06 model has a value of -85.34 mV. Experimentally obtained values (Drouin et al. 1998; Péréon & Demolombe 2000) are about -86mV. However, ORd has a shorter APD in comparison to the TP06 model because of its different parameter settings. $V_{max}$ values in these two models range from 37.3mV (TP06) to 44.2mV (ORd) resulting in AP amplitudes varying from 107.34mV (TP06) to 132.1mV (ORd). Experimental data (Drouin et al. 1998; Péréon & Demolombe 2000) describe AP amplitudes ranging from 95mV to 106mV. $V_{notch}$ values vary from 13.2 (TP06) to 33.9mV (ORd). $V_{plateau}$ values are 22mV for all cell types for the TP06 model, whereas the maximum plateau level varies from 30.6mV (epi cell type) to 42.2 (M cell type) for the ORd model. From the values of $V_{max}$, $V_{notch}$ and $V_{plateau}$ together presented in Table 6.2 and looking at Figure 6.1, it can be seen that the ORd model has the

sharper spike-notch-dome form in comparison to the TP06 model. APD varies from 293ms (epi cell type) and 294ms (endo cell type) to 379ms (M cell type) in the TP06 model compared to 233ms (epi cell type), 269ms (endo cell type) and 364ms (M cell type) in the ORd model. Experimentally reported APDs vary from around 325ms (Péréon & Demolombe 2000) to 350ms (Drouin et al. 1998) for (epicardial) human ventricular myocytes, to values from 316ms (Péréon & Demolombe 2000) to 350ms (Drouin et al. 1998) for (endocardial) human ventricular myocytes and to values from 430ms (Péréon & Demolombe 2000) to 450ms (Drouin et al. 1998) for (mid-myocardial) human ventricular myocytes .

**Table 6.2 Action potential characteristics representing epicardial, midmyocardial, and endocardial ventricular tissue layers; comparison of two simulated models (TP06 and ORd) with experimental observation (exp)**

| Model | Cell type | $V_{dia}$ | $V_{max}$ | $V_{notch}$ | $V_{plateau}$ | APA | APD |
|-------|-----------|-----------|-----------|-------------|---------------|-----|-----|
| TP06 | epi | -85.34 | 37.5 | 13.6 | 22 | 122.84 | 293 |
| | M | -85.34 | 37.3 | 13.2 | 22 | 122.64 | 379 |
| | endo | -85.34 | 37.5 | 22 | 22 | 107.34 | 294 |
| ORd | epi | -87.9 | 44.01 | 26.8 | 30.6 | 131.91 | 233 |
| | M | -87.9 | 43.9 | 33.4 | 42.2 | 131.8 | 364 |
| | endo | -87.9 | 44.2 | 33.9 | 36.0 | 132.1 | 269 |
| exp | epi | -86 | NA | NA | NA | 95±2 | 325-350 |
| | M | -86 | NA | NA | NA | 106±3 | 430-450 |
| | endo | -87 | NA | NA | NA | 101±2 | 316-350 |

$V_{dia}$ : *minimum membrane voltage during the diastolic interval; $V_{max}$ : maximum membrane voltage reached during the AP upstroke; $V_{notch}$ : minimum membrane voltage reached during the AP notch; $V_{plateau}$ : maximum membrane voltage reached during the AP plateau or dome phase; APA: action potential amplitude (APA= $V_{max}$- $V_{dia}$); APD: Action potential duration at 90% of repolarization;NA: Not Applicable*
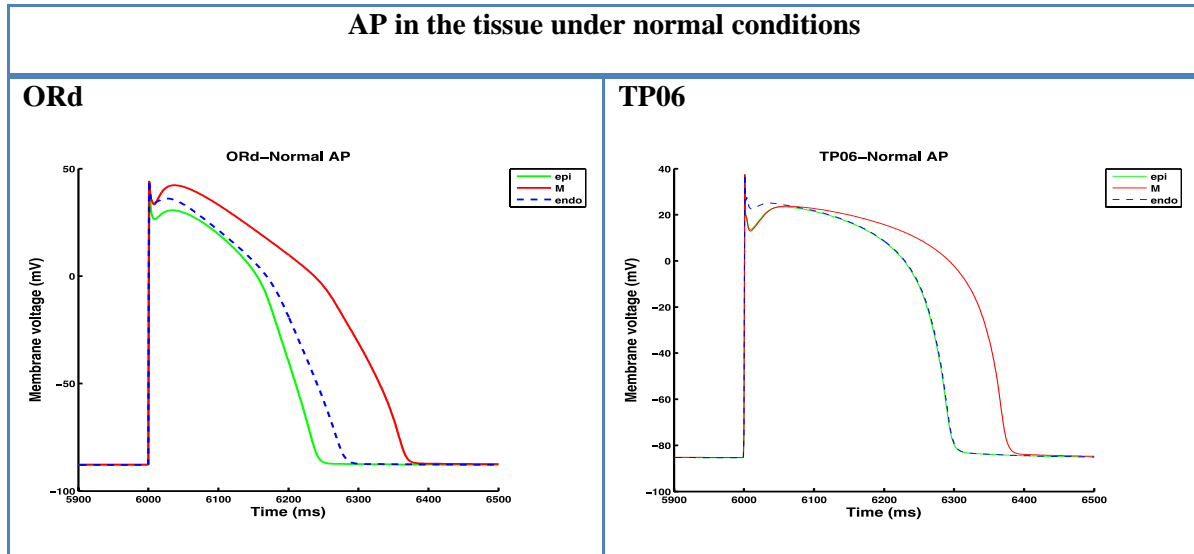
**Figure 6.1 Action potential morphologies from epicardial (green), mid-myocardial (red) and endocardial (blue) ventricular tissue layers for TP06 and ORd models**

### 6.3.1 Action Potential Duration Restitution (APDR)

The APDR for both computational models computed in a narrow strand of homogenous tissue is displayed in Figure 6.2. Curves were achieved by using the S1S2 restitution protocol at a basic cycle length of 1000 ms. The two model (TP06 and ORd) APDs lie in the middle-range of experimentally obtained APDs in single cell (336,298,360 and 310ms) (Li et al. 2004; Li et al. 1999; Li et al. 1998; Li et al. 1996) and tissue preparations (316, 325, 350 and 450 ms ) (Drouin et al. 1998; Péréon & Demolombe 2000).

Both models have different adjustments for various cell types as demonstrated in the restitution curves shown in Figure 6.2. Some differences are presented among the curves. A restitution curve reproduced in the TP06 model presents a high level of accuracy that is a close fit to experimentally obtained restitution curves. The ORd restitution curve is relatively flat in comparison to the TP06 model. The ORd model demonstrates a much larger disparity between epicardial and endocardial cell types compared to the TP06 model.

As shown in Figure 6.1, APs achieved by the ORd model have higher plateaus and smaller duration, and rate dependence is less than the TP06 model (Figure 6.2). The key trans-membrane currents ($I_{CaL}$, $I_{Kr}$, $I_{Ks}$ and $I_{to}$) were compared in single cells of the TP06 and ORd models for cycle lengths of 1000ms for the epicardial formulations (Figure 6.3). Because the L-type calcium current $I_{CaL}$ and the rapid and slow delayed rectifiers $I_{Kr}$ and $I_{Ks}$ are associated with rate dependence (Bueno-Orovio et al. 2008), these currents were chosen for comparison as they play a significant role in modulating the AP morphology. $I_{CaL}$ plays

145

an important role during the plateau phase of the AP. $I_{Kr}$ and $I_{Ks}$ play an important role in modulating the complete repolarisation phase of the AP. $I_{to}$ is responsible for the initial small repolarisation of phase one of the AP. As shown in Figure 6.3A, it is mainly peak $I_{CaL}$ that varies for the ORd and TP06 models, which gives rise to relatively flat APDR curves. Figure 6.3A shows the peak current is larger for the TP06 model (-9.07 pA/pF) than the ORd model (-1.4 pA/pF) displaying the longest AP plateau phase in the TP06 model. As shown in Figure 6.3.B, $I_{Kr}$ exhibits a larger value for the ORd model than the TP06 model, representing an important role during repolarization for the ORd model. In contrast, $I_{Ks}$ displays a greater peak amplitude for the TP06 model than for the ORd model by a factor of ten (Figure 6.3.C). This may be because the ORd model uses a different formulation that depends on $[Ca^{2+}]_i$ (O'Hara et al. 2011). For $I_{to}$ current, the peak current is thirteen times bigger for the TP06 model in comparison to the ORd model, which shows the greatest activity in the TP06 model. These results show the importance of $I_{Ks}$ activation and $I_{CaL}$ activation in modulating the restitution slope (Romero et al. 2009).
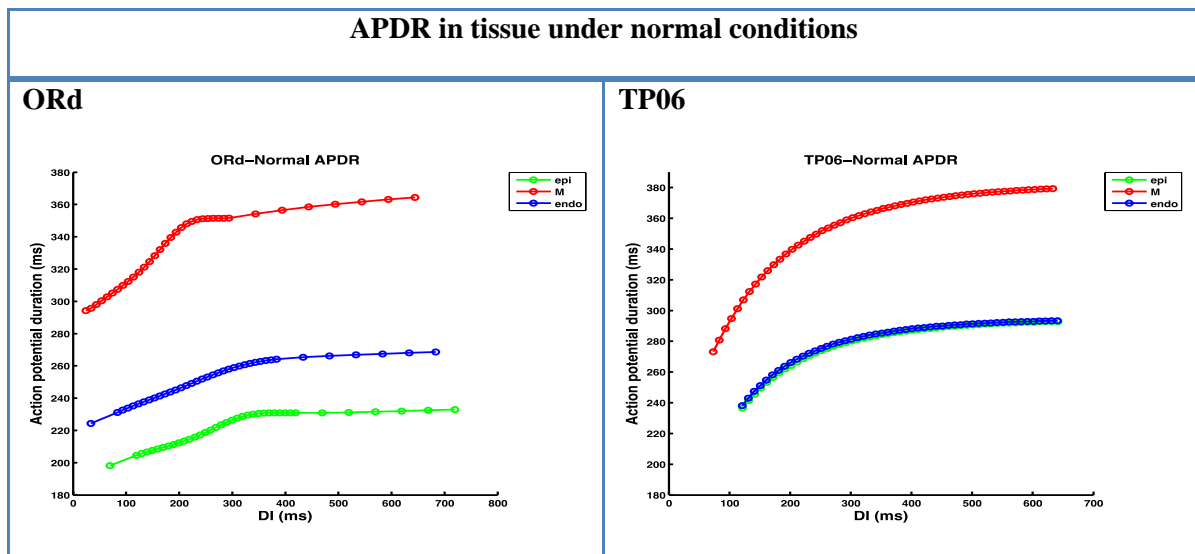


**Figure 6.2 Restitution Comparison: 2-D tissue rate dependences for the TP06 and ORd models. S1S2 APD restitution curves for epicardial (green), mid-myocardial (red) and endocardial (blue) cells**
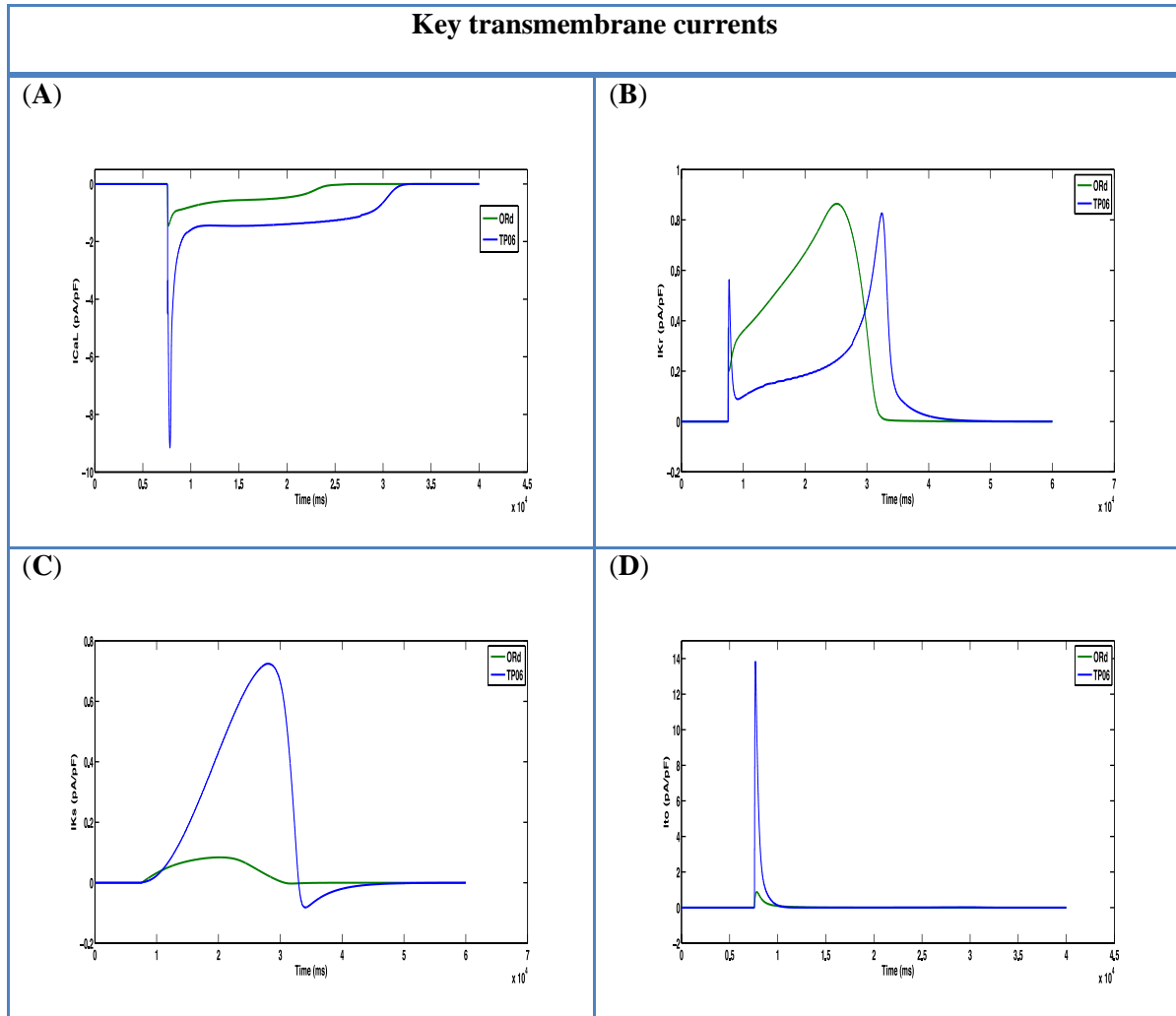
**Figure 6.3. Comparing trans-membrane currents, L-type calcium current ($I_{CaL}$), rapid delayed rectifier potassium current ($I_{Kr}$), slow delayed rectifier potassium current ($I_{Ks}$), and the transient outward potassium current ($I_{to}$) for the TP06 (blue) and ORd (green) models for cycle lengths of 1000ms and 0.005 maximum time step (ms) under normal conditions. These currents are compared to show their role in modulating the AP morphology in each model.**

### 6.3.2 Conduction Velocity Restitution

Figure 6.4 illustrates CVR curves achieved for the TP06 and ORd models measured in a narrow strand of homogenous tissue. The CV of the ORd model is un-physiologically slow with a maximum of about 0.37 m/s. This low velocity is correlated to the $Na^+$ channel formulation of the ORd model that was constructed based on data from Sakakibara et al. (1993).Thus, the ORd formulation of $I_{Na}$ was substituted with the TP06 $I_{Na}$ formulation to obtain a realistic range (Jongsma & Wilders 2000; Taggart et al. 2000; Nanthakumar et al. 2007) with a maximum of 0.71-0.74 m/s. In addition, to reach this realistic range, the value of the diffusion coefficient (*D*) of 1.171 $cm^2 \ s^{-1}$ was also reduced by a factor of four (*D* =

0.2975 $cm^2 s^{-1}$). The CV of the TP06 model is slightly slower, ranging from 0.62 to 0.65 m/s. The maximum conduction velocity values for the modified ORd model are between 0.60 and 0.75 m/s; this agrees well with the range of 0.65-0.87 m/s obtained in human heart studies (Taggart et al. 2000; Nanthakumar et al. 2007). In summary, the $I_{Na}$ substitution in tissue entails a growth in maximum CV to almost double its original value in the ORd model to provide a realistic CV.
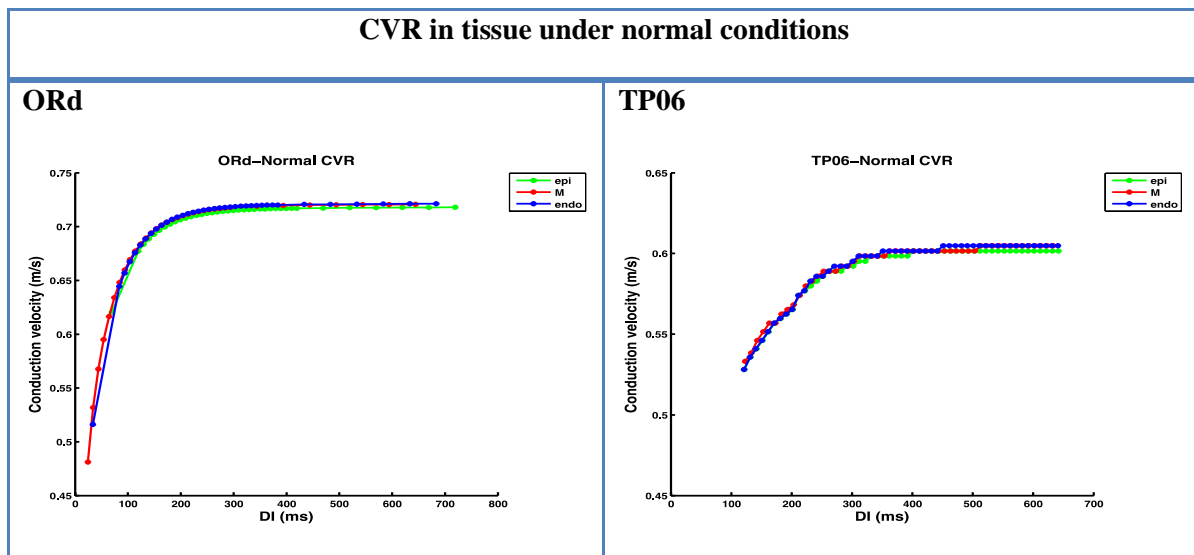


**Figure 6.4. CVR computed in a narrow strand of uniform tissue for TP06 and ORd models for epicardial (green), endocardial (blue), and mid-myocardial (red) cells. With the $I_{Na}$ substitution from TP06 model to ORd model and using a diffusion coefficient of 1.171 $cm^2 \ s^{-1}$ (TP06) and 0.2975 $cm^2 s^{-1}$ (ORd) to match the maximum CV with the range of 0.71-0.74 m/s**

## 6.4 Discussion

This study investigated the dynamic behaviour of two recent models of human ventricular myocytes (TP06 and ORd) under normal conditions. The model properties are compared with available observations, although the restitution of APD and CV in human ventricles has not yet been fully considered. Firstly, the influence of trans-mural heterogeneity on the propagation of normal beats during pacing at cycle length of 1000ms in an isotropic virtual tissue was examined. AP propagation was simulated in a narrow strand of tissue with dimensions of 0.75 × 25 mm of ventricular wall. The AP morphologies of epicardial, mid-

myocardial, and endocardial tissue layers for both the TP06 and the ORd models are shown in Figure 6.1. The ORd AP repolarization rate in this plot is more than for the TP06 model.

In spite of the limited human tissue experimental data on rate adaptation and restitution of APD, an attempt is made to compare the dynamic behaviour of these models to determine whether wave break and re-entry are achieved during ventricular arrhythmias. The restitution hypothesis is a very widely examined assumption for ventricular fibrillation (VF). The dynamic behaviour of APD has been presented in theoretical, experimental and computational studies as a main factor to determine wave front stability (Clayton & Taggart 2005). The dynamic behaviour of APD and CV are compared in Figures 6.2 and 6.4. Restitution curves were obtained by using the S1-S2 restitution protocol at a basic cycle length of 1000 ms. It is important to measure the slope of restitution curves because an APDR curve with a slope > 1 provides the main determinant of wave break. The S1-S2 restitution curve slopes in tissue for both the TP06 and ORd models are <1 on all DIs, with a maximum slope of 0.185 and 0.132 for the TP06 and ORd models respectively. Figure 6.5 shows a similar restitution curve shape; the largest slopes differ from a minimum value of 0.074 for the M-cell TP06 tissue model to a maximum value of 0.185 for the M-cell ORd tissue model. Nash et al. (Nash et al. 2006) presented maximum APDR curve slopes of 0.91 (S1-S2 protocol) in human epicardium. In addition, other early studies (Morgan et al. 1992; Taggart 2002) reported that the maximum slope of APDR curves in the human heart could be close to or a little more than 1.

The maximum slopes of the TP06 and ORd restitution curve in tissue computed by the S1-S2 protocol were significantly low: the TP06 model obtained a maximum slope of 0.135 for both epicardial and endocardial cell types, while maximum slopes for the ORd model were 0.132 for the epicardial cell type and 0.074 and 0.117 for the mid-myocardial and endocardial cell types respectively. Hence, neither model reaches a maximum restitution curve slope in tissue close to experimentally measured values. In Figure 6.4, CVR curves obtained for the TP06 and ORd tissue model are also shown. It was not possible to achieve reliable CV for the ORd model because of the limitation of its sodium channel formulation. Thus, TP06 $I_{Na^+}$ was substituted to the ORd model to provide an accurate CV. The primary effect of substitution of $I_{Na^+}$ in tissue is an increment in maximum CV to almost double its original value. The CVR curve in both the TP06 and ORd models has a very small slope (Max slope of CVR curves is 0.0002 and 0.0001 for TP06 and ORd tissue models respectively). Both TP06 and ORd

models demonstrate maximum restitution curve slope values lower than those reported from experimental measurements.



**Max slope of APDR Curves**

| Tissue model/cell type | epi | M | endo |
| --- | --- | --- | --- |
| TP06 | 0.135 | 0.185 | 0.135 |
| ORd | 0.132 | 0.074 | 0.117 |
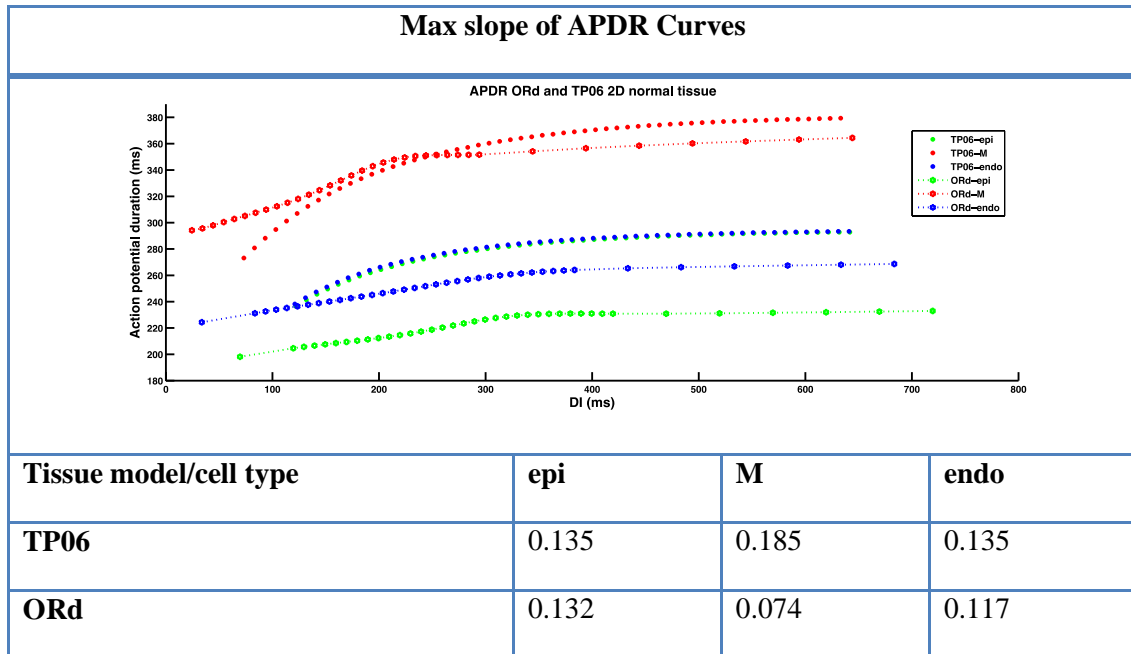
**Figure 6.5. Comparison of maximum slope of TP06 and ORd APDR curves for endocardial, mid-myocardial, and epicardial ventricular tissue layers under normal conditions.**

As for example, Cherry and Fenton (2004) showed, APDP steep slope may not be the sole mechanism to generate alternans in cardiac tissue. Other potential alternans mechanisms in cardiac tissue have been proposed, such as tissue heterogeneities; memory effects even with APD restitution slope >1; alternans in intracellular $Ca^{2+}$ concentration; and ischaemia despite the APD restitution curve flattening in ischaemic tissue (Cherry & Fenton 2004). The effect of ischaemia on dynamic behaviour of these two human models will be determined in Chapters 7-9.

# 7 Electrophysiological Influences of ATP Sensitive Potassium Current on the Dynamic Behaviour of Simulated Human Ventricular Tissue

*Activation of the ATP-sensitive $K^+$ ($K_{ATP}$) channels is very likely accountable for the reduction in action potential duration observed in cardiac cells where $[ATP]_i$ depletion is caused by hypoxia (Wilde et al. 1990). The dynamic behaviour of two human ventricular cell models, the TP06 and ORd models, have been studied quantitatively in 2-D tissue structures and the obtained properties compared with different $I_{K,ATP}$ models and with existing experimental and clinical data.*

*The aim was to demonstrate the effect of different $I_{K,ATP}$ models based on either animal or human data to examine how effective they would be for cardiac tissue studies under Anoxia/ischaemic conditions.*

## 7.1 Introduction

Different formulations of $I_{K,ATP}$ were compared to characterise the effect of hypoxia on cardiac cell electrophysiology in the two cell models in Chapter Five. The quantitative effects of three $I_{K(ATP)}$ models based on animal data, and one $I_{K(ATP)}$ model based on human data were assessed. For this purpose, first, the I-V dependence of each model without the conditions of elevated $[K^+]_0$ was computed in Chapter Five. In this chapter, the electrophysiological properties of each model $I_{K,ATP}$ are studied.

In this chapter, four simple Hill-type formulations of $I_{K,ATP}$ are tested (Shaw & Rudy 1997; Ferrero et al. 1996; Matsuoka et al. 2003; Kazbanov et al. 2014) to simulate the effects of changes in intracellular ATP level on electrophysiological tissue models.

**Aim and general outline**

This chapter examines how different $I_{K,ATP}$ models contribute to our understanding of the dynamic behaviour of the electrical activity of cardiac tissue during hypoxia/ischaemia. The aim was to test which $I_{K,ATP}$ model with small variations in [ATP]$_i$ has greatest effect. Electrophysiological aspects of $I_{K,ATP}$ changes are explored using two 2-D monodomain tissue models. Further details of arrhythmias related to two main components of ischaemia (hyperkalaemia and hypoxia) are considered in a 2-D and 3-D tissue model in Chapter Eight.

The first section of this chapter describes briefly the main changes in action potential morphology of two tissue models subjected to anoxia/ischaemia using four different $I_{K,ATP}$ formulations. The second section describes the major effects of $I_{K,ATP}$ changes on action potential duration restitution (APDR) and conduction velocity restitution (CVR) and compares how these changes result from each $I_{K,ATP}$ formulation. In the last section of this chapter, the role of the ATP sensitive potassium current on the dynamic behaviour of re-entry spiral waves in 2-D tissue models is considered.

**Objective**

In this chapter, two human ventricular cell models are used, the Ten Tusscher Panfilov 2006 (TP06) (Ten Tusscher & Panfilov 2006) and O'Hara-Rudy dynamic (ORd) (O'Hara et al. 2011). Three types of cells (epi, M and endo) are examined, with modification of the four different models of $K_{ATP}$ current to simulate anoxia/ischaemia. These are incorporated into 2-

D tissue models to assign restitution properties of APD and CV and to examine the dynamic behaviour of spiral wave re-entry. This allowed quantitative study of the impact of various $I_{K,ATP}$ formulations on tissue electrical activity.

## 7.2 Methods

**Simulated ischaemia in cell models**

The Ten Tusscher Panfilov 2006 (TP06) (Ten Tusscher & Panfilov 2006) and O'Hara-Rudy dynamic (ORd) (O'Hara et al. 2011) models were used to represent human cellular electrophysiology. The older TP06 model is based on a mixture of human and animal data, whereas the ORd model is a detailed model for human cells that has been developed recently from human experimental data. The parameters for epicardial, mid-myocardial and endocardial cells were used. The effects of $[ATP]_i$ depletion were investigated with four different formulations of the ATP activated $K^+$ current $I_{K,ATP}$ in this chapter. The current-voltage dependency of these formulations is described in detail in Chapter Five. The three different formulations of the ATP activated $K^+$ current $I_{K,ATP}$ (Shaw & Rudy 1997; Ferrero et al. 1996; Matsuoka et al. 2003) were based on animal data, and one formulation (Kazbanov et al. 2014) was based on in vitro experiments in human ventricular myocytes. The $I_{K,ATP}$ formulations were:

1. The Ferrero et al. (Ferrero et al. 1996) formulation was implemented as described by Equation 7.1, with modifications from the original description in Chapter Five:

$$I_{K,ATP} = g_0 \left(\frac{[K^+]_0}{5.4}\right)^{0.24} f_{ATP}(V_m - E_k) \quad (7.1)$$

2. The formulation described by Shaw and Rudy (Shaw & Rudy 1997):

$$I_{K,ATP} = G_{K,ATP} \frac{1}{1+\left(\frac{[ATP]_i}{K_{0.5}}\right)^H} \left(\frac{[K^+]_0}{5.4}\right)^n (V_m - E_k) \quad (7.2)$$

3. The formulation described by Matsuoka et al. (Matsuoka et al. 2003) was implemented as:

$$I_{K,ATP} = G_{K,ATP} \frac{0.8}{1+\left(\frac{[ATP]_i}{0.1}\right)^2} \left(\frac{[K^+]_0}{6.019\times10^6}\right)^{0.24} (V_m - E_k) \quad (7.3)$$

4. The formulation described by Kazbahnov et al. (Kazbanov et al. 2014) was implemented as:

$$I_{K,ATP} = Af_{ATP}\left(\frac{[K^+]_0}{5.4}\right)^{0.3}\frac{1}{40+3.5e^{0.025V}}(V_m - E_k) \quad (7.4)$$

In each of these formulations, $V_m$ is the membrane voltage and $E_k$ indicates reversal potential for potassium ions. The maximum conductance of $I_{K,ATP}$ ($G_{K,ATP}$) was fixed at $3.9\ mS\ mm^{-2}$ and $0.17674\ mS\ mm^{-2}$ for the Shaw and Rudy and Matsuoka et al. formulations respectively. A Hill coefficient (H) and n was set at 2.0 and 0.24 respectively (Nichols et al. 1991). $g_0$ is the maximum channel conductance in the absence of $Na^+$, $Mg^{2+}$ and ATP, set at $2.01\ mS\ mm^{-2}$ for epi cell type (Clayton et al. 2011) . $f_{ATP}$, the fraction of opened channels, was set between 0% for a non-ischaemic condition and 0.4% for ischaemia (Kazbanov et al. 2014). The scaling coefficient A was fitted to the formulation with a value of 155 (Kazbanov et al. 2014). The ischaemic input parameter values are sumerised in Table 7.1.

**Table 7.1. Input parameters used in this chapter to simulate ischaemia**

| Simulated model | Parameters | | | | $I_{K,ATP}$ models |
|---|---|---|---|---|---|
| | $[ATP]_i$ (mM) | $K_{0.5}$ (mM) | $f_{ATP}$ (%) | $[K^+]_o$ (mM) | |
| **Non-ischaemic** | 6.8 | 0.042 | | 5.4 | Ferrero et al. 1996 |
| **Ischaemic** | 6.0 | 0.117 | 0-0.5 | 6.0 | Shaw & Rudy 1997 |
| | 5.0 | 0.212 | | 7.0 | Matsuoka et al. 2003 |
| | 4.0 | 0.306 | | 8.0 | Kazbanov et al. 2014 |

**Numerical approaches in tissue models**

To study dynamic restitution properties and investigate re-entry, each $I_{K,ATP}$ model was embedded in a 2D monodomain tissue model with an isotropic diffusion coefficient of 1.171 $cm^2\ s^{-1}$ (TP06 model) and $0.2975\ cm^2 s^{-1}$ (ORd model). Membrane capacitance was set to 1 µF $cm^{-2}$. An explicit finite difference approach with a time step of 0.005 ms and a fixed space step of 0.2 mm was used to solve these models (Table 7.2). The gradient of membrane voltage was set to zero at boundary condition to show no-flux boundary conditions were applied at each edge.

**Table 7.2. Human cardiac ventricular cell model basic parameters used in this chapter**

| Cell Model | Stimulus | | Threshold (mV) | Diffusion ($cm^2$/ms) | Space steps (mm) | Time steps (ms) |
|---|---|---|---|---|---|---|
| | Amplitude (µA/µF) | Duration (ms) | | | | |
| TP06 | -52 | 1.0 | -65 | 0.0012 | 0.02 | 0.2 |
| ORd | -80 | 1.0 | -75 | 0.0003 | 0.02 | 0.005 |

## Initial condition of the model

To study the influence of each $I_{K,ATP}$ formulations on the properties of the tissue model, we measured how decreased $[ATP]_i$ affected APD and CV restitution. Measurements were made from a small slab of tissue of $3 \times 100$ grid points ($0.75 \times 25$ mm), with an S1S2 stimulus protocol with S1 CL of 1000 ms and S2 CL that changed between 1000 ms and 300 ms. A stimulus current of -52.0 (TP06 model) and -80 $pA\ pF^{-1}$ (ORd model) was used to deliver each stimulus at a small slab of tissue for 1ms. The 10 S1-1S2 stimulus was delivered with a CL of 1000 ms. The tissue was returned to its initial state after each S2 before the next S1S2 cycle.

## Simulated re-entry in a tissue model

The tissue simulations were run with a single re-entrant wave as an initial condition to examine the effects of each $I_{K,ATP}$ formulation on re-entry. A 2D tissue slab of $200 \times 200$ ($50 \times 50$ mm) grid points was used for these simulations. Re-entry was initiated in a 2D isotropic and homogeneous tissue slab by applying an Archimedean spiral to the tissue (Clayton & Holden 2002a; Clayton & Holden 2002b). These computational modelling process and parameter values are summarised in Table 7.3.

**Table 7.3. The tissue simulations settings**

| Geometry | Tissue size (mm) | Dimensions (grid points) | Simulation protocol |
|---|---|---|---|
| 2D (thin strip of tissue) | $0.75 \times 25$ | $3 \times 100$ | A standard 10 S1S2 stimulus TP06= -52.0 $pA\ pF^{-1}$ ORd= -80 $pA\ pF^{-1}$ |
| 2D (tissue slab) | $50 \times 50$ | $200 \times 200$ | a single re-entrant wave as an initial condition (applying an Archimedian spiral to the tissue) |

## 7.3 Results

### 7.3.1 AP Morphology Using Different $I_{K(ATP)}$ Formulations

Action potential characteristics of selection of $I_{K,ATP}$ models in two 2D monodomain tissue models are demonstrated in this section. Figure 7.1 shows the same AP morphology for all $I_{K(ATP)}$ formulations using $[ATP]_i$ with a normal value of 6.8 mM in all three cell (epi, M and endo) types. However, Figure 7.2 shows AP variations under ischaemic condition ($[ATP]_i =$ 4.0 mM) in each model. APD is observed to reduce in all three cell types. Figure 7.2 also supports the results in Chapter Five in that the variations in $[ATP]_i$ in the Matsuoka model were very small, reducing by 40 times ($[ATP]_i = 0.1$ mM) less than other $I_{K,ATP}$ models in the tissue model. Furthermore, $[ATP]_i$ changes in the original Matsuoka cell model are explored (figure 6.3). Figure 7.3 supports the results in that $[ATP]_i$ changes are negligible in the original Matsuoka cell model. Further details are presented of embedding Matsuoka $I_{K,ATP}$ formulation in tissue models by reduced $[ATP]_i$, from normal value of 6.8 mM to 6.0, 5.0, 4.0, 2.0 and 0.1 mM (Figure 7.4). The changes in AP shape are very small in both tissue models. Figure 7.2 also shows that the effects of $[ATP]_i$ reduction on AP shapes are slightly different in the TP06 and ORd models. APD reduction is greater with the Shaw and Rudy $I_{K,ATP}$ formulation in comparison to the Ferrero formulation in the TP06 model. However, these changes are inverted in the ORd model (except M cell type). In both tissue models, the Kazbahnov $I_{K,ATP}$ model has the smallest APD in comparison to the other $I_{K,ATP}$ models.
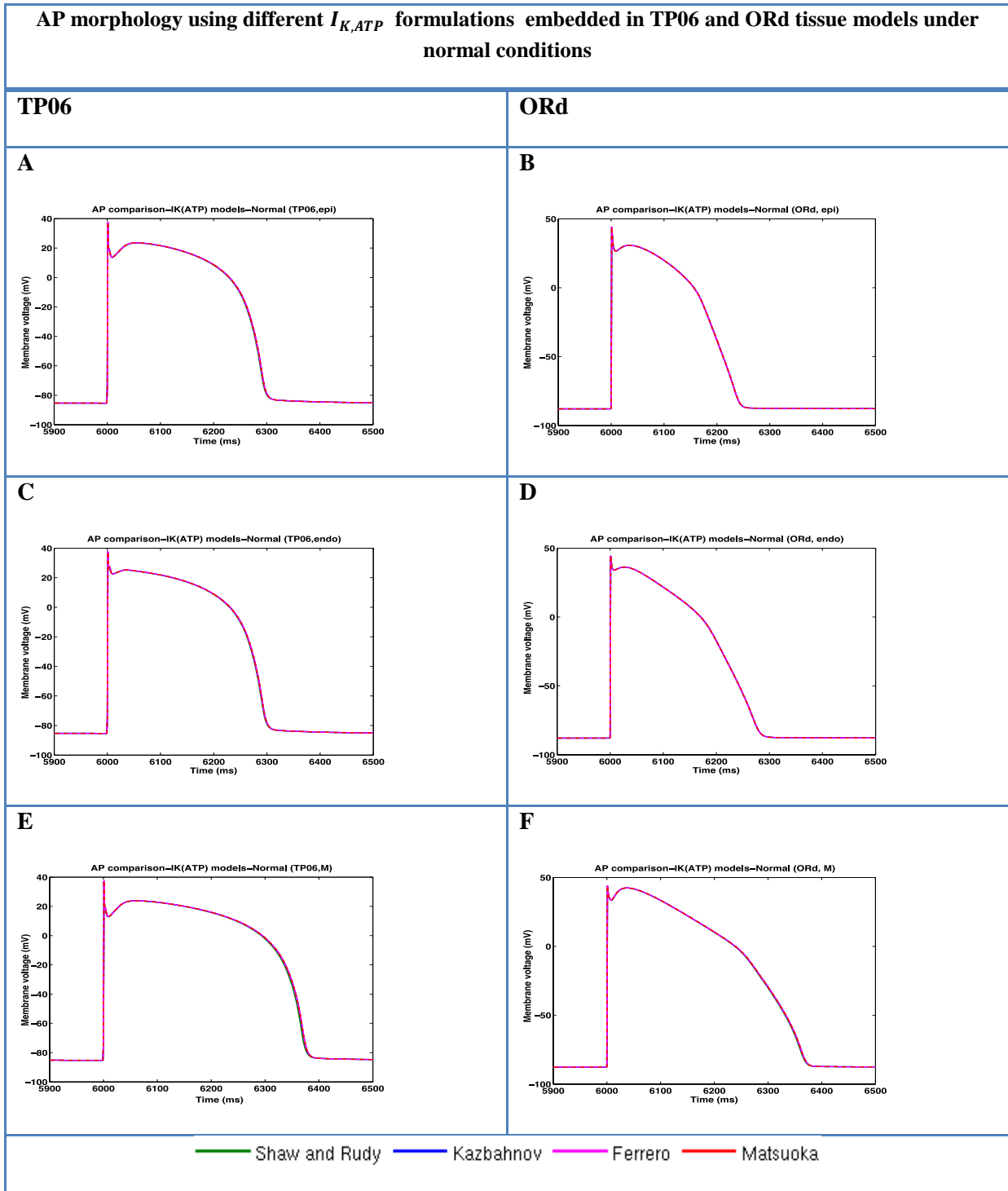
**Figure 7.1.** AP morphology for different $I_{K(ATP)}$ formulations with normal $[ATP]_i$ of 6.8 mM: A and B, represent action potential comparison for Shaw and Rudy, Kazbahnov, Ferrero and Matsuoka models in TP06 and ORd epi models respectively in a 2-D tissue model. C and D make the same comparison, but represent endo cell type in TP06 and ORd models respectively. E and F represent action potential comparison for M cell type in TP06 and ORd respectively with different $I_{K(ATP)}$ formulations.

| TP06 | ORd |
|---|---|
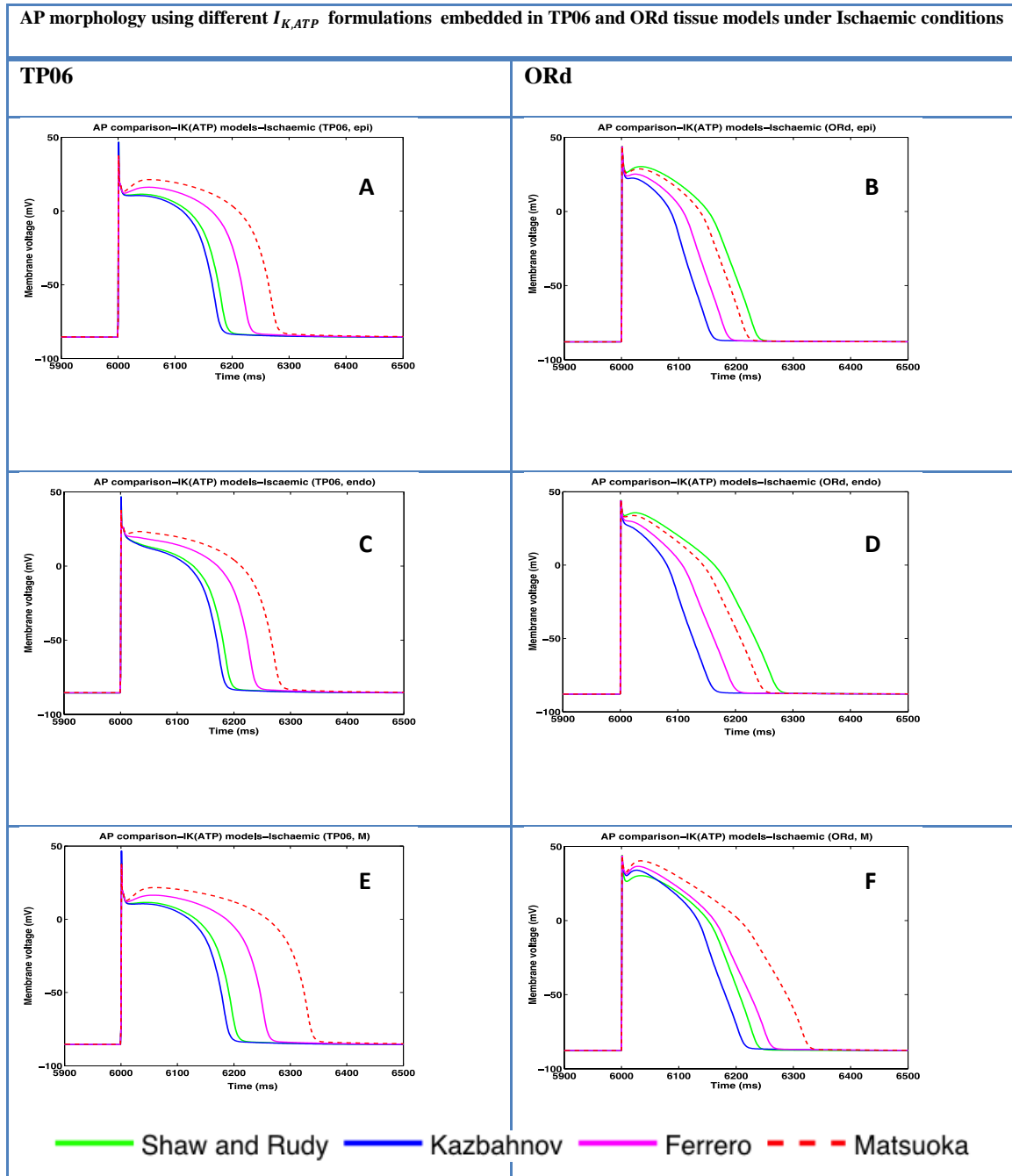


Figure 7.2. AP morphology for different $I_{K(ATP)}$ formulations, with $[ATP]_i$ decreased to 4.0 mM ($[ATP]_i$= 0.1 mM for Matsuoka model). A and B compare action potential for the Shaw and Rudy, Kazbahnov, Ferrero and Matsuoka models in the TP06 and ORd epi models respectively in a 2-D tissue model under ischaemic condition (reduction of $[ATP]_i$ to 4.0 mM). A shows the Matsuoka model has the least change in AP under ischaemic condition in the TP06 model; however, in B, Shaw and Rudy has the least change in AP with reduction of $[ATP]_i$ for the ORd model. C and E show the effect presented in Figure A in TP06 for endo and M cells respectively. D and F show changes in AP when $[ATP]_i$ decreased to 4.0 mM in the ORd model for endo and M cells respectively. Figure F shows the same change as the TP06 model presented for the M cell in E; in both models, the Matsuoka model has the least changes in comparison with the others.
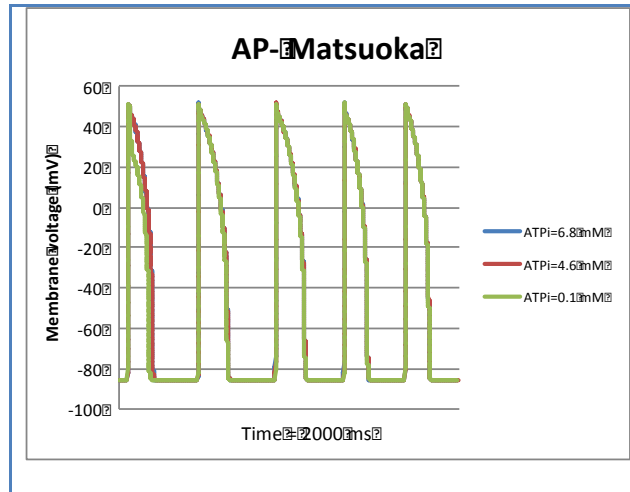
**Figure 7.3. AP morphology with different $[ATP]_i$ in the Matsuoka cell model from CellML**
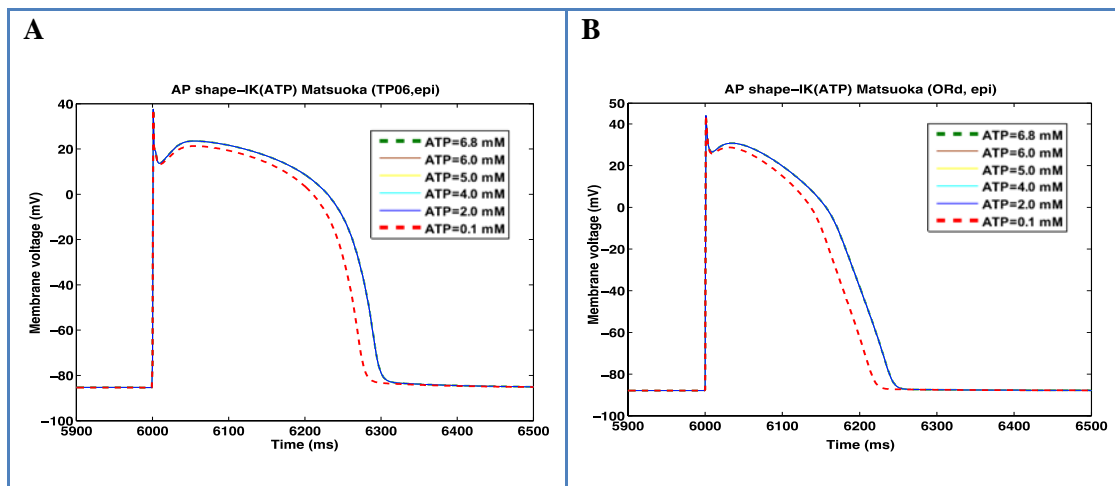


**Figure 7.4. AP morphology with different $[ATP]_i$ in the Matsuoka model embedded in the TP06 and ORd models**

### 7.3.2 Influence of $I_{K,ATP}$ on Action Potential Duration and Conduction Velocity

Figure 7.5 shows the effect of each $I_{K,ATP}$ formulation on APDR curves for each cell type in the TP06 and ORd tissue models. This figure shows the differences between each cell type under normal condition ($[ATP]_i$= 6.8 mM, $f_{ATP}$=0%, and $[K^+]_0$=5.4 mM) and ischaemic condition ($[ATP]_i$= 4.0 mM, $f_{ATP}$=0.4% and $[K^+]_0$=5.4 mM) for both tissue models. Due to the very small effect of the Matsuoka $I_{K,ATP}$ model on AP propagation (presented in the last section), this model was removed from the remaining simulations. Figure 7.5 (A, B and C) show that the effects of all $I_{K,ATP}$ models on APDR are the same in both tissue models. APDR differences between TP06 and ORd models are highlighted in the normal tissue results. The distances between APDR curves are noticeable in the epi cell type of these two

159

tissue models; for instance, the max APD at 950ms is 285.5ms (TP06) and 224ms (ORd). However, APDR changes are different in the ischaemic section of this figure. Furthermore, for better understanding of these changes APDR variations were compared under different $I_{K,ATP}$ activations in the TP06 and ORd tissue model in Figure 7.6. This figure displays significant decline for all $I_{K,ATP}$ activated models. However, this trend is less in the ORd model when the Shaw and Rudy $I_{K,ATP}$ formulation is used for both epi and endo cell types (Figure 7.6 A and B). The reduction in APD in the Shaw and Rudy model becomes greater for M cell type in the ORd model (Figure 7.6 C). Conversely, APD declines uniformly for all cell types in the TP06 model. Figure 7.6 also shows that the Kazbahnov APDR curve displays the biggest decrease in comparison to the Shaw and Rudy and Ferrero formulations in both tissue models.
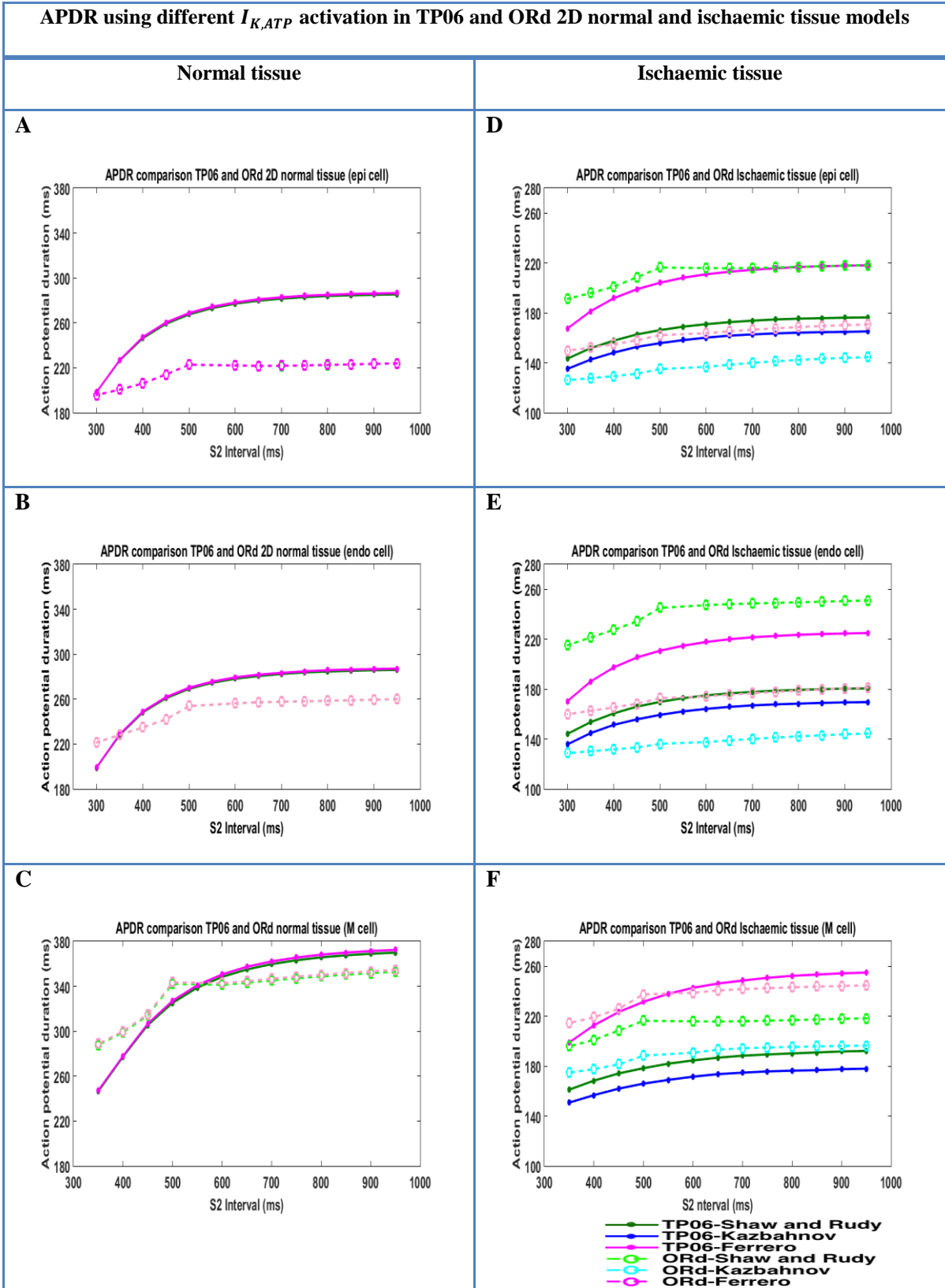
**Figure 7.5. APDR for different $I_{K(ATP)}$ formulations, with normal $[ATP]_i$ of 6.8 mM and with $[ATP]_i$ decreased to 4.0 mM. The dashed line with circle marker shows the ORd model and the solid line with full circle marker illustrates the TP06 model. Green, blue and pink colours indicate the Shaw and Rudy, Kazbahnov and Ferrero models respectively. The legend for all graphs is presented in F.**
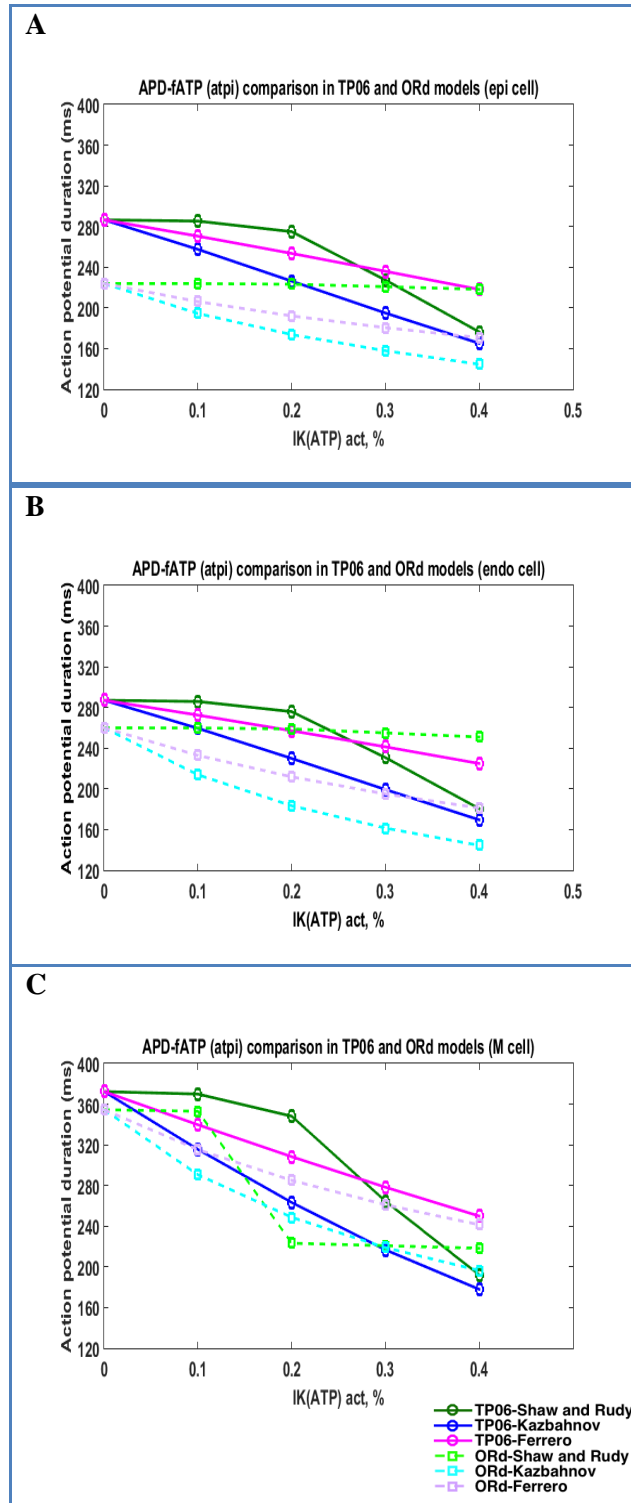
**Figure 7.6. Changes in action potential duration under different $I_{K,ATP}$ activation in TP06 and ORd tissue models: the dashed line with square marker shows the ORd model and the solid line with circle marker illustrates the TP06 model. Green, blue and pink colours indicate the Shaw and Rudy, Kazbahnov and Ferrero models respectively. The legend for all graphs is presented in C.**
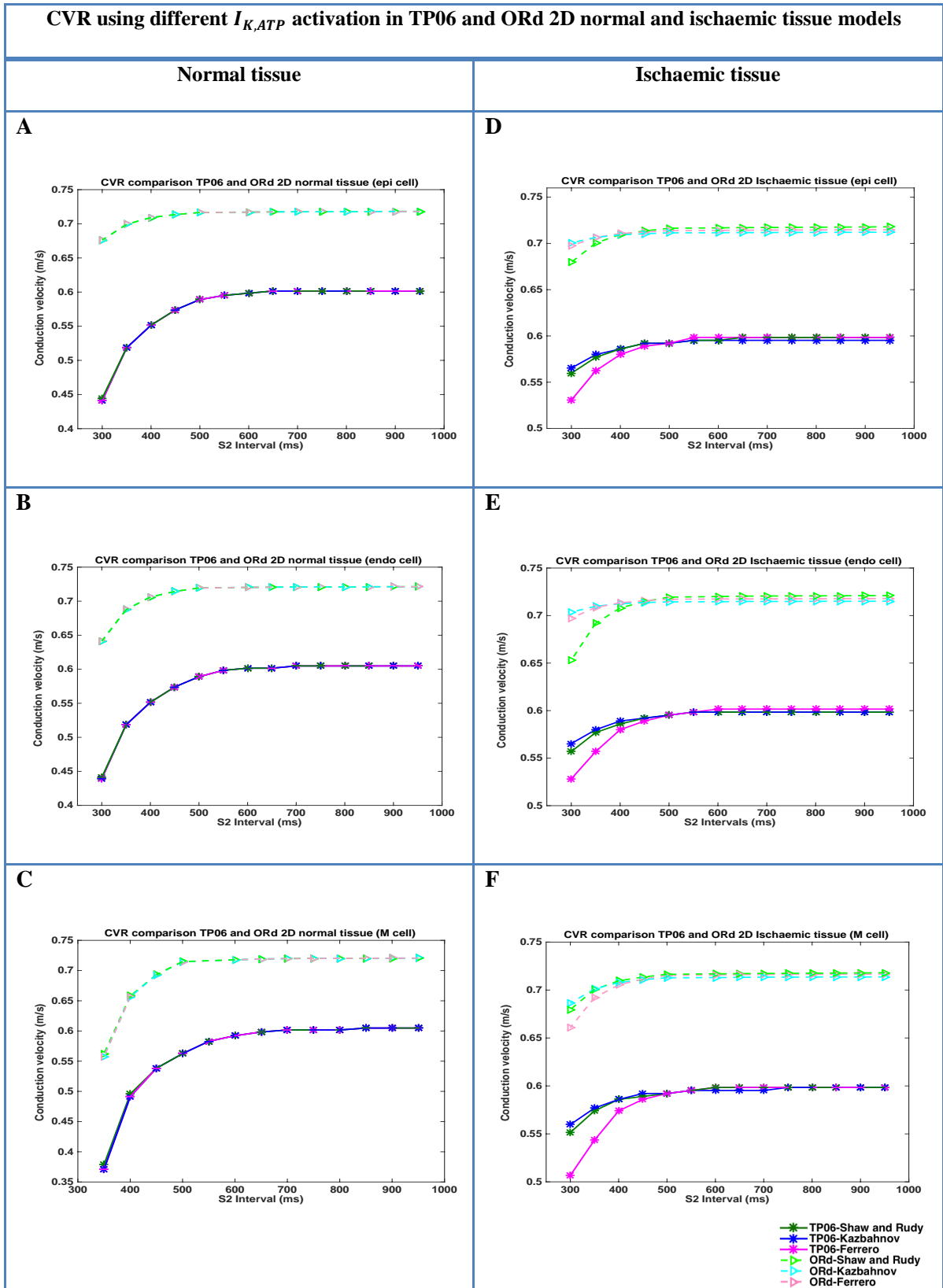
**Figure 7.7. CVR for different $I_{K(ATP)}$ formulations, with normal $[ATP]_i$ of 6.8 mM and with $[ATP]_i$ decreased to 4.0 mM: the dashed line with triangle marker shows the ORd model, and the solid line with asterisk marker illustrates the TP06 model. Green, blue and pink colours indicate Shaw and Rudy, Kazbahnov and Ferrero models respectively. The legend for all graphs is presented in F.**

The results also indicate that $I_{K,ATP}$ activation (reduced $[ATP]_i$ ) acts to shorten APD and flatten APD restitution. The TP06 model APD restitution was steeper in comparison to the ORd model (Figure 7.5). Although reduced $[ATP]_i$ shortened APD and flattened the APD restitution curve, it had little effect on CV restitution (Figure 7.7) for both tissue models.

### 7.3.3 Characteristic of the ATP Sensitive Potassium Current on the Dynamic Behaviour of Re-entry in the 2-D Tissue Model

In this section, spiral re-entry behaviour in non-ischaemic and ischaemic (reduction of $[ATP]_i$) cardiac tissue is simulated. For this simulation, a single re-entrant wave was used as the initial condition. Figure 7.8 shows the dynamics and stability of spiral waves re-entrant in 2-D homogeneous and isotropic tissue for both TP06 and ORd tissue models. The results showed stable re-entry with an average period of 230 ms (ORd) and 245 ms (TP06) in normal tissue related to a dominant frequency of 4.3 and 4.08 Hz. These values were in agreement with the value of the mean dominant frequency obtained in clinical data (Figure 7.10) by Bradley et al. (2011). The TP06 and ORd models with different levels of $I_{K(ATP)}$ activations display stable re-entry with no continued break up of spiral waves. The average period of re-entry for various $I_{K(ATP)}$ activations is compared for different $I_{K(ATP)}$ formulations in Figure 7.9. Reduced intracellular $[ATP]_i$ decreased the period of re-entry in all $I_{K(ATP)}$ formulations. These results were similar in both tissue models.

Increasing the stability of re-entry in ischaemic tissue would be expected from the flattening of APD restitution resulting from reduced $[ATP]_i$. This theory will be tested by simulating the effect of reduced $[ATP]_i$ and elevated $[K^+]_0$ on multiple wavelet re-entry in Chapter Eight.
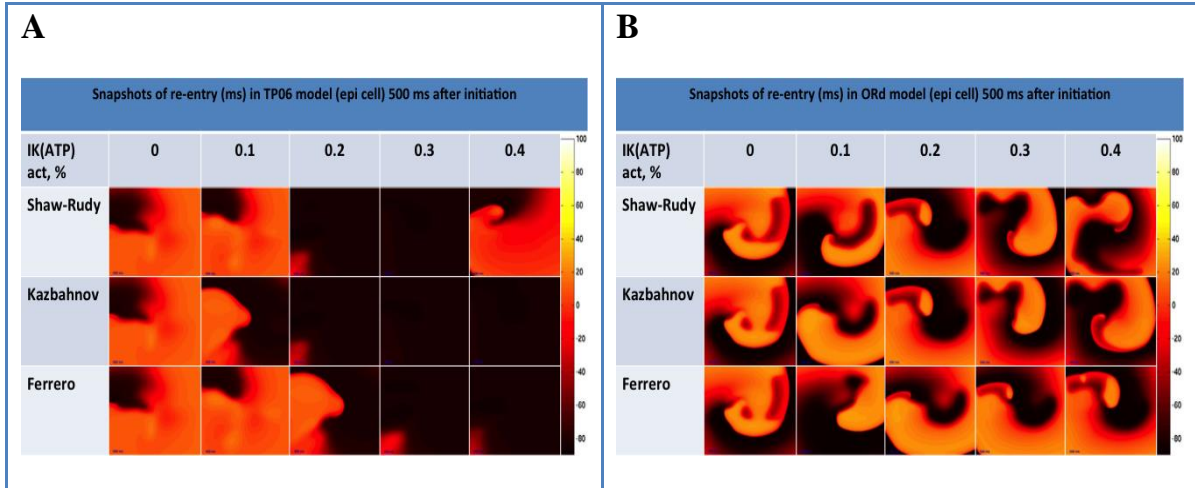
**Figure 7.8. Re-entry (ms) frames in TP06 and ORd models with various $I_{K(ATP)}$ activations, 500 ms after initiation. Colour intensity shows membrane voltage, with brighter colours indicating more depolarised tissue.**
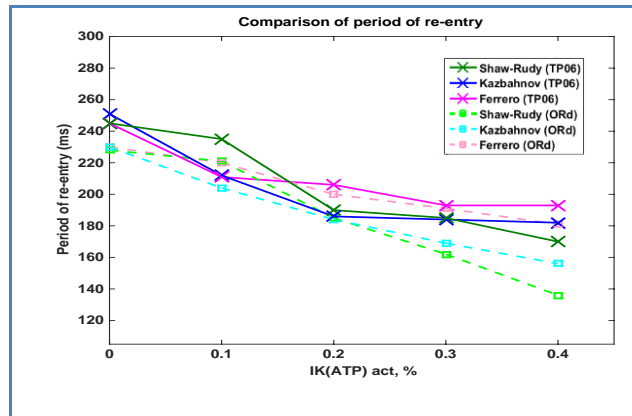


**Figure 7.9. Comparison of the average period of spiral wave re-entry (ms) using epicardial cells in TP06 and ORd models with different $I_{K(ATP)}$ formulations: the dashed line with square marker shows the ORd model and the solid line with cross marker illustrates the TP06 model. Green, blue and pink colours indicate Shaw and Rudy, Kazbahnov and Ferrero models respectively.**
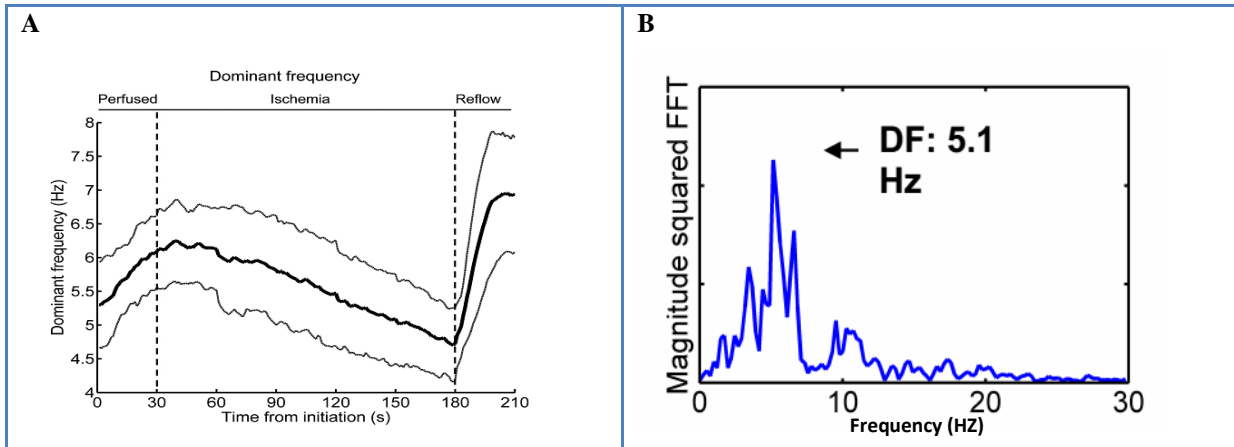
**Figure 7.10. Mean Dominant frequency (DF) data from 10 patients taken from an experimental study by Bradley et al. (2011) during global ischaemia (A). This figure shows the effect of ischaemia on VF with an initial increase in DF followed by a stable fall. The initial value of DF is 4.5 in normal tissue. B: Measurement of DF ischemic VF (Figure S5 from Bradley et al. (2011)). DF is the frequency of the dominant peak as shown in B.**

## 7.4 Discussion

The characteristics of different formulations of $I_{K,ATP}$ in two human ventricular cell models were considered in this chapter. Activation of the Matsuoka et al. model, with the lowest slope in I-V curve, had the smallest effect on AP shape (Figures 7.2, 7.3 and 7.4) and produced a small change in APD in comparison to the other models, even with the lowest levels of $[ATP]_i$=0.1 mM. Results here were consistent with outcomes from simulations applying the Matsuoka et al. $I_{K(ATP)}$ formulation for different levels of $[ATP]_i$ by Nickerson & Buist (2008). For this reason, this model was omitted from the restitution studies and spiral wave simulations.

The aim was to distinguish the electrophysiological properties of the different $I_{K(ATP)}$ models; however, a cause and effect relationship between the metabolic and ionic conditions of ischaemia and the ischaemic electrical variations has been shown in the complex interrelationships among events (acidosis, hyperkalaemia). The characteristic of the action potential shape and restitution properties of APD and CV are applied to clarify several mechanisms of spiral wave breakup in cardiac tissue (Fenton et al. 2002). The idea was tested that $I_{K,ATP}$ channel activation largely accounts for the changes in APD, resulting from the activation of any outward current or the decline of any inward current (Ferrero et al. 1996). The results illustrated that a fall in $[ATP]_i$ is responsible for action potential shortening

through activation of $I_{K,ATP}$ channels (Abbasi & Clayton 2014); this was similar to the results presented in experimental studies (Weiss et al. 1992; Nichols et al. 1991; Faivre & Findlay 1990). Our tissue models mimic action potential durations and a maximum conduction velocity value close to values obtained experimentally accompanied by clinically relevant dominant frequencies. Figure 7.9 shows that reduced intracellular $[ATP]_i$ decreased the period of re-entry to between (193, 181 and 170 ms (TP06)) and (181, 156 and 136 ms (ORd)) for Ferrero, Kazbahnov and Shaw-Rudy models respectively. The results show that unchanged CV resulting from decreased $[ATP]_i$ acts to decrease the period of re-entry and hence to increase activation rate. The results show that decreased $[ATP]_i$, the cause of unchanged CV, acts to reduce the period of spiral wave re-entry and thus to augment activation rate.

Despite different formulations of $I_{K(ATP)}$, depending on data from either animal or human ventricular myocytes, the dynamic behaviour and the response to simulated ischaemia in these models were similar (Abbasi & Clayton 2014). Although, the results support the key role of $I_{K(ATP)}$ in the reduction of APD, and the flattening of APD restitution as intracellular ATP concentration is reduced during acute ischaemia, the hypothetical simulations are not a comprehensive representation of all ischaemic conditions. Therefore, the most appropriate $I_{K,ATP}$ model cannot be suggested for use in simulations of ischaemia because several factors are not included; either their influences need more experimental data or their existence does not pertain during ischaemia. For example, the effect of acidosis on the cardiac potassium current is neglected in these formulations. The possibility of a role for intracellular calcium, the rise in $[Ca^{2+}]_i$ being concomitant with the secondary phase of $[K^+]_0$ rise (Shaw & Rudy 1997) and fast reduction of $[ATP]_i$, to electrical abnormalities associated with ischaemia is not included (Abbasi & Clayton 2014).

Transmural $I_{K,ATP}$ heterogeneity (the effects of endocardial and epicardial $I_{K,ATP}$ levels) is an important factor in activation rate gradient during early ventricular fibrillation. Furthermore, transient $I_{K,ATP}$ blockade during VF was shown to terminate arrhythmias (Boyle et al. 2013). The hypothesis that experimentally observed epicardial-to-endocardial activation rate gradient (ΔAR) in pigs must be supported by a relative abundance of $I_{K,ATP}$ expression on the epicardium was tested by (Boyle et al. 2013), who investigated the effects of endocardial and epicardial $I_{K,ATP}$ levels. They tested the idea that relatively long APs in low-$I_{K,ATP}$ regions

led to local conduction block of trans-mural propagation, and that the highest activation rates (AR) occurred overall in models with high $I_{K,ATP}$ throughout the heart. Farid et al. (2011) showed that cycle length is smaller in the endocardium in comparison to the epicardium, while activation rate is bigger in the endocardium in comparison to the epicardium in terms of ischaemic conditions (reduction of $[ATP]_i$). Boyle et al. (2013) tested the effect of $I_{K,ATP}$ levels by modulating the fraction of channels in the active state ($f_{ATP}$): low ($f_{ATP}$= 0.001%), medium ($f_{ATP}$ = 0.112%), and high ($f_{ATP}$ = 0.180%). They used these values to calculate restitution characteristics. Their results showed that for the low $I_{K,ATP}$, restitution characteristics were the same as in the unmodified model, whilst high $I_{K,ATP}$ had the shortest APs and the medium $I_{K,ATP}$ value showed that APD shortening was approximately 50% as severe as for high $I_{K,ATP}$. They presented a significant trans-mural ΔAR during VF with high epicardial $f_{ATP}$ and low endocardial $f_{ATP}$. They also showed global AR dropped abruptly and VF terminated when $I_{K,ATP}$ was blocked (Figure 7.12a); VF sustained without blockade of $I_{K,ATP}$. They conclude that differential $I_{K,ATP}$ across the ventricular wall is an important factor in activation rate gradients during VF.

Consequently, the role of $I_{K,ATP}$ as one of the ischaemic components in electrical heterogeneity will be examined in Chapter Eight. Finally, it was decided to apply the Shaw and Rudy $I_{K,ATP}$ formulation (Shaw & Rudy 1997) for the remaining ischaemic simulations in the next chapter, because this formulation was more effective than other $I_{K,ATP}$ models for the small variation in $[ATP]_i$ (Nickerson & Buist 2008; Clayton et al. 2011).

# 8 The Refractory Period and Post-Repolarization Refractoriness during Ischaemia

*The purpose of this chapter is to determine the phenomenon of post-repolarization refractoriness (PRR) during ischaemia in humans. Lengthening or shortening of the effective refractory period (ERP) are associated with Transmural ischaemia. The relation between ERP changes and action potential duration (APD) is considered in a 2D tissue model.*

## 8.1 Background information

Repolarisation changes are important for the creation of re-entrant arrhythmias (Coronel et al. 2012). The contribution of PRR to arrhythmogenesis during ischaemia may contribute to the maintenance of re-entry during VF (Coronel et al. 2012). The effect of ischaemia on ERP and PRR has been discussed in different experimental (Coronel 1994; Kuo et al. 1983) and theoretical studies (Faber & Rudy 2000; Burton & Cobbe 2001; Ferrero et al. 2003; Franz 2003). As discussed in section 2.5.3 of Chapter Two, these studies (Carmeliet 1999; Sutton et al. 2000; Faber & Rudy 2000; Burton & Cobbe 2001; Franz 2003; Ferrero et al. 2003; Ma & Wang 2007) examined the mechanism of arrhythmias during ischaemia by considering APD, measuring ERP and the relationship between APD and ERP. The aim of this chapter is to quantify the effect of ERP heterogeneities and the characterization of CV under ischaemic conditions and to explore the role of PRR phenomena and the initiation of re-entrant arrhythmia using computational models in ischaemia studies.

## 8.2 Method

**Cell model and simulated ischaemia**

Two human cardiac ventricular cell models, the TP06 (Ten Tusscher & Panfilov 2006) and ORd (O'Hara et al. 2011) models, were used to represent human cellular electrophysiology. Parameters for epicardial cells with modifications, which are described in detail in section 7.3 in Chapter Seven, were used to simulate a three-minute period of global ischaemia. The effects of elevated $[K^+]_o$ and and $[ATP]_i$ depletion were investigated. The Shaw and Rudy (Shaw & Rudy 1997) ATP activated $K^+$ current $I_{K,ATP}$ formulations were used. Ischaemic parameter values are summarised in Table 8.1 below.

**Table 8.1. Input parameters for ischaemia**

| Simulated model | Parameters | |
|---|---|---|
| | $[ATP]_i$ (mM) | $[K^+]_o$ (mM) |
| **Non-ischaemic** | 6.8 | 5.4 |
| **Ischaemic** | 6.0 | 6.0 |
| | 5.0 | 7.0 |
| | 4.0 | 8.0 |

**Tissue model and numerical approach**

All simulations were performed in a 2D monodomain model embedding the TP06 and ORd cell model described in detail in Chapter Seven (section 7.3) (see Ref: Clayton et al. 2011), with an isotropic diffusion coefficient of 1.171 $cm^2\ s^{-1}$ (TP06 model), and 0.2975 $cm^2 s^{-1}$ (ORd model). Membrane capacitance was set at 1 µF $cm^{-2}$. An explicit finite difference approach with a time step of 0.005 ms and a fixed space step of 0.2 mm was used to solve these models.

**Data analysis and dynamic properties of the model**

To examine the effects of the two main components of ischaemia on the tissue model, how $[K^+]_o$ accumulation and reduced $[ATP]_i$ affected APD, CV and ERP was measured. To make these measurements, a small slab of tissue of $3 \times 100$ grid points ($0.75 \times 25$ mm) was used, with an S1S2 stimulus protocol with S1 CL of 1000 ms and S2 CL that changed between 1000 ms and 250 ms. A stimulus current of -52.0 (TP06 model) and -80 $pA\ pF^{-1}$ (ORd model) was used to deliver each stimulus to the small slab of tissue for 1ms. The 10 S1-1S2 stimulus was delivered with a CL of 1000 ms. The tissue was returned to its initial state after each S2 before the next S1S2 cycle. In this thesis, all measurements of APD computed at 90% repolarization correspond to $APD_{90}$. CV was measured in the middle of the strand. To examine the effect of ischaemic components on re-entry, tissue simulations were run with an initial condition of a single re-entrant wave (all details of re-entry simulations are described in Chapters Eight and Nine, sections 8.2 and 9.2.). The ERP was determined for each extra stimulus (S1S2 interval) and the corresponding APD at 90% repolarization ($APD_{90}$), both during normal and ischaemia conditions. The APD is defined as the time between depolarization and the time of repolarization to -85 mV. ERP is the period of time after initiation of an AP in which a new action potential cannot be initiated. During this period, depolarization in the current cell has to refract back to AP resting phase before a new action potential can activate it. This happens because the fast sodium channels remain closed until the cell fully repolarizes. The ERP is associated to Phases 0, 1, 2, and 3 of the cardiac action potential cycle as the cell will not respond to a stimulus that comes from an adjacent cell. Nevertheless, if the stimulus is strong enough, a new depolarization could occur, and this can lead to arrhythmias. In this study, an extra-stimulus technique was used to take the ERP as the minimum S1S2 interval (greater than APD) (Sutton et al. 2000), demonstrated in

Figure 8.2. This could support a propagation AP along the strand (defined as having a plateau phase above -20 mV)(Sutton et al. 2000). The S1S2 interval (in ms) was specified as the interval between the latest S1(10th S1) and S2 (Figure 8.1). PRR (Figure 8.2) was defined as the differences between ERP and APD (Franz et al. 2014; Cabo 2015).
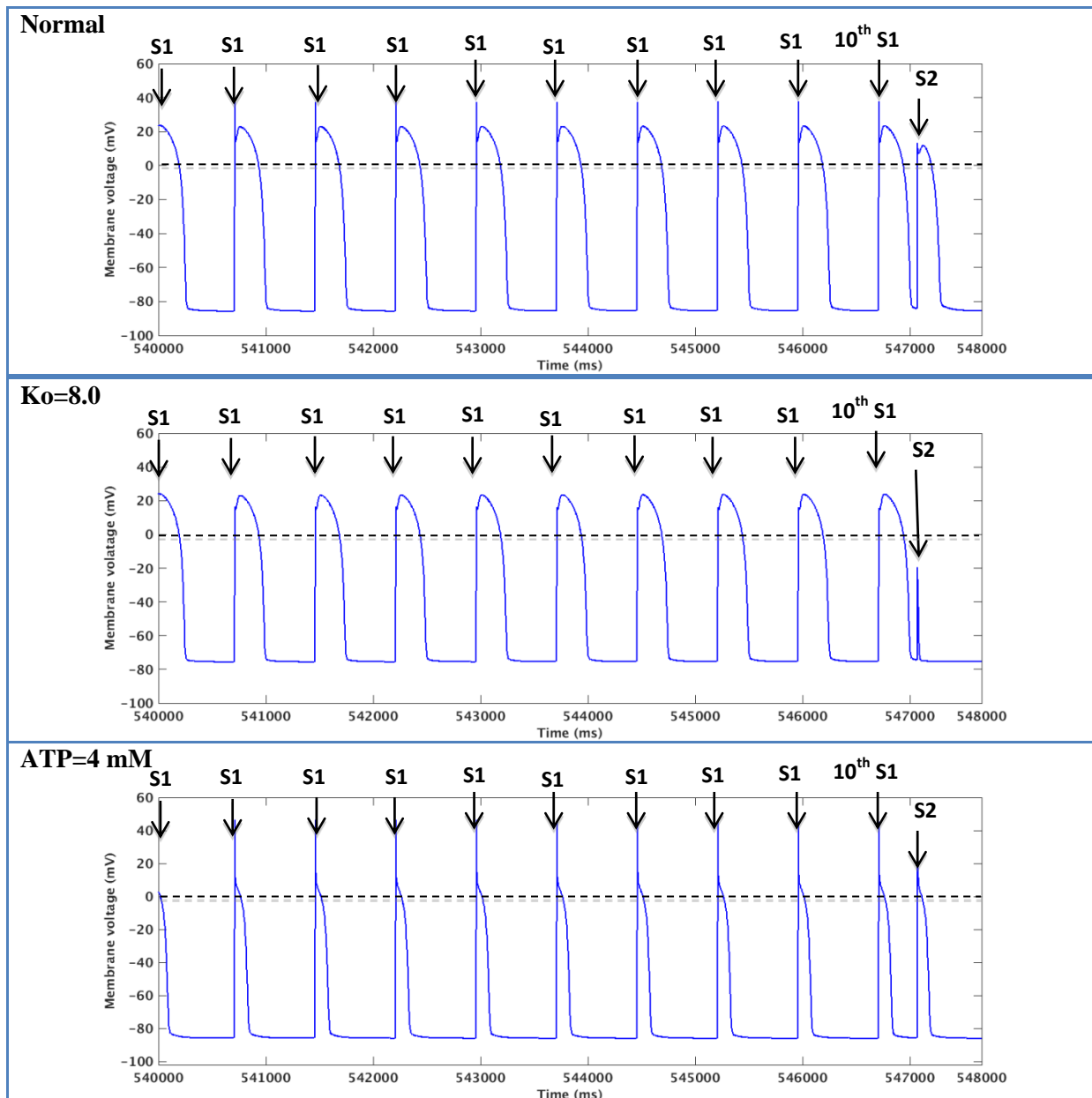


**Figure 8.1. Determination of S1S2 stimulus protocol used for measurement of APD and ERP in TP06 model: after a train of 10 regular S1 stimuli with a CL of 1000 ms, an extra stimulus S2 with different coupling intervals was applied. The S1S2 interval (in ms) was specified as the interval between the 10th S1 and S2. The S1S2 coupling interval was decreased until the ERP was reached. This approach was used in normal and ischaemic (elevated $[K^+]_o$ to 8mM and reduced $[ATP]_i$ to 4.0 mM) tissue models.**
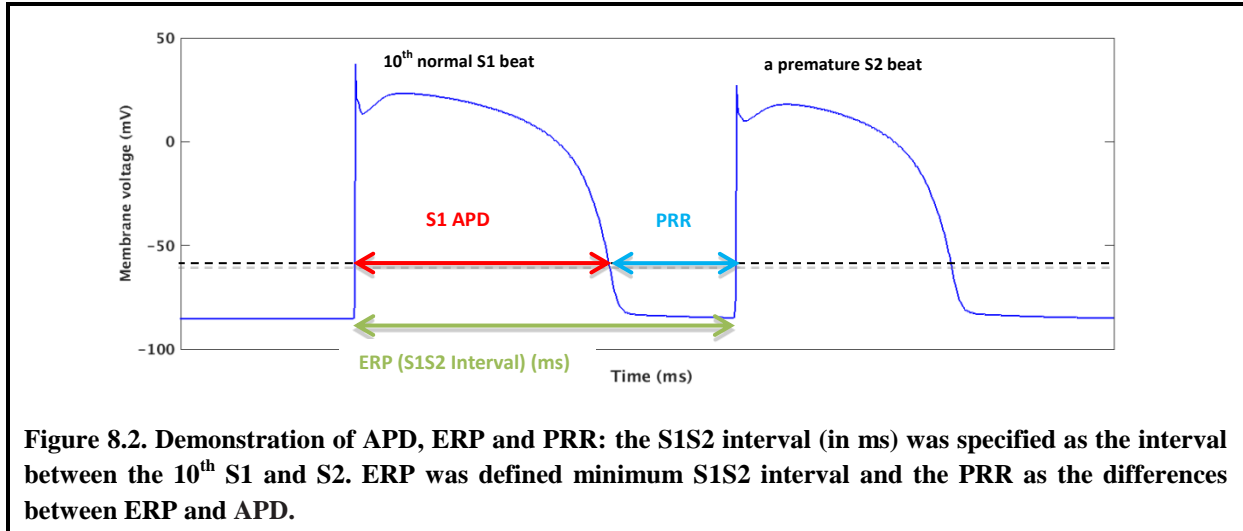
**Figure 8.2. Demonstration of APD, ERP and PRR: the S1S2 interval (in ms) was specified as the interval between the 10ᵗʰ S1 and S2. ERP was defined minimum S1S2 interval and the PRR as the differences between ERP and APD.**

## 8.3   Results

A summary of some important measured electrophysiological parameters is presented in Table 8.2. The data in Table 8.1 and Figures 8.3 and 8.4 demonstrate the effect of ischaemic components on APD, ERP, CV and PRR. The simulated ischaemic tissue was characterised by a reduction in APD, slower APD upstroke and increasing resting membrane potential, in agreement with experimental observations (Carmeliet 1999). The main features of simulated ischaemia are shown in Figures 8.3 and 8.4, where the effect of lowered $[ATP]_i$ and accumulated $[K^+]_o$ on ERP and APD for both TP06 and ORd models is demonstrated. Reduced $[ATP]_i$ activated $I_{K,ATP}$ abbreviated APD and ERP (Figure 8.3.d and 8.4.d).

Reduced $[ATP]_i$ had a negligible effect on CV (Figures 8.3.f and 8.4.f). However, elevated $[K^+]_o$ had little effect on APD, but operated to increase ERP (Figures 8.3.a and 8.4.a) and reduce CV (Figures 8.3.c and 8.4.c). Figures 8.3.a and 8.4.a show ERP values increasing from 295 and 272.34 ms (non-ischaemic) to 408.6 and 359.79 (ms) (ischaemic, $[K^+]_o$=8.0 mM) in TP06 and ORd respectively. The increase in ERP is significant for both models and in agreement with experimental observations (Sutton et al. 2000). However, the ERP increment is much lower in hypoxia in comparison with hyperkalemia conditions in the ORd model (Figure 8.4.d) and even this value is decreased by 55 ms in the TP06 model (Figure 3.d) when $[ATP]_i$ decreased to 4.0 mM. In addition, ischaemic results show the property of PRR. The development of PRR (Figures 8.3.b, 8.3.e, 8.4.b and 8.4.e) reflected the combination of reduced APD (Figure 8.3.d and 8.4.d) and prolonged ERP (Figures 8.3.a and 8.4.a) in both models.

The average period of re-entry for different levels of $[ATP]_i$ and $[K^+]_o$ has been shown with the changes in ERP and PRR (Figures 8.5 and 8.6). The reduced CV and prolonged ERP resulting from accumulated $[K^+]_o$ operated to increase the period of re-entry (Figures 8.5.a and 8.6.a), and consequently reduce activation rate. In contrast, the period of re-entry decreased (Figures 8.5.c and 8.6.c) due to the ERP shortening and unchanged CV subsequent to $[ATP]_i$ depletion. This acted to increase activation rate.

**Table 8.2. Measured parameters (electrophysiological measurements): figures 8.3 and 8.4, a-f are summarised in this table.**

| Model | Hyperkalemia | | | | | Hypoxia | | | | |
|---|---|---|---|---|---|---|---|---|---|---|
| **TP06** | $[K^+]_o$ (mM) | 5.4 | 6 | 7 | 8 | $[ATP]_i$ (mM) | 4 | 5 | 6 | 6.8 |
| | APD | 287 | 286.2 | 284.8 | 284.2 | APD | 113 | 229 | 276.6 | 287 |
| | ERP | 295 | 300.8 | 317.8 | 408.6 | ERP | 240 | 241 | 285.6 | 295 |
| | PRR | 8 | 14.6 | 33 | 124.4 | PRR | 126.2 | 12 | 9 | 8 |
| | CV | 0.6016 | 0.5653 | 0.2834 | 0.206 | CV | 0.5921 | 0.5984 | 0.6016 | 0.6016 |
| **ORd** | $[K^+]_o$ (mM) | 5.4 | 6 | 7 | 8 | $[ATP]_i$ (mM) | 4 | 5 | 6 | 6.8 |
| | APD | 229.01 | 225.74 | 222.19 | 223.05 | APD | 126.86 | 182.13 | 216.93 | 229.01 |
| | ERP | 272.34 | 275.57 | 283.11 | 359.79 | ERP | 287.93 | 281.77 | 275.25 | 272.34 |
| | PRR | 43.33 | 49.83 | 60.92 | 136.74 | PRR | 161.07 | 99 | 59 | 43.33 |
| | CV | 0.7181 | 0.7204 | 0.5111 | 0.3806 | CV | 0.6922 | 0.6735 | 0.6398 | 0.7181 |



**Figure 8.3. Relation between APD, ERP(a,d), PRR(b,e) and CV (c,f) with the effect of elevated $[K^+]_o$ and decreased $[ATP]_i$**
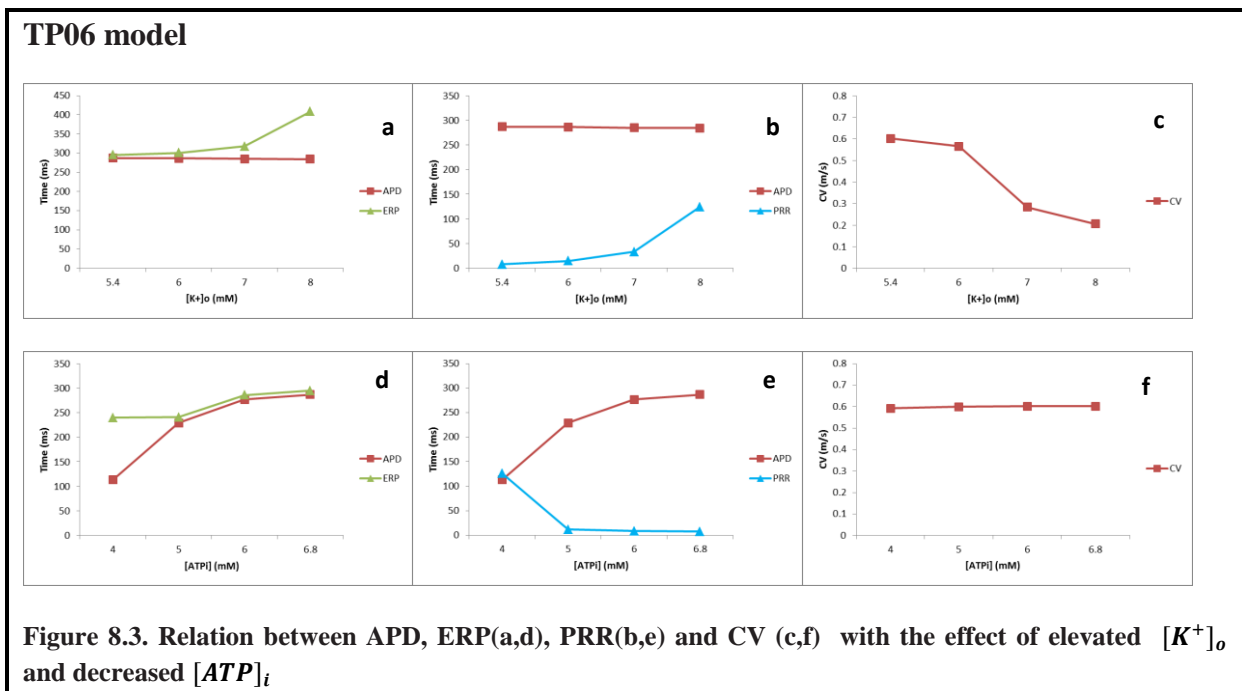
**ORd model**
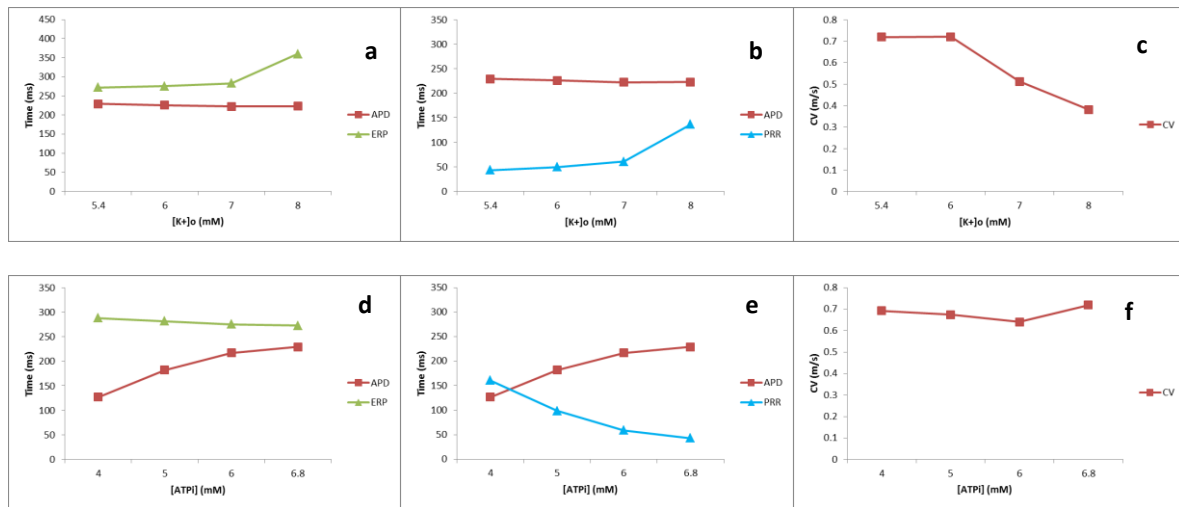


**Figure 8.4. Relation between APD, ERP(a,d), PRR(b,e) and CV (c,f) with the effect of elevated $[K^+]_o$ and decreased $[ATP]_i$**

## 8.4 Discussion

The main ischaemic electrophysiological characterisation (Figures 8.4 and 8.5) caused by an increase in the $[K^+]_o$ in combination with hypoxia showed the ERP prolongation resulted from the delayed recovery from inactivation of the $Na^+$ channel which prolongs repolarization and displays PRR despite shortening of the APD.

Ischaemia induced changes in refractoriness have been shown in various studies (Carmeliet 1999; Sutton et al. 2000; Faber & Rudy 2000; Burton & Cobbe 2001; Franz 2003; Ferrero et al. 2003; Ma & Wang 2007); the longer refractory period has been reported in tens or even hundreds of milliseconds, mostly related to severe ischaemia. ERP prolongation in humans over a wide range of stimulus strengths is affected by the combined influences of hypoxia and hyperkalemia (Sutton et al. 2000).

The utility of the ERP and PRR phenomena correlated with APD and CV changes as a reliable endpoint for study of the spiral wave variation in ischaemic tissue was validated. ERP examination is a key aspect of spiral wave studies because wave break in fibrillation results from wave fronts meeting tissue which is still refractory (Xie et al. 2002). To determine the stability of spiral waves in simulated ventricular tissue, the period of re-entry was measured for each ischaemic component as well as measuring ERP. In addition, PRR has the key role in the formation of ERP heterogeneities and in characterising conduction block

175

and induction of re-entrant wave under ischaemia conditions (Cabo 2015). It has been shown that the period of re-entry was increased when the ERP prolonged with decreased CV under hyperkalemia conditions (Figures 8.5.a and 8.6.a). Contrary to these results (hyperkalemia), the reduced ERP (unchanged ERP in the ORd model) and unchanged CV resulting from reduced $[ATP]_i$ act to decrease the period of re-entry (Figure 8.5.c and 8.6.c) and thus to enhance activation rate. Slow conduction affects the re-entry mainly in the areas of prolonged refractoriness (Coronel et al. 2012). It has been noticed that in the region of the block due to the ERP heterogeneities, the premature impulses cannot excite the region distal because the time of propagation of the premature impulse around the line of block is not sufficient to recover its excitability (Cabo 2015).The combination of PRR, reduced excitability, and reduced effectiveness of the conducted wave front resulting from ischemic myocardium, shown in experimental evidence (Sutton et al. 2000; Coronel et al. 2012), was clearly shown in our simulation results.



**Figure 8.5. Relation between ERP (a,c), PRR (a,c), Period of re-entry (a,c), and CV (b,d) with the effect of elevated $[K^+]_o$ and decreased $[ATP]_i$.**
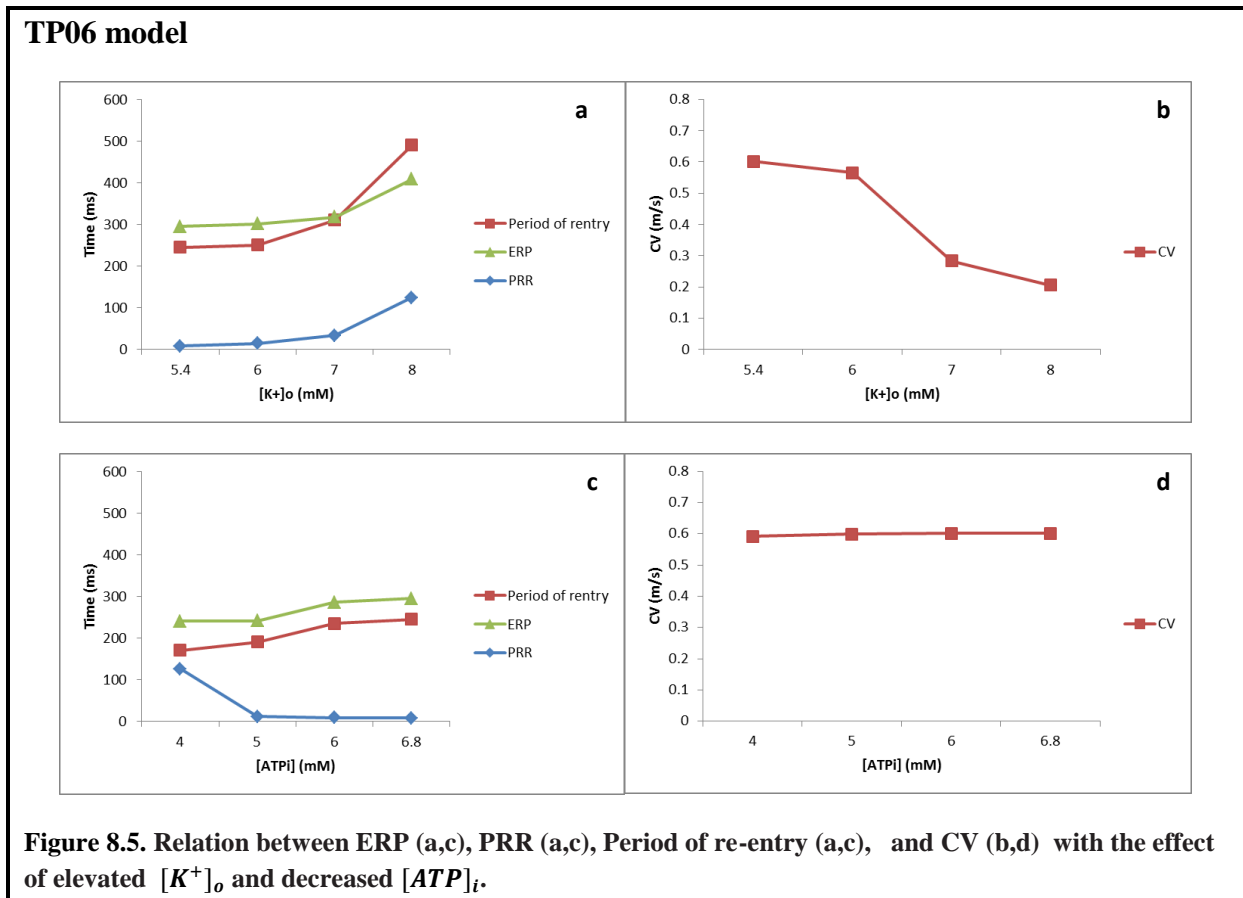
**ORd model**
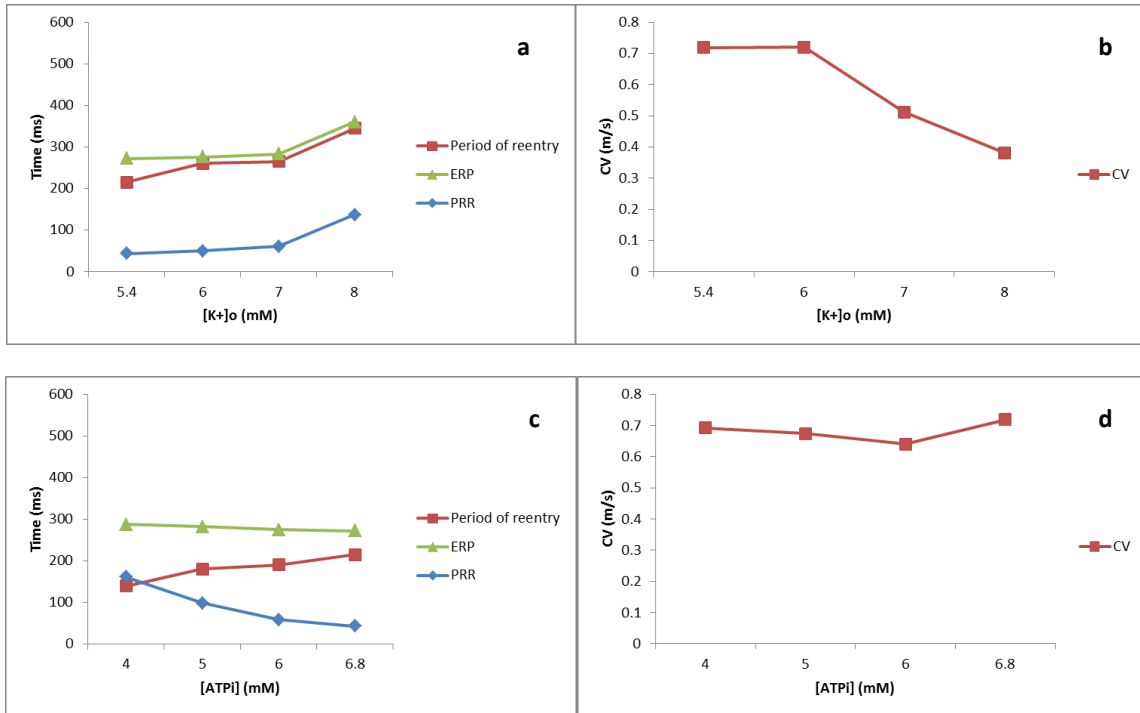


**Figure 8.6.** Relation between ERP (a,c), PRR (a,c), Period of re-entry (a,c), and CV (b,d) with the effect of elevated $[K^+]_o$ and decreased $[ATP]_i$.

**Experimental study by Sutton et al. (2000)**
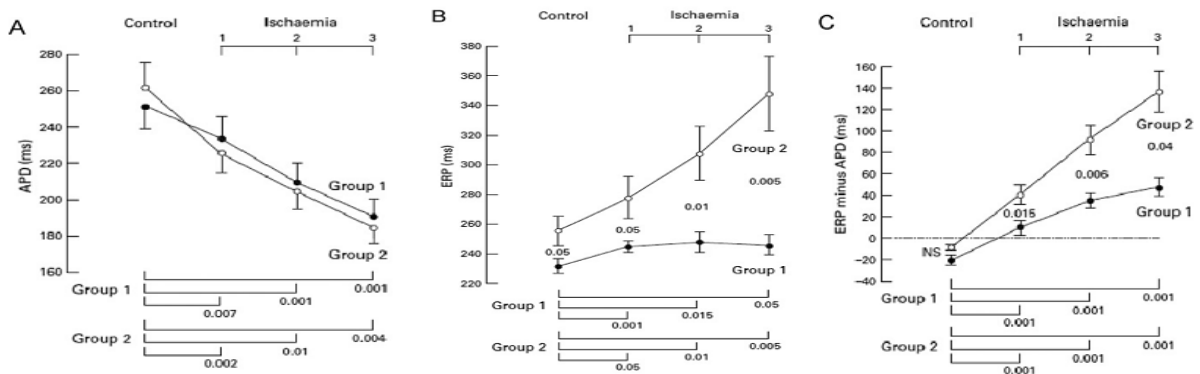


**Figure 8.7.** Relation between APD, ERP and PRR. Observation from an experimental study with permission from Sutton et al. (2000); A: APD during 3 minutes of global ischaemia in the human heart, B: ERP, C: PRR (ERP-APD)

Simulation observations (Figures 8.3 and 8.4) were compared with experimental findings (Figure 8.7) to check the accuracy of the simulation results. In an experimental study by Sutton et al. (2000), monophasic APs and refractor periods were recorded during electrical and optical mapping of propagating impulses from a single left ventricular epicardial site in patients undergoing coronary artery surgery. The ERP was estimated using extra stimulus technique during a 3-minute period of global ischemia. During this period, APD decreased (Figure 8.7.A), ERP prolonged (Figure 8.7.B) and consequently PRR increased resulting from differences between APD and ERP (Figure 8.7.C). The changed excitability accompanying PRR during ischemia has been shown in the two simulation studies here (Figures 8.3 and 8.4) that were in agreement with experimental results by Sutton et al. (2000). There was a good correlation between the ischaemic simulation results here and their experimental study. For example, the difference in refractory periods reported in their study was 100 ms; in this simulation study (under conditions of hyperkalemia (between 5.4 and 8.0 mM)) this was 113.6 ms (TP06 model) and 87.45 (ORd model).

Simulation results here have shown that PRR increases are likely to contribute to maintenance of re-entry (Figures 8.5.a, b and 8.6.a, b) because they produce ERP changes. These results have proven that ERP heterogeneities may be adequate for initiation of arrhythmias in ischaemic myocardium. However, this study neglects tissue structural heterogeneities (Dillon et al. 1988; Cabo et al. 1996; Cabo et al. 2006; Ciaccio et al. 2007; Ciaccio et al. 2014; Cabo 2014), which may modulate ERP and contribute to the formation of block and initiation of re-entry. The interactions between tissue structure heterogeneities and ERP (Spach et al. 1989; Laurita & Rosenbaum 2000; Sampson et al. 2001; Jie & Trayanova 2011) and their characterization in the ischaemic heart need further study which is not in the scope of this thesis.

In summary, it is demonstrated that refractory period is lengthened due to the long recovery time of excitability during 3 minutes of global cardiac ischaemia despite the APD shortening. Observations in this research have shown that the occurrence of PRR causes ERP to outlast APD by over 100 ms; these results may contribute to maintenance of re-entry.

Another scenario in assessing the stability of re-entry spiral wave during ischaemia is examination of the rate dependence of APD and CV in the ischaemic tissue. It was expected that the flattening of APD restitution and the ERP lengthening resulting from lowered $[ATP]_i$

and elevated $[K^+]_o$ would increase the stability of re-entry in ischaemic tissue. This hypothesis will be investigated by performing a complete restitution study and simulating re-entry in 2D and 3D tissue models in the next chapter.

# 9 Dynamic Behaviour and Impact of Simulated Global Cardiac Ischaemia

*The aim of this chapter is to examine the consequences of global ischaemia on the behaviour of ventricular arrhythmias in the human heart. Global cardiac ischaemia is simulated by reducing $[ATP]_i$ concentration and increasing $[K^+]_0$ concentration. The effect of acidosis (resulting in reduced magnitude of the L-type $Ca^+$ current $I_{Ca,L}$) is neglected here in the simulations, because the relative effect of reduced $I_{Ca,L}$ associated with acidosis has been found to be small in global cardiac ischaemia (Clayton et al. 2011). Dynamic behaviour of simulated ischaemia on tissue included reduction of action potential duration, reduction of conduction velocity, and flattening of restitution. These outcomes resulted in slower re-entrant activity in the model, which was in agreement with findings in the human heart (Clayton et al. 2011). Although the flattening of restitution would be expected to stabilise re-entrant waves, other elements such as structural or functional parameter variation are important in maintaining wave break during human ventricular fibrillation with global myocardial ischaemia (Clayton et al. 2011). A 3D computational model of human ventricular tissue was used to show the maximal impact of global cardiac ischaemia on the processes of sustaining ventricular arrhythmias. The influences of simulated ischaemia are examined at the cellular level that affects the performance of re-entry at the tissue level. The aim was to link these simulation outcomes with empirical evidence.*

## 9.1 Introduction

Global cardiac ischaemia accompanies VT and VF, and results in contraction failure, changes in electrical behaviour and death of the cell. To study the impact of global ischaemia on the dynamic behaviour of the heart, a computer model has been used. Electrophysiological differences at the cellular and tissue levels show a shortening of the action potential, reduction in CV, and change in excitability (Carmeliet 1999). The relative influence of each ischaemic component to APD and CV changes, and cardiac excitability has been determined. The mechanisms of APD and CV Restitution, which are key parameters in the induction and maintenance of re-entry, are also explored. This section presents a short overview of how dynamic factors interact with ischaemic tissue to encourage ventricular arrhythmias. The complete background is provided in Chapter Two.

**Simulated ischaemia and its effects on spiral wave stability**

Different factors resulting from ischaemia are responsible for the variations in cardiac cell and tissue electrophysiology. These changes result mostly from the $[ATP]_i$ reduction as an outcome of hypoxia, which triggers $K_{ATP}$ channels, inducing an extra outward $K^+$ current, $[K]_o$ accumulation that increases the cell resting membrane potential and a decrease in intracellular pH ( Weiss et al. 1992; Carmeliet 1999; Janse & Wit 1989). In addition to these changes, decreasing excitability and reducing conduction, APD shortening, APD restitution flattening, and refractoriness prolongation (Taggart et al. 1996) are consequences of ischaemia that affect the behaviour of spiral wave re-entry. Many experimental studies (Janse & Wit 1989; De Groot & Coronel 2004; Tabereaux et al. 2009) support the idea that cardiac arrhythmias of ventricular tachycardia (VT) and fibrillation (VF) are continued by spiral wave re-entry. Break up of re-entrant waves can occur as a result of these mechanisms: fundamental 3-D instabilities, gradient (steep slope) of the APDR curve, and the effects of rotational anisotropy in the ventricular wall (Clayton & Holden 2004b).

To determine the mechanisms of stability of re-entrant waves in cardiac tissue, the dynamic instability of cardiac electrical wave propagation has been studied in detail (Karma 1993; Garfinkel et al. 2000). In 2D models, the stability of re-entry is affected by the gradient of the APD restitution curve (Weiss et al. 2000). However, some other factors shown in modelling studies (Fenton et al. 2002) can influence re-entry instability. In this chapter, a computational model of AP propagation of human ventricular tissue based on reaction-diffusion equations

(Clayton et al. 2006) was used to investigate the behaviour of re-entry by simulating ischaemia at the cell and tissue level.

**Aim and general outline**

In this chapter, the electrical activation of human ventricular tissue is simulated in homogenous 2-D and 3-D scenarios with cellular electrophysiology described by the TP06 and ORd models to examine the propagation of normal rhythms and arrhythmias. The aim of this study is to illustrate how simulated global cardiac tissue can affect the dynamic behaviour of normal beats and re-entry. The interest here is in the electrophysiological changes during ischaemia and arrhythmias for a more appropriate examination of arrhythmia mechanisms.

The ionic changes during ischaemia are discussed in Section 9.3, including a description of the variations in resting membrane and AP. Section 9.3.1 contains the electrophysiological changes at the tissue level. The effect of each ischaemic component on APD and CV restitution was determined in 2-D models. Section 9.3.2 starts with an analysis of the behaviour of spiral wave re-entry during global cardiac ischaemia. Section 9.3.3 describes the behaviour of spiral wave re-entry involved in the arrhythmias, followed by a description of the type of arrhythmias. Finally, in Section 9.3.4, using a 3-D model, the possible mechanisms of ventricular arrhythmias compatible with the variations in activation patterns detected during VF in the human heart with global ischaemia are discussed. Simulations of ventricular arrhythmias were performed using a 3D model of the human ventricles to determine the effect of each ischaemic component on the stability of ventricular fibrillation. The discussion concludes that hyperkalaemia is the main component responsible for the alteration in activation rate during ischaemia. The effect of two ischaemic components on the complication of VF demonstrated by the number of scroll wave filaments was analysed.

## 9.2   Methods

### A.   Cell model and simulated ischaemia

Two theoretical ionic-based models of the cardiac ventricular cell were used: the Ten Tusscher Panfilov 2006 (TP06) (Ten Tusscher & Panfilov 2006); and O'Hara-Rudy dynamic (ORd) (O'Hara et al. 2011) models. Three parameter sets for epicardial, endocardial and mid-

myocardial cells were used. These parameters were modified to simulate ischaemia as discussed in detail below. Two major component conditions of ischaemia (hyperkalemia and hypoxia) were simulated at the level of single ionic currents and ionic concentrations. Ischaemic components were applied independently and in combination to recognise ionic functions responsible for decreased excitability at resting potentials, delayed recovery of excitability, and reduced APD. The ionic and metabolic conditions of ischaemia were simulated as: (1) elevated $[K]_o$ concentration (hyperkalaemia) and (2) decreased $[ATP]_i$ concentration (hypoxia). The method and theoretical implementations of each condition are discussed briefly below.

1.     Hyperkalemia (elevated $[K^+]_o$ concentration)

The range of typical $[K^+]_o$ concentrations that occur during ischaemia was examined  . First, $[K^+]_o$ was assigned to the normal value of 5.4 mM. Then, $[K^+]_o$ was elevated from its normal value to values between 6.0, 7.0 and 8.0 mM, set for up to 3-6 min of ischaemia (Janse & Wit 1989), because in every minute of ischaemia, $[K^+]_o$  increases by between 0.5 and 1 mM (Weiss et al. 1992).

2.     Hypoxia (decreased $[ATP]_i$ concentration)

To model anoxia, the formulation of the ATP activated $K^+$ current $I_{K,ATP}$ described by Shaw and Rudy (1997) was used due to its greater effectiveness over other $I_{K,ATP}$ models for the small changes in $[ATP]_i$  (Clayton et al. 2011; Nickerson & Buist 2008). The details of this formulation are discussed in Chapters Five and Seven. The ischaemic parameter values have been set as presented in Table 5.1 in Chapter Five.

The $I_{K,ATP}$ formulation used in this chapter is described below:

$$I_{K,ATP} = G_{K,ATP} \frac{1}{1+\left(\frac{[ATP]_i}{K_{0.5}}\right)^H} \left(\frac{[K^+]_0}{5.4}\right)^n (V_m - E_k) \qquad (9.1)$$

Here, $V_m$ is the membrane voltage and $E_k$ indicates reversal potential for potassium ions. $[K^+]_0$ concentration was set at 5.4 mM. A Hill coefficient (H) and n was set to 2.0 and 0.24 respectively (Nichols et al. 1991).

The effect of acidosis (pH imbalance, decreasing pH) in these cardiac cell models was neglected because of its small effect on the simulated AP during global cardiac ischaemia and VF. Thus, the effects of acidosis were not involved in this study.

## B.    Numerical method in the tissue model

To characterize restitution properties and consider re-entry period, each cell model was embedded in a 2-D monodomain tissue model using isotropic diffusion and a diffusion coefficient of 1.171 $cm^2\ s^{-1}$ (TP06 model) as calculated for human ventricular tissue (Bueno-Orovio et al. 2008), 0.2975 $cm^2 s^{-1}$ (ORd model), and a specific capacitance of 1 µF $cm^{-2}$ (Noble, 1979). It is important to choose an appropriate time and space step to ensure the AP upstroke is sufficiently resolve in time and a propagating wave-front is sufficiently resolved in space.  These requirements are considered to choose the resolution based on the reaction-diffusion properties. For the space step the size of the wave-front, and for the time step the upstroke velocity of the AP were determined. A spatial resolution of between 0.1 and 0.2 mm and a time step of between 0.01 and 0.02 ms have been used for simulation of tissue volumes for the diffusion component of the model.  Typically, a practical approach is to compare the CV measured using given spatial and temporal resolutions in the tissue model to consider the adequate resolution. The numerical accuracy of the CV for different space and time steps in the tissue model will be described in the next section (Section 9.2.1). An explicit finite difference approach with a fixed space step of 0.2 mm and time step of 0.005 ms were used to solve these models. The gradient of membrane voltage was set at zero at boundary condition to show no-flux boundary conditions were applied at each edge.

## C.    Initial condition of the model set up

The influence of combinations of reduced $[ATP]_i$ and increased $[K^+]_0$ on APDR and CVR on the TP06 and ORd 2-D tissue models was studied. A small slab of tissue of $3 \times 100$ grid points ($0.75 \times 25$ mm) was used for the measurements. In each simulation, an S1S2 stimulus protocol was used with S1=1000 ms and S2 CL that changed between 1000 ms and 300 ms. A stimulus current of -52.0 (TP06 model) and -80 $pA\ pF^{-1}$ (ORd model) was used to deliver each stimulus to the small slab of tissue for 1ms. The 10 S1-1S2 stimulus was delivered with a CL of 1000 ms. The tissue was returned to its initial state after each S2 before the next S1S2 cycle.

## D.    Simulated re-entry in a tissue model

To examine the effect of the combination of ischaemic components (elevated $[K^+]_0$ and lowered $[ATP]_i$) on re-entry behaviour, simulations were run with either a single re-entrant wave or multiple re-entrant waves as an initial condition. A single re-entrant wave was initiated in a 2-D isotropic and homogeneous tissue sheet ($200 \times 200$ ($50 \times 50$ mm) grid points) as the initial condition by imposing an Archimedean spiral on the tissue. The cell model variables were set at grid points occurring on circles to a complete action potential cycle (Clayton et al. 2011). Ventricular arrhythmias were simulated in a 3-D slab of $100 \times 100 \times 15$ mm (equivalent grid points: $400 \times 400 \times 60$). The anisotropic slab was proposed to reproduce part of the human left ventricular wall. Re-entry with multiple wavelets was initiated in the TP06 tissue model with changes in the slope of APDR set to 1.8 according to the slope description in Table 2 of the TP06 paper (Ten Tusscher & Panfilov 2006). The initial spiral wave break up accrued when these values were applied in the model. In these simulations, a time delay of 20 ms was used when the simulated voltage is transformed into phase to determine the number of phase singularities. The topological charge method (Clayton et al. 2006) was used to identify phase singularities. In numerical simulations of re-entry, phase singularity points in 2D, and 3D are located when the activation and recovery curves cross (Clayton et al. 2006).

## E.    Configuration of filaments (detecting and tracking phase singularities and filaments)

A scroll wave is a deployment of 2-D spiral waves into 3-D and filaments are known as lines of wave break around which a scroll wave rotates. Identifying filaments are aimed to find this wave break. Phase singularities and filaments can move and their movements depend on tissue electrophysiological properties, local parameter gradients, refractoriness gradients, and the structure of the tissue (Clayton et al. 2006). Filament behaviour here was quantified in simulations of a 3-D tissue slab.

It is difficult to identify re-entrant cores in experimental data because the membrane voltage is measured at the cardiac surfaces, which are noisy, and recovery variables are not (Clayton & Holden 2002a). Therefore, computational techniques are used to identify PS from phase representations of electrical activity at each point in the experimental data (Valderrábano et al. 2001; Gray et al. 1998) and following movement of each point at the border of wave fronts (Rogers et al. 1999). For detection of filaments, a technique based on phase space

analysis was used (Clayton 2008) throughout simulations of 2000 ms. In this method, membrane voltage is transformed into phase operating time delay inserting with a delay of 20 ms for simulations. The convolution kernels technique was used to identify voxels containing filaments. In addition, a smoothing algorithm based on a 3×3×3 boxcar filter (Clayton 2008) was used to guarantee the filaments were combined of linked voxels. Then, each incessant filament was detected and marked by a grassfire algorithm. The method of detecting an unlabelled filament voxel, labelling it with a unique label, and then using the same tag for all linked filament voxels was repeated until all of the filament voxels were tagged (Clayton 2008). Then, filaments were tracked individually by detecting the intersection of filament voxels from one portrait to the next. Finally, the output of the filament tracking algorithms was displayed in a graph (Clayton & Holden 2002a; Clayton 2009).

### 9.2.1 Stability of the numerical simulations (Testing Temporal and Spatial Resolution)

As discussed in Chapter 3 (section 3.4.4), it is important to select a suitable spatial and temporal resolution for a tissue model to guarantee numerical stability and accuracy. In tissue models (2D or 3D), the system dynamics can be determined by spatial and temporal resolution. The spatial and temporal resolution can influence spiral wave properties (Panfilov & Keener 1995; Fenton et al. 2002; Panfilov, 2002; Bueno-Orovio et al. 2008). To ensure this, adequate resolutions were used in the model, and CV (Tables 9.1 and 9.2) was measured at different resolutions because CV is much more sensitive to spatial resolution than APD.

**Table 9.1. Numerical accuracy of the CV for different space step and time step in a 2D thin strip of tissue at S1S2 interval of 700 ms for the TP06 model**

| Space steps (mm) | Time steps (ms) | | | | TP06 model |
| --- | --- | --- | --- | --- | --- |
| | **0.2** | 0.1 | 0.05 | 0.005 | |
| 1 | 0 | 0 | 0 | 0 | CV (m/s) in a 2D thin strip of tissue |
| 0.5 | 0 | 0 | 0 | 0 | |
| 0.125 | 0.208 | 0.2089 | 0.209 | 0.208 | |
| **0.02** | 0.601 | 0.618 | 0.625 | 0.623 | |

**Table 9.2. Numerical accuracy of the CV for different space step and time step in a 2D thin strip of tissue at S1S2 interval of 700 ms for the ORd model**

| Space steps (mm) | Time steps (ms) | | | | ORd model |
| | 0.2 | 0.1 | 0.05 | **0.005** | |
|---|---|---|---|---|---|
| 1 | inf | inf | inf | inf | |
| 0.5 | inf | inf | inf | inf | CV (m/s) in a 2D thin strip of tissue |
| 0.125 | 0.158 | 0.159 | 0.159 | 0.160 | |
| **0.02** | 0.6818 | 0.711 | 0.718 | 0.717 | |

To test the numerical stability, a 2D isotropic epi tissue (thin strip) was used to run simulations with different space steps and time steps. CV was measured at the S1S2 interval of 700 ms with a diffusion of 0.0012 $cm^2/ms$ (TP06) and 0.0003 $cm^2/ms$ (ORd). A summary of the results from testing the stability of the numerical simulations is illustrated in tables 9.1 and 9.2; the reliable temporal and spatial resolution used in this thesis is highlighted in bold.

**Table 9.3. Numerical accuracy (comparison of CV) for the selection of proper diffusion coefficient for TP06 and ORd tissue model**

| CV (m/s) values at S1S2 interval of 700 ms | 2D tissue model | Diffusion ($cm^2/ms$) | | | |
| | | D1= 0.0012 | D2=0.0006 | D3=0.0004 | D4=0.0003 |
|---|---|---|---|---|---|
| | TP06 | 0.601 | 0.415 | 0.333 | 0.2507 |
| | ORd | 1.691 | 1.124 | 0.869 | 0.717 |

To obtain the maximum CV of paced depolarisation wave 0.7 m/s along fibre (Taggart et al. 2000) in the ORd tissue model, different isotropic diffusion coefficient were tested. Although replacement of ORd model $Na^+$ current formulation was suggested with the TP06 model, this failed to provide reliable CV and stable re-entry in the ORd. Therefore, different diffusion coefficients were tested in this model. Table 9.3 shows reliable CV obtained in a tissue model based on different isotropic diffusion coefficients. After testing numerical accuracy, it was decided to use the values illustrated in Table 9.4 in the simulations.

**Table 9.4. Human cardiac ventricular cell model basic parameters used in this thesis**

| Model | Number of state variables | Stimulus | | Threshold (mV) | Diffusion ($cm^2/ms$) | Space steps (mm) | Time steps (ms) |
| | | Amplitude (μA/μF) | Duration (ms) | | | | |
|---|---|---|---|---|---|---|---|
| TP06 | 21 | -52 | 1.0 | -65 | 0.0012 | 0.02 | 0.2 |
| ORd | 41 | -80 | 1.0 | -75 | 0.0003 | 0.02 | 0.005 |

**Table 9.5. The numerical performance: execution times (wall clock times) and maximum virtual memory (Mb:MegaByte, Gb:GigaByte) for simulations in this thesis for both models (TP06, ORd), using parallel computing method (openMP: 4 threads) running the simulation in the University of Sheffield High Performance Computing Cluster (Iceberg).**

| Models | 2D thin strip of tissue (3 × 100 grid points ) (with 16 S1S2 intervals) | | 2D slab of tissue (200 × 200 grid points) spiral wave simulation | | 3D slab of tissue | |
|---|---|---|---|---|---|---|
| | Time | memory | Time | memory | Time | memory |
| **TP06** | 22 minutes | 2.660 Mb | 2 hours and 30 minutes | 229.375 Mb | 3 days and 16 hours | 4.289 Gb |
| **ORd** | 13 hours and 16 minutes | 2.281 Mb | 27 hours and 30 minutes | 131.260 Mb | Aborted after reaching maximum run time (one week) | NA |

In Table 9.5, the main advantage of the TP06 model is compared to the ORd model. The TP06 model is computationally cheaper to use in cardiac tissue electrophysiological simulations because it is mathematically less complex (less variables (21) compared to 41 variables in the ORd model) and faster to run simulations. This table shows why the TP06 model was selected for the 3D simulations. This thesis used the TP06 model to simulate 3D tissue because it was not possible to simulate a 3D tissue model with the ORd model even when using a parallel computing method. In this work a shared memory model, OpenMP, was used as an efficient parallelisation strategy. In this shared-memory programming, the serial programs were parallelised using compiler directives. In this method, all the available CPUs were utilised. It was important to interpret the memory requirement per process for parallel jobs.

For example a job issued as:

```
qsub myxyzjob -pe openmp 4 -l mem=16G -l rmem=10G
```

will need a machine with 4*10 = 40 GBytes of physical memory.

A standard design to define computational tasks and control their execution by scheduling algorithms to map tasks onto the processing elements of the target computer system was vital for the high-performance computing.

## 9.3  Results

**Electrophysiological Effects of Myocardial Ischaemia**

This section aims to show the effect of hyperkalaemia and anoxia on AP shape for each cell type in two tissue models. Electrophysiological changes in the cardiac cells in terms of ischaemia conditions were examined. These electrophysiological variants are important and contribute to the occurrence of ventricular arrhythmias. For example, changes in resting membrane potential and inward and outward currents during the AP lead to changes in conduction, refractoriness, and automaticity (Janse & Wit 1989).

**1- Resting membrane potential**

Figure 9.1 shows that resting membrane potential increased with increasing $[K^+]_o$. Membrane potential increased from normal values of -85.3 mV (TP06) and -87.89 mV (ORd) to -75.19 mV (TP06) and -77.44 mV (ORd) after $[K^+]_o$ was increased to 8.0 mM. Our results are in agreement with experimental studies which have shown that during global ischaemia caused by stopping total perfusion, resting membrane potential is decreased (Janse & Wit 1989). The fall in resting potential in the whole heart has been linked to changes in distribution of $K^+$ across the cell membrane. However, there was no alteration in resting potential in hypoxic tissue, which is one component of the ischaemic environment. These variants are the same for all three cell types.

**2- Transmembrane action potential**

Figure 9.1 shows that upstroke velocity, and duration of ventricular muscle action potentials decrease with the depolarization of resting membrane potential. This figure illustrates the decrease in amplitude and upstroke velocity of APs from normal values of 37.5 mV and 44.01 mV to 15.47 mV and 24.07 mV in the TP06 and ORd models respectively. Some experimental observations (Cranefield et al. 1972; Janse & Wit 1989) indicate that the decreased amplitude and velocity of depolarization of action potentials with partially depolarized membrane potentials may be caused by either a reduced fast $Na^+$ current or by the slow inward current during ischaemia. The reduction of the APD was a result of hypoxia in our simulations. Although hypoxia shortens the action potential, there is only a slight decrease in resting membrane potential and maximum upstroke velocity. The causes of AP

shortening during hypoxia are likely to be a decrease in the slow inward current and an increase in outward current (Janse & Wit 1989).
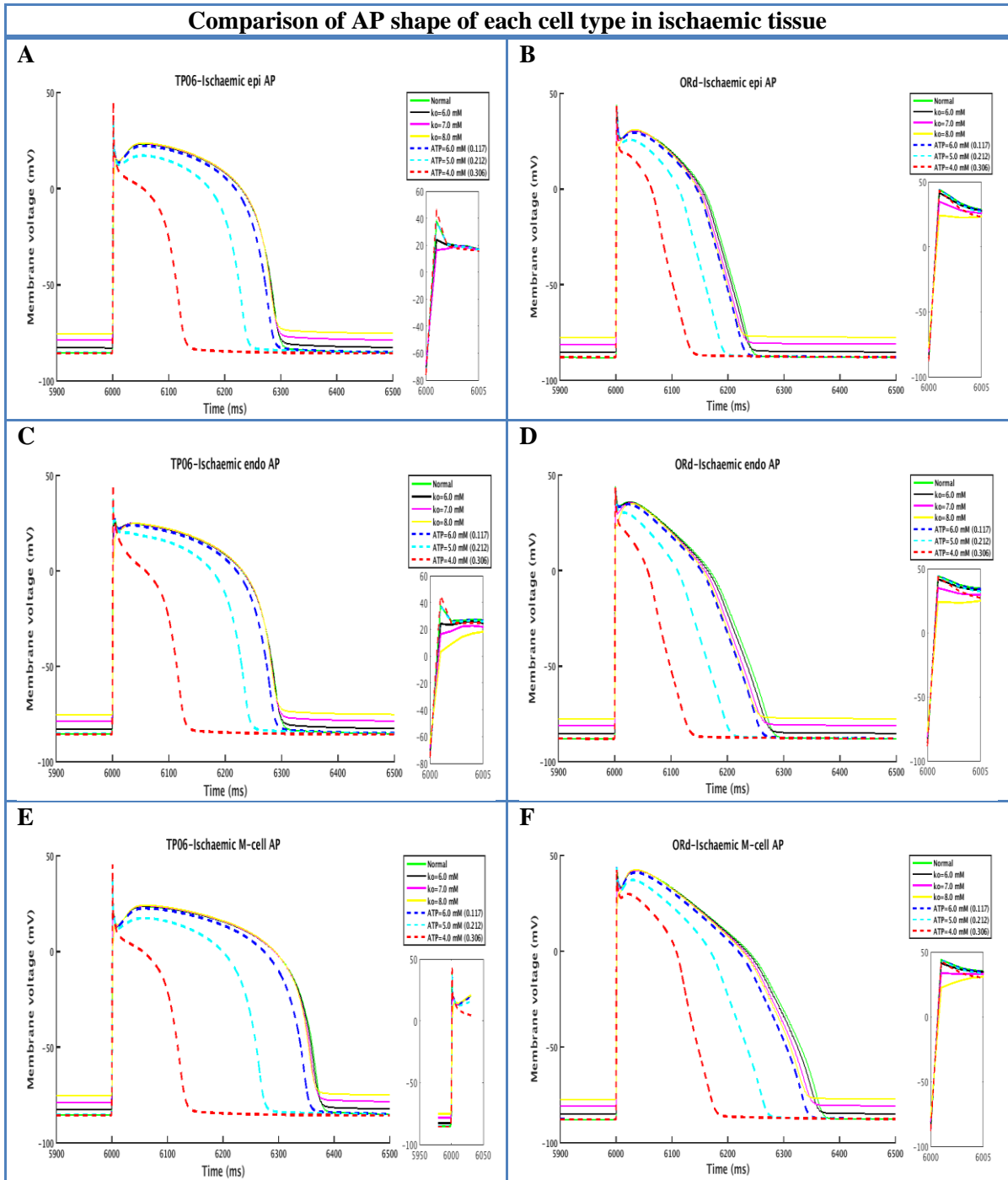
**Figure 9.1. Effect of $[ATP]_i$ decreased and increased $[K^+]_o$ on action potential shape in TP06 and ORd models: normal action potentials, applying the Shaw and Rudy (1997) $I_{K,ATP}$ formulation with a normal value of $[ATP]_i$ (6.8 mM) and $[K^+]_o$ (5.4 mM); outcomes from simulations of the Shaw and Rudy (1997) $I_{K,ATP}$ channel formulation with changing levels of $[ATP]_i$ (legend) to represent hypoxia/ischaemic condition. The value of the K0.5 parameter is displayed in bracketed legend (0.042 for the non-ischaemic case and 0.117, 0.212 and 0.306 for ischaemic simulations). Elevated $[K^+]_o$ (legend) with values between 6.0, 7.0 and 8.0 mM for the ischaemic conditions; A,C and E, represent AP changes with varying ischaemic components values in the TP06 model for epi, endo and M cell type respectively. B,D and F show AP morphology with varying ischaemic component values in the ORd model representing epi, endo and M cell type respectively.**

### 9.3.1 Influence of Cardiac Ischaemia on Action Potential Duration (APD) and Conduction Velocity (CV) Restitution

The changes in the resting membrane potential, the depolarization phase of the AP, and the APD are important factors in ischaemic simulations for restitution studies. In this section, the influence of decreased $[ATP]_i$ and elevated $[K^+]_o$ on APD restitution (APDR) and CV restitution (CVR) is examined. The APDR and CVR changes for each of the three cell types in two virtual tissues are shown in Figures 9.2 and 9.3 respectively. The effect of elevated $[K^+]_o$ on APDR was small compared to the reduced $[ATP]_i$ (Figure 9.2). However, elevated $[K^+]_o$ significantly influences the tissue CV in comparison to hypoxic tissue (Figure 9.3). The increment of resting potential in the hyperkalaemia tissue can be a cause of CV reduction. The major cause for the decrease in CV is the decrease in upstroke velocity and in amplitude of the AP during membrane depolarization due to the reduction of the magnitude of the inward $Na^+$ current. The total outward current was elevated during repolarisation when the reduced $[ATP]_i$ triggered the $I_{K,ATP}$ channel, hence abbreviating APD. APDR curve was flattened due to reduction of $[ATP]_i$ (Figure 9.2).

**Comparison of APDR of each cell type in Ischaemic tissue**

**A** TP06-Ischaemic epi APDR

**B** ORd-Ischaemic epi APDR

**C** TP06-Ischaemic endo APDR

**D** ORd-Ischaemic endo APDR

**E** TP06-Ischaemic M-cell APDR

**F** ORd-Ischaemic M-cell APDR

Legend:
- Normal
- ko=6.0 mM
- ko=7.0 mM
- ko=8.0 mM
- ATP=6.0 mM (0.117)
- ATP=5.0 mM (0.212)
- ATP=4.0 mM (0.306)
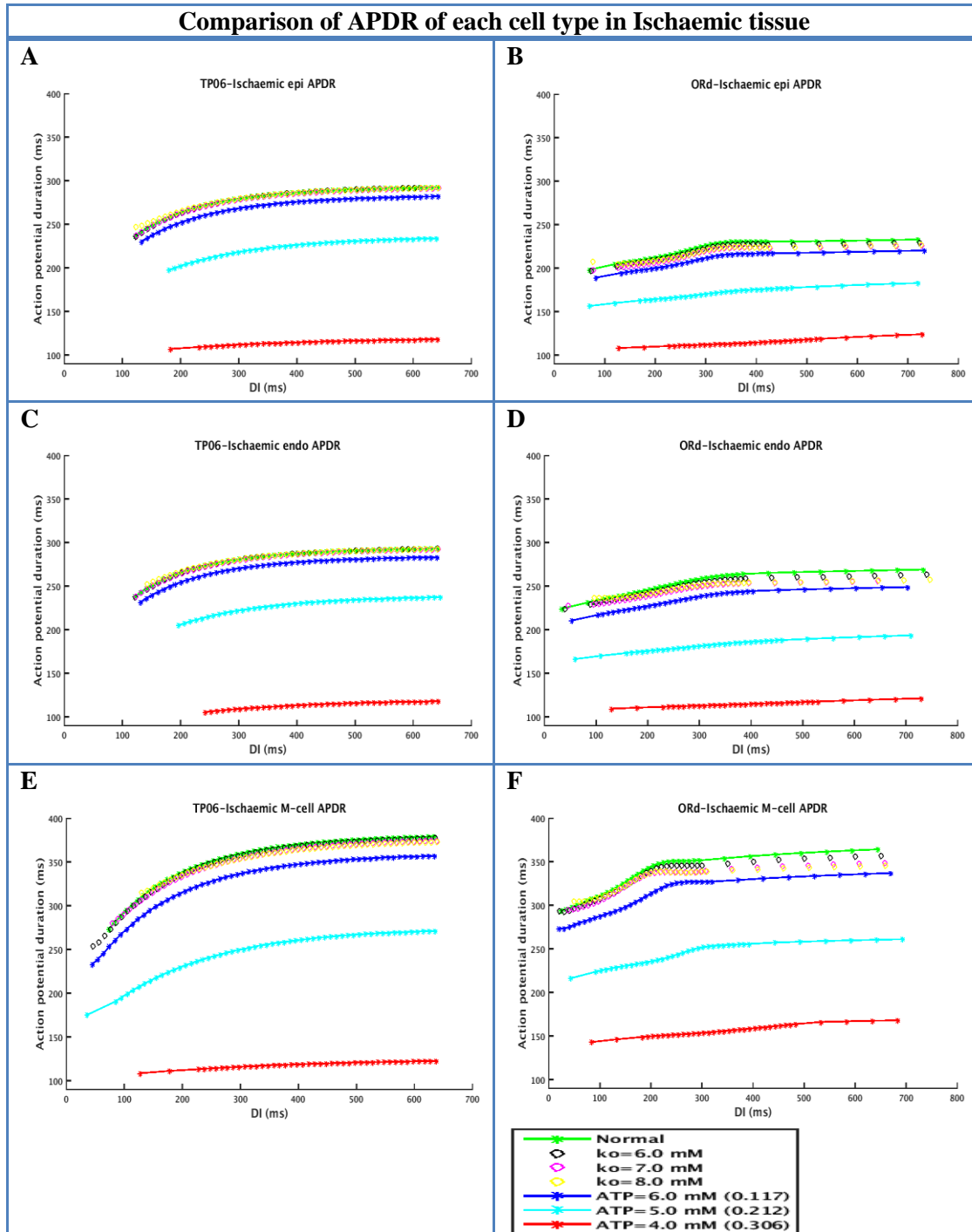
**Figure 9.2. Effect of decreased $[ATP]_i$ and increased $[K^+]_o$ on APDR in TP06 and ORd models: the current is presented using the Shaw and Rudy (1997) formulation with a normal value of $[ATP]_i$ (6.8 mM) and $[K^+]_o$ (5.4 mM) (green). Outcomes from simulations of the Shaw and Rudy (1997) $I_{K,ATP}$ channel formulation with changing levels of $[ATP]_i$ (values of 6.0 (dark blue), 5.0 (light blue) and 4.0 (red) mM), representing hypoxia/ischaemic condition. The K0.5 parameter was set at 0.042 for the non-ischaemic case and 0.117, 0.212 and 0.306 for ischaemic simulations. $[K^+]_o$ was elevated with values between 6.0 (black), 7.0 (pink) and 8.0 (yellow) mM to represent hyperkalaemia. A, C and E represent APD restitution variations for epi, endo and M cell types in the TP06 model respectively. B, D and F represent APD restitution variations for epi, endo and M cell types, respectively in the ORd model.**

**Comparison of CVR of each cell type in Ischaemic tissue**
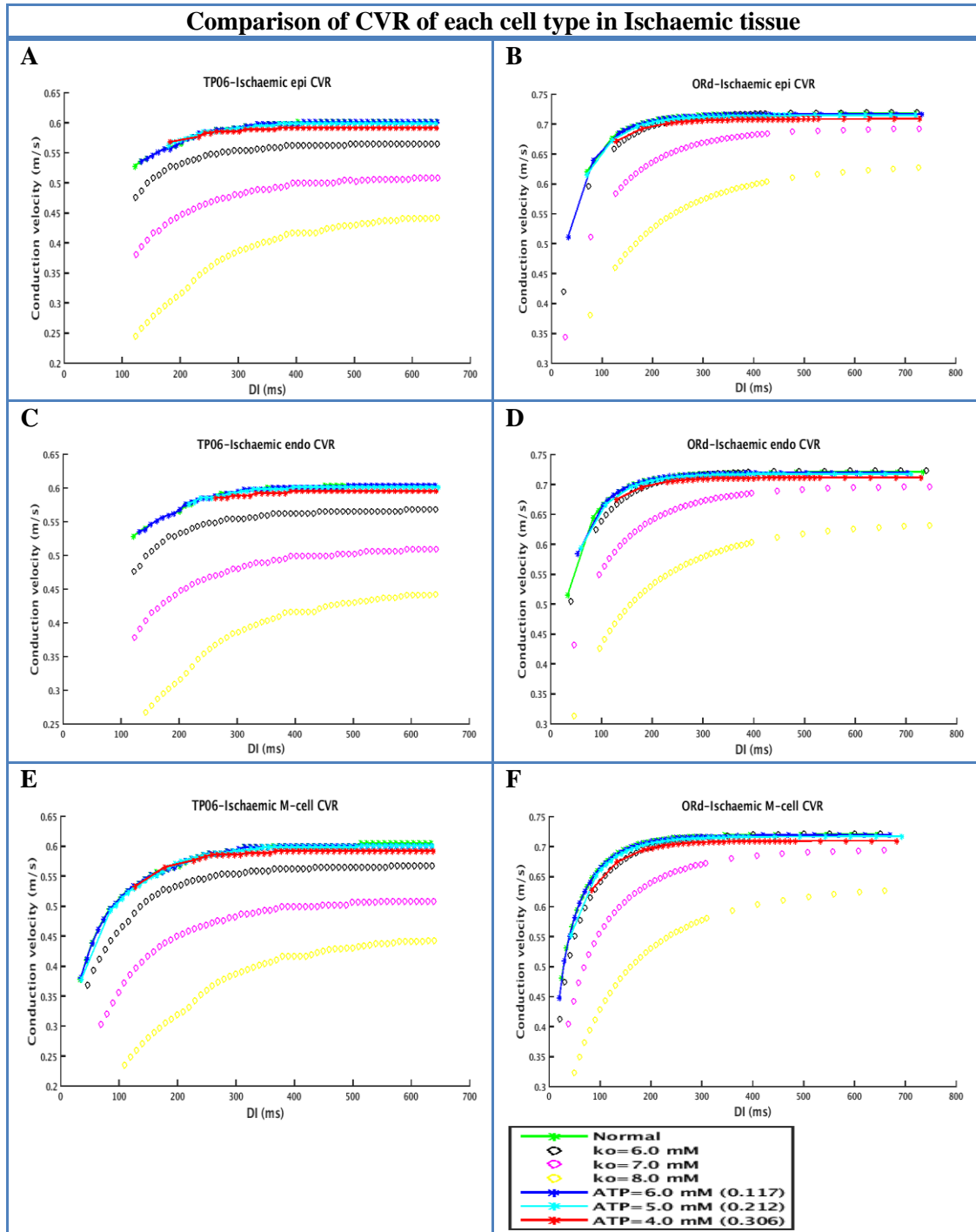
**Figure 9.3.** Effect of $[ATP]_i$ decreased and increased $[K^+]_o$ on CVR in TP06 and ORd models: the current is presented using the Shaw and Rudy (1997) formulation with a normal value of $[ATP]_i$ (6.8 mM) and $[K^+]_o$ (5.4 mM) (green). Outcomes from simulations of the Shaw and Rudy (1997) $I_{K,ATP}$ channel formulation with changing levels of $[ATP]_i$ (values of 6.0 (dark blue), 5.0 (light blue) and 4.0 (red) mM), representing hypoxia/ischaemic conditions. The K0.5 parameter was set at 0.042 for the non-ischaemic case and 0.117, 0.212 and 0.306 for ischaemic simulations. $[K^+]_o$ was elevated with values between 6.0 (black), 7.0 (pink) and 8.0 (yellow) mM representing hyperkalaemia. A, C and E, represent CV restitution variations for epi, endo and M cell types in the TP06 model respectively; B, D and F, represent CV restitution variations for epi, endo and M cell types in the ORd model respectively.

### 9.3.2 Behaviour of Spiral Wave Re-entry during Global Myocardial Ischaemia

In this section, a single spiral wave re-entry was used as the initial condition for simulating the behaviour of spiral re-entry waves with all combinations of $[ATP]_i$ and $[K^+]_o$ (Figure 8.4). Stable re-entry occurred for all combinations. The average period of re-entry is summarized in Table 8.1 for various combinations of $[K^+]_o$ and $[ATP]_i$ using three cell types (epi, M and endo). Although the reduced CV consequent to increased $[K^+]_o$ acts to prolong the period of re-entry, the unchanged CV resulting from reduced $[ATP]_i$ acts to shorten the period of re-entry (Table 9.6) and therefore to augment activation rate.

Results show a stable re-entrant wave with an average period of 245, 240 and 310 ms (TP06) and 215, 255 and 330 ms (ORd) respectively for epi, endo and M cells in normal tissue. The ORd periods correspond to dominant frequencies between 3.03 Hz (M cell), 3.92 Hz (endo) and 4.65 Hz (epi). The TP06 dominant frequencies for the normal re-entry periods are 3.22 Hz (M cell), 4.08 Hz (epi) and 4.16 Hz (endo). These results are well matched with the value of average dominant frequency obtained in clinical data (Bradley et al. 2011). A stable re-entry resulted with an augmented average period of 250, 310 and 490 ms in respect to elevating $[K^+]_o$ to 6.0, 7.0 and 8.0 mM in the TP06 (epi) model. Similar results were obtained for the ORd model (Table 9.6). The prolongation in period during ischaemia was compatible with the decrease in dominant frequency obtained in clinical data (Bradley et al. 2011).
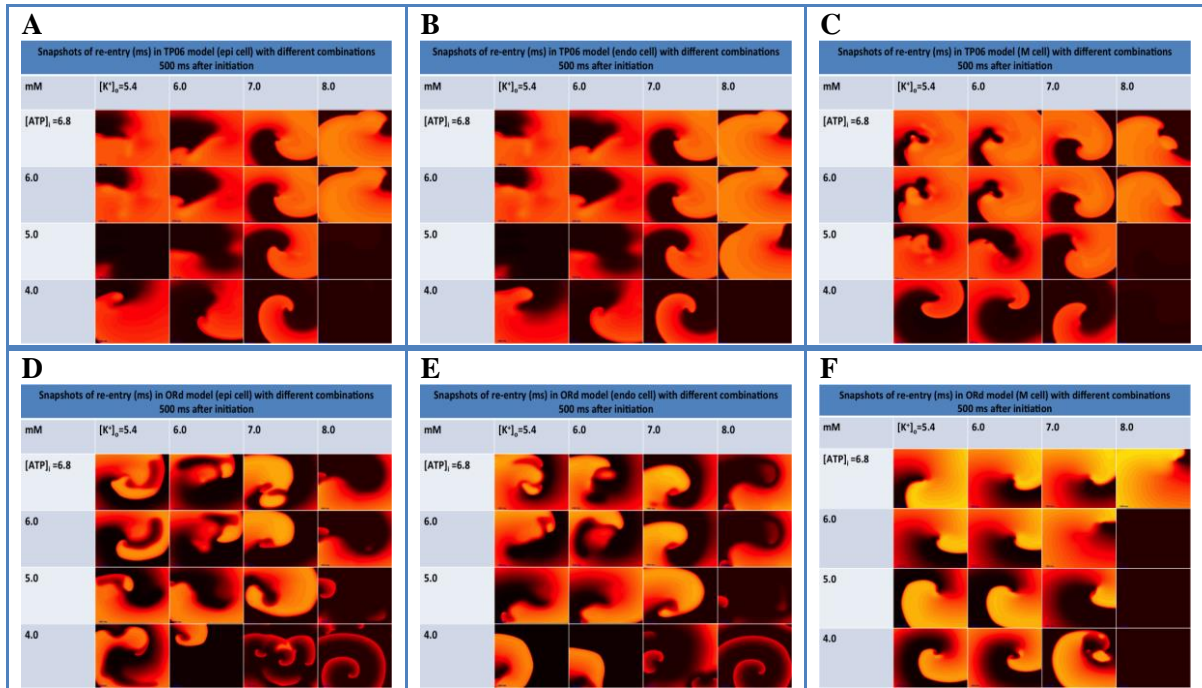
**Figure 9.4. Snapshots of re-entry (ms) in TP06 and ORd models using three cell types (epi, M and endo) with various combinations of $[K^+]_o$ and $[ATP]_i$, 500 ms after initiation: colour intensity shows membrane voltage, with brighter colours indicating more depolarised tissue. A, B and C represent spiral wave re-entry changes with a combination of ischaemic components for epi, endo and M cell types in the TP06 model respectively. D, E and F represent spiral wave re-entry changes with a combination of ischaemic components for epi, endo and M cell types in the ORd model respectively.**

**Table 9.6. Average period of spiral wave re-entry (ms) in respect to simulations of various combinations of $[K^+]_o$ and $[ATP]_i$ for TP06 and ORd models: A, C and E represent average period of spiral wave re-entry (ms) for epi, endo and M cell types in the TP06 model respectively, B, D and F average period of spiral wave re-entry (ms) for epi, endo and M cell types in the ORd model respectively. Empty cells (-) mean no stable re-entry was observed for these parameters.**

**Average period of spiral wave re-entry (ms)**

**TP06**

**A**

TP06 model epi cell: Average period of spiral wave re-entry (ms)

| $[ATP]_i/[K^+]_o$ (mM) | 5.4 | 6.0 | 7.0 | 8.0 |
|---|---|---|---|---|
| 6.8 | 245 | 250 | 310 | 490 |
| 6.0 | 235 | 250 | 310 | 490 |
| 5.0 | 190 | 210 | 285 | - |
| 4.0 | 170 | 180 | 235 | - |

**B**

ORd model epi cell: Average period of spiral wave re-entry (ms)

| $[ATP]_i/[K^+]_o$ (mM) | 5.4 | 6.0 | 7.0 | 8.0 |
|---|---|---|---|---|
| 6.8 | 215 | 260 | 265 | 345 |
| 6.0 | 190 | 220 | 220 | 310 |
| 5.0 | 180 | 190 | 200 | 205 |
| 4.0 | 140 | 150 | 180 | - |

**C**

TP06 model endo cell: Average period of spiral wave re-entry (ms)

| $[ATP]_i/[K^+]_o$ (mM) | 5.4 | 6.0 | 7.0 | 8.0 |
|---|---|---|---|---|
| 6.8 | 240 | 250 | 310 | 480 |
| 6.0 | 210 | 250 | 305 | 450 |
| 5.0 | 190 | 210 | 300 | 400 |
| 4.0 | 160 | 180 | 240 | - |

**D**

ORd model endo cell: Average period of spiral wave re-entry (ms)

| $[ATP]_i/[K^+]_o$ (mM) | 5.4 | 6.0 | 7.0 | 8.0 |
|---|---|---|---|---|
| 6.8 | 255 | 290 | 310 | 390 |
| 6.0 | 260 | 260 | 270 | 360 |
| 5.0 | 200 | 190 | 260 | 330 |
| 4.0 | 140 | 170 | 190 | 310 |

**E**

TP06 model M cell: Average period of spiral wave re-entry (ms)

| $[ATP]_i/[K^+]_o$ (mM) | 5.4 | 6.0 | 7.0 | 8.0 |
|---|---|---|---|---|
| 6.8 | 310 | 340 | 380 | 510 |
| 6.0 | 290 | 325 | 360 | - |
| 5.0 | 245 | 278 | 330 | - |
| 4.0 | 180 | 220 | 255 | - |

**F**

ORd model M cell: Average period of spiral wave re-entry (ms)

| $[ATP]_i/[K^+]_o$ (mM) | 5.4 | 6.0 | 7.0 | 8.0 |
|---|---|---|---|---|
| 6.8 | 330 | 345 | 360 | 455 |
| 6.0 | 330 | 330 | 350 | - |
| 5.0 | 260 | 265 | 300 | - |
| 4.0 | 170 | 185 | 240 | - |

To test the stability of re-entry in tissue with various heterogeneities of $[K^+]_o$ and $[ATP]_i$ in the TP06 model, re-entry in $100 \times 100$ mm ($400 \times 400$ grid points) 2D virtual tissue with epicardial cell type was induced by applying an Archimedian spiral as an initial condition operating the phase technique (Clayton & Holden 2002a; Clayton & Holden 2002b). Figure 9.5 shows activation isochrones in this model for a re-entry cycle beginning 500ms after launch. The re-entry was stable during the 2 seconds of running simulation. The period of re-entry is summarized in Table 9.7 for TP06 epicardial tissue. Figure 9.6 shows the number of phase singularity changes for each simulation and highlights the steadying effect of elevated $[K^+]_o$ and decreased $[ATP]_i$. These results indicate that the influence of global cardiac ischaemia with increase of $[K^+]_o$ is to steady spiral wave re-entry, decreasing the number of phase singularities and wave fronts. Although the reduced $[ATP]_i$ and increased $[K^+]_o$

suppress wave break and the formation of new phase singularity, these results (Figure 9.6) are not compatible with the stable augmentation in phase singularity and wave fronts obtained in clinical data (Bradley et al. 2011; Clayton et al. 2011).



Table 9.7. Average period of spiral wave re-entry (ms) in simulations with various combinations of $[K^+]_o$ and $[ATP]_i$ for TP06 model (epi cell).

| TP06 model epi cell: Average period of spiral wave re-entry (ms) | | | | |
|---|---|---|---|---|
| $[ATP]_i/[K^+]_o$ (mM) | 5.4 | 6.0 | 7.0 | 8.0 |
| 6.8 | 245 | 250 | 310 | 490 |
| 6.0 | 235 | 250 | 310 | 490 |
| 5.0 | 190 | 210 | 285 | - |
| 4.0 | 170 | 180 | 235 | - |
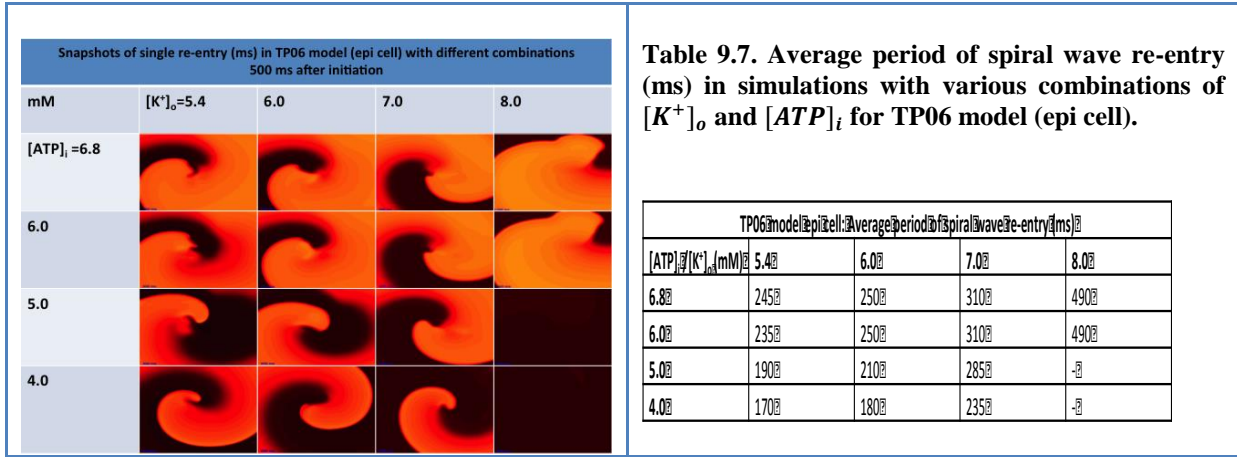
**Figure 9.5. Snapshots of re-entry (ms) in TP06 model (epi cell) with different combinations of $[ATP]_i$ and $[K^+]_o$, 500 ms after initiation: colour intensity shows membrane voltage, with brighter colours indicating more depolarised tissue. Empty cells (-) mean no stable re-entry was observed for these parameters.**

| $[ATP]_i/$ $[K^+]_o$ mM | 5.4 | 6 | 7 | 8 |
|---|---|---|---|---|
| 6.8 | | | | |
| 6.0 | | | | |
| 5.0 | | | | |
| 4.0 | | | | |
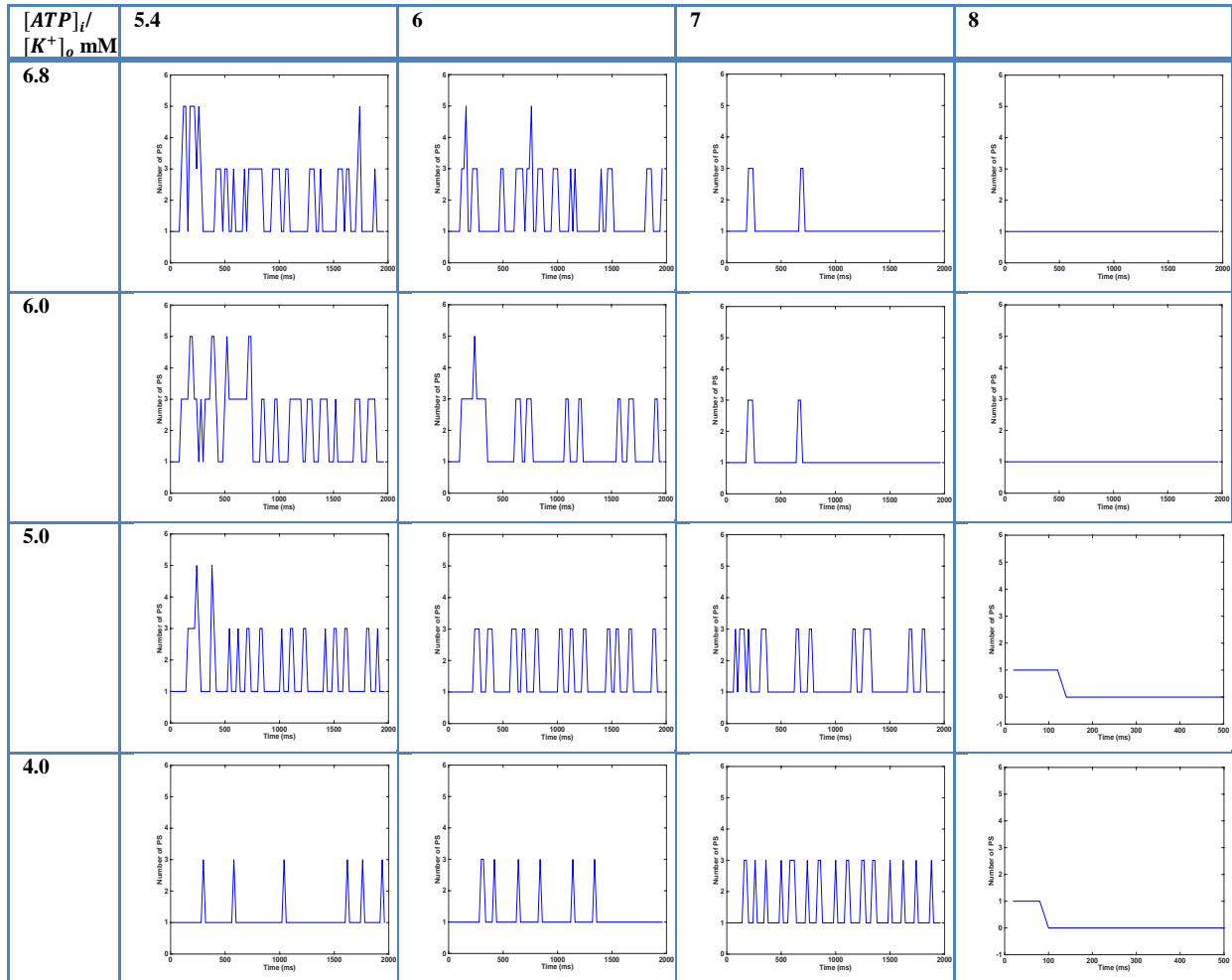
**Figure 9.6. The number of PSs during 2 seconds of simulations presented in Figure 9.5: simulations have been done for the setting with the parameter values from Table 2 of the TP06 paper (Ten Tusscher & Panfilov 2006) corresponding to a restitution slope of 1.1 (normal).**

The next section (Section 9.3.3) examines the idea that the flattening of APDR consequent to decreased $[ATP]_i$ and increased $[K^+]_o$ would be expected to augment re-entry stability in ischaemic cardiac tissue. Multiple wavelet re-entries (simulated by applying a restitution slope of 1.8) as an initial condition for simulations with hypoxia and hyperkalaemia were applied to test this hypothesis.

### 9.3.3 Effects of Simulated Ischaemia on Spiral Wave Re-entry (2D Model) Behaviour during Arrhythmia

The effect of the flattening of APD restitution resulting from increased $[K^+]_o$ and decreased $[ATP]_i$ was explored to test the stability of re-entry in ischaemic cardiac tissue. For this purpose, multiple wavelet re-entries (with a restitution slope set at 1.8) as an initial condition were used for simulations with increased $[K^+]_o$ and decreased $[ATP]_i$. Figure 9.7 shows snapshots of spiral wave dynamics for the setting with an APDR slope of 1.8 in non-

199

ischaemic tissue. Spiral wave dynamics were simulated for 2s. This figure represents spiral break up with intermittent wave break. In Figure 9.8 simulations with depleted $[ATP]_i$ and elevated $[K^+]_o$ represent a better trend of the multiple wavelets to stabilise re-entrant waves.
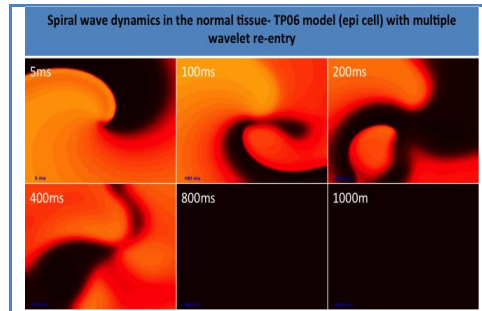


**Figure 9.7. Snapshots of re-entry in TP06 model (epi cell) applying a restitution slope of 1.8 related to the parameter values in the TP06 paper (Table 2) (Ten Tusscher & Panfilov 2006) in normal tissue.**
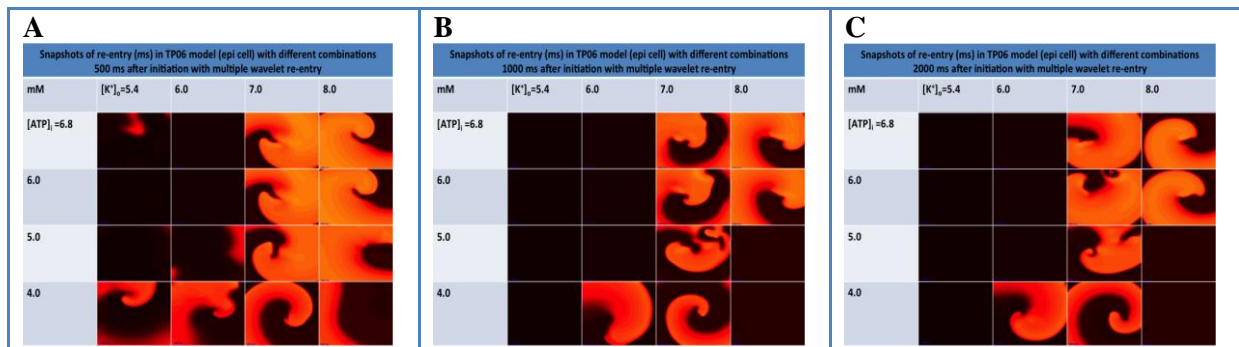


**Figure 9.8. Snapshots of re-entry in TP06 model (epi cell) with various combinations of $[K^+]_o$ and $[ATP]_i$ with a restitution slope set to 1.8 representing the parameter values in the TP06 paper (Table 2) (Ten Tusscher & Panfilov 2006), (A) 500 ms after initiation, (B) 1000 ms after initiation and (C) 2000 ms after initiation.**

Figure 9.9 illustrates the total number of PSs in the simulations with various combinations of $[ATP]_i$, and $[K^+]_o$. The top row demonstrates outcomes for tissue with $[K^+]_o$ of 5.4, 6.0, 7.0 and 8.0 mM and $[ATP]_i$ of 6.8mM. Simulations with $[ATP]_i$ reduced to 6.0, 5.0 and 4.0 mM are shown in the second, third and fourth (bottom) rows. For simulations with different $[K^+]_o$ the number of PSs slowly reduced for the period of 2 s. In the simulation with $[ATP]_i$ of 4.0 mM, Figure 9.9 shows the activation pattern is stabilised rapidly. Similarly to the previous section (simulation with a single spiral wave re-entry), the results indicate that the elevated $[K^+]_o$ and depleted $[ATP]_i$ prevent wave break and the formation of new PS.

| $[ATP]_i/$ $[K^+]_o$ mM | 5.4 | 6 | 7 | 8 |
|---|---|---|---|---|
| 6.8 | | | | |
| 6.0 | | | | |
| 5.0 | | | | |
| 4.0 | | | | |
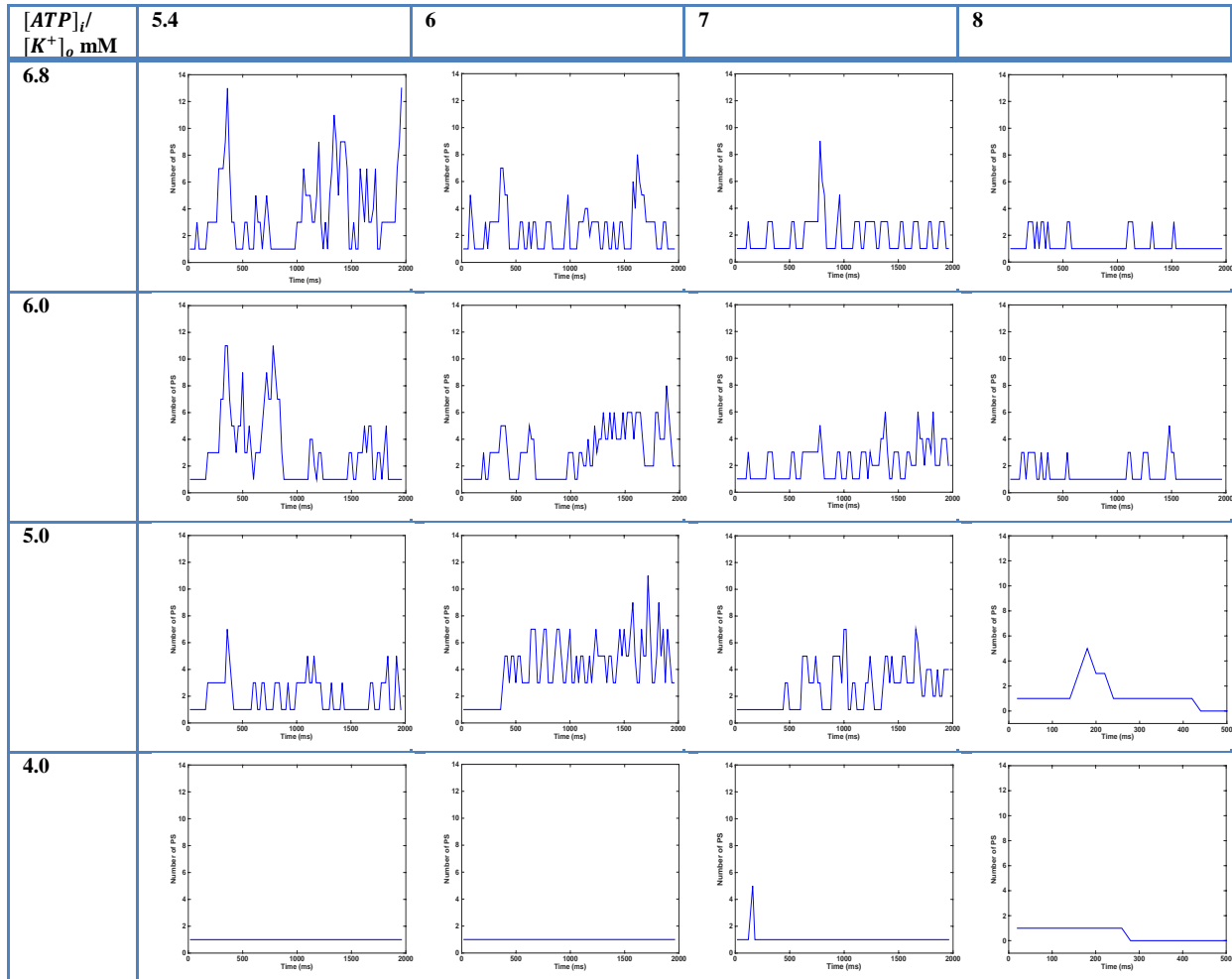


**Figure 9.9. The number of PSs in the 2s simulations presented in Figure 9.8: simulations were run with a restitution slope of 1.8, and correlated to the parameter values in the TP06 paper (Table 2) (Ten Tusscher & Panfilov 2006).**

### 9.3.4 Effects of Simulated Ischaemia on Scroll Wave Re-entry (3D Model) Behaviour during Arrhythmia

It is difficult to quantify and analyse the complexity of surface activation patterns during both experimental and computational VF (Clayton & Holden 2002a). The complicated behaviour can be explained by analysis of filament movement and dynamics. For instance, detection of phase singularity points and the movement of activation wavelets in experimental VF (Gray et al. 1998; Rogers et al. 1999) have been used to identify the intersections of filaments with the surface (Clayton & Holden 2002a). The computational models studied the movement of phase singularities in 2D simulations, and the stability and the size and rotation of filaments in 3D simulations (Biktashev et al. 1994; Biktashev & Holden 1998; Fenton & Karma 1998). The behaviour of re-entry with filaments was examined within the virtual tissue (anisotropic 3-D slabs, $100 \times 100 \times 15$ mm) in this section. How ischaemic components can affect the

stability of re-entrant waves was investigated. Figure 9.11 shows the portraits of the filaments 100, 400, 900 and 1800 ms after initiation for $D_{||} = 0.0121$ and $D_{\perp} = 0.0928\ mm^2 ms^{-1}$ for the non-ischaemic tissue. It can be seen that the number of filaments increased throughout an initial period up to 2000 ms for all of the simulations.



| 100 ms | 400ms | 900 ms | 1800 ms |
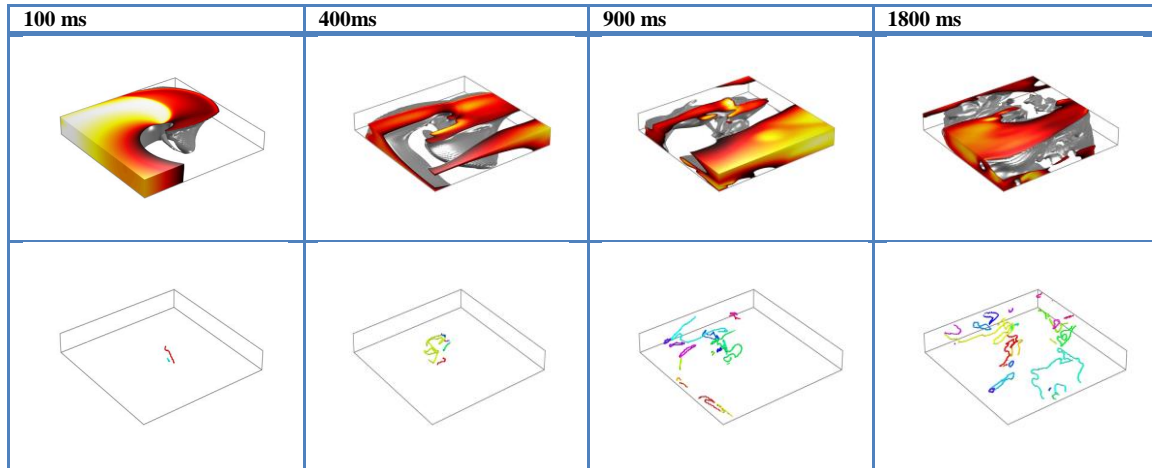
**Figure 9.11. Filament configuration and interactions in uniform anisotropic model (Clayton et al. 2006) (non-ishchaemic tissue) with excitability modelled by the TP06 model. Top row; examples of 3D re-entry with multiple scroll waves (voltage field, with depolarized regions enclosed by an isosurface (Clayton 2008)). Bottom row: examples of multiple filaments at 100 ms after initiation, and portraits displaying later activity at 400, 900 and 1800 ms.**

Figure 9.12 shows the characteristics of filaments obtained over time in each ischaemic model. Example snapshots of 3-D re-entry with multiple scroll waves and the filaments 1800 ms after initiation are shown in the same figure. The number of filaments was decreased by increasing $[K^+]_o$. In contrast, with $[ATP]_i$ reduction there are not only more filaments in comparison with elevated $[K^+]_o$ simulations, but there is a greater complexity and wave break (instability) associated with $[ATP]_i$ fall. Figure 9.13 emphasises that the sum of filaments was reduced by applying ischaemic conditions (especially for the elevated $[K^+]_o$) in a virtual slab of tissue as observed in Figure 9.12.

Although Figure 9.9 and 9.13 indicate a similar result (reduction of PS and filament numbers by applying ischaemic conditions), the numbers of PSs were less than the number of filaments. Alterations in CV, consequence of the different diffusion (anisotropy diffusion for 3D simulations Figure 9.13 and isotropic diffusion for 2-D simulations Figure 9.9) ratio, were taken into account. This examination corresponded to the results in a study by ten Tusscher et al. (Ten Tusscher et al. 2007) using a biophysically and anatomically detailed model of VF in the human heart.

| $[ATP]_i$/ $[K^+]_o$ | 5.4 mM | 6.0 mM | 7.0 mM | 8.0 mM |
|---|---|---|---|---|
| 6.8 mM | | | | |
| 6.0 mM | | | | |
| 5.0 mM | | | | |
| 4.0 mM | | | | |
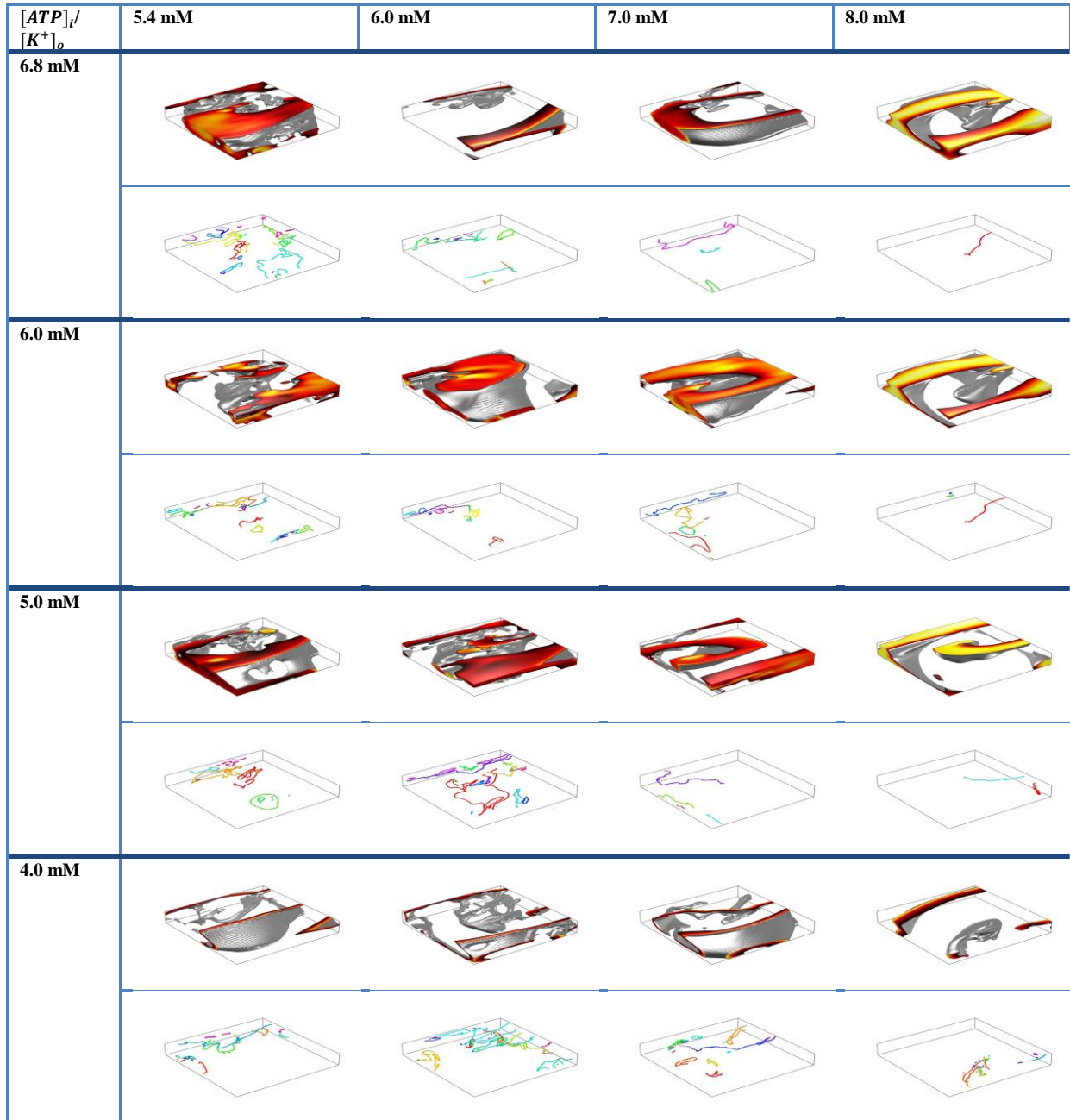
**Figure 9.12. Filament formation and connections in a homogenous anisotropic model (with various $[K^+]_o$, and $[ATP]_i$) with excitability described by the TP06 model. Top row; examples of 3D re-entry with multiple scroll waves (voltage field, with depolarized regions enclosed by an isosurface (Clayton 2008)). Bottom row: examples of multiple filaments after 1800 ms of initiation of 3-D scroll wave.**

| $[ATP]_i/$ $[K^+]_o$ | 5.4 mM | 6.0 mM | 7.0 mM | 8.0 mM |
|---|---|---|---|---|
| 6.8 mM | | | | |
| 6.0 mM | | | | |
| 5.0 mM | | | | |
| 4.0 mM | | | | |
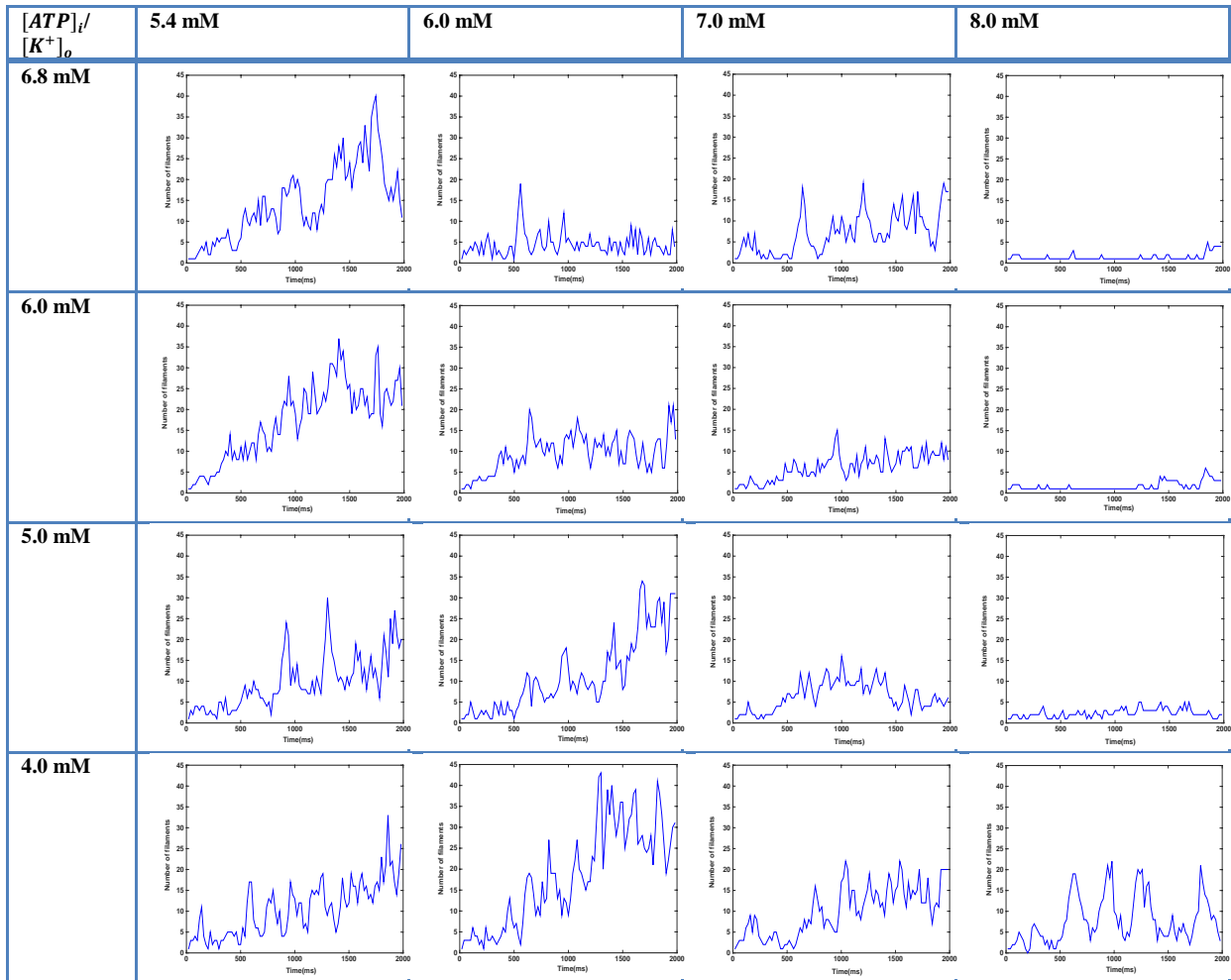
**Figure 9.13. Number of filaments for simulations with different $[K^+]_o$, and $[ATP]_i$ in an anisotropic slab geometry. All the simulations depicted used the TP06 model with a restitution slope of 1.8 related to the parameter values in the TP06 paper (Table 2) (Ten Tusscher & Panfilov 2006).**

## 9.4 Discussion

This chapter presents the effects of global ischaemia on the dynamic behaviour of ventricular arrhythmias in the human heart. Different approaches (restitution studies, 2-D spiral wave re-entry and 3-D scroll wave simulations) were used in various computational studies that represent the electrical activities in the virtual tissue during ventricular arrhythmias (e.g. VF). A computational model has been used in this study with the effects of ischaemia cellular changes on a simplified tissue geometry to describe the changes in VF activation rate obtained in empirical studies. Although a quantitative analysis of spiral wave re-entry period, PS and filament behaviour in our model is provided, further association between experimental and computational studies is required.

### 9.4.1 Effects of Ischaemic Components

The simulations show that elevated $[K^+]_o$ had a significant influence on cell excitability by depolarizing resting membrane, causing reduction in sodium channel availability (Shaw & Rudy 1997) and acted to increase wavelength and reduce CV, while reduced $[ATP]_i$ and triggering the ATP-dependent potassium current, $I_{K,ATP}$, acted to decrease APD (Figure 9.2) and mimic AP shape variations (Figure 9.1) that are detected experimentally (Ettinger et al. 1974; Kodama et al. 1984). The formulation of $I_{K,ATP}$ described by Shaw and Rudy (1997) was chosen to show the influence of lowering $[ATP]_i$ on the APD changes. $[ATP]_i$ value was decreased to a lowest value of 4.0 Mm that might be less than the value expected for around 3 min of ischaemia. Results here are consistent with experimental studies (Sutton et al. 2000) in that APD is reduced from around 256 ms to 189 ms during 3 min of ischaemia. Changes in resting potential caused by increased $[K^+]_o$ tend to reduce the magnitude of $I_{Na}$ during depolarisation and reduce maximum upstroke velocity, $(dV_m/dt)_{max}$, and consequently reduce CV (Figure 9.3). These results would be expected from experimental findings ( Wilde et al. 1990; Kodama et al. 1984). Although modelling (Shaw & Rudy 1997) and experimental (Kodama et al. 1984) studies demonstrate that extracellular accumulation of $K^+$ can be related to APD shortening, results here obtained little change (Figure 9.2).

### 9.4.2 Role of Restitution Heterogeneity

Theoretical and experimental studies have shown that electrical stability in the myocardium can be determined by the APD restitution properties which play a major role in the onset of ventricular fibrillation (VF). Clinical and computational studies in ventricular muscle have

shown that the electrical restitution of the APD and CV in ventricular muscle is an important factor in controlling the dynamic instability, and can contribute to the wave break that operates fibrillation (Karma 1994; Qu et al. 1999; Riccio et al. 1999; Xie et al. 2001; Garfinkel et al. 2000; Qu et al. 2000; Weiss et al. 2000). For instance, parameter variation in restitution slopes (steepening of the slope of APD restitution) has been presented as encouraging wave-break and VF (Keldermann et al. 2008). Two human ventricular cell models (TP06 and ORd) were used here to investigate spiral wave stability influenced by the electrical restitution properties in simulated 2-D cardiac tissue (homogeneous) with global myocardial ischaemia. The stabilisation of spiral wave re-entry can be explained by the flattening of APD restitution from reduced $[ATP]_i$ and elevated $[K^+]_o$ obtained from both models in ischaemic tissue.

### 9.4.3  Dynamic Behaviour of Spiral Wave Re-entry during Global myocardial Ischaemia

The effects of ischaemic components (hyperkalaemia and hypoxia) were simulated to determine the behaviour of spiral wave re-entry in simulated 2-D cardiac tissue using the TP06 and ORd ventricular action potential models, which contain detailed physiological formulations of most of the important cardiac ionic currents. The results obtained from both models were similar and indicate that simulated ischaemia (for all combinations of $[ATP]_i$ and $[K^+]_o$) increased the stability of re-entry. The period of re-entry increased by elevating $[K^+]_o$ due to a reduction in CV, while unchanged CV caused by reduced intracellular $[ATP]_i$ acted to reduce the period of re-entry and thus to raise the activation level (Table 9.6). The flattening of APD restitution from increased $[K^+]_o$ and lowered $[ATP]_i$ in ischaemic tissue can explain the stability of spiral wave re-entry. This idea was tested by operating multiple wavelet re-entry (unstable re-entry generated by steep restitution gradients) for simulations with increased $[K^+]_o$ and reduced $[ATP]_i$ to convert unstable re-entry to stable re-entry. For this purpose, the numbers of PSs obtained from both simulations were compared (Figures 9.6 and 9.9). The results emphasize that ischaemia acts to reduce instability of re-entry (Figure 9.9). Figure 9.6 shows that elevation of $[K^+]_o$ in the tissue had significant electrophysiological effects on spiral wave dynamics and the reduction of numbers of PSs, whilst Figure 9.9 showed the lowered $[ATP]_i$ as the most effective ischaemic component in reduction of instability of re-entry. This is because the flattening of APD restitution resulting from reduced $[ATP]_i$ tended to augment the sustainability of re-entry.

### 9.4.4 Interaction of Ischaemic Simulations and Human Ventricular Arrhythmia

Experimental data from the human heart (Bradley et al. 2011) indicate that the major consequences of global myocardial ischaemia on VF activation are dominant frequency (DF) reduction, and an increment in the total number of PSs and wave fronts. Although results in this study showed that the main effect of $[K^+]_o$ accumulation was a moderate decrease in CV and thus a fall in DF, during simulated re-entry in the 2-D model, the activation frequency in normal and ischaemic tissue was less than the DFs obtained in the human heart. This difference could be due to the complexity of surface excitation patterns (Keldermann et al. 2008; Ten Tusscher et al., 2009) that can be observed from 3-D tissue simulation of VF in comparison to 2-D tissue . The influence of simulated reflow was neglected in this study. Simulated reflow would have a significant effect on excitation rate that could be the consequence of $[K^+]_o$ washout (Clayton et al. 2011). One factor which may play a role in preventing wave break and promoting stable rotors (Figure 7.9) is the effects of flattening of APD restitution due to the hypoxia/ischaemia (reduction of $[ATP]_i$). Results here (Figure 9.9) are in agreement with a recent study (Boyle et al. 2013) that show $I_{K,ATP}$ blockade as a crucial factor leading to a drop in activation rate and VF termination.

Although our results from ischaemic simulations (Figures 9.6 and 9.9) act to stabilise re-entry, parameter variation can act in sustaining wave break observed in experimental data (Bradley et al. 2011) and in our 3-D simulations (Figures 9.12 and 9.13); several mechanisms have been discussed (Panfilov & Keener 1995; Fenton et al. 2002; Panfilov, 2002; Bueno-Orovio et al. 2008) to clarify the different mechanisms of wave break during human VF and how they operate in 3-D tissue. These mechanisms may be associated with negative filament tension related to decreased excitability (Biktashev et al. 1994). In addition, the shape, size and structure of the ventricular walls, trans-mural electrophysiological heterogeneities in AP shape and APD, and regional changes with regard to $K_{ATP}$ channels and $I_{K,ATP}$ activation (Michailova et al. 2007; Weiss et al. 2009) might play an important role in wave break (Clayton et al. 2011) and VF modulation as ischaemia progresses (Bradley et al. 2011). The total number of filaments sustaining VF can be obtained from the geometric characteristics of cardiac tissue, such as size of the ventricles and the wavelength of re-entry (Clayton et al. 2006). Thus, further work is required to quantify these possible effects.

### 9.4.5  Conclusion

Computational models were used in this study to show the mechanisms of re-entry and ventricular arrhythmias during global ischaemia. However, the anatomy and electrophysiology of real cardiac ventricles are more complex than the simulations (Clayton & Holden 2002a) presented in this study. A number of features are not involved in this study, such as non-uniform anisotropic virtual tissue geometries, regional differences in cellular electrical properties and the influences of drug interventions that can affect the complexity of re- entrant activity during fibrillation (Clayton & Holden 2002b). Thus, it is important to understand how these aspects influence filament interaction and movement to investigate the basic mechanisms of VF and propose new protective approaches.

Despite all these limitations, the major electrical changes associated with ischaemia were simulated in 2D and 3D models. The tissue models mimic APDs and maximum CV values (measured by pacing protocols) close to experimental observation along with clinically relevant dominant frequencies. Finally, further study is suggested to investigate the effect of tissue thickness and anatomy on the stability of re-entry when the heart becomes globally ischaemic during VF.

# 10  Summarizing Discussion

*This section summarises the discussions in this thesis by presenting the main achievements. The study investigated models of human cardiac cell and tissue, with a special focus on global cardiac ischaemia. Ischaemia heterogeneities during ventricular arrhythmias were characterised by analysing recent human AP ventricular models under varied ischaemic conditions using 2-D and 3-D computational models. Then, the limitations of this study are described, followed by directions for future work and concluding comments.*

## 10.1 Review

This thesis aimed to study the dynamic behaviour of human cardiac tissue during ventricular arrhythmias under ischaemic conditions. Two main studies were planned to investigate the effects of simulated ischaemia at the cellular level on the behaviour (and period) of spiral wave re-entry at tissue level (2-D and 3-D) and to determine the possible link between the activation patterns in a simulation with electrical patterns recorded from a surface of the human heart. These investigations may be useful in examining the consequences of global ischaemia on the regulation of ventricular arrhythmias in the human heart. Therefore, this thesis was divided into two parts:

**Part I (Chapters 4-5)** dealt with cardiac cellular modelling with a focus on electrophysiology models of human ventricular myocytes. Several human ventricular cell models were compared to propose an appropriate model for examination of ventricular arrhythmias. Different $I_{K,ATP}$ models to simulate hypoxia/ischaemia were also studied.

**Part II (Chapters 6-9)** dealt with cardiac tissue modelling with focus on the effects of heterogeneous action potential duration restitution and effective refractory period with the potential role of ischaemic components and 3-D models of tissue heterogeneity to address the influence of ischaemia on the stability of re-entry.

**Part I**

**Chapter Four** presented a general review of modelling the cardiac cell comparing different human ventricular cells models. A general description of the electrical activities for each model was provided and some of the deformations of the cellular action potential shapes that may affect cardiac excitable behaviour were described. The physiological mechanism underpinning the electrophysiological behaviour of each cell model was compared in this chapter. AP features achieved from the epicardial cell type of the six cellular human ventricular models were compared. The strengths and limitations of each model were discussed to select the best model to utilize for cardiac tissue studies. Although similarity of the simulated electrical behaviour was observed in all single cell models (described in this chapter), these simulations were not an exhaustive representation of all conditions; this precluded selection of a definitive model for the simulations.

At the end of this chapter, two human ventricular AP models were selected as suitable for the study of ventricular arrhythmias. The Ten Tusscher and Panfilov (TP06) model (Ten

Tusscher & Panfilov 2006) and the O'Hara, Vira, Varro and Rudy (ORd) model (O'Hara et al. 2011) were proposed for the study of the electrical activity of ventricular cells at tissue level. These two models were chosen for two main reasons:

Firstly, the TP06 model is the most extensively used model, including many reformulated currents, and simulates physiological restitution and alternans (O'Hara et al. 2011).

Secondly, the ORd model includes more detailed physiological data concerning intracellular calcium dynamics and trans-membrane currents.

**Chapter Five** described four different formulations of $I_{K,ATP}$ that play an important role in hypoxic/ischemic episodes. For example, it is known that $K_{ATP}$ channels are linked to the shortening of the AP during hypoxia and ischaemia. The interaction of each formulation on the electrophysiological variations at the level of ion channels was investigated.

One of the main effects of modulation of $I_{K,ATP}$ was the voltage changes with reduction of $I_{K,ATP}$ in each model. Current-voltage properties of each $I_{K,ATP}$ model and their slope of voltage dependency were compared to evaluate the quantitative influences of $I_{K,ATP}$ formulations. Although the results show the similarity of dynamic behaviour and response to simulated ischaemia in these models despite different formulations of $I_{K,ATP}$, it was concluded that the Shaw and Rudy formulation had a greater influence than other $I_{K,ATP}$ formulations for modest changes in $[ATP]_i$. Thus, this $I_{K,ATP}$ formulation was selected for use in the simulations of ischaemia at tissue level in **Chapters 7 to 9**. Furthermore, the simulations here support the idea that $K_{ATP}$ channel activation does not completely interfere with the experimental cellular $K^+$ efflux throughout hypoxia/isachaemia.

One of the important limitations in this study was that due to a lack of a physiological role during hypoxia and lack of sufficient experimental data, all factors which may contribute to $I_{K,ATP}$ models during hypoxic/ischaemic situations are not considered in most of these studies to formulate a reliable model.

**Part II**

The dynamic behaviour of normal tissue was studied in **Chapter Six**. For this, the influences of APD and CV restitution on human ventricular 2-D tissue were examined. Restitution properties of epicardial (epi cell), mid-myocardial (M cell), and endocardial (endo cell) cells

in cardiac tissue were measured. This was considered a reasonable first step for investigating mechanisms of normal activation and propagation in simulated cardiac tissue. Electrical restitution properties are important factors in controlling the dynamic instability of spiral wave re-entry. This chapter compared the human model (TP06 and ORd) properties and the dynamic behaviour of each model. For example, the slope of restitution curves were measured as the main determinant of wave break. The results show that all restitution curves obtained from TP06 and ORd models have a similar shape with almost identical slopes under normal conditions. To find other possible mechanisms for arrhythmias in cardiac tissue, ischaemia was simulated in 2-D homogenous tissue in **Chapters Seven and Eight** and in 3-D heterogeneous tissue in **Chapter Nine**.

Study of the electrophysiological effects of ATP sensitive potassium current on the dynamic behaviour of simulated human ventricular tissue was continued in **Chapter Seven**. Action potential characteristics of a selection of $I_{K,ATP}$ models on two 2-D monodomain tissue models were analysed. The results show that $I_{K,ATP}$ activation acts to shorten APD and flatten APDR in all models; this was similar to the results presented in experimental studies (Weiss et al. 1992; Nichols et al. 1991; Faivre & Findlay 1990). The behaviour of spiral wave re-entry in normal and hypoxic/ischaemic (reduction of $[ATP]_i$) cardiac tissue was also studied. As expected, unchanged CV resulting from lowered $[ATP]_i$ tended to reduce the re-entry period and consequently to augment excitation rate. From comparison of different formulations of $I_{K(ATP)}$ embedded in two tissue models, it was found that the dynamic behaviour and the response to simulated ischaemia in these models was similar.

In **Chapter Eight,** repolarisation and refractoriness changes during ischaemia were examined in two 2-D tissue computational models. The relation between ERP changes and APD was discussed in this chapter. In agreement with experimental observation, the simulation results showed that effective refractoriness is prolonged despite the APD shortening. These results may contribute to maintenance of re-entry.

Finally, in **Chapter Nine**, the dynamic behaviour and impact of simulated global cardiac ischaemia during ventricular arrhythmias in the human heart was studied. Electrophysiological changes during ischaemia and arrhythmias were investigated for a better understanding of arrhythmia mechanisms. To overcome most of the limitations of the 2-D tissue models (**Chapters Six and Seven**), it was decided to use a more realistic 3-D

electrophysiological model of the human left ventricle. In this chapter, first, ischaemia effects on APD and CV restitution in 2-D models were determined followed by analysis of the behaviour of spiral wave re-entry. Then, the behaviour of spiral wave re-entry involved in sustaining arrhythmias was examined. Subsequently, a 3-D model with detailed electrophysiological properties of human ventricular cells (TP06 model) was used to investigate the possible mechanisms of ventricular arrhythmias which were related to the alterations in activation patterns detected during VF in the human heart with global ischaemia.

The simulations showed that the main component accountable for the alteration in activation rate during ischaemia was hyperkalemia, while hypoxia was responsible for APD reduction and AP shape changes observed experimentally (Ettinger et al. 1974; Kodama et al. 1984; Wilde et al. 1990; Sutton et al. 2000). The restitution simulations indicated that the flattening of APDR resulting from reduced $[ATP]_i$ increased the stability of re-entry in ischaemic tissue. In addition, the accumulation of $[K^+]_o$ in the tissue had major electrophysiological effects on spiral wave dynamics and reduction of number of PSs.

Indeed, the complexity of VF was observed through presentation of the number of scroll wave filaments (Figure 9.11). A study by Clayton et al. (2011) experimentally demonstrated that the major outcomes of global ischaemia on VF dynamics are DF reduction and an increment in the number of PSs and wave fronts in the human heart. The computational results in this study showed that the main effect of $[K^+]_o$ accumulation was a moderate decrease in CV and thus a fall in DF. The results suggest that ischaemic simulations (Figures 9.6 and 9.9) act to stabilise re-entry; however, it is believed that parameter variation acts to sustain wave break (Figures 9.12 and 9.13). In addition, different factors could be responsible for the mechanisms of wave break during human VF. For example, the geometrical characteristics of cardiac tissue (Clayton et al. 2006), shape , size and structure of the ventricular wall and decreased electrical activation and generated negative filament tension (Biktashev et al. 1994) might play important roles in wave break.

## 10.2 Limitations

There are some limitations in this study. Firstly, the 3-D simulations were restricted to the epicardium cells. They do not involve the reported sensitivity of multicellular (epicardium and endocardium) layers to ischaemia and VF dynamics. In addition, the Purkinje system, which may contribute to mechanism of VF maintenance (Tabereaux et al. 2009), was not

included in this study. Secondly, the models used in this study make some simplifying assumptions. These simplifications are summarized below:

First, isotropic or homogeneous anisotropic simplified virtual tissue geometries were used in this computational study. However, some experimental evidence (Yan et al. 1998) indicates that the tissue resistivity is high in a transitional zone between the sub-epicardial and mid-myocardial layers (Clayton & Holden 2004b).

Second, the mechanical behaviour of cardiac cells and tissue that might have an effect on the stability of re-entrant wave was ignored (Keldermann et al. 2010).

Third, the details of the cell metabolism modified by ischaemia were not considered (Michailova et al. 2007; Terkildsen et al. 2007), and the regional effects of ion channel communication were not accounted for (Weiss et al. 2009).

Fourth, the potential role of gap junction conductance affected by prolonged and sustained ischaemia (De Groot & Coronel 2004) was not studied; this is thought to support wave break.

Fifth, a monodomain model of cardiac tissue was applied in all the simulations; however, the bidomain model (used for more realistic boundary conditions) suggests that the filament behaviour close to the surface may be affected by the type of boundary  (Clayton et al. 2006).

Another limitation is the effect of the meander pattern of spiral waves on the filament dynamics (Clayton et al. 2006). In the 2-D simulations in this study, the meander varies for both the cell models used. Although the main results obtained for the ischaemic simulations are expected to be valid for filament changes, most studies indicate that filaments associated with fibre structure used models with stable and non-meandering filaments (Clayton et al. 2006).

An additional limitation is the possibility of result dependency on model type. Although the models studied in many cases display observed biological variability that match experimental data for some properties satisfactorily (Bueno-Orovio et al. 2008), reproducing experimental dynamic properties of the human ventricles remains a major modelling challenge. For example, the ORd model was not used in the 3-D modelling studies. It is emphasized that the unsuitability of the ORd model may have arisen for many possible reasons. Although the TP06 $I_{Na}$ formulation was substituted into the ORd model to provide a realistic CV, the

results showed that the ORd model failed to reproduce a reasonable restitution curve in tissue studies. The uniformity of the TP06 restitution curves represent a more stable model, which is a better match for the important properties in human cardiac tissue and more closely reproduces arrhythmia behaviour in experimental measurements. This was the justification for choice of the TP06 model to investigate arrhythmias in 3-D simulations.

Finally, another important limitation could be the difficulty of parameterisation for ischaemic simulation at the cell scale to provide reasonable parameter values (Romero et al. 2009). These are important in characterising the parameter sensitivity in cardiac cell models such as those associated with ischaemia, which will affect the tissue scale. Generating suitable tools and developing computational simulations are of significance in silico medicine to make a closer link between model and experiment. For example, the cardiac cells and tissue behaviour could be investigated in terms of development of myocardial ischaemia for longer simulations during the course of ischaemia (Clayton et al. 2011). Thus, due to the high computational cost and the time course of the variations in ischaemic components in the human heart, further studies are required in this field.

## 10.3  Future work

In this thesis, the role of global cardiac ischaemia on the dynamic behaviour of ventricular arrhythmias was studied. The effects of restitution data on the dynamics of ventricular arrhythmias were examined using two detailed ionic models to explain electrophysiological cell properties of human ventricular cells. It is believed that the addition of electrophysiological data and clinically measured tissue parameter variation are needed in the models to advance anatomical modelling of the human heart. The analysis of activation in the complex shape and fibre-sheet anatomy of the ventricular wall remains a future challenge (Clayton & Holden 2004b). Real cardiac ventricles are orthotropically anisotropic (LeGrice et al. 1995; Legrice et al. 1997) and that will affect electrophysiological properties such as filament dynamics and the stability and organization of VF; clearly, it would be interesting to incorporate this in future versions of the existing 3-D models used here.

More work is needed to investigate overall filament interactions and different types of filaments (short and longer) and their motion to study static and dynamic heterogeneity, and cardiac mechanics for filament stability in cardiac tissue in terms of ischaemia. In addition,

the effect of the shape and anisotropy of the ventricles as important impacts on filament behaviour needs to be quantified (Clayton et al. 2006).

## 10.4    Conclusion

This thesis investigated the dynamic behaviour of ventricular arrhythmias, focusing on the role of global cardiac ischaemia and tissue heterogeneity. Different models were used with different levels of complexity for modelling cardiac excitability, modelling cardiac ischaemia and the geometry of cardiac tissue. For cardiac excitability, cell models and tissue models were used. The simulations reproduced some important computable features of cardiac tissue, such as overall shape of the AP, AP and CV restitution properties, and the effects of ischaemia and parameter variation. By adding different $I_{K,ATP}$ models, as an important component of ischaemia, the impact of $I_{K,ATP}$ variability on human ventricular cellular electrophysiology was described. However, these models do not fully represent the detailed biophysical mechanisms of cardiac excitation in human ischaemic cardiac tissue; there is an incomplete understanding of the physiological effects of hypoxia, and a lack of sufficient data on different ionic channel dynamics within the cardiac cell membrane.

The conclusion regarding tissue parameter variation is that, although APD is essential for the initiation of wave breaks and re-entry, it also affects the dynamic behaviour of ventricular arrhythmias. The results here from ischaemic 3-D simulations indicate that parameter variation can act to sustain wave break detected in empirical data. Nevertheless, several factors can be effective in modulating mechanisms of wave break during human ventricular arrhythmias.

Although computational simulations are used to explore issues that cannot be addressed experimentally, a mixture of experimental, clinical, and computational studies will be required to fully investigate the different aspects of filament behaviour throughout ventricular arrhythmias. This computational study provided a comprehensible vision of the mechanisms that sustain arrhythmias during ischaemia.

In summary, the main novel contributions of this study are as follows:

The applicability of the most important recent human ventricular cell models was investigated in our tissue computational models to simulate global cardiac ischaemia. The results highlighted the limitations and advantages of each model in selecting the most appropriate cell model in tissue modelling.

Four different $I_{K,ATP}$ models were investigated for use in simulations of ischaemia. The question addressed was whether models based on data from guinea pig cells are relevant for simulating $I_{K,ATP}$ in human myocytes. In general, the results from models of $I_{K,ATP}$ presented in this study were well matched to experimental measurements.

Finally, for the main aim of this thesis: 'studying the effects of global cardiac ischaemia on the dynamics of ventricular arrhythmias in the human heart', recent detailed human ventricular cell models and a 3-D tissue model of the human left ventricle were used to examine filament behaviour during ventricular arrhythmias and the mechanisms that sustain arrhythmias.

# Appendix

**Contribution to SCAM**

- Converting ORd cell code to 2D tissue code according to available 2D TP06 code in the SCAM platform.
- Applying modifications to the code according to the requirements for all research questions defined for this PhD project.

This section presents a summary of the ORd 2D code representing APD and CV measurements in Section1 (Personal project). The Ischaemia simulation code is shown in Code A.2.1 and Code A.2.2. Section 3 shows how to compile and execute source code in a normal Linux console accompanying a script file (Code A.3.1).

## 1. Personal project

**Summary of the ORd 2D simulation code (used for restitution study)**

**Code A.1.1 Header**

The header file contains all required libraries, definitions and specifications of the size of 2D array, number of parameters specified in the array u, maximum space step (cm), time step (ms) with diffusion ($cm^2$/ms) and membrane capacitance ($\mu F/cm^2$).

**Code A.1.2 Constant values**

In this section cell type, pacing cycle length, timing and counting parameters are initialised.

**Code A.1.3 ORd current function**

This function includes model concentrations, buffers and all current formulations and functions related to the ORd human cell model. All the ionic currents are output of this function.

**Code A.1.4 Main function**

In the beginning of the main function local variables, variables related to S1 and S2 stimulus and all arrays are defined and initialised. The function for creating geometry and nearest neighbour arrays and initialising model state are listed in the main function. These steps were applied to the 2D code to express the requirements associated to the restitution studies:

- calculate current and APD for s1 stimulus
- solve monodomain equation by looping through each point
- store initial updates for voltage
- using loops through row and column so that stimulus can be applied to the left hand end (columns 1-3) of the 2D sheet

To apply PDE solver in ORd 2D code the following steps are designed in the main function:

❖ The PDE is solved using operator splitting, with a maximum dt as defined in the header file
➢ set up parameters for integration with adaptive time step
➢ Integration of ORd code with Euler method
➢ Calculation of diffusion
➢ Calculating new value of membrane voltage for current point
➢ update Vm with operator split diffusion steps, using dummy variables for speed

The APD and CV were measured in this function. The details of these measurements are shown in the code. At the end of the main function, all outputs are printed in the output files.

```c
                            Code A.1.1 Header

#include <math.h>

#include <stdlib.h>

#include <stdio.h>

#define ROWS            3       /* domain size, ny */

#define COLUMNS         100     /* domain size, nx */

#define NUM_PARAMETERS  41      /* number of parameters in u array */

#define NUM_ITERATIONS  25000

#define DT              0.005   /* maximum timestep (ms) */

#define DX              0.02    /* cm : Assume dx = dy */

/*original DIFFUSION =0.001171, but we reduced it by dividing by 4*/

#define DIFFUSION       0.00029275   /* cm2/ms :isotropic diffusion */

#define CM              1.0     /* Membrane capacitance (uF/cm2) */
```

```
                    Code A.1.2 Constant values

const int celltype=1;  //defining cell type: endo = 0, epi = 1, M = 2

const double CL=1000;  //pacing cycle length

double t0=0; /*introduce timing and counting parameters*/



                    Code A.1.3 ORd current function

double calculate_ORd_current_2D(double **u, int n, double dt, int celltype,
double Ist)

{

/* all ORd human model concentrations, buffers and all currents
formulations and functions are placed here */

return(INa+INaL+Ito+IKatp+ICaL+ICaNa+ICaK+IKr+IKs+IK1+INaCa+INaK+INab+IKb+I
pCa+ICab+Ist);

}
```

```
                    Code A.1.4 Main function

int main(int argc, char **argv)

{

/* local variables */

  int n;

  const int tmax = NUM_ITERATIONS;

  const int num_parameters = NUM_PARAMETERS;

  const int N = ROWS * COLUMNS;

  const int nrows = ROWS;

  const int ncols = COLUMNS;

  const double D = DIFFUSION;

  const double dx2 = DX*DX;

  const double dx = DX;

  const int V = 1;

  int **geom, **nneighb;
```

```c
int row, col;

double **u;

double Ist = 0.0;

double *new_Vm,*old_Vm;

double dummy1;

double outputCounter = 0.0;

//stimulus amplitude in uA/uF

const double amp=-80;

//start time of the stimulus, relative to each beat

const double start=0;

//duration of the stimulus in ms

const double duration=1.0;

double membraneCurrent = 0.0;

double diffusionCurrent = 0.0;

double thresh = -75;

double *u0, *u1, *d0, *d1;

double *cl, *di, *apd;

double distance;

double upstroke,downstroke,apd1,cv;

// variables related to S1 and S2 stimulus

int count= 0.0;

double junk = 0.0;

const double dt = DT;//in ms

const double s1 = 750;//in ms

// initialise S2 array

double s2[]=
{1000,950,900,850,800,750,700,650,600,550,500,450,400,350,300,250,0};

double time= 0.0;

double a1,u_n1,u_n2;

int t=0.0;
```

```c
    int x1,x2,n1,n2;

    int n_s2 = 0;

    int apply_stimulus;

    const double end_s1 = 9*s1+1;//10 s1's including stimulus at 0 plus 1ms

    int s2_stimulus =0;

    int loop_counter =0;

    double e_s1= end_s1/dt;
 /* defining output files */

    FILE *egptr;

    FILE *apdptr;

    FILE *cvptr;
/* Initialise arrays */

    u = fmatrix( 1, N, 1, num_parameters );

    new_Vm = fvector( 1, N );

    old_Vm = fvector( 1, N );

    geom = imatrix( 1, nrows, 1, ncols );

    nneighb = imatrix( 1, N, 1, 8 );

    u0 = fvector(1,N);

    u1 = fvector(1,N);

    d0 = fvector(1,N);

    d1 = fvector(1,N);

    di = fvector(1,N);

    cl = fvector(1,N);

    apd = fvector(1,N);

    for (n=1;n<=N;n++)

    {

        u0[n] = 0; u1[n] = 0;

        d0[n] = 0; d1[n] = 0;

        cl[n] = 0;

        di[n] = 0;
```

```c
        apd[n] = 0;

        old_Vm[n] = 0;

   }

/* open files for output */

  egptr = fopen("eg.out","w");

  apdptr= fopen("apd.out","w");

  cvptr= fopen("cv.out","w");

/* Create geometry and nearest neighbour arrays */

  initialise_geometry ( geom, nrows, ncols, N, u, nneighb );

/* Initialise model state */

  initialise_variables_2D ( u, N );

/* Main loop */

      While (s2[n_s2] > 0) // this prevents reading beyond end of s2 array

      {

      /* count keeps track of time in integer count*dt will give the time*/

        count++;

        loop_counter++;

        time = count*dt;

        a1 = modf((double)loop_counter*dt/s1, &junk);

        /* default condition is no stimulus */

        apply_stimulus = 0;

/* for the sequence of S1 stimuli, the s2_stimulus flag is remains    at
zero, and stimuli are delivered with an interval of S1 */

        if (s2_stimulus == 0) // outer condition to speed up computation

        {

            if (a1 <= 0.001)

            {

                    apply_stimulus = 1;

            }

        }
```

```c
        /* once count is more than e_s1, the s2_stimulus flag is set */

        if ((s2_stimulus == 0)&&(loop_counter >= e_s1))

        {

            s2_stimulus = 1;

        }

      /* if s2_stimulus flag is set then the s2 stimulus is delivered

      once the time criteria are met */

 if (s2_stimulus == 1)

      {

if((loop_counter >= (e_s1 + (s2[n_s2])/dt)) && (loop_counter < e_s1 +
((s2[n_s2] + 1)/dt)))

          {

Printf ("apply s2 %f ms at time %1.7f, count %d, e_s1
%f\n",s2[n_s2],time,count,e_s1);

               apply_stimulus = 1;

          }

      }

                    /******** PDE solver ********/

/* calculate current and apd for s1 stimulus*/

/* solve monodomain equation by looping through each point */

/* store initial updates for voltage in new_Vm, so present */

/* states u[n][1] are used in the calculations, not the updated */

/* ones */

/* use loops through row and column so that we can apply stimulus to */

/* the left hand end (columns 1-3) of the 2D sheet */

for (row = 1; row <= nrows; row++)

{

for (col = 1; col <= ncols; col++)

{

n = geom[row][col];
```

```c
                if ((col <= 3) && (apply_stimulus == 1))

                    Ist = amp;

                else

                    Ist = 0.0;

/* first, integrate ORd code with Euler */

membraneCurrent = calculate_ORd_current_2D(u, n, dt, celltype, Ist);

            /* second, calculate diffusion */

            diffusionCurrent = diffusion_2D( u, nneighb, n, N, D, dx2 );

/* third, calculate new value of membrane voltage for current point */

                dummy1 = u[n][V];

                old_Vm[n]= dummy1;

        new_Vm[n] = dummy1 + dt * (diffusionCurrent - membraneCurrent);

                }

            }

/* now update u[n][1] with the update values from new_Vm, using dummy
variable */

/* to optimise use of cache and speed everything up */

            for (n = 1; n <= N; n++)

                {

                dummy1 = new_Vm[n];

                u[n][V] = dummy1;

                }

/***calculation of distance to measure Conduction Velocity***/

distance = (double) (ncols - 10)*dx*10.0; // in mm (50-10)*0.02*10=8mm

int n1=geom[3][5];

int n2=geom[3][ncols-60];

/************** APD calculation and CV measurement*****************/

for (n = 1; n <= N; n++)

    {

      /* detect upstoke */
```

```c
       If ((new_Vm[n] > thresh)&&( old_Vm[n]<= thresh))

         {

             upstroke = count*dt;

             if(n==n1)

             u_n1=upstroke;

             printf ("u_n1 is %1.6f\n",u_n1);

             if(n==n2)

             u_n2=upstroke;

             printf ("u_n1 is %1.6f\n",u_n1);

             //CV measurement

             cv = distance /(u_n2-u_n1);

             printf("CV is %f\n",cv);

          }

        /* detect downstroke */

        If ((new_Vm[n] < thresh)&&(old_Vm[n]>= thresh))

          {

             downstroke = count*dt;

             apd1 = downstroke-upstroke;

             printf ("downstroke is %1.6f\n",downstroke);

             apd[n] = (d1[n] - u1[n])*dt;

             printf("APD is %1.6f\n",apd1);

          }

      }//end of for loop
/* print vm to file every ms -- so you can plot the output */

 if (modf(time,&junk) == 0)

    fprintf(egptr,"%5.2f %5.2f\n",time,new_Vm[1]);

/* reset s2_stimulus flag once the s2 stimulus has elapsed, it is better

  to test greater than rather than equality because equating an integer

   with a double that may be very small can be unpredictable */

/* at this point we re-initialise the model state so that each sequence
```

```c
   of s1 and s2 starts from the same initial conditions */
if ((s2_stimulus == 1) && (loop_counter >= (e_s1 + ((s2[n_s2]+1000)/dt))))

   {

     printf("resetting s2_stimulus to 0, time %f, count %d, count >= %f\n",

           time, count, ((e_s1 + s2[n_s2] + 1000)/dt));

     initialise_variables_2D( u, N );

     s2_stimulus = 0;

     loop_counter = 0;

     n_s2++;

     printf("s2_stimulus %d, loop_counter %d, n_s2 %d\n",s2_stimulus

           ,loop_counter, n_s2);

     fprintf(apdptr,"%f %f %f\n",apd1,s2[n_s2],time);

     fprintf(cvptr,"%f %f %f\n",cv,s2[n_s2],time);

   }

}/*end while*/
/* Free memory and close files */
  free_fmatrix(u,1,N,1,num_parameters);

  free_imatrix(geom, 1, nrows, 1, ncols);

  free_imatrix(nneighb, 1, N, 1, 8);

  free_fvector(new_Vm, 1, N );

  free_fvector(old_Vm, 1, N );

  fclose(egptr);

  fclose(apdptr);

  fclose(cvptr);

} /*end of main*/
```

## 2. Ischaemic simulation

**Summary of Ischaemic simulation**

The Shaw and Rudy $I_{K,ATP}$ formulation was used as the main model to simulate ischaemia in this thesis. The details of the parameters and values related to this formulation are presented

in Code A.2.1. The utility of this formulation has been discussed in detail in Chapters Five and Seven. Code A.2.2 was written in Matlab to describe current-voltage (I-V) dependency of the KATP Current illustrated in Chapter Five.

**Code A.2.1 Related IK,ATP simulation code**

```c
/* Parameters for IKATP Shaw-Rudy model */

/* K reversal potential (mV) */

double ekatp;

/* Conductance of the ATP-sensitive K channel (nS/uF) */

double gkbaratp;

/*Maximum conductance of the ATP-sensitive K channel (nS/uF)*/

const double gkatp = 3.9 ; // (nS/pF) or (mS/uF) = 0.039 nS/nF;

/* Percentage availability of open channels */

double patp;

/* K dependence of ATP-sensitive K current */

const double natp = 0.24;

/* Intracellular ATP concentration (mM) */

const double atpi = 6.8;   // 4.6 ischaemia or 6.8 normal

/* Hill coefficient */

const double hatp = 2.0;

/* Half-maximal saturation point of ATP-sensitive K current (mM) */

const double katp = 0.042; // 0.25 ischaemia, 0.042 normal

     // ATP    6.8   6.5   6.0   5.5   5.0   4.5   4.0

     // kATP   0.042 0.070 0.117 0.164 0.212 0.259 0.306

/* ATP dependent K current */

patp = 1.0/(1.0+(pow((atpi/katp),hatp)));

gkbaratp = gkatp*patp*(pow((Ko/KoNorm),natp));
```

```matlab
IKatp = gkbaratp*(U[V]-Ek);
```

**Code A.2.2 Single channel current-voltage (I-V) dependency for the KATP Current written in MATLAB**

```matlab
%/******Parameters for each IKATP model******/%

% Parameters for IKATP
    double ekatp;
% K reversal potential (mV)
    double gkbaratp;
% Conductance of the ATP-sensitive K channel (nS/uF)
    double gkatp;
    gkatp= 3.9 ; % (nS/pF) or (mS/uF) = 0.039 nS/nF;
% Maximum conductance of the ATP-sensitive K channel (nS/uF)
    double patp;
% Percentage availability of open channels */
    double natp;
    natp= 0.24;
% K dependence of ATP-sensitive K current */
    double atpi;
    atpi= 6.8;   % 4.6 ischaemia or 6.8 normal  /* Intracellular
ATP concentration (mM) */
    double hatp;
    hatp= 2.0;   % Hill coefficient */
    double katp;
    katp = 0.042; % 0.25 ischaemia, 0.042 normal
%/* Half-maximal saturation point of ATP-sensitive K current (mM) */
    % ATP    6.8   6.5   6.0   5.5   5.0   4.5   4.0
    % kATP   0.042 0.070 0.117 0.164 0.212 0.259 0.306

double KoNorm;
KoNorm = 5.4;
ko=5.4;

EK=(R*T/F)* log(ko/KI);

fileID =fopen('iv.txt','w');

%***ATP dependent K current***%

for V=-100:10:50

    patp = 1.0/(1.0+(((atpi/katp)^hatp)));
    gkbaratp = gkatp*patp*(((ko/KoNorm)^natp));

    IKatp = gkbaratp*(V-EK);

    fprintf(fileID,'%f %f\r\n',IKatp,V);
end

fclose(fileID);
```

## 3. Running simulation and defining outputs

The simulations were run on Linux and Sun Microsystems Grid Engine. The command line for running C code to generate output file and to submit in the Iceberg (The University of Sheffield High performance Computing Cluster) is:

```
gcc ORd.c -lm -o out
```

```
qsub output.sh
```

Execution scripts were written in Linux.

```
                Code A.3.1 Execution scripts (output.sh)

#!/bin/bash

#$ -m be

#$ -l h_rt=168:00:00

#$ -l mem=6G

#$ -l rmem=6G

#$ -pe openmp 4

#$ -v OMP_NUM_THREADS=4

#$ -M mail@sheffield.ac.uk

/pwd/……/out
```

## List of Publications

➢ Simulating the effect of global cardiac ischaemia on dynamics of Ventricular arrhythmias in the human heart (Journal of Theoretical Biology, in preparation)

➢ Abbasi, M. & Clayton, R., 2014. Formulation of ATP sensitive K + Current and Action Potential Shape in Models of Human Ventricular Myocytes Results. Computing in Cardiology Conference (CinC), pp.201–204.

➢ Abbasi, M. & Clayton, R., 2013. A Comparison of Two Models of Human Ventricular Tissue: Simulated Ischaemia and Re-entry. Computing in Cardiology Conference (CinC), pp.385–388.

## List of conferences and workshops

**Sep 2014**: 'Formulation of ATP sensitive K + Current and Action Potential Shape in Models of Human Ventricular Myocytes Results'. Paper presented at the 41st annual conference of Computing in Cardiology held in Cambridge, Massachusetts, USA.

**May 2014**: Computational Cardiac EP Workshop held at Imperial College London. Poster presentation: 'Effect of simulated ischaemia on two models of human ventricular tissue'.

**Apr 2014**: Northern Cardiovascular Research Group (NCRG) Conference held at Manchester Royal Infirmary, Manchester. Poster presentation: 'Effect of simulated ischaemia on two models of human ventricular tissue'.

**Sep 2013**: 'A Comparison of Two Models of Human Ventricular Tissue : Simulated Ischaemia and Re-entry'. Paper presented at the 40st annual conference of Computing in Cardiology held in Zaragoza, Spain.

**Feb 2013**: The 2020 Science Tools Workshop at Microsoft Research Cambridge.

**July 2012**: Workshop (Mayneord-Phillips School) Cardiac imaging and modelling: Principles, methods and clinical relevance held at The Queens' College, University of Oxford. Oral and Poster presentation: 'Effect of simulated ischaemia on the behaviour of re-entry in the human heart'

# References

Abbasi, M. & Clayton, R., 2014. Formulation of ATP sensitive K + Current and Action Potential Shape in Models of Human Ventricular Myocytes Results. *Computing in Cardiology Conference (CinC)*, pp.201–204.

Aggarwal, R. & Boyden, P.A., 1995. Diminished Ca2+ and Ba2+ Currents in Myocytes Surviving in the Epicardial Border Zone of the 5-Day Infarcted Canine Heart. *Circulation Research* , 77 (6 ), pp.1180–1191.

Allen, D.G. & Orchard, C.H., 1987. Myocardial contractile function during ischemia and hypoxia. *Circulation Research*, 60(2), pp.153–168.

Ashcroft, S.J.H. & Ashcroft, F.M., 1990. Properties and functions of ATP-sensitive K-channels. *Cellular Signalling*, 2(3), pp.197–214.

Austin, T.M., Hooks, D. a, Hunter, P.J., Nickerson, D.P., Pullan, A.J., Sands, G.B., Smaill, B.H. & Trew, M.L., 2006. Modeling cardiac electrical activity at the cell and tissue levels. *Annals of the New York Academy of Sciences*, 1080, pp.334–47.

Babenko, a. P., Gonzalez, G., Aguilar-Bryan, L. & Bryan, J., 1998. Reconstituted Human Cardiac KATP Channels : Functional Identity With the Native Channels From the Sarcolemma of Human Ventricular Cells. *Circulation Research*, 83(11), pp.1132–1143.

Barr, R.C. & Plonsey, R., 1984. Propagation of excitation in idealized anisotropic two-dimensional tissue. *Biophysical journal*, 45(6), pp.1191–202.

Befroy, D. & Powell, T., 1999. Osmotic shock: modulation of contractile function, pHi, and ischemic damage in perfused guinea pig heart. *The American journal of physiology*, pp.1236–1244.

Bénitah, J.P., Bailly, P., D'Agrosa, M.C., Da Ponte, J.P., Delgado, C. & Lorente, P., 1992. Slow inward current in single cells isolated from adult human ventricles. *Pflugers Archiv : European journal of physiology*, 421(2-3), pp.176–187.

Bernus, O., Wellner, M. & Pertsov, A.M., 2004. Intramural wave propagation in cardiac tissue: Asymptotic solutions and cusp waves. *Physical Review E - Statistical, Nonlinear, and Soft Matter Physics*, 70(6 1).

Bernus, O., Zemlin, C.W., Zaritsky, R.M., Mironov, S.F. & Pertsov, A.M., 2005. Alternating conduction in the ischaemic border zone as precursor of reentrant arrhythmias: a simulation study. *Europace : European pacing, arrhythmias, and cardiac electrophysiology : journal of the working groups on cardiac pacing, arrhythmias, and cardiac cellular electrophysiology of the European Society of Cardiology*, 7 Suppl 2, pp.93–104.

Bers, D.M., 2000. Calcium fluxes involved in control of cardiac myocyte contraction. *Circulation research*, 87, pp.275–281.

Bers, D.M., 2002. Cardiac excitation-contraction coupling. *Nature*, 415(6868), pp.198–205.

Biktashev, V.N. & Holden, a. V., 1998. Reentrant waves and their elimination in a model of mammalian ventricular tissue. *Chaos: An Interdisciplinary Journal of Nonlinear Science*, 8, p.48.

Biktashev, V.N., Holden, a. V. & Zhang, H., 1994. Tension of Organizing Filaments of Scroll Waves. *Philosophical Transactions of the Royal Society A: Mathematical, Physical and Engineering Sciences*, 347(1685), pp.611–630.

Biktashev, V.N. & Holden, A. V, 1999. Re-entrant Arrhythmias and their Control in Models of Mammalian Cardiac Tissue. *Journal of Electrocardiology*, 32, pp.76–83.

Bode, F., Kilborn, M., Karasik, P. & Franz, M.R., 2001. The repolarization-excitability relationship in the human right atrium is unaffected by cycle length, recording site and prior arrhythmias. *Journal of the American College of Cardiology*, 37(3), pp.920–925.

Bondarenko, V.E., Szigeti, G.P., Bett, G.C.L., Kim, S.-J. & Rasmusson, R.L., 2004. Computer model of action potential of mouse ventricular myocytes. *American journal of physiology. Heart and circulatory physiology*, 287(3), pp.H1378–403.

Boyle, P.M., Massé, S., Nanthakumar, K. & Vigmond, E.J., 2013. Transmural IK(ATP) heterogeneity as a determinant of activation rate gradient during early ventricular fibrillation: mechanistic insights from rabbit ventricular models. *Heart rhythm : the official journal of the Heart Rhythm Society*, 10(11), pp.1710–7.

Bradley, C., Bowery, A., Britten, R., Budelmann, V., Camara, O., Christie, R., Cookson, A., Frangi, A.F., Gamage, T.B., Heidlauf, T., et al., 2011. OpenCMISS: A multi-physics & multi-scale computational infrastructure for the VPH/Physiome project. *Progress in biophysics and molecular biology*, pp.1–16.

Bradley, C.P., Clayton, R.H., Nash, M.P., Mourad, A., Hayward, M., Paterson, D.J. & Taggart, P., 2011. Human ventricular fibrillation during global ischemia and reperfusion: paradoxical changes in activation rate and wavefront complexity. *Circulation. Arrhythmia and electrophysiology*, 4(5), pp.684–91.

Bueno-Orovio, A., Cherry, E.M. & Fenton, F.H., 2008. Minimal model for human ventricular action potentials in tissue. *Journal of theoretical biology*, 253(3), pp.544–60.

Burton, F.L. & Cobbe, S.M., 2001. Dispersion of ventricular repolarization and refractory period. *Cardiovascular Research*, 50(1), pp.10–23.

C. BOUNTRA & R. D. JONES, V., 1989. EFFECT OF INTRACELLULAR AND EXTRACELLULAR pH ON CONTRACTION IN ISOLATED, MAMMALIAN CARDIAC MUSCLE. , pp.163–187.

Cabo, C., 2014. Dynamics of propagation of premature impulses in structurally remodeled infarcted myocardium: A computational analysis. *Frontiers in Physiology*, 5(Nov), pp.1–12.

Cabo, C., 2015. Post-repolarization refractoriness increases vulnerability to block and initiation of reentrant impulses in heterogeneous infarcted myocardium. *Computers in Biology and Medicine*, 65, pp.209–219.

Cabo, C. & Boyden, P.A., 2003. Electrical remodeling of the epicardial border zone in the canine infarcted heart: a computational analysis. *American journal of physiology. Heart and circulatory physiology*, 284(1), pp.H372–84.

Cabo, C., Pertsov, a M., Davidenko, J.M., Baxter, W.T., Gray, R. a & Jalife, J., 1996. Vortex shedding as a precursor of turbulent electrical activity in cardiac muscle. *Biophysical journal*, 70(3), pp.1105–11.

Cabo, C., Pertsov, A.M., Baxter, W.T., Davidenko, J.M., Gray, R.A. & Jalife, J., 1994. Wave-front curvature as a cause of slow conduction and block in isolated cardiac muscle. *Circulation research*, 75, pp.1014–1028.

Cabo, C., Yao, J., Boyden, P. a., Chen, S., Hussain, W., Duffy, H.S., Ciaccio, E.J., Peters, N.S. & Wit, A.L., 2006. Heterogeneous gap junction remodeling in reentrant circuits in the epicardial border zone of the healing canine infarct. *Cardiovascular Research*, 72(2), pp.241–249.

Caldwell, B.J., Trew, M.L., Sands, G.B., Hooks, D.A., LeGrice, I.J. & Smaill, B.H., 2009. Three distinct directions of intramural activation reveal nonuniform side-to-side electrical coupling of ventricular myocytes. *Circulation: Arrhythmia and Electrophysiology*, 2(4), pp.433–440.

Camacho, A., Figuredo, V., Brandes, R. & Weiner, M., 1993. Ca2 + -dependent fluorescence transients and phosphate metabolism during low-flow ischemia.

Carmeliet, E., 1999. Cardiac Ionic Currents and Acute Ischemia : From Channels to Arrhythmias. , 79(3), pp.917–1017.

Carmeliet, E., 1999. Cardiac ionic currents and acute ischemia: from channels to arrhythmias. *Physiological reviews*, 79(3), pp.917–1017.

Carro, J., Rodríguez, J.F., Laguna, P. & Pueyo, E., 2011. A human ventricular cell model for investigation of cardiac arrhythmias under hyperkalaemic conditions. *Philosophical transactions. Series A, Mathematical, physical, and engineering sciences*, 369(1954), pp.4205–32.

Carusi, A., Burrage, K. & Rodríguez, B., 2012. Bridging experiments, models and simulations: an integrative approach to validation in computational cardiac electrophysiology. *American journal of physiology. Heart and circulatory physiology*, 303(2), pp.H144–55.

Cascio, W.E., Yan, G.X. & Kléber, a G., 1990. Passive electrical properties, mechanical activity, and extracellular potassium in arterially perfused and ischemic rabbit ventricular muscle. Effects of calcium entry blockade or hypocalcemia. *Circulation research*, 66(6), pp.1461–1473.

Cassia-Moura, R., Xie, F. & Cerdeira, H. a., 2004. Effect of Heterogeneity on Spiral Wave Dynamics in Simulated Cardiac Tissue. *International Journal of Bifurcation and Chaos*,

14(09), pp.3363–3375.

Chabiniok, R., Wang, V.Y., Hadjicharalambous, M., Asner, L., Lee, J., Sermesant, M., Kuhl, E., Young, A. a, Moireau, P., Nash, M.P., et al., 2016. Multiphysics and multiscale modelling, data– model fusion and integration of organ physiology in the clinic: ventricular cardiac mechanics. *the Royal Society*.

Cherry, E.M., Greenside, H.S., Henriquez, C.S., 2003. Efficient simulation of three-dimensional anisotropic cardiac tissue using an adaptive mesh refinement method. Chaos 13, 853-865.

Cherry, E.M. & Fenton, F.H., 2004. Suppression of alternans and conduction blocks despite steep APD restitution: electrotonic, memory, and conduction velocity restitution effects. *American journal of physiology. Heart and circulatory physiology*, 286, pp.H2332–H2341.

Choi, B.R., Liu, T. & Salama, G., 2001. The distribution of refractory periods influences the dynamics of ventricular fibrillation. *Circulation research*, 88, pp.E49–E58.

Choi, B.R., Nho, W., Liu, T. & Salama, G., 2002. Life span of ventricular fibrillation frequencies. *Circulation Research*, 91, pp.339–345.

Ciaccio, E.J., Ashikaga, H., Coromilas, J., Hopenfeld, B., Cervantes, D.O., Wit, A.L., Peters, N.S., McVeigh, E.R. & Garan, H., 2014. Model of bipolar electrogram fractionation and conduction block associated with activation wavefront direction at infarct border zone lateral isthmus boundaries. *Circulation: Arrhythmia and Electrophysiology*, 7(1), pp.152–163.

Ciaccio, E.J., Ashikaga, H., Kaba, R. a, Cervantes, D., Hopenfeld, B., Wit, A.L., Peters, N.S., Mcveigh, E.R., Garan, H. & Coromilas, J., 2007. Determined by Activation Mapping. *Heart rhythm*, 4(8), pp.1034–1045.

Clarke, K., Stewart, L.C., Neubauer, S., Balschi, J.A., Smith, T.W., Ingwall, J.S., Nedelec, J.F., Humphrey, S.M., Kleber, A.G. & Springer, C.S.J., 1993. Extracellular volume and transsarcolemmal proton movement during ischemia and reperfusion: a 31P NMR spectroscopic study of the isovolumic rat heart. *NMR in biomedicine*, 6(4), pp.278–286.

Clayton, R., Bernus, O., Cherry, E.M., Dierckx, H., Fenton, F.H., Mirabella, L., Panfilov, a V, Sachse, F.B., Seemann, G. & Zhang, H., 2011. Models of cardiac tissue electrophysiology: progress, challenges and open questions. *Progress in biophysics and molecular biology*, 104(1-3), pp.22–48.

Clayton, R.H., 2001. Computational models of normal and abnormal action potential propagation in cardiac tissue: linking experimental and clinical cardiology. *Physiological measurement*, 22, pp.R15–R34.

Clayton, R.H., 2009. Influence of cardiac tissue anisotropy on re-entrant activation in computational models of ventricular fibrillation. *Physica D: Nonlinear Phenomena*, 238(11-12), pp.951–961.

Clayton, R.H., 2008. Vortex filament dynamics in computational models of ventricular fibrillation in the heart. *Chaos (Woodbury, N.Y.)*, 18(4), p.043127.

Clayton, R.H., Bernus, O., Cherry, E.M., Dierckx, H., Fenton, F.H., Mirabella, L., Panfilov, A. V., Sachse, F.B., Seemann, G. & Zhang, H., 2011. Models of cardiac tissue electrophysiology: Progress, challenges and open questions. *Progress in Biophysics and Molecular Biology*, 104(1-3), pp.22–48.

Clayton, R.H. & Holden, A. V, 2002a. A method to quantify the dynamics and complexity of re-entry in computational models of ventricular fibrillation. *Physics in Medicine and Biology*, 47(2), pp.225–238.

Clayton, R.H. & Holden, A. V, 2002b. A method to quantify the dynamics and complexity of re-entry in computational models of ventricular fibrillation. *Physics in medicine and biology*, 47(2), pp.225–38.

Clayton, R.H. & Holden, A. V, 2001. cardiac tissue : a model study. , p.43498.

Clayton, R.H. & Holden, A. V, 2002c. Dynamics and interaction of filaments in a computational model of re-entrant ventricular fibrillation. *Physics in medicine and biology*, 47(10), pp.1777–92.

Clayton, R.H. & Holden, A. V, 2004a. Filament behavior in a computational model of ventricular fibrillation in the canine heart. *IEEE transactions on bio-medical engineering*, 51(1), pp.28–34.

Clayton, R.H. & Holden, A. V, 2004b. Propagation of normal beats and re-entry in a computational model of ventricular cardiac tissue with regional differences in action potential shape and duration. *Progress in biophysics and molecular biology*, 85(2-3), pp.473–99.

Clayton, R.H., Nash, M., Bradley, C.P., Panfilov, a V, Paterson, D.J. & Taggart, P., 2011. Experiment-model interaction for analysis of epicardial activation during human ventricular fibrillation with global myocardial ischaemia. *Progress in biophysics and molecular biology*, 107(1), pp.101–11.

Clayton, R.H. & Nash, M.P., 2015. Analysis of Cardiac Fibrillation Using Phase Mapping. *Cardiac Electrophysiology Clinics*, 7(1), pp.49–58.

Clayton, R.H. & Panfilov, a V, 2008. A guide to modelling cardiac electrical activity in anatomically detailed ventricles. *Progress in biophysics and molecular biology*, 96(1-3), pp.19–43.

Clayton, R.H. & Taggart, P., 2005. Regional differences in APD restitution can initiate wavebreak and re-entry in cardiac tissue: a computational study. *Biomedical engineering online*, 4, p.54.

Clayton, R.H., Zhuchkova, E. a & Panfilov, a V, 2006. Phase singularities and filaments: simplifying complexity in computational models of ventricular fibrillation. *Progress in biophysics and molecular biology*, 90(1-3), pp.378–98.

Clemo, H.F., Stambler, B.S. & Baumgarten, C.M., 1998. Swelling-activated chloride current is persistently activated in ventricular myocytes from dogs with tachycardia-induced congestive heart failure. *Circulation research*, 84(2), pp.157–65.

COLLI FRANZONE, P. & PAVARINO, L.F., 2004. A PARALLEL SOLVER FOR

REACTION–DIFFUSION SYSTEMS IN COMPUTATIONAL ELECTROCARDIOLOGY. *Mathematical Models and Methods in Applied Sciences*, 14(06), pp.883–911.

Cook, D.L., Satin, L.S., Ashford, M.L.J. & Hales, C.N., 1988. Perspectives in Diabetes ATP-Sensitive K + Channels in Pancreatic p-Cells Spare-Channel Hypothesis. , 37(May), pp.495–498.

Coronel, R., 1994. Heterogeneity in extracellular potassium concentration during early myocardial ischaemia and reperfusion: implications for arrhythmogenesis. *Cardiovascular research*, 28, pp.770–777.

Coronel, R., Fiolet, J.W., Wilms-Schopman, J.G., Opthof, T., Schaapherder, a F. & Janse, M.J., 1989. Distribution of extracellular potassium and electrophysiologic changes during two-stage coronary ligation in the isolated, perfused canine heart. *Circulation*, 80(1), pp.165–77.

Coronel, R., Janse, M.J., Opthof, T., Wilde, A.A. & Taggart, P., 2012. Postrepolarization refractoriness in acute ischemia and after antiarrhythmic drug administration: Action potential duration is not always an index of the refractory period. *Heart Rhythm*, 9(6), pp.977–982.

Coronel, R., Wilms-Schopman, F.J., Opthof, T., Cinca, J., Fiolet, J.W. & Janse, M.J., 1992. Reperfusion arrhythmias in isolated perfused pig hearts. Inhomogeneities in extracellular potassium, ST and TQ potentials, and transmembrane action potentials. *Circulation research*, 71(5), pp.1131–1142.

Coulombe, A., Coraboeuf, E. & Deroubaix, E., 1980. Computer simulation of acidosis-induced abnormal repolarization and repetitive activity in dog Purkinje fibers. *J Physiol (Paris)*, 76(2), pp.107–112.

Courdiere, Y. & Pierre, C., 2006. Stability and convergence of a finite volume method for two systems of reaction-diffusion equations in electro-cardiology. *Nonlinear Analysis: Real World Applications*, 7(4), pp.916–935.

Cranefield, P.F., Wit, a L. & Hoffman, B.F., 1972. Conduction of the cardiac impulse. 3. Characteristics of very slow conduction. *The Journal of general physiology*, 59, pp.227–246.

Davidenko, J.M. & Antzelevitch, C., 1986. Electrophysiological mechanisms underlying rate-dependent changes of refractoriness in normal and segmentally depressed canine Purkinje fibers. The characteristics of post-repolarization refractoriness. *Circulation research*, 58(2), pp.257–68.

Dennis, S.., W.Geveres & Opie, L.H., 1991. Protons in Ischemia: Where Do They Come From; Where Do They Go To? , 1086, pp.1077–1086.

Deutsch, N. & Weiss, J.N., 1993. ATP-sensitive K+ channel modification by metabolic inhibition in isolated guinea-pig ventricular myocytes. *The Journal of physiology*, 465, pp.163–179.

Dillon, S.M., Allessie, M. a, Ursell, P.C. & Wit, a L., 1988. Influences of anisotropic tissue

structure on reentrant circuits in the epicardial border zone of subacute canine infarcts. *Circulation research*, 63(1), pp.182–206.

Donoso, P., Mill, J.G.G., O'Neill, S.C.C. & Eisner, D. a. a, 1992. Fluorescence measurements of cytoplasmic and mitochondrial sodium concentration in rat ventricular myocytes. *Journal of Physiology*, 448(1), pp.493–509.

Downar, E., Janse, M.J. & Durrer, D., 1977. The effect of "ischemic" blood on transmembrane potentials of normal porcine ventricular myocardium. *Circulation*, 55(3), pp.455–62.

DROUIN, E., CHARPENTIER, F., GAUTHIER, C., LAURENT, K. & MAREC, H. LE, 1995. Electrophysiologic Characteristics of Cells Spanning the Left Ventricular Wall of Human Heart : Evidence for Presence of M Cells. , 26(1), pp.185–192.

Drouin, E., Lande, G. & Charpentier, F., 1998a. Amiodarone reduces transmural heterogeneity of repolarization in the human heart. *Journal of the American College of Cardiology*, 32(4), pp.1063–1067.

Drouin, E., Lande, G. & Charpentier, F., 1998b. Amiodarone reduces transmural heterogeneity of repolarization in the human heart. *Journal of the American College of Cardiology*, 32(4), pp.1063–1067.

Dzhura, I., Wu, Y., Colbran, R.J., Balser, J.R. & Anderson, M.E., 2000. Calmodulin kinase determines calcium-dependent facilitation of L-type calcium channels. *Nature Cell Biology*, 2(3), pp.173–177.

van Echteld, C.J. a, Kirkels, J.H., Eijgelshoven, M.H.J., van der Meer, P. & Ruigrok, T.J.C., 1991. Intracellular sodium during ischemia and calcium-free perfusion: A 23Na NMR study. *Journal of Molecular and Cellular Cardiology*, 23(3), pp.297–307.

Elshrif, M.M. & Cherry, E.M., 2014. A quantitative comparison of the behavior of human ventricular cardiac electrophysiology models in tissue. *PLoS ONE*, 9(1).

Emous, J.G. Van, Nederhoff, M.G.J., Ruigrok, T.J.C. & Echteld, C.J.A. Van, 1997. The Role of the Na + Channel in the Accumulation of Intracellular Na + During Myocardial Ischemia : Consequences for Post-ischemic Recovery. , 96, pp.85–96.

Ethier, M. & Bourgault, Y., 2008. SEMI-IMPLICIT TIME-DISCRETIZATION SCHEMES FOR THE BIDOMAIN MODEL. *SIAM J.*, 46(5), pp.2443–2468.

Ettinger, P., Regan, T.J. & Oldewurtel, H. a, 1974. Hyperkalemia, cardiac conduction, and the electrocardiogram: A review. *American Heart Journal*, 88(3), pp.360–371.

Faber, G.M. & Rudy, Y., 2000. Action potential and contractility changes in [Na(+)](i) overloaded cardiac myocytes: a simulation study. *Biophysical journal*, 78(5), pp.2392–2404.

Faivre, J.F. & Findlay, I., 1990. Action potential duration and activation of ATP-sensitive potassium current in isolated guinea-pig ventricular myocytes. *Biochimica et biophysica acta*, 1029(1), pp.167–72.

Farid, T. a., Nair, K., Massé, S., Azam, M.A., Maguy, A., Lai, P.F.H., Umapathy, K., Dorian,

P., Chauhan, V., Varró, A., et al., 2011. Role of KATP channels in the maintenance of ventricular fibrillation in cardiomyopathic human hearts. *Circulation Research*, 109(11), pp.1309–1318.

Fast, V.G. & Kléber, A.G., 1997. Role of wavefront curvature in propagation of cardiac impulse. *Cardiovascular Research*, 33, pp.258–271.

Fenton, F. & Karma, A., 1998. Vortex dynamics in three-dimensional continuous myocardium with fiber rotation: Filament instability and fibrillation. *Chaos (Woodbury, N.Y.)*, 8(1998), pp.20–47.

Fenton, F.H., Cherry, E.M., Hastings, H.M. & Evans, S.J., 2002. Multiple mechanisms of spiral wave breakup in a model of cardiac electrical activity. *Chaos*, 12(2002), pp.852–892.

Ferrero, J.M., Sáiz, J., Ferrero, J.M. & Thakor, N. V, 1996. Simulation of action potentials from metabolically impaired cardiac myocytes. Role of ATP-sensitive K+ current. *Circulation research*, 79, pp.208–221.

Ferrero, J.M., Sáiz, J. & Thakor, N. V, 1996. Simulation of action potentials from metabolically impaired cardiac myocytes. Role of ATP-sensitive K+ current. *Circulation research*, 79(2), pp.208–221.

Ferrero, J.M., Trénor, B., Rodríguez, B. & Sáiz, J., 2003. Electrical Activity and Reentry During Regional Myocardial Ischemia: Insights From Simulations. *International Journal of Bifurcation and Chaos*, 13(12), pp.3703–3715.

Findlay, I. & Faivre, J.-F., 1991. ATP-sensitive K channels in heart muscle Spare channels. *FEBS Letters*, 279(1), pp.95–97.

Fink, M., Niederer, S. a, Cherry, E.M., Fenton, F.H., Koivumäki, J.T., Seemann, G., Thul, R., Zhang, H., Sachse, F.B., Beard, D., et al., 2011. Cardiac cell modelling: observations from the heart of the cardiac physiome project. *Progress in biophysics and molecular biology*, 104(1-3), pp.2–21.

Flaim, S.N., Giles, W.R. & McCulloch, A.D., 2006. Contributions of sustained INa and IKv43 to transmural heterogeneity of early repolarization and arrhythmogenesis in canine left ventricular myocytes. *American journal of physiology. Heart and circulatory physiology*, 291(6), pp.H2617–29.

Fox, J.J., McHarg, J.L. & Gilmour, R.F., 2002a. Ionic mechanism of electrical alternans. *American journal of physiology. Heart and circulatory physiology*, 282(2), pp.H516–30.

Fox, J.J., McHarg, J.L. & Gilmour, R.F., 2002b. Ionic mechanism of electrical alternans. *American journal of physiology. Heart and circulatory physiology*, 282(2), pp.H516–30.

Fozzard, H. a & Makielski, J.C., 1985. The Electrophysiology of Acute Myocardial Ischemia. *Annual Review of Medicine*, 36(1), pp.275–284.

Franz, M.R., 2003. The Electrical Restitution Curve Revisited:. Steep or Flat Slope-Which is Better? *Journal of Cardiovascular Electrophysiology*, 14(s10), pp.S140–S147.

Franz, M.R., Gray, R. a, Karasik, P., Moore, H.J. & Singh, S.N., 2014. Drug-induced post-

repolarization refractoriness as an antiarrhythmic principle and its underlying mechanism. *Europace*, 16(suppl 4), pp.iv39–iv45.

Franz, M.R., Swerdlow, C.D., Liem, L.B. & Schaefer, J., 1988. Cycle length dependence of human action potential duration in vivo. Effects of single extrastimuli, sudden sustained rate acceleration and deceleration, and different steady-state frequencies. *Journal of Clinical Investigation*, 82(3), pp.972–979.

Fukuda, H., Luo, C.S., Gu, X., Guo, L., Digerness, S.B., Li, J. & Pike, M.M., 2001. The effect of K(atp)channel activation on myocardial cationic and energetic status during ischemia and reperfusion: role in cardioprotection. *Journal of molecular and cellular cardiology*, 33(3), pp.545–60.

Fülöp, L., Bányász, T., Magyar, J., Szentandrássy, N., Varró, a & Nánási, P.P., 2004. Reopening of {L-type} calcium channels in human ventricular myocytes during applied epicardial action potentials. *Acta Physiol Scand*, 180, pp.37–94.

Garfinkel, a, Kim, Y.H., Voroshilovsky, O., Qu, Z., Kil, J.R., Lee, M.H., Karagueuzian, H.S., Weiss, J.N. & Chen, P.S., 2000. Preventing ventricular fibrillation by flattening cardiac restitution. *Proceedings of the National Academy of Sciences of the United States of America*, 97(11), pp.6061–6.

Gasser, R.N. & Vaughan-Jones, R.D., 1990. Mechanism of potassium efflux and action potential shortening during ischaemia in isolated mammalian cardiac muscle. *The Journal of physiology*, 431, pp.713–741.

Gilbert, S.H., Benson, A.P., Li, P. & Holden, A. V., 2007. Regional localisation of left ventricular sheet structure: integration with current models of cardiac fibre, sheet and band structure. *European Journal of Cardio-thoracic Surgery*, 32(2), pp.231–249.

Glitsch, H.G. & Tappe, a, 1995. Change of Na+ pump current reversal potential in sheep cardiac Purkinje cells with varying free energy of ATP hydrolysis. *The Journal of physiology*, 484 ( Pt 3, pp.605–616.

Grandi, E., Pasqualini, F.S. & Bers, D.M., 2010. A novel computational model of the human ventricular action potential and Ca transient. *Journal of molecular and cellular cardiology*, 48(1), pp.112–21.

Grant, A.O., 2009. Cardiac ion channels. *Circulation: Arrhythmia and Electrophysiology*, 2, pp.185–194.

Gray, R.A., Jalife, J., Panfilov, A. V., Baxter, W.T., Cabo, C., Davidenko, J.M., Pertsov, A.M., Panfilov, A. V., Hogeweg, P. & Winfree, A.T., 1994. Mechanisms of Cardiac Fibrillation. *Science*, 591(1990), pp.7–8.

Gray, R.A., Pertsov, A.M. & Jalife, J., 1998. Spatial and temporal organization during cardiac fibrillation. *Nature*, 392(6671), pp.75–78.

Greenstein, J. & Winslow, R., 2002. An Integrative Model of the Cardiac Ventricular Myocyte Incorporating Local Control of Ca 2+ Release. *Biophysical journal*, 83(6), pp.2918–2945.

De Groot, J.R. & Coronel, R., 2004. Acute ischemia-induced gap junctional uncoupling and

arrhythmogenesis. *Cardiovascular Research*, 62, pp.323–334.

Haigney, M.C., Lakatta, E.G., Stern, M.D. & Silverman, H.S., 1994. Sodium channel blockade reduces hypoxic sodium loading and sodium-dependent calcium loading. *Circulation*, 90(1), pp.391–9.

Han, J. & Moe, G.K., 1964. Nonuniform Recovery of Excitability in Ventricular Muscle. *Circulation research*, 14(January), pp.44–60.

Hanck, D. & Sheets, M., 1992. Time-dependent changes in kinetics of Na + current in single canine cardiac Purkinje cells. *American Physiology Society*.

Hartmann, M., Decking, U.K.M. & Schrader, J., 1998. Cardioprotective actions of KC 12291II. Delaying Na+ overload in ischemia improves cardiac function and energy status in reperfusion. *Naunyn-schmiedebergs Archives of Pharmacology*, 358(5), pp.554–560.

Heidenreich, E., Ferrero, J. & Rodríguez, J., 2012. Modeling the human heart under acute ischemia. *... Computational Modeling*, pp.1–24.

Henriquez, C.S., 1993. Simulating the electrical behavior of cardiac tissue using the bidomain model. *Critical reviews in biomedical engineering*, 21(1), pp.1–77.

Henriquez, C.S. & Papazoglou, A.A., 1996. Using computer models to understand the roles of tissue structure and membrane dynamics in arrhythmogenesis. *Proceedings of the IEEE*, 84(3), pp.334–354.

Henriquez, C.S., Tranquillo, J.V., Weinstein, D., Hsu, E. & Johnson, C.R., 2004. *Three-dimensional propagation in mathematical models: Integrative model of the mouse heart*,

Hiraoka, M., 1997. Pathophysiological functions of ATP-sensitive K+ channels in myocardial ischemia. *Japanese heart journal*, 38, pp.297–315.

Hodgkin, A.L. & Huxley, A.F., 1952. A Quantitative Description of Membrane Current and its Application to Conduction and Excitation in Nerves. *J. Physiol.*

HOFFMAN, B. F., and P.F.C., 1960. *Electrophysiology of the Heart*, New YorK: McGraw-Hill Book Co. Inc.

Hoffman, B.F. & Dangman, K.H., 1987. Mechanisms for cardiac arrhythmias. *Experientia*, 43(10), pp.1049–1056.

Holden, A. V. & Biktashev, V.N., 2002. Computational biology of propagation in excitable media models of cardiac tissue. In *Chaos, Solitons and Fractals*. pp. 1643–1658.

Horie, B.Y.M., Irisawa, H. & Noma, A., 2014. Voltage-dependent magnesium block of adenosine-triphosphate-sensitive potassium channel in guinea-pig ventricular cells by. , (1987), pp.251–272.

HORT, W., 1960. [Studies on the functional morphology of the connective tissue framework and blood vessels of the left ventricular wall]. *Virchows Archiv für pathologische Anatomie und Physiologie und für klinische Medizin*, 333, pp.565–81.

Huang, J., 2003. Evolution of activation patterns during long-duration ventricular fibrillation in dogs. *AJP: Heart and Circulatory Physiology*, 286(3), p.1193H–1200.

Huizar, J.F., Warren, M.D., Shvedko, A.G., Kalifa, J., Moreno, J., Mironov, S., Jalife, J. & Zaitsev, A. V, 2007. Three distinct phases of VF during global ischemia in the isolated blood-perfused pig heart. *American journal of physiology. Heart and circulatory physiology*, 293(3), pp.H1617–28.

Hund, T.J. & Rudy, Y., 2004. Rate dependence and regulation of action potential and calcium transient in a canine cardiac ventricular cell model. *Circulation*, 110, pp.3168–3174.

Ingwall, J.S., 2002. ATP and the Heart. , 11.

Iost, N., Virág, L., Opincariu, M., Szécsi, J., Varró, A. & Papp, J.G., 1998. Delayed rectifier potassium current in undiseased human ventricular myocytes. *Cardiovasc Res*, 40(3), pp.508–515.

Irvine, L. a, Jafri, M.S. & Winslow, R.L., 1999. Cardiac sodium channel Markov model with temperature dependence and recovery from inactivation. *Biophysical journal*, 76(4), pp.1868–1885.

Iyer, V., Mazhari, R. & Winslow, R.L., 2004. A computational model of the human left-ventricular epicardial myocyte. *Biophysical journal*, 87(3), pp.1507–25.

Jacquemet, V. & Henriquez, C.S., 2005. Finite volume stiffness matrix for solving anisotropic cardiac propagation in 2-D and 3-D unstructured meshes. *IEEE Transactions on Biomedical Engineering*, 52(8), pp.1490–1492.

Jalife, J., 2000. Ventricular fibrillation: mechanisms of initiation and maintenance. *Annual review of physiology*, 62, pp.25–50.

Janse, M.J. & Wit, A.L., 1989. Electrophysiological mechanisms of ventricular arrhythmias resulting from myocardial ischemia and infarction. *Physiological reviews*, 69, pp.1049–1169.

Janse, M.J. & Wit, A.L., 1989. Electrophysiological mechanisms of ventricular arrhythmias resulting from myocardial ischemia and infarction. *Physiological reviews*, 69(4), pp.1049–1169.

Jessen, M., Abd-Elfattah, A. & Wechsler, A., 1996. Neonatal myocardial oxygen consumption during ventricular fibrillation, hypothermia, and potassium arrest. *The Annals of thoracic surgery*, 4975(95).

Jie, X. & Trayanova, N.A., 2011. Mechanisms for Initiation of Reentry in Acute Regional Ischemia Phase 1B. , 18(11), pp.1492–1501.

Johnson, J.P., Mullins, F.M. & Bennett, P.B., 1999. Human Ether-à-go-go – related Gene K $2$ Channel Gating Probed with Extracellular Ca 2 $2$ Evidence for Two Distinct Voltage Sensors. , 113(April).

Jongsma, H. & Wilders, R., 2000. Gap junctions in cardiovascular disease. *Circulation Research*.

Jost, N., Acsai, K., Horv??th, B., B??ny??sz, T., Baczk??, I., Bitay, M., Bog??ts, G. & N??n??si, P.P., 2009. Contribution of IKr and IK1 to ventricular repolarization in canine and human myocytes: Is there any influence of action potential duration? *Basic Research in Cardiology*, 104(1), pp.33–41.

Kakei, B.Y.M., Noma, A. & Shibasaki, T., 1985. PROPERTIES OF ADENOSINE-TRIPHOSPHATE-REGULATED POTASSIUM CHANNELS IN GUINEA-PIG VENTRICULAR CELLS. *Physiology*, 363, pp.441–462.

Kalb, S.S., Dobrovolny, H.M., Tolkacheva, E.G., Idriss, S.F., Krassowska, W. & Gauthier, D.J., 2004. The restitution portrait: a new method for investigating rate-dependent restitution. *Journal of cardiovascular electrophysiology*, 15(6), pp.698–709.

Kanda, A., Watanabe, I., Williams, M.L., Engle, C.L., Li, S., Koch, G.G. & Gettes, L.S., 1997. Unanticipated Lessening of the Rise in Extracellular Potassium During Ischemia by Pinacidil. *Circulation*, 95(7), pp.1937–1944.

Kanki, H., Mitamura, H., Takatsuki, S., Sueyoshi, K., Shinagawa, K., Sato, T. & Ogawa, S., 1998. Postrepolarization refractoriness as a potential anti-atrial fibrillation mechanism of pilsicainide, a pure sodium channel blocker with slow recovery kinetics. *Cardiovascular Drugs and Therapy*, 12(5), pp.475–482.

Kantor, P.F., Coetzee, W. a., Carmeliet, E.E., Dennis, S.C. & Opie, L.H., 1990. Reduction of ischemic K+ loss and arrhythmias in rat hearts. Effect of glibenclamide, a sulfonylurea. *Circulation Research*, 66(2), pp.478–485.

Kaplinsky, E., Ogawa, S., Balke, C.W. & Dreifus, L.S., 1979. Two periods of early ventricular arrhythmia in the canine acute myocardial infarction model. *Circulation*, 60(2), pp.397–403.

Karma, A., 1994. Electrical alternans and spiral wave breakup in cardiac tissue. *Chaos*, 4(1994), pp.461–472.

Karma, A., 1993. Spiral breakup in model equations of action potential propagation in cardiac tissue. *Physical review letters*, 71(7), pp.1103–1107.

Kazbanov, I. & Clayton, R., 2014. Effect of Global Cardiac Ischemia on Human Ventricular Fibrillation: Insights from a Multi-scale Mechanistic Model of the Human Heart. *PLoS computational ...*, pp.1–17.

Kazbanov, I. V., Clayton, R.H., Nash, M.P., Bradley, C.P., Paterson, D.J., Hayward, M.P., Taggart, P. & Panfilov, A. V., 2014. Effect of Global Cardiac Ischemia on Human Ventricular Fibrillation: Insights from a Multi-scale Mechanistic Model of the Human Heart. *PLoS Computational Biology*, 10(11), p.e1003891.

Keener, J.P. & Bogar, K., 1998a. A numerical method for the solution of the bidomain equations in cardiac tissue. *Chaos (Woodbury, N.Y.)*, 8(1), pp.234–241.

Keener, J.P. & Bogar, K., 1998b. A numerical method for the solution of the bidomain equations in cardiac tissue. *Chaos (Woodbury, N.Y.)*, 8(1), pp.234–241.

Keener, J.P. & Sneyd, J., 2008. *Mathematical Physiology*, Springer Science & Business Media.

Keldermann, R.H., Nash, M.P., Gelderblom, H., Wang, V.Y. & Panfilov, a V, 2010. Electromechanical wavebreak in a model of the human left ventricle. , (64), pp.134–143.

Keldermann, R.H., Ten Tusscher, K.H.W.J., Nash, M.P., Hren, R., Taggart, P. & Panfilov, a V, 2008. Effect of heterogeneous APD restitution on VF organization in a model of the human ventricles. , pp.764–774.

Kihara, Y., Grossman, W. & Morgan, J.P., 1989. Direct measurement of changes in intracellular calcium transients during hypoxia, ischemia, and reperfusion of the intact mammalian heart. *Circulation research*, 65, pp.1029–1044.

Kim, J., Ghosh, S., Nunziato, D. a. & Pitt, G.S., 2004. Identification of the components controlling inactivation of voltage-gated Ca2+ channels. *Neuron*, 41(5), pp.745–754.

Kirkels, J.H., van Echteld, C.J. a & Ruigrok, T.J.C., 1989. Intracellular magnesium during myocardial ischemia and reperfusion: Possible consequences for postischemic recovery. *Journal of Molecular and Cellular Cardiology*, 21(11), pp.1209–1218.

Kléber, a G., 1983. Resting membrane potential, extracellular potassium activity, and intracellular sodium activity during acute global ischemia in isolated perfused guinea pig hearts. *Circulation research*, 52(4), pp.442–450.

Kleber, a G., Janse, M.J., Wilmsschopmann, F.J.G., Wilde, a a M. & Coronel, R., 1986. Changes in Conduction-Velocity during Acute-Ischemia in Ventricular Myocardium of the Isolated Porcine Heart. *Circulation*, 73(1), pp.189–198.

Kléber, a G., Riegger, C.B. & Janse, M.J., 1987. Electrical uncoupling and increase of extracellular resistance after induction of ischemia in isolated, arterially perfused rabbit papillary muscle. *Circulation research*, 61(2), pp.271–279.

Kléber, A.G. & Rudy, Y., 2004a. Basic mechanisms of cardiac impulse propagation and associated arrhythmias. *Physiological reviews*, 84(2), pp.431–488.

Kléber, A.G. & Rudy, Y., 2004b. Basic mechanisms of cardiac impulse propagation and associated arrhythmias. *Physiological reviews*, 84, pp.431–488.

Kléber, A.G. & Rudy, Y., 2004c. Basic mechanisms of cardiac impulse propagation and associated arrhythmias. *Physiological reviews*, 84(2), pp.431–88.

Knopf, H., McDonald, F.M., Bischoff, A., Hirche, H. & Addicks, K., 1988. Effect of Propranolol on Early Postischemia arrhythmias and Noradrenaline and Potassium Release of Ischemic Myocardium in Anesthetized Pigs. , pp.S41–S47.

Knopf, H., Theising, R. & Hirche, H., 1988. The Effect of Desipramine on Ischemia-Induced Changes in Extracellular K+, Na+ and H+ Concentrations. *Journal of Cardiovascular Pharmacology*, 12(Supplement 1), pp.S8–S14.

Kodama, I., Wilde, a, Janse, M.J., Durrer, D. & Yamada, K., 1984. Combined effects of hypoxia, hyperkalemia and acidosis on membrane action potential and excitability of guinea-pig ventricular muscle. *Journal of molecular and cellular cardiology*, 16, pp.247–259.

Koller, M.L., Riccio, M.L. & Gilmour, R.F., 1998. Dynamic restitution of action potential

duration during electrical alternans and ventricular fibrillation. *The American journal of physiology*, 275(5 Pt 2), pp.H1635–H1642.

Kuo, C.S., Munakata, K., Reddy, C.P. & Surawicz, B., 1983. Characteristics and possible mechanism of ventricular arrhythmia dependent on the dispersion of action potential durations. *Circulation*, 67(6), pp.1356–1367.

Lamont, C. & Eisner, D. a., 1996. The sarcolemmal mechanisms involved in the control of diastolic intracellular calcium in isolated rat cardiac trabeculae. *Pflugers Archiv European Journal of Physiology*, 432(6), pp.961–969.

Laurita, K.R. & Rosenbaum, D.S., 2000. Interdependence of modulated dispersion and tissue structure in the mechanism of unidirectional block. *Circulation research*, 87(10), pp.922–928.

Lee, C. & Hryshko, L. V, 2004. SEA0400: a novel sodium-calcium exchange inhibitor with cardioprotective properties. *Cardiovascular drug reviews*, 22(4), pp.334–347.

Lee, R.J., Liem, L.B., Cohen, T.J. & Franz, M.R., 1992. Relation between repolarization and refractoriness in the human ventricle: Cycle length dependence and effect of procainamide. *Journal of the American College of Cardiology*, 19(3), pp.614–618.

Legrice, I.J., Hunter, P.J. & Smaill, B.H., 1997. Laminar structure of the heart: a mathematical model. *The American journal of physiology*, 272, pp.H2466–H2476.

LeGrice, I.J., Smaill, B.H., Chai, L.Z., Edgar, S.G., Gavin, J.B. & Hunter, P.J., 1995. Laminar structure of the heart: ventricular myocyte arrangement and connective tissue architecture in the dog. *The American journal of physiology*, 269, pp.H571–H582.

Li, G., Feng, J., Yue, L. & Carrier, M., 1998. Transmural heterogeneity of action potentials andI to1 in myocytes isolated from the human right ventricle. *American Journal of physiology*, pp.369–377.

Li, G.-R., Feng, J., Yue, L., Carrier, M. & Nattel, S., 1996. Evidence for Two Components of Delayed Rectifier K+ Current in Human Ventricular Myocytes. *Circulation Research* , 78 (4 ), pp.689–696.

Li, G.-R., Lau, C.-P., Leung, T.-K. & Nattel, S., 2004. Ionic current abnormalities associated with prolonged action potentials in cardiomyocytes from diseased human right ventricles. *Heart rhythm : the official journal of the Heart Rhythm Society*, 1(4), pp.460–8.

Li, G.-R., Yang, B., Feng, J., Bosch, R.F., Carrier, M. & Nattel, S., 1999. Transmembrane ICa contributes to rate-dependent changes of action potentials in human ventricular myocytes. *Am J Physiol Heart Circ Physiol*, 276(1), pp.H98–106.

Li, G.R., Feng, J., Yue, L., Carrier, M. & Nattel, S., 1996. Evidence for two components of delayed rectifier K+ current in human ventricular myocytes. *Circulation research*, 78(4), pp.689–96.

Li, G.R. & Nattel, S., 1997. Properties of human atrial ICa at physiological temperatures and relevance to action potential. *American Journal of Physiology - Heart and Circulatory Physiology*, 272(1), pp.H227–H235.

Li, R. a, Vélez, P., Chiamvimonvat, N., Tomaselli, G.F. & Marbán, E., 2000. Charged residues between the selectivity filter and S6 segments contribute to the permeation phenotype of the sodium channel. *The Journal of general physiology*, 115(January), pp.81–92.

Lou, Q., Li, W. & Efimov, I.R., 2012. The role of dynamic instability and wavelength in arrhythmia maintenance as revealed by panoramic imaging with blebbistatin vs. 2,3-butanedione monoxime. *AJP: Heart and Circulatory Physiology*, 302, pp.H262–H269.

Luo, C.H. & Rudy, Y., 1994. A dynamic model of the cardiac ventricular action potential. I. Simulations of ionic currents and concentration changes. *Circulation Research*, 74(6), pp.1071–1096.

Luo, C.H. & Rudy, Y., 1994. A dynamic model of the cardiac ventricular action potential. I. Simulations of ionic currents and concentration changes. *Circulation research*, 74(6), pp.1071–1096.

Luo, C.H. & Rudy, Y., 1991. Original Contributions A Model of the Ventricular Cardiac Action Potential. *Circulation Research*, 68(6), pp.1501–1526.

Ma, L. & Wang, L., 2007. EXPERIMENTAL CARDIOLOGY : ORIGINAL ARTICLE Effect of acute subendocardial ischemia on ventricular refractory periods. , 12(2), pp.63–66.

Magyar, J., Szentandrássy, N., Bányász, T., Fülöp, L., Varró, A. & Nánási, P.P., 2002. Effects of thymol on calcium and potassium currents in canine and human ventricular cardiomyocytes. *British journal of pharmacology*, 136(2), pp.330–338.

Mahajan, A., Shiferaw, Y., Sato, D., Baher, A., Olcese, R., Xie, L.-H., Yang, M.-J., Chen, P.-S., Restrepo, J.G., Karma, A., et al., 2008. A rabbit ventricular action potential model replicating cardiac dynamics at rapid heart rates. *Biophysical journal*, 94(2), pp.392–410.

Makita, N., Shirai, N., Wang, D.W., Sasaki, K., George, a L., Kanno, M. & Kitabatake, a, 2000. Cardiac Na(+) channel dysfunction in Brugada syndrome is aggravated by beta(1)-subunit. *Circulation*, 101(1), pp.54–60.

Malloy, C.R., Buster, D.C., Castro, M.M., Geraldes, C.F., Jeffrey, F.M. & Sherry, A.D., 1990. Influence of global ischemia on intracellular sodium in the perfused rat heart. *Magn Reson Med*, 15(1), pp.33–44.

Maltsev, V. a, Sabbah, H.N., Higgins, R.S., Silverman, N., Lesch, M. & Undrovinas, a I., 1998. Novel, ultraslow inactivating sodium current in human ventricular cardiomyocytes. *Circulation*, 98(23), pp.2545–52.

Maltsev, V.A. & Undrovinas, A.I., 2006. A Multi-Modal Composition of the Late Na+ Current in Human Ventricular Cardiomyocytes. *Cardiovasc Res*, 72(2), pp.181–204.

Mandapati, R., Asano, Y., Baxter, W.T., Gray, R., Davidenko, J. & Jalife, J., 1998a. Quantification of effects of global ischemia on dynamics of ventricular fibrillation in isolated rabbit heart. *Circulation*, 98, pp.1688–1696.

Mandapati, R., Asano, Y., Baxter, W.T., Gray, R., Davidenko, J. & Jalife, J., 1998b.

Quantification of effects of global ischemia on dynamics of ventricular fibrillation in isolated rabbit heart. *Circulation*, 98(16), pp.1688–1696.

Marban, E., Kitakaze, M., Koretsune, Y., Yue, D.T., Chacko, V.P. & Pike, M.M., 1990. Quantification of [ Ca2 '] i in Perfused Hearts Critical Evaluation of the 5F-BAPTA and Nuclear Magnetic Resonance Method as Applied to the Study of Ischemia and Reperfusion. , pp.1255–1267.

Marchlinski, F.E. & Betensky, B.P., 2012. Mechanisms of Cardiac Arrhythmias. *Revista Española de Cardiología*, 65(2), pp.174–185.

Marieb, E.N. & Hoehn, K., 2010. *Human Anatomy & Physiology*,

Massé, S., Farid, T., Dorian, P., Umapathy, K., Nair, K., Asta, J., Ross, H., Rao, V., Sevaptsidis, E. & Nanthakumar, K., 2009. Effect of global ischemia and reperfusion during ventricular fibrillation in myopathic human hearts. *American journal of physiology. Heart and circulatory physiology*, 297(Lv), pp.H1984–H1991.

Matsuoka, S., Sarai, N. & Kuratomi, S., 2003. Role of individual ionic current systems in ventricular cells hypothesized by a model study. *The Japanese journal …*, 53(2), pp.105–123.

Mewes, T. & Ravens, U., 1994. L-type calcium currents of human myocytes from ventricle of non-failing and failing hearts and from atrium. *Journal of molecular and cellular cardiology*, 26(10), pp.1307–1320.

Michailova, A., Lorentz, W. & McCulloch, A., 2007. Modeling transmural heterogeneity of K(ATP) current in rabbit ventricular myocytes. *American journal of physiology. Cell physiology*, 293(2), pp.C542–57.

Michailova, A., Saucerman, J., Belik, M.E. & McCulloch, A.D., 2005. Modeling regulation of cardiac KATP and L-type Ca2+ currents by ATP, ADP, and Mg2+. *Biophysical journal*, 88(3), pp.2234–49.

Mohabir, R., Lee, H.C., Kurz, R.W. & Clusin, W.T., 1991. Effects of ischemia and hypercarbic acidosis on myocyte calcium transients, contraction, and pHi in perfused rabbit hearts. *Circulation research*, 69(6), pp.1525–37.

Moreno, J., Zaitsev, A. V, Warren, M., Berenfeld, O., Kalifa, J., Lucca, E., Mironov, S., Guha, P. & Jalife, J., 2005. Effect of remodelling, stretch and ischaemia on ventricular fibrillation frequency and dynamics in a heart failure model. *Cardiovascular research*, 65(1), pp.158–66.

Morgan, J.M., Cunningham, D. & Rowland, E., 1992. Dispersion of monophasic action potential duration: demonstrable in humans after premature ventricular extrastimulation but not in steady state. *Journal of the American College of Cardiology*, 19(May), pp.1244–1253.

Murphy, E., Steenbergen, C., Levy, L. a, Raju, B. & London, R.E., 1989. Cytosolic free magnesium levels in ischemic rat heart. *The Journal of biological chemistry*, 264(10), pp.5622–5627.

Muzikant, a. L. & Henriquez, C.S., 1998. Validation of three-dimensional conduction

models using experimental mapping: Are we getting closer? *Progress in Biophysics and Molecular Biology*, 69, pp.205–223.

Nagatomo, T., Fan, Z., Ye, B., Tonkovich, G.S., January, C.T., Kyle, J.W. & Makielski, J.C., 1998. Temperature dependence of early and late currents in human cardiac wild- type and long Q-T DeltaKPQ Na+ channels. *Am J Physiol*, 275(6 Pt 2), pp.H2016–24.

Nanthakumar, K., Jalife, J., Massé, S., Downar, E., Pop, M., Asta, J., Ross, H., Rao, V., Mironov, S., Sevaptsidis, E., et al., 2007. Optical mapping of Langendorff-perfused human hearts: establishing a model for the study of ventricular fibrillation in humans. *American journal of physiology. Heart and circulatory physiology*, 293(1), pp.H875–80.

Nash, M.P., Bradley, C.P., Sutton, P.M., Clayton, R.H., Kallis, P., Hayward, M.P., Paterson, D.J. & Taggart, P., 2006. Whole heart action potential duration restitution properties in cardiac patients: a combined clinical and modelling study. *Experimental physiology*, 91(2), pp.339–54.

Nash, M.P., Mourad, A., Clayton, R.H., Sutton, P.M., Bradley, C.P., Hayward, M., Paterson, D.J. & Taggart, P., 2006. Evidence for multiple mechanisms in human ventricular fibrillation. *Circulation*, 114(6), pp.536–42.

Nattel, S. & Zeng, F.D., 1984. Frequency-dependent effects of antiarrhythmic drugs on action potential duration and refractoriness of canine cardiac Purkinje fibers. *Journal of Pharmacology and Experimental Therapeutics* , 229 (1 ), pp.283–291.

Nerbonne, J. & Kass, R., 2005. Molecular physiology of cardiac repolarization. *Physiological reviews*, pp.1205–1253.

Nichols, Ripoll, C. & Lederer, W.J., 1991. ATP-sensitive potassium channel modulation of the guinea pig ventricular action potential and contraction. *Circulation research*, 68(1), pp.280–287.

Nichols, C.G. & Lederer, W.J., 1990. The regulation of ATP-sensitive K+ channel activity in intact and permeabilized rat ventricular myocytes. *The Journal of Physiology* , 423 (1 ), pp.91–110.

Nichols, C.G., Ripoll, C. & Lederer, W.J., 1991. ATP-sensitive potassium channel modulation of the guinea pig ventricular action potential and contraction. *Circulation Research*, 68(1), pp.280–287.

Nichols, G., Ripoll, C. & Lederer, W.J., 1991. ATP-sensitive potassium channel modulation of the guinea pig ventricular action potential and contraction. *Circulation Research*, 68(1), pp.280–287.

Nickerson, D. & Buist, M., 2008. Practical application of CellML 1.1: The integration of new mechanisms into a human ventricular myocyte model. *Progress in biophysics and molecular biology*, 98(1), pp.38–51.

Niederer, S. a, Fink, M., Noble, D. & Smith, N.P., 2009. A meta-analysis of cardiac electrophysiology computational models. *Experimental physiology*, 94(5), pp.486–95.

Niederer, S. a & Smith, N.P., 2007. A mathematical model of the slow force response to stretch in rat ventricular myocytes. *Biophysical journal*, 92(11), pp.4030–4044.

Nielsen, P.M., Le Grice, I.J., Smaill, B.H. & Hunter, P.J., 1991. Mathematical model of geometry and fibrous structure of the heart. *The American journal of physiology*, 260(4 Pt 2), pp.H1365–1378.

Noble, D., 1962. A modification of the Hodgkin--Huxley equations applicable to Purkinje fibre action and pace-maker potentials. *The Journal of physiology*, 160, pp.317–352.

Noble, D., 2007. From the Hodgkin-Huxley axon to the virtual heart. *The Journal of physiology*, 580(Pt 1), pp.15–22.

Noble, D., Varghese, a, Kohl, P. & Noble, P., 1998. Improved guinea-pig ventricular cell model incorporating a diadic space, IKr and IKs, and length- and tension-dependent processes. *The Canadian journal of cardiology*, 14(1), pp.123–134.

Noma, A., 1983. ATP-regulated K&plus; channels in cardiac muscle. *Nature*, 305(5930), pp.147–8.

Nordin, C., 1993. Computer model of membrane current and intracellular Ca2+ flux in the isolated guinea pig ventricular myocyte. *The American journal of physiology*, 265(6 Pt 2), pp.H2117–36.

O'Hara, T., Virág, L., Varró, A. & Rudy, Y., 2011. Simulation of the undiseased human cardiac ventricular action potential: model formulation and experimental validation. *PLoS computational biology*, 7(5), p.e1002061.

Pandit, S. V, Clark, R.B., Giles, W.R. & Demir, S.S., 2001. A mathematical model of action potential heterogeneity in adult rat left ventricular myocytes. *Biophysical journal*, 81(6), pp.3029–3051.

Pandit, S. V. & Jalife, J., 2013. Rotors and the dynamics of cardiac fibrillation. *Circulation Research*, 112, pp.849–862.

Panfilov, a. & Keener, J.P., 1995. Re-entry in an anatomical model of the heart. *Chaos, Solitons & Fractals*, 5(3-4), pp.681–689.

Panfilov, A.V., 2002. Sprial breakup in an array of coupled cells: the role of the intercellular conductance. Physical Review Letters 88, 118101.

Panfilov, a. V. & Zemlin, C.W., 2002. Wave propagation in an excitable medium with a negatively sloped restitution curve. *Chaos (Woodbury, N.Y.)*, 12(3), pp.800–806.

Panfilov, A. V. & Keener, J.P., 1995. Re-entry in three-dimensional Fitzhugh-Nagumo medium with rotational anisotropy. *Physica D: Nonlinear Phenomena*, 84(3-4), pp.545–552.

Pathmanathan, P., Bernabeu, M.O., Bordas, R., Cooper, J., Garny, A., Pitt-Francis, J.M., Whiteley, J.P. & Gavaghan, D.J., 2010. A numerical guide to the solution of the bidomain equations of cardiac electrophysiology. *Progress in Biophysics and Molecular Biology*, 102(2-3), pp.136–155.

Pelzmann, B., Schaffer, P., Bernhart, E., Lang, P., Machler, H., Rigler, B. & Koidl, B., 1998. L-type calcium current in human ventricular myocytes at a physiological temperature from children with tetralogy of Fallot. *Cardiovasc Res*, 38, pp.424–432.

Penland, R.C., Harrild, D.M. & Henriquez, C.S., 2002. Modeling impulse propagation and extracellular potential distributions in anisotropic cardiac tissue using a finite volume element discretization. *Computing and Visualization in Science*, 4(4), pp.215–226.

Péréon, Y. & Demolombe, S., 2000. Differential expression of KvLQT1 isoforms across the human ventricular wall. *American Journal of …*, pp.1908–1915.

Pike, M., Luo, S.U., Daniel, M., Pohost, M., Martin, M., Luo, C.S., Clark, M.D., Kirk, K.A., Kitakaze, M., Michael, C., et al., 1993. NMR measurements of Na + and cellular rat heart : role of Na + -H + exchange energy in ischemic.

Pitt-Francis, J., Bernabeu, M.O., Cooper, J., Garny, A., Momtahan, L., Osborne, J., Pathmanathan, P., Rodriguez, B., Whiteley, J.P. & Gavaghan, D.J., 2008. Chaste: using agile programming techniques to develop computational biology software. *Philosophical transactions. Series A, Mathematical, physical, and engineering sciences*, 366(1878), pp.3111–36.

Pogwizd, S.M. & Corr, P.B., 1987. Reentrant and nonreentrant mechanisms contribute to arrhythmogenesis during early myocardial ischemia: results using three-dimensional mapping. *Circ Res*, 61(3), pp.352–371.

Pogwizd, S.M., Onufer, J.R., Kramer, J.B., Sobel, B.E. & Corr, P.B., 1986. Induction of delayed afterdepolarizations and triggered activity in canine Purkinje fibers by lysophosphoglycerides SM Pogwizd, JR Onufer, JB Kramer, BE Sobel and PB Corr Circ. Res. 1986;59;416-426. *American Aeart association*.

Pollard, A.E. & Barr, R.C., 1991. Computer Simulations of Activation in an Anatomically Based Model of the Human Ventricular Conduction System. *IEEE Transactions on Biomedical Engineering*, 38(10), pp.982–996.

Potse, M., Dubé, B., Richer, J., Vinet, A. & Gulrajani, R.M., 2006. A comparison of monodomain and bidomain reaction-diffusion models for action potential propagation in the human heart. *IEEE transactions on bio-medical engineering*, 53(12 Pt 1), pp.2425–35.

Press, W.H., Teukolsky, S. a, Vetterling, W.T. & Flannery, B.P., 1992. *Numerical recipes in C (2nd ed.): the art of scientific computing*,

Priebe, L. & Beuckelmann, D.J., 1998. Simulation Study of Cellular Electric Properties in Heart Failure. *Circulation Research*, 82(11), pp.1206–1223.

Puglisi, J.L. & Bers, D.M., 2001. LabHEART: an interactive computer model of rabbit ventricular myocyte ion channels and Ca transport. *Am J Physiol Cell Physiol*, 281(6), pp.C2049–2060.

Pullan, A.J., Buist, M.L., Sands, G.B., Cheng, L.K. & Smith, N.P., 2003. Cardiac electrical activity--from heart to body surface and back again. *Journal of electrocardiology*, 36 Suppl, pp.63–67.

Qu, Z., Garfinkel,  a, Chen, P.S. & Weiss, J.N., 2000. Mechanisms of discordant alternans and induction of reentry in simulated cardiac tissue. *Circulation*, 102, pp.1664–1670.

Qu, Z., Hu, G., Garfinkel, A. & Weiss, J.N., 2014. Nonlinear and stochastic dynamics in the

heart. *Physics Reports*.

Qu, Z., Kil, J., Xie, F., Garfinkel, A. & Weiss, J.N., 2000. Scroll wave dynamics in a three-dimensional cardiac tissue model: roles of restitution, thickness, and fiber rotation. *Biophysical journal*, 78(6), pp.2761–75.

Qu, Z., Weiss, J.N. & Garfinkel, a, 1999. Cardiac electrical restitution properties and stability of reentrant spiral waves: a simulation study. *The American journal of physiology*, 276, pp.H269–H283.

Qu, Z., Xie, F., Garfinkel, a & Weiss, J.N., 2000. Origins of spiral wave meander and breakup in a two-dimensional cardiac tissue model. *Annals of biomedical engineering*, 28, pp.755–771.

Riccio, M.L., Koller, M.L. & Gilmour, R.F., 1999. Electrical restitution and spatiotemporal organization during ventricular fibrillation. *Circulation research*, 84, pp.955–963.

Rodriguez, B., Eason, J.C., Tice, B., Ferrero, J.M.. J. & Trayanova, N., 2003. Effect of acute global ischemia on cardiac vulnerability to electrical shocks. *Proceedings of the 25th Annual International Conference of the IEEE Engineering in Medicine and Biology Society (IEEE Cat. No.03CH37439)*, 1, pp.151–154.

Rodríguez, B., Tice, B.M., Eason, J.C., Aguel, F., Ferrero, J.M. & Trayanova, N., 2004. Effect of acute global ischemia on the upper limit of vulnerability: a simulation study. *American journal of physiology. Heart and circulatory physiology*, 286(6), pp.H2078–88.

Rodríguez, B., Trayanova, N. & Noble, D., 2006. Modeling cardiac ischemia. *Annals of the New York Academy of Sciences*, 1080, pp.395–414.

Rodriguez, J.F., Heidenreich, E.A., Romero, L., Jr, J.M.F., Doblare, M., Zaragoza, U. De & Valencia, U.P. De, 2008. Post-Repolarization Refractoriness in Human Ventricular Cardiac Cells. , pp.581–584.

Rogers, J.M., Huang, J., Smith, W.M. & Ideker, R.E., 1999. Incidence, evolution, and spatial distribution of functional reentry during ventricular fibrillation in pigs. *Circulation research*, 84, pp.945–954.

Rohr, S., Kucera, J.P. & Fast, V.G., 1997. Paradoxical Improvement of Impulse Conduction in Cardiac Tissue by Partial Cellular Uncoupling. , 275(February).

Romero, L., Heidenreich, E., Rodriguez, J.F., Trenor, B., Ferrero, J.M., Saiz, J. & Doblare, M., 2008. Reentrant activity in a virtual 3D ventricular slab preparation subject to regional simulated ischemia: role of the ischemic zone size. In *Computers in Cardiology*. pp. 1025–1028.

Romero, L., Pueyo, E., Fink, M. & Rodríguez, B., 2009a. Impact of ionic current variability on human ventricular cellular electrophysiology. *American journal of physiology. Heart and circulatory physiology*, 297(4), pp.H1436–45.

Romero, L., Pueyo, E., Fink, M. & Rodríguez, B., 2009b. Impact of ionic current variability on human ventricular cellular electrophysiology. *American journal of physiology. Heart and circulatory physiology*, 297, pp.H1436–H1445.

Romero, L., Trénor, B., Alonso, J.M., Tobón, C., Saiz, J. & Ferrero, J.M., 2009. The relative role of refractoriness and source-sink relationship in reentry generation during simulated acute ischemia. *Annals of Biomedical Engineering*, 37(8), pp.1560–1571.

Rudy, Y., Silva, J.R. & Einstein, A., 2007. NIH Public Access. *Cell*, 39(1), pp.57–116.

Russ, U., Englert, H., Scholkens, B. a & Gogelein, H., 1996. Simultaneous recording of ATP-sensitive K+ current and intracellular Ca2+ in anoxic rat ventricular myocytes. Effects of glibenclamide. *Pflugers Arch*, 432(1), pp.75–80.

Sah, R., Ramirez, R.J., Oudit, G.Y., Gidrewicz, D., Trivieri, M.G., Zobel, C. & Backx, P.H., 2003. Regulation of cardiac excitation-contraction coupling by action potential repolarization: role of the transient outward potassium current (I(to)). *The Journal of physiology*, 546(March 2002), pp.5–18.

SAKAKIBARA, Y., FURUKAWA, T., SINGER, D.H., JIA, H., BACKER, C.L., ARENTZEN, C.E. & ANDREW, J.W., 1993. Sodium current in isolated human ventricular myocytes. *American Journal of …*.

Sakakibara, Y., Wasserstrom, J. a, Furukawa, T., Jia, H., Arentzen, C.E., Hartz, R.S. & Singer, D.H., 1992. Characterization of the sodium current in single human atrial myocytes. *Circulation research*, 71(3), pp.535–546.

Sampson, K.J., Henriquez, C.S., Engineering, B., Carolina, N., Kevin, J. & Simula-, C.S.H., 2001. Presence of Structural and Ionic Heterogeneity. *Society*, pp.2597–2603.

Sasaki, N., Mitsuiye, T., Noma, A. & Powell, T., 1999. Sarcomere length during contraction of isolated guinea-pig ventricular myocytes. *Pflugers Archiv : European journal of physiologygers Archiv European Journal of Physiology*, 437(6), pp.804–811.

Schmitt, N., Grunnet, M. & Olesen, S.-P., 2014. Cardiac potassium channel subtypes: new roles in repolarization and arrhythmia. *Physiological reviews*, 94, pp.609–53.

Schneider, M., Proebstle, T., Hombach, V., Hannekum, a. & R??del, R., 1994. Characterization of the sodium currents in isolated human cardiocytes. *Pfl??gers Archiv European Journal of Physiology*, 428(1), pp.84–90.

Schreur, J.H., de Beer, R., Van Echteld, C.J. & Ruigrok, T.J., 1993. Post-ischemic contractile dysfunction does not correlate with an elevated intracellular free [Mg2+]: a 31P-NMR study on isolated rat and rabbit hearts. *J Mol Cell Cardiol*, 25(9), pp.1015–1024.

Seemann, G., Sachse, F.B., Karl, M., Weiss, D.L., Heuveline, V. & Dössel, O., 2010. Framework for modular, flexible and efficient solving the cardiac bidomain equation using PETSc. *Mathematics in Industry*, 15(2), pp.363–369.

Shannon, T.R., Wang, F., Puglisi, J., Weber, C. & Bers, D.M., 2004. A mathematical treatment of integrated \textit{{C}a} dynamics within the ventricular myocyte. *Biophys. J*, 87(November), pp.3351–3371.

Shannon, T.R., Wang, F., Puglisi, J., Weber, C. & Bers, D.M., 2004. A mathematical treatment of integrated Ca dynamics within the ventricular myocyte. *Biophysical journal*, 87(5), pp.3351–71.

Shaw, R. & Rudy, Y., 1994. Electrophysiological changes of ventricular tissue under ischemic conditions: a simulation study. *Computers in Cardiology 1994*, pp.641–644.

Shaw, R.M. & Rudy, Y., 1997. Electrophysiologic effects of acute myocardial ischemia: a theoretical study of altered cell excitability and action potential duration. *Cardiovascular research*, 35(2), pp.256–72.

Silverman, H.S., Di Lisa, F., Hui, R.C., Miyata, H., Sollott, S.J., Hanford, R.G., Lakatta, E.G. & Stern, M.D., 1994. Regulation of intracellular free Mg2+ and contraction in single adult mammalian cardiac myocytes. *Am J Physiol*, 266(1 Pt 1), pp.C222–33.

Smith, G.L. & Allen, D.G., 1988. Effects of metabolic blockade on intracellular calcium concentration in isolated ferret ventricular muscle. *Circulation research*, 62(6), pp.1223–1236.

Smith, P.L. & Yellen, G., 2002. Fast and slow voltage sensor movements in HERG potassium channels. *The Journal of general physiology*, 119(3), pp.275–93.

Smith, W.T., Fleet, W.F., Johnson, T.A., Engle, C.L., Cascio, W.E. & Carolina, for the E.C.G.U. of N., 1995. The Ib Phase of Ventricular Arrhythmias in Ischemic In Situ Porcine Heart Is Related to Changes in Cell-to-Cell Electrical Coupling. *Circulation* , 92 (10 ), pp.3051–3060.

Spach, M.S., Dolber, P.C. & Heidlage, J.F., 1989. Interaction of inhomogeneities of repolarization with anisotropic propagation in dog atria. A mechanism for both preventing and initiating reentry. *Circulation research*, 65(6), pp.1612–1631.

Spach, M.S., Heidlage, J.F., Dolber, P.C. & Barr, R.C., 2000. Electrophysiological effects of remodeling cardiac gap junctions and cell size: experimental and model studies of normal cardiac growth. *Circulation research*, 86(3), pp.302–311.

Stolze, C.H., 1978. A history of the divergence theorem. Historia Mathematica, 5(4), pp.437–442.

SURAWICZ, B., 1985. Ventricular fibrillation. *La Presse medicale*, 76(6), pp.1825–1826.

Sutton, P.M., Taggart, P., Opthof, T., Coronel, R., Trimlett, R., Pugsley, W. & Kallis, P., 2000a. Repolarisation and refractoriness during early ischaemia in humans. *Heart (British Cardiac Society)*, 84(4), pp.365–9.

Sutton, P.M., Taggart, P., Opthof, T., Coronel, R., Trimlett, R., Pugsley, W. & Kallis, P., 2000b. Repolarisation and refractoriness during early ischaemia in humans. *Heart (British Cardiac Society)*, 84(4), pp.365–9.

Tabereaux, P.B., Dosdall, D.J. & Ideker, R.E., 2009. Mechanisms of VF maintenance: Wandering wavelets, mother rotors, or foci. *Heart Rhythm*, 6(3), pp.405–415.

Taggart, P., 2002. Effect of Adrenergic Stimulation on Action Potential Duration Restitution in Humans. *Circulation*, 107(2), pp.285–289.

Taggart, P., Sutton, P.M., Boyett, M.R., Lab, M. & Swanton, H., 1996. Human ventricular action potential duration during short and long cycles. Rapid modulation by ischemia. *Circulation*, 94(10), pp.2526–2534.

Taggart, P., Sutton, P.M., Opthof, T., Coronel, R., Trimlett, R., Pugsley, W. & Kallis, P., 2000a. Inhomogeneous transmural conduction during early ischaemia in patients with coronary artery disease. *Journal of molecular and cellular cardiology*, 32(4), pp.621–30.

Taggart, P., Sutton, P.M., Opthof, T., Coronel, R., Trimlett, R., Pugsley, W. & Kallis, P., 2000b. Inhomogeneous transmural conduction during early ischaemia in patients with coronary artery disease. *Journal of molecular and cellular cardiology*, 32(4), pp.621–630.

Takayama, E., Guo, L.-L., Digerness, S.B. & Pike, M.M., 2004. Early reperfusion levels of Na(+) and Ca(2+) are strongly associated with postischemic functional recovery but are disassociated from K(ATP) channel-induced cardioprotection. *Journal of molecular and cellular cardiology*, 37(2), pp.483–96.

Tanaka, M., Gilbert, J. & Pappano, A.J., 1992. Inhibition of Sodium Pump by l-Palmitoylcarnitine Ventricular Myocytes in single. , 720.

Tani, M. & Neely, J.R., 1989. Role of intracellular Na+ in Ca2+ overload and depressed recovery of ventricular function of reperfused ischemic rat hearts. Possible involvement of H+-Na+ and Na+-Ca2+ exchange. *Circulation research*, 65(4), pp.1045–1056.

Terkildsen, J.R., Crampin, E.J. & Smith, N.P., 2007. The balance between inactivation and activation of the Na+-K+ pump underlies the triphasic accumulation of extracellular K+ during myocardial ischemia. *American journal of physiology. Heart and circulatory physiology*, 293(5), pp.H3036–45.

Terzic, a, Jahangir, a & Kurachi, Y., 1995. Cardiac ATP-sensitive K+ channels: regulation by intracellular nucleotides and K+ channel-opening drugs. *The American journal of physiology*, 269(Table 1), pp.C525–C545.

Thandroyen, F.T., Morris, a C., Hagler, H.K., Ziman, B., Pai, L., Willerson, J.T. & Buja, L.M., 1991. Intracellular calcium transients and arrhythmia in isolated heart cells. *Circ Res*, 69(3), pp.810–819.

Trafford, A.W., Díaz, M.E., Negretti, N. & Eisner, D.A., 1997. Enhanced Ca2+ current and decreased Ca2+ efflux restore sarcoplasmic reticulum Ca2+ content after depletion. *Circulation research*, 81(4), pp.477–84.

Tran, D.X., Yang, M.-J., Weiss, J.N., Garfinkel, A. & Qu, Z., 2007. Vulnerability to re-entry in simulated two-dimensional cardiac tissue: effects of electrical restitution and stimulation sequence. *Chaos (Woodbury, N.Y.)*, 17(4), p.043115.

Trayanova, N., 2006. Defibrillation of the heart: insights into mechanisms from modelling studies. *Experimental physiology*, 91(2), pp.323–337.

Trenor, B., Romero, L., Cardona, K., Gomis, J., Saiz, J., Maria, J. & Jr, F., 1952. Multiscale Modeling of Myocardial Electrical Activity : From Cell to Organ. , 1952.

Trew, M., Le Grice, I., Smaill, B. & Pullan, A., 2005. A finite volume method for modeling discontinuous electrical activation in cardiac tissue. *Ann Biomed Eng*, 33(5), pp.590–602.

Ten Tusscher, K.H.W.J. and A.V.P. & Panfilov, A. V, 2006. Alternans and spiral breakup in

a human ventricular tissue model. *American journal of physiology. Heart and circulatory physiology*, 291(3), pp.H1088–H1100.

Ten Tusscher, K.H.W.J., Mourad, A., Nash, M.P., Clayton, R.H., Bradley, C.P., Paterson, D.J., Hayward, M.P., Panfilov, A.V., Taggart, P., 2009. Organization of ventricular fibrillation in the human heart: experiments and models. Experimental Physiology 94,pp. 553-562.

Tusscher, K.H.W.J. & Panfilov, A. V, 2006. Alternans and spiral breakup in a human ventricular tissue model. *American Journal of …*, pp.1088–1100.

Ten Tusscher, K.H.W.J., Hren, R. & Panfilov, A. V, 2007. Organization of ventricular fibrillation in the human heart. *Circulation research*, 100(12), pp.e87–101.

ten Tusscher, K.H.W.J., Noble, D., Noble, P.J. & Panfilov, A. V, 2004. A model for human ventricular tissue. *American journal of physiology. Heart and circulatory physiology*, 286(4), pp.H1573–89.

Ten Tusscher, K.H.W.J. & Panfilov, V., 2006. Alternans and spiral breakup in a human ventricular tissue model. *American Journal of*, 291(3), p.H1088.

Valderrábano, M., Lee, M.H., Ohara, T., Lai, a C., Fishbein, M.C., Lin, S.F., Karagueuzian, H.S. & Chen, P.S., 2001. Dynamics of intramural and transmural reentry during ventricular fibrillation in isolated swine ventricles. *Circulation research*, 88, pp.839–848.

Valderrábano, M., Yang, J., Omichi, C., Kil, J., Lamp, S.T., Qu, Z., Lin, S.F., Karagueuzian, H.S., Garfinkel, A., Chen, P.S., et al., 2002. Frequency analysis of ventricular fibrillation in swine ventricles. *Circulation Research*, 90, pp.213–222.

Vanheel, B. & Hemptinne, a D., 1992. Influence of KATP channel modulation on net potassium efflux from ischaemic mammalian cardiac tissue. *Cardiovascular Research*, 26(11), pp.1030–1039.

Venable, P.W., Taylor, T.G., Shibayama, J., Warren, M. & Zaitsev, A. V, 2010. Complex structure of electrophysiological gradients emerging during long-duration ventricular fibrillation in the canine heart. *American journal of physiology. Heart and circulatory physiology*, 299(5), pp.H1405–18.

Verkerk, a O., Veldkamp, M.W., van Ginneken, a C. & Bouman, L.N., 1996. Biphasic response of action potential duration to metabolic inhibition in rabbit and human ventricular myocytes: role of transient outward current and ATP-regulated potassium current. *Journal of Molecular and Cellular Cardiology*, 28(12), pp.2443–2456.

Vigmond, E., Vadakkumpadan, F., Gurev, V., Arevalo, H., Deo, M., Plank, G. & Trayanova, N., 2009. Towards predictive modelling of the electrophysiology of the heart. *Experimental physiology*, 94(5), pp.563–77.

Vigmond, E.J., Aguel, F. & Trayanova, N. a., 2002. Computational techniques for solving the bidomain equations in three dimensions. *IEEE Transactions on Biomedical Engineering*, 49(11), pp.1260–1269.

Viswanathan, P.C., Bezzina, C.R., George, A.L., Roden, D.M., Wilde, A. a M. & Balser,

J.R., 2001. Gating-Dependent Mechanisms for Flecainide Action in SCN5A -Linked Arrhythmia Syndromes. *American Heart Association*.

Viswanathan, P.C. & Rudy, Y., 2000. Cellular arrhythmogenic effects of congenital and acquired long-QT syndrome in the heterogeneous myocardium. *Circulation*, 101(10), pp.1192–1198.

Wagner, S., Dybkova, N., Rasenack, E.C.L., Jacobshagen, C., Fabritz, L., Kirchhof, P., Maier, S.K.G., Zhang, T., Hasenfuss, G., Brown, J.H., et al., 2006. Ca 2/calmodulin-dependent protein kinase II regulates cardiac Na channels. *Journal of Clinical Investigation*, 116(12), pp.3127–3138.

Wagner, S., Wu, S.T. & Parmley, W.W., 1990. Influence of ischemia on [ Ca *'] i transients following drug therapy in heatis from aortic constricted rats. , pp.431–444.

Wan, X., Chen, S., Sadeghpour,  a, Wang, Q. & Kirsch, G.E., 2001. Accelerated inactivation in a mutant Na(+) channel associated with idiopathic ventricular fibrillation. *American journal of physiology. Heart and circulatory physiology*, 280(1), pp.H354–H360.

Wang, D.W., Makita, N., Kitabatake,  a, Balser, J.R. & George Jr.,  a L., 2000. Enhanced Na(+) channel intermediate inactivation in Brugada syndrome. *Circ.Res.*, 87(1524-4571 SB - IM), pp.E37–E43.

Wang, L.J. & Sobie, E. a, 2008. Mathematical model of the neonatal mouse ventricular action potential. *American journal of physiology. Heart and circulatory physiology*, 294, pp.H2565–H2575.

Wang, S.Y., Dong, L. & Langer, G. a, 1997. Matching Ca efflux and influx to maintain steady-state levels in cultured cardiac cells. Flux control in the subsarcolemmal cleft. *Journal of molecular and cellular cardiology*, 29(5), pp.1277–87.

Watanabe, I., Kanda, A., Engle, C.L. & Gettes, L.S., 1997. Comparison of the Effects of Regional Ischemia and Hyperkalemia on the Membrane Action Potentials of the In Situ Pig  Heart. *Journal of Cardiovascular Electrophysiology*, 8, pp.1229–1236.

Watson, C.L. & Gold, M.R., 1995. Effect of intracellular and extracellular acidosis on sodium current in ventricular myocytes. *American Journal of Physiology*, 268(4 Pt 2), pp.H1749–56.

Weiss, D.L., Ifland, M., Sachse, F.B., Seemann, G. & Dössel, O., 2009. Modeling of cardiac ischemia in human myocytes and tissue including spatiotemporal electrophysiological variations. *Biomedizinische Technik. Biomedical engineering*, 54(3), pp.107–25.

Weiss, J., Venkatesh, N. & Lamp, S., 1992. ATP-sensitive K+ channels and cellular K+ loss in hypoxic and ischaemic mammalian ventricle. *The Journal of physiology*, (1992), pp.649–673.

Weiss, J.N., Chen, P.S., Qu, Z., Karagueuzian, H.S. & Garfinkel,  a, 2000. Ventricular fibrillation: how do we stop the waves from breaking? *Circulation research*, 87, pp.1103–1107.

Weiss, J.N., Qu, Z., Chen, P.-S., Lin, S.-F., Karagueuzian, H.S., Hayashi, H., Garfinkel, A. & Karma, A., 2005. The dynamics of cardiac fibrillation. *Circulation*, 112(8), pp.1232–40.

Weiss, J.N. & Shine, K.I., 1982. Extracellular K+ accumulation during myocardial ischemia in isolated rabbit heart. *American Journal of Physiology*, 242(4), pp.H619–28.

Wellens, H.J., 2004. Cardiac Electrophysiology: From Cell to Bedside, Fourth Edition. *Circulation*, 110(17), pp.e453–e453.

Wilde, a. a., Escande, D., Schumacher, C. a., Thuringer, D., Mestre, M., Fiolet, J.W. & Janse, M.J., 1990. Potassium accumulation in the globally ischemic mammalian heart. A role for the ATP-sensitive potassium channel. *Circulation Research*, 67(4), pp.835–843.

Wilde, A. a. M., Escande, D., Schumacher, C. a., Thuringer, D., Mestre, M., Fiolet, J.W.T. & Janse, M.J., 1990. Potassium accumulation in the globally ischemic mammalian heart. A role for the ATP-sensitive potassium channel. *Circulation Research*, 67(4), pp.835–43.

Wilde, A.A. & Aksnes, G., 1994. Myocardial potassium loss and cell depolarisation in ischaemia and hypoxia. *Cardiovascular Research*, 28(9), pp.1–15.

Wilensky, R.L., Tranum-Jensen, J., Coronel, R., Wilde, a a, Fiolet, J.W. & Janse, M.J., 1986. The subendocardial border zone during acute ischemia of the rabbit heart: an electrophysiologic, metabolic, and morphologic correlative study. *Circulation*, 74(5), pp.1137–1146.

Winfree, A.T., 1998. A spatial scale factor for electrophysiological models of myocardium. Progress in Biophysics & Molecular Biology 69,pp. 185-203.

Winslow, R.L., Rice, J., Jafri, S., Marban, E. & O'Rourke, B., 1999. Mechanisms of Altered Excitation-Contraction Coupling in Canine Tachycardia-Induced Heart Failure, II : Model Studies. *Circulation Research*, 84(5), pp.571–586.

Wu, M.L. & Vaughan-Jones, R.D., 1994. Effect of metabolic inhibitors and second messengers upon Na(+)-H+ exchange in the sheep cardiac Purkinje fibre. *J Physiol*, 478 ( Pt 2, pp.301–313.

Wu, T.J., Lin, S.F., Weiss, J.N., Ting, C.T. & Chen, P.S., 2002. Two types of ventricular fibrillation in isolated rabbit hearts: Importance of excitability and action potential duration restitution. *Circulation*, 106, pp.1859–1866.

Xie, F., Qu, Z., Garfinkel, a & Weiss, J.N., 2001. Electrophysiological heterogeneity and stability of reentry in simulated cardiac tissue. *American journal of physiology. Heart and circulatory physiology*, 280, pp.H535–H545.

Xie, F., Qu, Z., Garfinkel, A. & Weiss, J.N., 2002a. Electrical refractory period restitution and spiral wave reentry in simulated cardiac tissue. *American journal of physiology. Heart and circulatory physiology*, 283, pp.H448–H460.

Xie, F., Qu, Z., Garfinkel, A. & Weiss, J.N., 2002b. Electrical refractory period restitution and spiral wave reentry in simulated cardiac tissue. *American journal of physiology. Heart and circulatory physiology*, 283(1), pp.H448–H460.

Xie, F., Qu, Z., Yang, J. & Baher, A., 2004. A simulation study of the effects of cardiac anatomy in ventricular fibrillation. *The Journal of Clinical Investigation*, 113(5).

Xu, A. & Guevara, M.R., 1998. Two forms of spiral-wave reentry in an ionic model of

ischemic ventricular myocardium. *Chaos*, 8(1), pp.157–174.

Yan, G.X., Park, T.H. & Corr, P.B., 1995. Activation of thrombin receptor increases intracellular Na+ during myocardial ischemia. *Am J Physiol*, 268(0002-9513), pp.H1740–H1748.

Yan, G.X., Shimizu, W. & Antzelevitch, C., 1998. Characteristics and distribution of M cells in arterially perfused canine left ventricular wedge preparations. *Circulation*, 98, pp.1921–1927.

Yan, G.X., Yamada, K. a., Kleber, a. G., McHowat, J. & Corr, P.B., 1993. Dissociation between cellular K+ loss, reduction in repolarization time, and tissue ATP levels during myocardial hypoxia and ischemia. *Circulation Research*, 72(3), pp.560–570.

Yue, A.M., Franz, M.R., Roberts, P.R. & Morgan, J.M., 2005. Global endocardial electrical restitution in human right and left ventricles determined by noncontact mapping. *Journal of the American College of Cardiology*, 46(6), pp.1067–1075.

Zhang, H., Holden, a V, Kodama, I., Honjo, H., Lei, M., Varghese, T. & Boyett, M.R., 2000. Mathematical models of action potentials in the periphery and center of the rabbit sinoatrial node. *Am J Physiol Heart Circ Physiol*, 279(1), pp.H397–421.

Zhang, J.F. & Siegelbaum, S. a, 1991. Effects of external protons on single cardiac sodium channels from guinea pig ventricular myocytes. *J Gen Physiol*, 98(6), pp.1065–1083.

Zhou, Z., Gong, Q., Ye, B., Fan, Z., Makielski, J.C., Robertson, G. a & January, C.T., 1998. Properties of HERG channels stably expressed in HEK 293 cells studied at physiological temperature. *Biophysical journal*, 74(1), pp.230–41.

Zhuchkova, E. & Clayton, R., 2005. Methods for identifying and tracking phase singularities in computational models of re-entrant fibrillation. *Functional Imaging and Modeling of the Heart*, pp.246–255.

**Websites:**

Carp.meduni-graz.at,. 'Cardiac Arrhythmia Research Package'. Web. 5 Mar. 2015.

Cellml.org,. 'The Cellml Project Cellml'. Web. 5 Mar. 2015.

Continuity.ucsd.edu,. 'Continuity - Cardiac Mechanics Research Group'. Web. 5 Mar. 2015.

Cor.physiol.ox.ac.uk,. 'COR: C: - Sites - COR'. Web. 5 Mar. 2015.

'Index Of /Cardiac Arrhythmia'. *Scholarpedia.com*. N.p., 2008.

Gimias.org,. 'Graphical Interface For Medical Image Analysis And Simulation'. Web. 5 Mar. 2015.

LifeV.org,. 'Lifev'. Web. 5 Oct. 2015.

Oxford, University. 'Chaste - Cancer, Heart And Soft Tissue Environment'. *Cs.ox.ac.uk*. Web. 5 Mar. 2015.

Physiome.org,. 'Jsim Home Page'. Web. 5 Mar. 2015.

Physiomeproject.org,. 'Physiome Project: Opencmiss'. Web. 5 Mar. 2015.